Impact of laser powder bed fusion process defects on mechanical properties of Ti6Al4V mandible implants

-Johan Adriaan Wessels-

Dissertation submitted in fulfilment of the requirements for the degree

MASTER of ENGINEERING in MECHANICAL ENGINEERING

in the Department of Mechanical and Mechatronics Engineering

Faculty of Engineering, Built Environment and Information Technology

at the Central University of Technology, Free State

Supervisor: Dr Ina Yadroitsava, Ph.D.

Co-supervisors: Prof Ihar Yadroitsau, D.Eng.

Mr Johan Els, M.Eng.

Bloemfontein

July 2020

It's not about having the skill to do something.
It's about having the will, desire & commitment to be your best.

Robert Hernandez

Declaration of independent work

I, Johan Adriaan Wessels, identity number and student number , do hereby declare that this research project submitted to the Central University of Technology, Free State (CUT, FS) for the Master of Engineering in Mechanical Engineering degree, is my own independent work; and complies with the Code of Academic integrity, as well as other relevant policies, procedures, rules and regulations of the Central University of Technology, Free State; and has not been submitted previously to any institution by myself or any other person in fulfilment of the requirements for the attainment of any qualification.

SIGNATURE OF STUDENT:  DATE: 27 July 2020

Acknowledgements

First and foremost, I would like to thank God for his never-ending grace, mercy, and provision during this journey. It can be so easy to give into worry, fear and despair, but with Him we can find strength, and look forward to wonderful things. The Lord gives us hope.

Psalm 23: 1-3. "[1]The Lord is my shepherd; I shall not want. [2]He makes me lie down in green pastures. He leads me beside still waters .[3]He restores my soul. He leads me in paths of righteousness for his name's sake."

Mark 10:27. [27]Jesus looked at them and said, "With men it is impossible but with God; for with GOD ALL THINGS ARE POSSIBLE".

I would like to express my deep gratitude to my research supervisors, Dr Ina Yadroitsava, Prof Ihar Yadroitsau and Mr Johan Els, for their patient guidance, enthusiastic encouragement and useful critiques of this research work. I would like to express my very great appreciation to Prof Anton du Plessis for his assistance in academic writing and professional microCT scanning contributions.

Dr Maina Maringa provided me with very valuable mathematical guidance in stress analysis. Advice given by Mr Francis Monaheng has been a great help. I wish to acknowledge the assistance provided by Mr Dean Kouprianoff in experimental inputs and proceedings. My special thanks are extended to the staff of PDTS for the mechanical refinement of the tested samples and Marius Zwemstra at Ametex (Pty) Ltd for the exceptional assistance in FEA analysis.

No words can express the power and heroism of a parent's love. The most overwhelming key to my success is the positive involvement of my parents. Last but not least, to my friends for making so many ordinary moments extraordinary; few have the privilege of having such supportive friends.

This work was supported by the South African Research Chairs Initiative of the Department of Science and Technology and National Research Foundation of South Africa (Grant №97994) and the Collaborative Program in Additive Manufacturing (Contract №CSIR-NLC-CPAM-15-MOA-CUT-01).

Motivation:

God's plan for you is bigger than your past. *Proverbs 16:9 "[9]A man's heart plans his way, but the Lord directs his steps"*. Never let fear decide your future. *"Our deepest fear is not that we are inadequate. Our deepest fear is that we are powerful beyond measure. It is our light not our darkness, that most frightens us. We ask ourselves, 'who am I to be brilliant, gorgeous, talented, and famous?' Actually, who are you not to be? You are a child of God"…*

Maryanne Williamson

Abstract

Each year millions of patients' quality of life is improved through surgical procedures involving medical implanted devices. The need for new implants, treatments and prostheses, as well as prolonging the life span of current implants has increased; the global prosthetics and orthotics market size is expected to reach $11.7 billion by 2025, as indicated in Healthcare Market Report (2020). Additive manufacturing (AM) was implemented in the medical field fairly recently. Despite the enormous contribution medical devices have made to the public health, there is a fear of possible liability exposure in the event of device malfunction or failure. Efficient quality control of implants produced by new AM technologies is an important task for suppliers in order to be in full compliance with existing regulations and certification of such implants. If any defects occur, implant strength will directly influence the part's mechanical properties and performance, leading to the redistribution of stress and change in displacements affecting attached bone tissue and mineral matrix of the bone, resulting in implant failure. For wide applications in the medical industry, it is crucial that AM implants comply with international standards with regard to their mechanical properties. Three point bending tests (TPB) were carried out in this work on AM Ti6Al4V ELI specimens. TPB is a common tool used to characterize bone material properties and mechanical performance of biomaterials. Powder bed fusion is the unique AM method to produce metal objects with complex geometries and internal structures; it permits the manufacture of complex-shaped functional 3D objects such as customized implants. The benefits of AM in bone reconstruction using metal alloys are unquestionable in terms of customization of implants and production time. Comprehensive analysis of the laser powder bed fusion (LPBF) process together with functional anatomy biomechanics of the human mandible was done in this work. Some case studies on defects found in LPBF implants were evaluated. Based on biomechanics of the human mandible, LPBF Ti6Al4V ELI samples were designed. Experiments and numerical simulations of samples with sizes and placements of artificial pores were done. All samples were tested perpendicular to the vertical building direction and showed no signs of failure at a single loading pattern. Defects were designed and induced in the additive manufacturing of test samples of titanium, with different size and placement. Results indicate that defects of 1000 µm×300 µm×210 µm and 1000 µm×500 µm×420 µm at various depth to the neutral axis had no significant outcome on the mechanical performance of the samples with size of 100 mm ×15 mm × 2.5 mm when it was tested statically at loading of 800, 900 and 1500 N, representing a maximum biting force. This approach is a promising method of setting up a critical pore size to failure tolerance for AM implants with some defects.

TABLE OF CONTENTS

List of Figures

List of Tables

Glossary

3D	3-Dimensional
AD	Artificial Defect
AM	Additive Manufacturing
ASTM	American Society for Testing and Materials
BCC	Body Centered Cubic
CAD	Computer Aided Design
CAD	ComputerAided Design
CRPM	Centre for Rapid Prototyping and Manufacturing
CT	Computer Tomography
CUT	Central University of Technology, Free State
DMLS	Direct Metal Laser Sintering
EBM	Electron Beam Melting
ECM	Extracellular Matrix
ELI	Extra Low Interstitials
EOS	Electro Optical Systems
FE	Finite Element
FEA	Finite Element Analysis
FEM	Finite Element Modelling
FFF	Fibular Flap
FoS	Factor of Safety
HCP	Hexagonal Close Packed
HIP	Hot Isostatic Pressing
ISO	International Organization for Standardization
LBM	Laser Beam Melting
LM	Laser Melting
LMF	Laser Metal Fusion
LPBF	Laser Powder Bed Fusion
MPB	Molten Pool Boundaries
MRI	Magnetic Resonance Imaging
PBF	Powder Bed Fusion
PMC	Polymer Matrix Composite

RP	Rapid Prototyping
RS	Reference Sample
SD	Standard Deviation
SEM	Scanning Electron Microscopy
SLM	Selective Laser Melting
SLS	Selective laser sintering
STL	Standard Triangle Language
TE	Tissue Engineering
TPB	Three-Point Bending

Nomenclature

Beam thickness	d
Bending moment	Mx
Contact area	$b_{contact}$
Contact modulus	E^*
Contact stress	$Pmax$
Crosshead	D
Deflection	y
Distance	a, x
Effect of the reaction force	R
Elastic modulus	E
Flexural strain	ε_f
Flexural stress	σ_f-
Load	P
Loading force	F
Nose radius	r
Poisson's ratio	υ
Second moment of area	I_x
Slope of the tangent	m
Span length	L
Width of the beam	b

Publications

Wessels, J., du Plessis, A., Els, J., Yadroitsava, I., and Yadroitsev, I. Laser powder bed fusion process defects and mechanical properties of Ti6Al4V ELI mandible implants. *In Proc. RAPDASA 19th International Conference "Additive Manufacturing as a key driver of the 4th Industrial Revolution",* Resolution Circle Towers, Johannesburg, South Africa, November, 6–9, 2018.

Wessels, J., du Plessis, A., Yadroitsava, I., Els, J., and Yadroitsev, I. Influence of large artificial porosity on bending behaviour of TI6AL4V ELI additively manufactured specimens subjected to typical loads during mastication. *Submitted to Annual International Rapid Product Development Association of South Africa*, November, 4–6, 2020.

Presentations

Wessels, J., Yadroitsava, I., Els, J., du Plessis, A., and Yadroitsev, I. Mandibular implants: Numerical simulation and experimental tests with artificial porosity.. *RAPDASA 20th International Conference "*Creating the future of manufacturing – layer by layer" with sub-theme "Establishing the 3D printing process chain" Emoya Estate, Bloemfontein, South Africa, November 6–8, 2019. *(Presentation and published extended abstract in proceedings).*

Wessels, J.A., Els, J., du Plessis, A., Yadroitsava, I., and Yadroitsev, I. Mandible implants by additive manufacturing: present problems and future prospects. (*Presented at 17th Research seminar of Faculty of Engineering and Information Technology, Central University of Technology Free State, October 17, 2018*).

CHAPTER 1: INTRODUCTION

1.1 Background

Additive Manufacturing is defined by ASTM as "a *process of joining materials to make objects from 3D model data, usually layer upon layer, as opposed to subtractive manufacturing methodologies*" (ASTM F2792-12a). Synonyms are additive fabrication, additive processes, additive technologies, additive layer manufacturing, layer manufacturing, and freeform fabrication (Wohlers Associates). Additive manufacturing (AM), also referred to as 3D printing, is a transformative approach that enables the creation of lighter and even stronger parts that can be produced by conventional methods. AM's processability of products that were previously unthinkable present endless possibilities for product development and manufacturing around the world. The strength of AM lies in the area where conventional manufacturing reaches its limits. It enables a design-driven manufacturing process, where design determines production and not the other way around. A perfect trifecta of advance materials, novel design methods, and complex geometric features are reasons why AM surpasses traditional manufacturing strategies in methods of manufacturing (Huff and Wohlers, 2018). Objects are digitally defined by computer-aided-design (CAD) software that is used to create STL files that virtually slice the object into ultra-thin layers, creating a sequence of layers. This information guides the laser beam and melts the material layer by layer until a three-dimensional model is formed.

AM applications are limitless. The flexibility and ability to generate a product quickly are key to AM's success. AM has the capacity to produce almost any part; it is about using the technology in a way that actually brings a definable advantage, rather than simply using it because it is possible. Parts can be manufactured in a more complete state, thus reducing the amount of 'connective tissue' required to put them together and thereby decreasing part count. The reduced part count means fewer fasteners, less cost, less weight in assembly, and fewer parts that need to be re-created, lowering the supply chain count. Fewer links in the supply chain reduces logistics, shipping, outsourcing time and energy. Energy and resources are national assets and national focus. The excitement generated by AM includes many fields, from computer science and product design to new materials and engineering. A number of metal sintering methods are available (Figure 1) depending on the heat source, such as laser, electron beam melting, arc, etc.

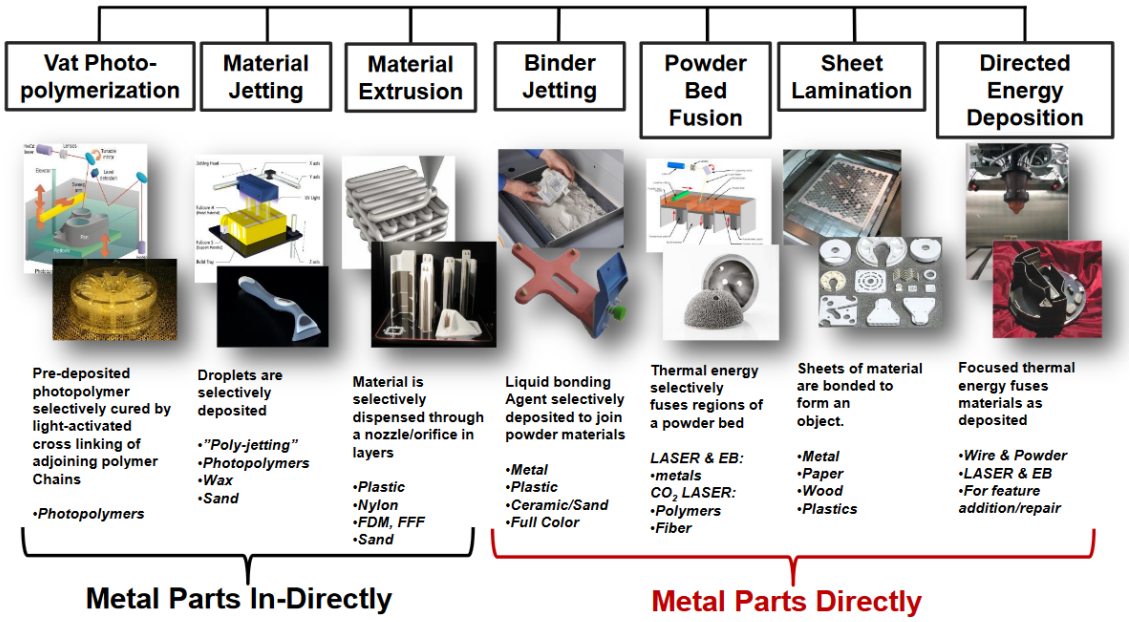

Figure 1: Overview of the most widely used 3D printing technologies according to ASTM Committee F42 (Kardus, 2017).

Many AM machine suppliers make use of a similar manufacturing principle which has a pre-deposited powder and laser heat source. Metal AM consist of various processes which include: Direct Metal Laser Sintering (DMLS), Selective Laser Melting (SLM), Selective Laser Sintering (SLS), Laser Metal Fusion (LMF), and Laser Melting (LM).

The transition of RP techniques to AM has taken place in less than 40 years. Through this period, various techniques have been developed and the application of AM has evolved into manufacturing end-part products. The various and versatile applications that AM are involved in prove the fact that it is on the right track of development (Al-Makky and Mahmoud, 2016).

The Wohlers Reports (Wohlers, 2013, 2017) show that AM applications and industries have grown considerably in the past decades due to the great benefits the manufacturing industry has gained from the technology, (Figure 2). According to the Wohlers Report 2013, the largest application in AM was functional parts, representing 28.1 % of the applications. Second was fit and assembly at 17.5 % and third, patterns for prototype tooling. The years following 2012 have been filled with unprecedented excitement, investment, new research, commercialization activity, and promise. The application of functional parts has drastically increased to 33.8 % in 2017. Javaid and Haleem, 2018 show AM applications in medical research are on the increase.

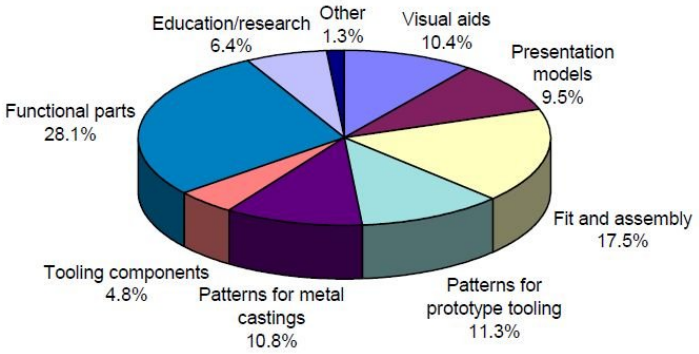

(a)

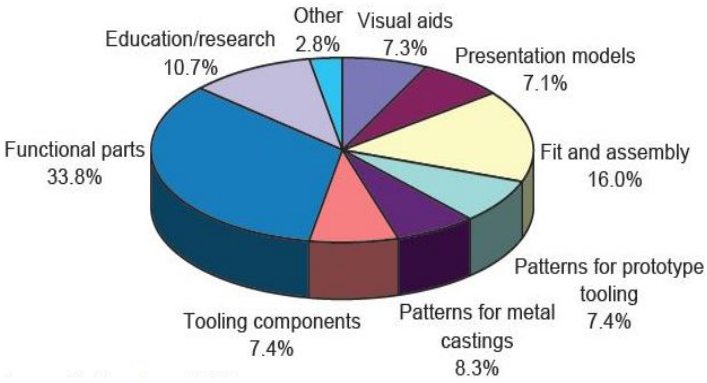

(b)

Figure 2: Using industrial AM systems for a range of applications in 2012 (a) and in 2016 (b) (Wohlers report, 2013, 2017).

(Wohlers and Gornet, 2014; Dormehl, 2019) show a historical background of where AM originated. The AM benefits are: geometrical freedom, shortened design-to-product time, fewer processes, mass customization, and the variety of materials available.

AM, or 3D printing as it is commonly known, has some attractive capabilities compared to conventional fabrication processes. 3D printing is useful in applications where only a few parts are needed or where every part needs to be customized to an individual fit. In medical and dental applications, prostheses, implants and other devices ideally should be customized to fit the patient. Metal AM can reduce material costs and scrap, which can provide savings when manufacturing costly titanium and nickel alloy parts (Kardys, 2017). Table 1 shows the factors to consider when comparing metal AM methods and conventional methods.

Table 1: Selection factors in AM versus conventional fabrication processes (Kardys, 2017)

Factors favouring additive/3D Printing	Factors favouring conventional methods
Prototyping, short runs/ low volume	Large production volumes
High material costs (e.g., scrap reduces)	Low material cost
Distributed or remote manufacturing required (space station, military base, research site)	Centralized manufacturing
Difficult or impossible to fabricate materials	Materials easily fabricated by forming, casting, machining, stamping, or other processes
High transportation and logistic costs	Low transportation and logistics costs
High machining or fabrication costs	Low machining or fabrication costs
Unique materials, complex geometries & combinations (e.g., composition gradients or changes; internal flow cavities, printed foam core or honeycombing)	Simply shaped or geometry (e.g., 2D or flat parts) from run-of-mill wrought materials
Consolidation of complex assemblies into single complex part feasible	Consolidation of parts not feasible
Rougher surface finishes acceptable	Machined or ground surface finishes required
Non-critical parts open to new methods	Mission critical parts requiring established processes, materials specifications, testing standards, and codes

The medical devices sector is one of the most highly regulated and technically complex engineering sectors. So much more is now known about the human body than in the past; the ability to artificially regenerate is something highly prized by medical scientists, which has the potential to at least overcome the ravages of disease, illness, disability, and injury. The process chain in AM for medical applications is shown in Figure 3. The process chain for implants starts with a diagnosis, followed by imaging and scanning, which is generated through various scanning procedures, such as computer tomography (CT), to convert data into a 3D digital form. AM transforms the original design of the customized implant to the physical model. The

medical industry has successfully utilized the layer-by-layer laser powder bed fusion (LPBF) technology to manufacture complex shapes from biocompatible powder materials to produce implants using CAD geometry based on CT scan data. After building the implant, post-processing, such as stress relieving, heat treatment and surface finish, is required to comply with the mechanical and fatigue properties of bones (Javaid and Haleem, 2018; Newby, 2018).

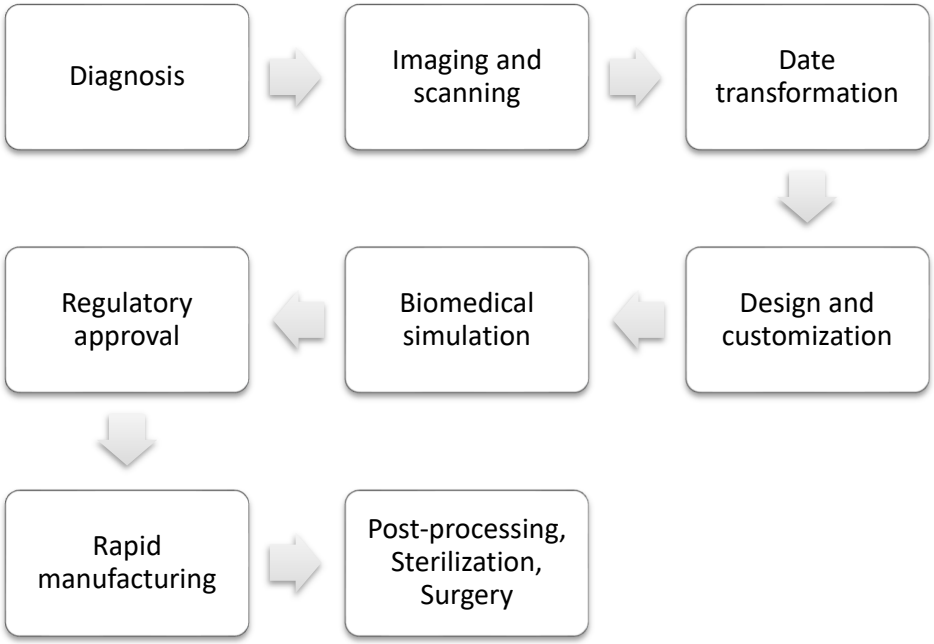

Figure 3: Process chain development in medical application of AM (Javaid and Haleem, 2018, modified by Newby, 2018).

Incorporation of the new AM technology for the development of implantable devices has brought a robust change in the life of people because AM is able to produce customized implants on the basis of CT scans data (Khan et al., 2014). The clinical goal of implants is to serve as replacement for muscle and loading, either during normal activities or after trauma, to recreate the skeleton's original stress-strain trajectories. The risks associated with medical implants include surgical risks during implant insertion or removal, infections, implant failure, and allergic reaction to implant metal. Materials used for implants, especially for load-bearing applications, should have excellent biocompatibility, superior corrosion resistance in the body environment, a combination of high strength but low modulus mechanical properties, high fatigue and wear resistance, high ductility and should not be toxic to the surrounding tissue. Failure of implants can be reduced by selecting property-specific bio-materials and which improve the mechanical properties of manufactured implants. Ti6Al4V alloy is one of the most

suitable materials of choice for medical implants, due to its incredible strength, low weight ratio and outstanding corrosion resistance (Fabriker, 2018).

It is credible to use AM for the production of different types of parts including the manufacture of medical applications (Shuaib et al., 2016). One of the benefits of AM is its ability to manufacture complex internal mesh structures and porous structures; AM also enables the variation of density to match the stiffness of the surrounding bones (Al-Makky and Mahmoud, 2016).

In medical applications, models manufactured using AM are also useful in pre-operative surgical planning. This technology also plays a significant role in reverse engineering applications (Javaid and Haleem, 2018). Geometric models of human bones created with AM can be used for education of medical practitioners or preoperative planning. The geometry of these models can be changed and adapted to the specific patient, based on the values of parameters acquired from medical images (X-ray) (Vitkovic et al., 2015).

1.2 The aim of the project

Each year, the quality of life of millions of patients are improved through surgical procedures that involve implanted medical devices. The need for new implants, treatments and prostheses as well as prolonging the lifespan of current techniques and implants has increased. The aim of this study is to understand critical size and shape of defects which influence mechanical performance of additively manufactured mandibular implants using LPBF.

1.3 The scope of the project

The combination of three-dimensional data of pore shapes and their locations with experimental and numerical simulations can potentially be very useful to predict the effect of the pores on the performance of the LPBF mandibular implant.

1.4 Research methodology

The step-by-step systematic approach of determining defects in LPBF and their influence on mechanical properties will be used for the current research (Figure 4). Furthermore, the main stages of the study have to be mentioned:

- studying human mandible functioning,
- analysis of stresses and critical points for different types of mandibular reconstruction,
- LPBF process and EOSINT M 280 system

- analysis of defects during LPBF of mandibular implants on the basis of CRPM experience and literature sources,
- numerical simulations and mechanical testing.

Critical size and shape of the defects that influence mechanical performance of additively manufactured mandibular implants will be found. The test samples will have geometrical characteristics typical to the mandible and mechanical testing will be conducted according to mastication loadings.

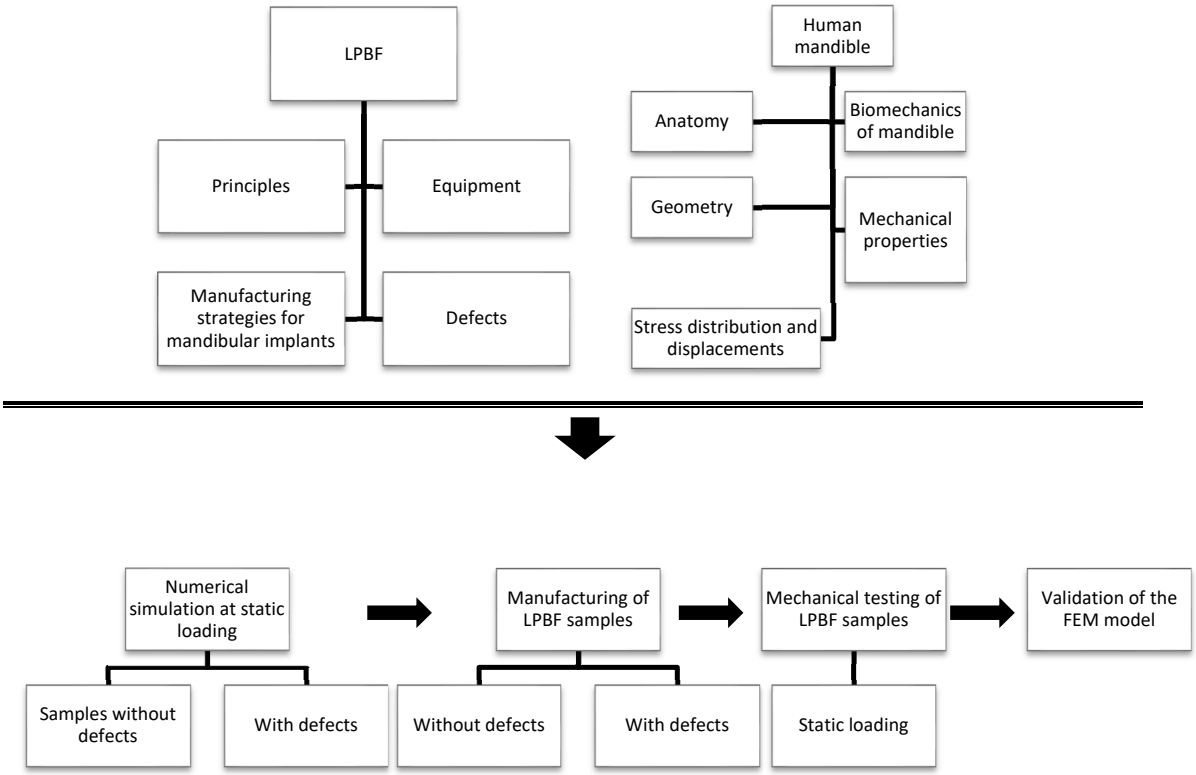

Figure 4: Flow chart for the methodology of proposed research project.

1.5 Objectives

- Biomedical investigation of human mandible functioning;
- Analysis of critical points for different types of mandible reconstruction;
- Analysis of porosity in LPBF mandible implants;
- Production and exact treatment of samples for certified mandible implant;
- Experimental testing of Ti6Al4V ELI samples with prescribed sample size, pore size and shape, and loading;

- Numerical simulation and validation data compiled from numerical simulation with mechanical testing.

1.6 Dissertation overview

- Chapter 1 – Introduction: A brief introduction and background to this study is presented, along with the aim and methodology.
- Chapter 2 – Literature review: Careful anatomical reviews are listed, as well as the study of critical areas where porosity is found in mandibular implants manufactured using LPBF. FEA is carefully reviewed for sample analysis.
- Chapter 3 – Materials and methods: Systematic approach in producing quality medical-grade titanium implants is presented, as well as selected equipment.
- Chapter 4 – Results and discussion: Experimental testing and numerical simulation comparisons are drawn and validated in this chapter.
- Chapter 5– Conclusion: Conclusions are drawn from the study.

1.7 Expected contributions

This study validates critical size and shape of defects influencing mechanical performance of additively manufactured mandibular implants.

CHAPTER 2: LITERATURE REVIEW

2.1. LASER POWDER BED FUSION

2.1.1 Background of LPBF process

American Society for Testing and Material (ASTM) defines powder bed fusion (PBF) as an "*Additive Manufacturing (AM) process where thermal energy selectively fuses regions of a powder bed to produce complex geometry parts* (ASTM F2792-12a)". PBF utilizes thermal energy to fuse selected areas during the PBF process; powder particles directly absorb heat energy from photons of the laser beam (Gong et al., 2014).

Advantages of LPBF include its high dimensional accuracy for making small complex parts, fabrication with or without supports, and a broad range of printable powders (Bose et al., 2018).

In the LPBF process, a thin layer of powder is spread on a building platform with a re-coater (Figure 5**)**. A laser beam selectively melts the material specifically to the part's design, building platform then descends, new powder layer is delivered and process is repeated. LPBF is a unique method to produce objects with complex geometries and internal structures; it permits the manufacture of complex-shaped functional 3D objects such as customized implants (Aumund-Kopp and Riou, 2015). Several parts can be built simultaneously so that the build chamber is fully utilized (English et al., 2011; Vayre et al., 2012).

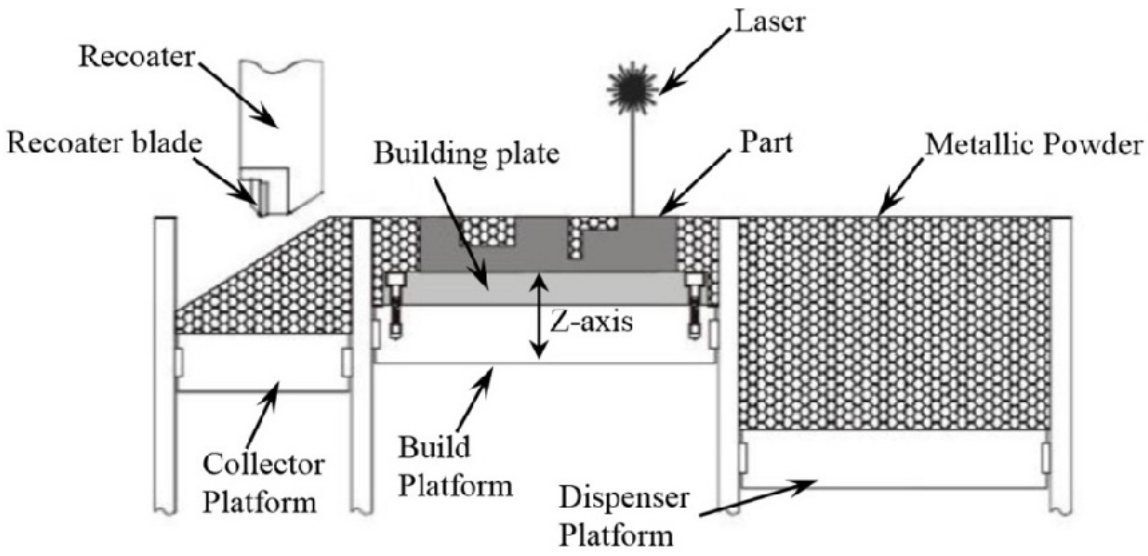

Figure 5: Schematic of LPBF process (Todorov et al., 2014).

Given the high cost of metal powders, it is essential to recover unmelted powder left over in the build chamber and recycle it in subsequent builds and in so doing save on costs in purchasing additional virgin powder (Dawes et al., 2015). Despite these savings, re-used powder undergoes partial sintering with each build, due to latent heat from the melt pool, leading to subsequent changes in the powder size distribution (Slotwinski et al., 2014). The grain morphology and texture of any part produced by LPBF is strongly affected by the solidification rate, **(**Figure 6**)** owing to the high cooling rate and large thermal gradient (Dunbar, 2016; Zhao et al., 2017; Yadroitsev et al., 2018; Kazantseva te al., 2018). This phenomenon creates non-spherical particles and satellites, leading to porosity and rough surfaces (Slotwinski and Garboczi, 2015). However, it has been reported that powder reuse does not have any deteriorating effect on the metallurgical or mechanical properties of the fabricated parts (Schmidt et al., 2017).

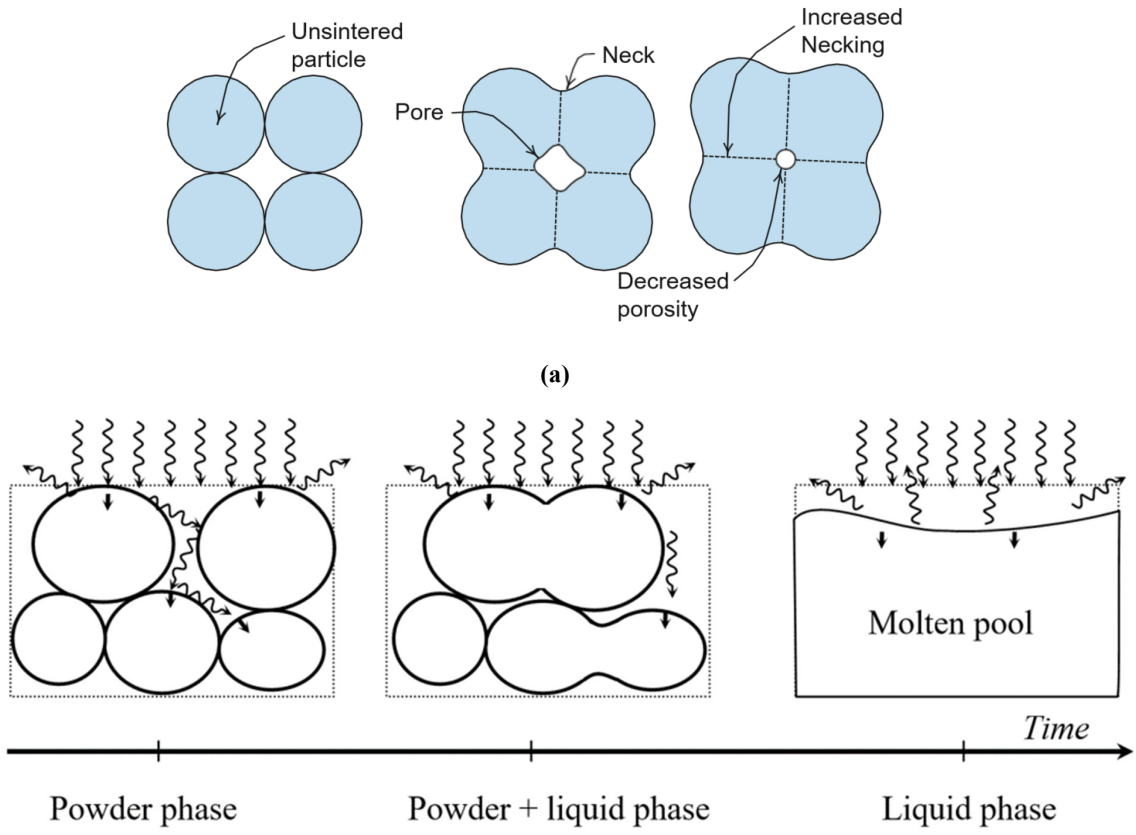

Figure 6: Metal powder components melt due to the absorbed energy during sintering: melting effect of powder particles (Gibson et al., 2010) (a), and the melting effect on the absorption of material (b) (Yadroitsev, 2009).

The quality of the additively manufactured parts are significantly influenced by the characteristics of the feedstock material (Zhao et al., 2008; Karlsson et al., 2013), including the shape, size distribution, surface morphology, composition, and flow ability of the powder (Sames et al., 2016). Typically, the particle sizes used for LPBF range between 10–60 µm. Scanning electron microscopy (SEM), X-ray and computed tomography (CT) are used to examine the shape and the surface morphology of the powder particles. Flowability of the powder is measured by a Hall flow meter, and to ensure consistent size distribution of powder particles, the laser diffraction and sieving methods are used (Santomaso et al., 2003; Slotwinski et al., 2014).

After a complete build process, PBF parts may have internal voids (porosity) and residual stress which requires post-processing via stress relief, heat treatment, annealing, shot peening, hot isostatic pressing (HIP) or tomographic inspection in order to meet performance requirements (Moylan et al., 2013).

Central University of Technology, Free State (CUT) uses an EOSINT M 280 (200 W) LPBF system **(**Figure 7**)** to manufacture medical implants. The system operates in a protective argon (Ar) atmosphere and is equipped with a 200 W Yb (ytterbium) fibre laser operated at 1064 nm, It has a build volume of 250 mm × 250 mm × 325 mm.

Figure 7: EOSINT M 280 system (EOS GmbH, 2019).

Ti6Al4V alloy is well-known light alloy and is characterized by having excellent mechanical properties and corrosion resistance combined with low specific weight and biocompatibility. This allows the production of parts or tools with fine, delicate geometries and the highest

standards in terms of surface quality with a minimum layer thickness of 20 µm (Technical Description EOSINT M 280, EOS GmbH).

2.1.2 Single track formation

The LPBF process works by melting the selected locations in a layer of the powder bed. The area to be processed is first divided into stripes. Each stripe consists of multiple tracks separated by a hatch distance. Each track is processed with the laser beam at a constant scan velocity. After a track is completed by the movement of the laser in one direction, **(**Figure 8, **a**) the laser turns off and shifts towards the next unprocessed track, where it turns back on and starts moving in the opposite direction of the previous track (Arisoy et al., 2017).

Laser melting of powders is often accompanied by a balling process, that can occur at non-optimized parameters. A laser beam melts material along a given path predetermined by the software interface, forming a molten track/vector. This track can break up into a row of independent spheres/drops **(**Figure 8**, b**). The fragments of the tracks, referred to as “balling”, are a well-known drawback of laser-sintered parts

During laser treatment, only part of the radiation is absorbed by the particles at the outer surface of the loose powder layer. The rest of the radiation penetrates through the interstitial spaces/pores and interacts with the underlying particles. The depth of radiation penetrating into the powder layer and the depth of the direct laser heating is comparatively small (Fischer et al., 2003; Tolochko et al., 2004; Yadroitsev et al., 2015). At the beginning of the laser treatment (, a cake in the shape of a comparatively thin spherical segment is formed. The irregular distribution of the heat over the thickness of the powder layer results in irregular sintering of the powder particles located on different levels of this layer (Klocke and Wagner, 2003). The features of the balling process depend on laser irradiation parameters, powder layer thickness and substrate material.

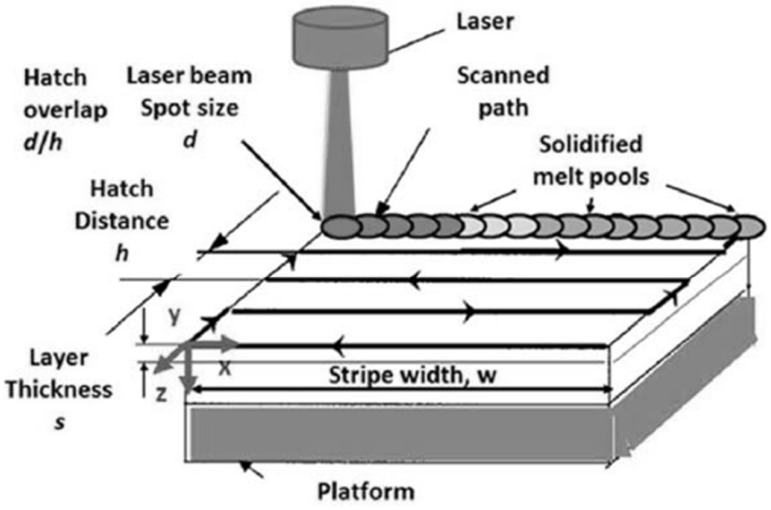

,

(a)

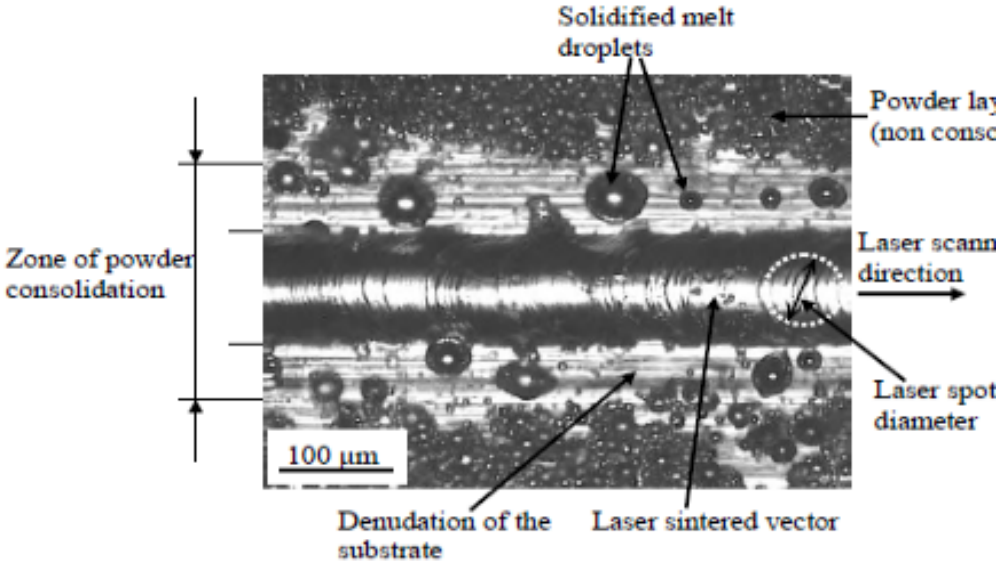

(b)

Figure 8: LPBF terminology (Criales et al., 2016) (a), and laser-sintered single track (Yadroitsev, 2009) (b).

For a successful build, it is critical that the melt pool size is large enough to connect the tracks and stripes in each layer, and deep enough to connect to the previous layer. The laser scanning patterns will influence porosity level, microstructure, surface roughness and heat build-up in the finished metal components. The stripe pattern is a band defined by the scan vector (stripe

width), the hatching space between the adjacent tracks and the scan direction, as well as the overlap with the neighbouring stripes (Carter et al., 2014; Aumund-Kopp and Riou, 2015).

Stable tracks are the basis of producing non-porous objects with reliable properties, thus optimal process parameters have to be used to produce continuous tracks with stable geometry. A 3D object produced by laser sintering consists of a set of individual single layers and tracks **(**Figure 9**)**.

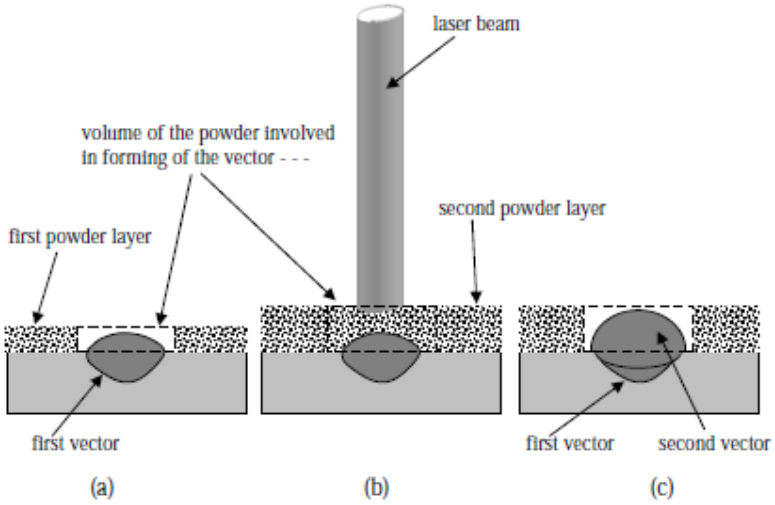

Figure 9: Cross-section of a laser-sintered track/vector and metal powder on a substrate: first sintered track (a), second layer powder deposition (b), and first and second tracks (c), (Yadroitsev and Smurov, 2010).

The depth of the penetration into the previous/substrate layer is an important characteristic of track formation and structure. The melt pool must be deep enough so that the melted powder adheres to the previous layer. Too deep a melt pool could indicate keyhole-mode melting that could result in voids, thus lowering the density of the part. The remelted depth determines the metallurgical bond with the previous layer. The metallurgical bond between the solidified layers is of course a critical issue as this generates a solid platform for the part to be successfully built. Remelting of the powder in the scanning zone and its adhesion to the previous layer are extremely important for a non-porous part (Kamath et al., 2013).

Su and Yang, 2012 studied three different types of track overlapping regimes (intra-layer, inter-layer and mixed overlapping regimes) in order to select the best approach to improve fabrication efficiency as well as the relative density of a laser melted process **(**Figure 10**)**.

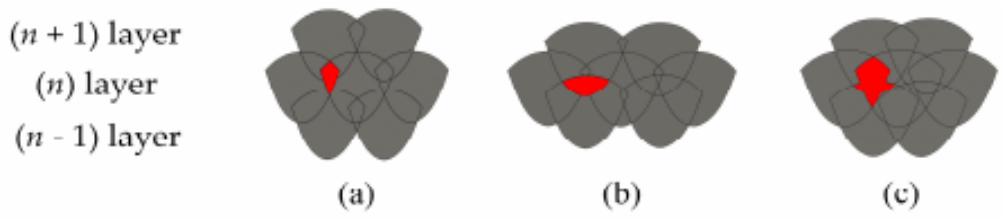

Figure 10: Types of overlapping regimes under inter-layer stagger scanning strategy: intra-layer (a), inter-layer (b), and mixed overlapping regime (c) (Trevisan et al., 2017).

2.1.3 Single layer formation

Surface morphology of single layers depends on the geometrical characteristics of single tracks, scanning strategies, and hatch distance, which shifts between tracks in the plane of the laser beam scanner. The zone of powder consolidating is broader than the solidification track. Each single layer is a superposition of the synthesized single track. Because of the substrate denudation, the zone of the consolidation powder diminishes with the next scanning, and the volume of powder involved in the melting process is reduced and therefore the geometrical characteristics of the second track will differ from the previous one. The morphology of a single layer after a follow-up scan (one-zone strategy) is complex. If the hatch distance is more than a single track width, powder is melted in a sequence of individual tracks. Non-optimal hatch distance can result in the formation of gaps between tracks in a single layer, which will lead to chains of pores in the final laser-manufactured part (Gong et al., 2014; Yadroitsev et al., 2015). The hatch distance has a different effect on the morphology of the layer. As the hatch distance increases, the gap increases accordingly between two neighbouring tracks/vectors. The variation in hatch spacing shows that a hatch increase results in more powder being left unmelted **(**Figure 11**).** Choosing the correct hatch distance is important to avoid pore formation in 3D object; therefore, optimal parameters will lead to a homogenous layer with constant thickness and bonding between two tracks. A non-uniform powder layer thickness of the powder layer is critical, because defective porous structure with chains of pores will be produced (Yadroitsev, 2009).

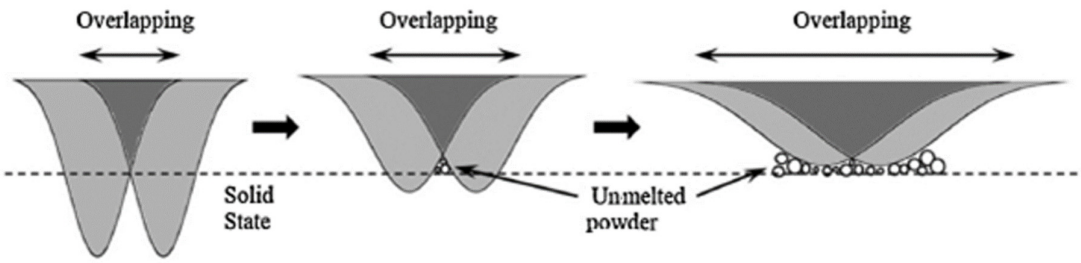

Figure 11: Schematic of melting pool with increased focus offset (Gong et al., 2014).

The hatch distance is important to ensure excellent metallurgical bonds between tracks. The object build strategy in laser-melted parts could be varied from one-directional overlapped tracks (one-zone strategy) to a stochastic exposure strategy in line with the "island principle" (Concept Laser GmbH). In a two-zone strategy, each layer is processed twice with the laser: first, the laser beam melts the powder layer with a certain hatch distance and subsequently the laser beam passes in between sintered tracks and remelts (Figure 12) the two neighbouring tracks. Rescanning, or a two-zone strategy, also significantly improves surface quality of single layers (Yadroitsev, 2009; Yasa et al., 2011).

Figure 12: Top view of a single layer produced with one-zone and two-zone strategies (Yadroitsev et al. 2015).

Patterns can, therefore, be the same through multiple layers, in either x or y directions. The scanning direction can also be rotated from layer to layer (Figure 13), for example, raster scan tracks are used for a stripe pattern. Within each new layer of stripe, the stripes are rotated counterclockwise by 67 degrees (Anam et al., 2014).

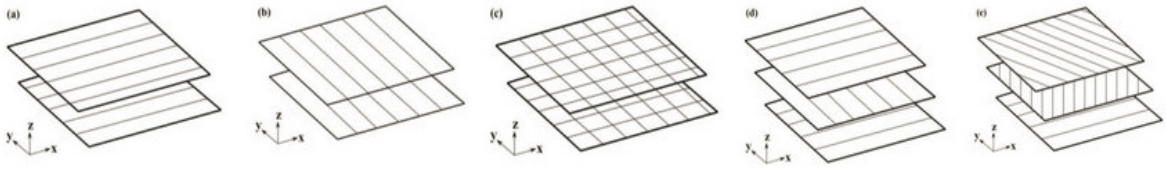

(a) (b) (c) (d) (e)

Figure 13: Different scan patterns for consistent layers: one direction (a), double scanning each layer (b), alternating scanning (c), and rotated scanning to specific angle between consecutive layers (d, e) (Aumund-Kopp and Riou, 2015).

Other scanning strategies can be used to manufacture LPBF parts. Concept Laser uses an "island principle" scanning strategy (Figure 14): these islands differ in size from 1 mm×1 mm up to 10 mm×10 mm. These individual squares are not necessarily scanned coincidently with each other but stochastically (Qiu et al., 2013; Concept Laser, 2015).

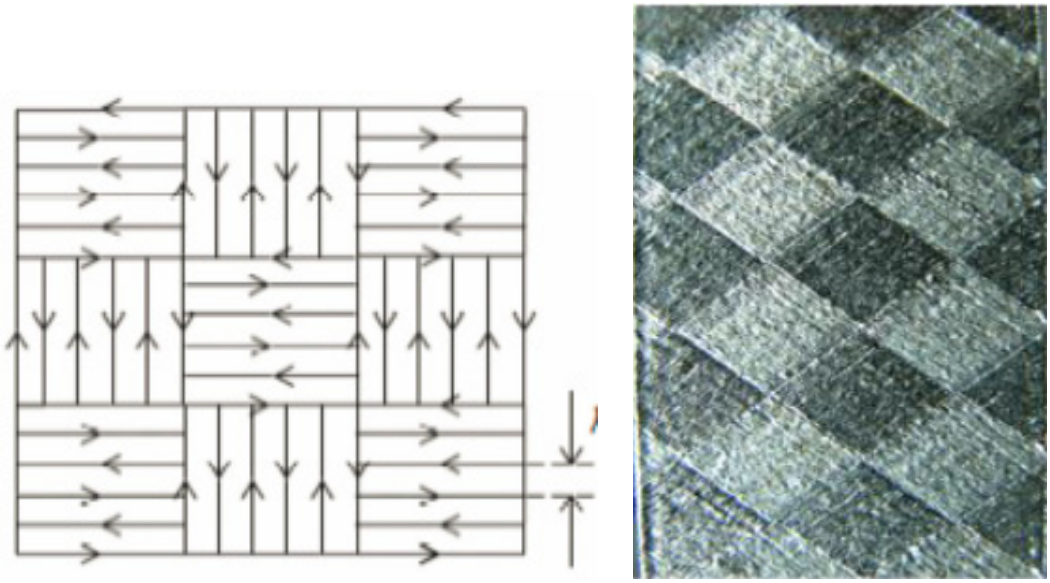

Figure 14: Schematic of the island scans strategy (Mezzetta, 2016; Trevisan et al., 2017).

Another strategy, known as the band/strip strategy, is utilized by EOS M 280 (Figure 15): this back-and-forth scanning strategy has bands about 5 mm in width which extend across the entire layer. Contouring is done before the bands are produced and thereafter post-contouring is done. Contouring is when a laser scans the perimeter of an object, forming a distinct shape within the powder bed.

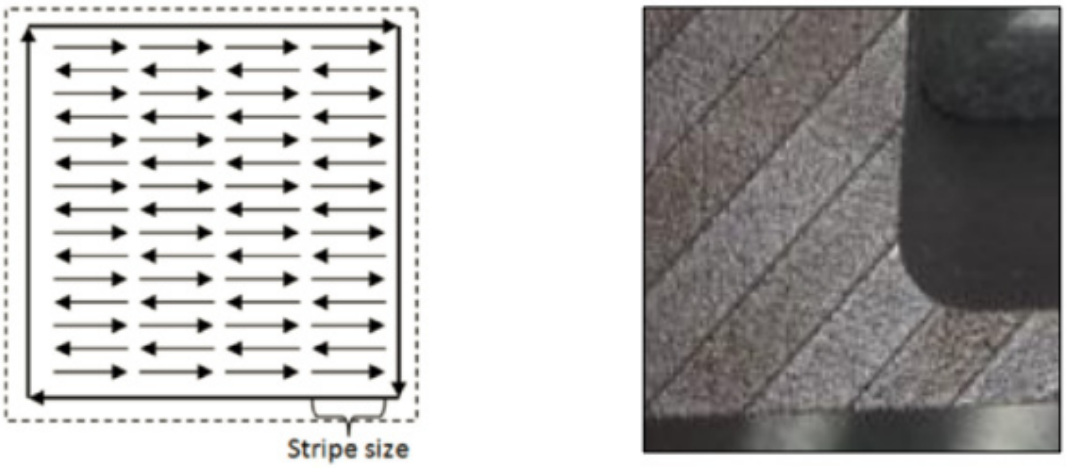

Figure 15: Schematic view of band stripes and top view of EOSINT M 280 band/stripe scanning strategy (van Zyl, 2016).

One-layer scanning strategies, scan patterns for consistent layers, contouring and build direction define the properties of a 3D laser-sintered object (van Zyl, 2016).

2.1.4 Parameters influencing LPBF parts

Designers often overlook the importance of part orientation in the quality of a 3D-printed part. The following categories showcase the important aspects of part orientation; manufacturing time, the part accuracy, surface finish and strength of a 3D-printed part. A product-specific design parameter that has to be considered is the printing orientation of the product. Mechanical properties of LPBF-printed products are to a large extent independent of the printing direction; however, they also depend on the scan strategy. The orientation of the product with respect to the build plate can be selected in a trade-off between productivity (the number of parts stacked on the build plate for one printing run) versus the interaction of the “squeegee” (the risk of damaging thin-walled parts of the object). Stress-relief consideration also plays a role in determining the optimum printing orientation. An alternative is to increase the stiffness by adding support structures, for example, bridges connecting vulnerable parts (van Gastel, 2016). The fabrication of a high-quality product is a multi-integrated process. The levels of importance in the final quality of the product are single tracks, single layers and final 3D objects. Several parameters play an important role in every level, thus a loop feedback is vital to formulate optimal process parameters. Optimization parameters for PBF/SLM for a high-quality 3D

object, can be described by an algorithm based on the suggested hierarchical design principles (Figure 16).

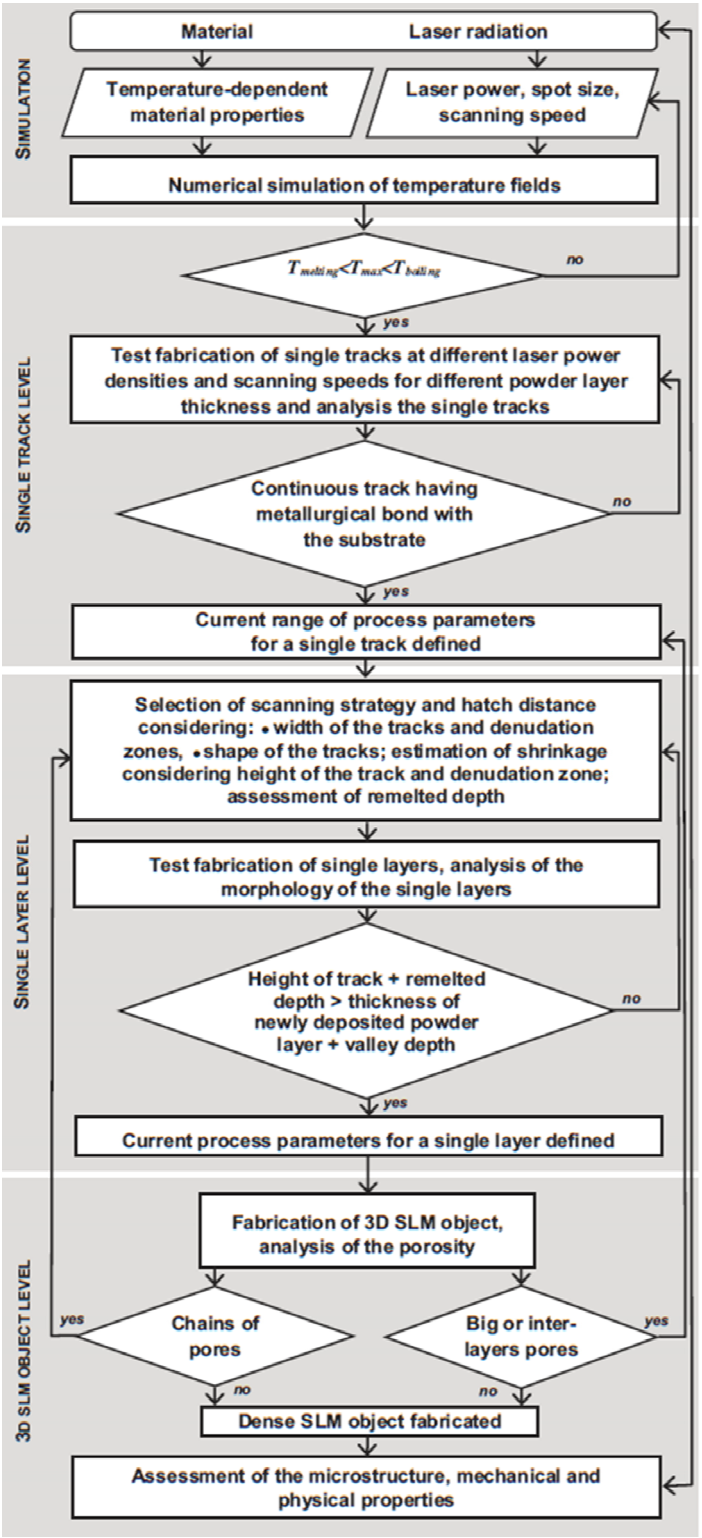

Figure 16: Optimal LPBF process parameters algorithm (Yadroitsev et al., 2015).

2.1.4.1 Build orientation

It is important to select an appropriate build orientation that considers the loading direction applied to the part. To determine a build orientation that ensures optimal performance and quality of AM parts at the lowest cost, it is necessary to simultaneously optimize different objectives (Brika et al., 2017). Surface roughness mainly depends on the layer thickness but is also affected by the build orientation, since the side surfaces generally present a better finish than up-facing or down-facing surfaces (Bacchewar et al., 2007). In 3D printing, parts can be manufactured in different orientations **(**Figure 17**)** depending on the desired outcomes (Townsend and Urbanic, 2012; Wu et al., 2014).

Printing orientation has a strong correlation with manufacturing time and how many parts fit in one production run. Placing a part vertically gives space for more parts but increases the build time, whereas a horizontal orientation leads to shorter build times at the cost of less space in the building chamber (Zhang and Bernard, 2014). Additionally, the orientation layout of a part determines the amount of support structures required for the production of a specific part. By orientating the part in different directions, there will be a significant difference in the print quality. The cost of support material is significant and should be considered in the planning in 3D printing (Li et al., 2010). Some 3D-printed parts have inherently anisotropic properties, meaning some parts are much stronger in the XY-direction than in the Z-direction. For functional parts, it is important to consider the application and the direction of applied loads. Part orientation is an important parameter in the planning of a rapid prototyping (RP) process as it directly governs productivity, part quality and cost of manufacturing (Phatak and Pande, 2012).

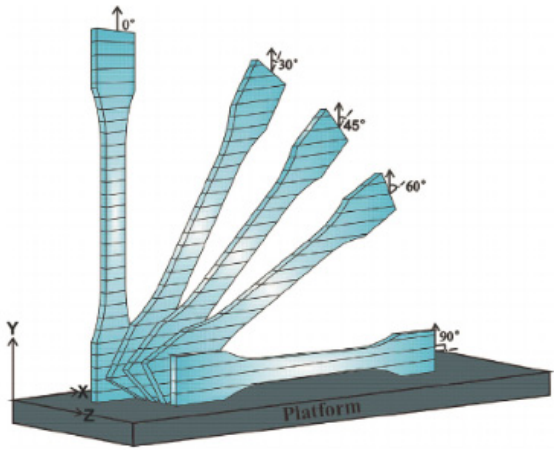

Figure 17: Schematic view of a 3D-manufactured part placement orientation (Zou et al., 2016).

LPBF parts need support structures to sustain overhanging surfaces to avoid build failure. Support structures are needed, when a model or part has overhangs, channels or holes, or a bridge which is not supported by anything below it. To avoid the collapse of a part and avoid build failure, support structure is needed to sustain overhanging surfaces and thin features. (Chakravorty, 2018). Thus, a suitable build orientation can minimize the amount of overhanging surfaces and in turn, reduce the amount of support structures needed. This approach avoids using extra material and reduces the time needed to build the support structures and to remove them (Brika et al., 2017).

Knowing the priorities for the part in terms of strength, surface finish, and also minimizing support material can help zone in on the best possible orientation. Support structures have to be avoided as much possible, as their printing and removal afterwards takes up additional process time and introduces the risk of damaging the part. Merely tilting the original design may decrease the need for supports.

Parts printed in LPBF with overhanging features typically require unique support structures, although in some small overhanging parts, preheated powder or excess powder can hold parts together serving as support structure. Not all overhangs need to be supported; however, when the angle α is tilted lower than 45^0 (Järvinen et al., 2014; Schnabel et al., 2017) from the horizontal (Figure 18), support structures must be included to avoid poor surface roughness as well as distortion and warping, which will lead to build failure (Aumund-Kopp and Riou, 2015). One of the reasons failure may occur in a build is insufficient or poorly designed support structure.

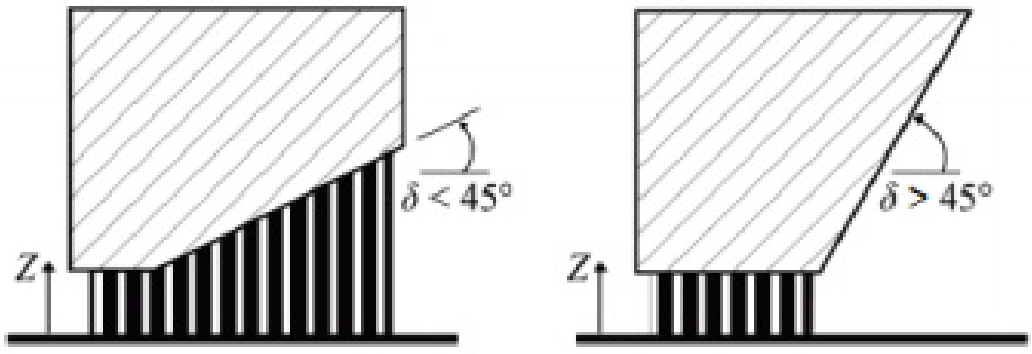

Figure 18: Guideline for use of support structures (VDI-Guidelines).

Overhangs differ from self-supporting angles in that they are abrupt changes in part geometry. The direct metal laser sintering (DMLS) process is fairly limited in its support of overhangs when compared to other 3D printing technologies. In some cases, overhangs greater than 0.5 mm will require additional support to prevent damage to the part. When designing overhangs, it is wise to err on the side of caution as large overhangs can lead to reduction in a part's detail or worse, lead to crashing the whole built.

2.1.4.2 Porosity

Special microstructure and high residual stress are peculiarities of LPBF material that have an influence on mechanical properties. Also, consecutive layer-by-layer delivery of powder material sometimes tends to clump the material together causing pores in the final product. LPBF process parameters, scanning and manufacturing strategies of complex objects can lead to fractures, warps, and pores within the LPBF part as was shown by defect analysis using CT scans and cross-sectioning of LPBF samples (du Plessis et al., 2016a; Yadroitsev et al., 2018). The required properties of a part are more complex than simply defining a strength value.

The concerns regarding metal parts produced by LPBF relate to internal stresses that occur during manufacturing processes, normally from steep temperature gradients and high cooling rates (Knowles et al., 2012). This occurrence of internal stresses of as-built components may result in pores (Leuders et al., 2013).

It is known that phase composition and size, and porosity are the two largest factors dictating mechanical performance. Porosity is a dominant and physical defect; its presence affects the performance of as-built parts and is particularly detrimental to mechanical strength and fatigue performance (Wycisk et al., 2014). The presence of internal defects makes the material inhomogeneous, but inhomogeneities can be randomly distributed within the volume of the mechanical component (Brusa et al., 2017).

Various studies focused on the porosity of additively manufactured parts found that the levels of porosity can vary considerably depending on the system and the parameters used. Two main types of porosity are known to occur (Sharratt, 2015). Lack of fusion; defects are irregularly shaped, and in contrast, gas entrapment porosity is very spherical. Generally, the average porosity in a part built with good specifications is >99.5 % dense, this means 0.5 % porosity or less (Vandenbroucke and Kruth, 2007; du Plessis et al., 2016b). Porosity in LPBF is expected when the applied laser energy is either too low to result in lack of fusion, or when the energy

density is too high and keyhole pores occur, or process parameters such as hatch distance or layer thickness are too high.

Melt pool variation and defect generation can be easily characterized if some parameters are kept constant. In the current LBPF case study, many holes can be observed on the top surface (Figure 19) due to powder particles attaching to single beads. These holes may be attributed to gas bubble ejection from the melt pool. When a laser spot with high energy density is applied to a powder bed, gas bubbles may form in the melt pool due to vaporization of low melting point constituents within the alloy (Li, 2006).

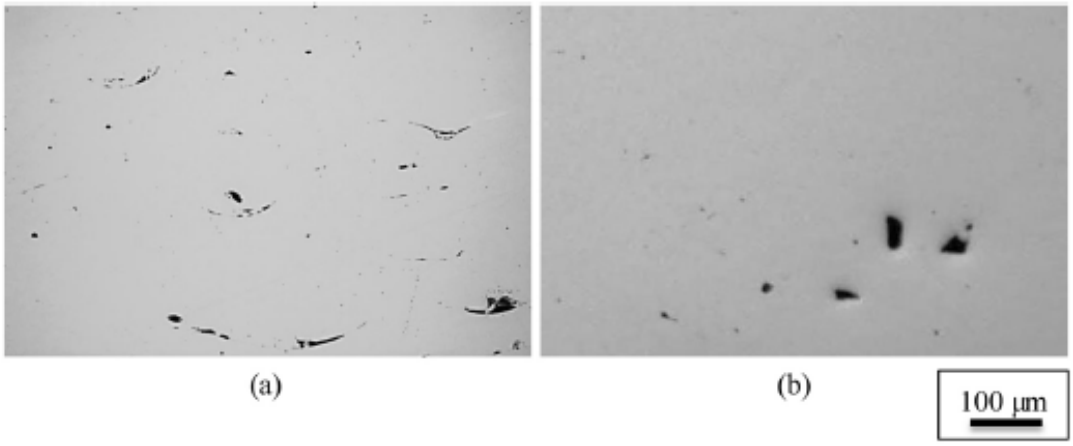

Figure 19: Characteristic species of pores in SLM samples produced with two-zone strategy and scanning speed V = 0.12 m/s, hatch distance s = 120 µm, powder layer thickness h = 50 µm: P = 50 W (a), and P = 70 W (b), (Yadroitsev et al., 2015).

In general, the melting methods seem to attract more attention; this can be reasonably attributed to the fact that the resultant build is more likely to exhibit better mechanical performance characteristics. The characteristics of the built part depend on the processing parameters: power energy source (Figure 20), focused spot size, layer thickness, scan speed, etc. (Gong et al., 2014; Sharratt, 2015). It was demonstrated that building platform heating can act as an in situ ageing heat treatment following the fast cooling that arises during laser scanning. A 17 % higher ultimate tensile strength was achieved by the selection of the optimum building platform temperature (Aversa et al., 2017).

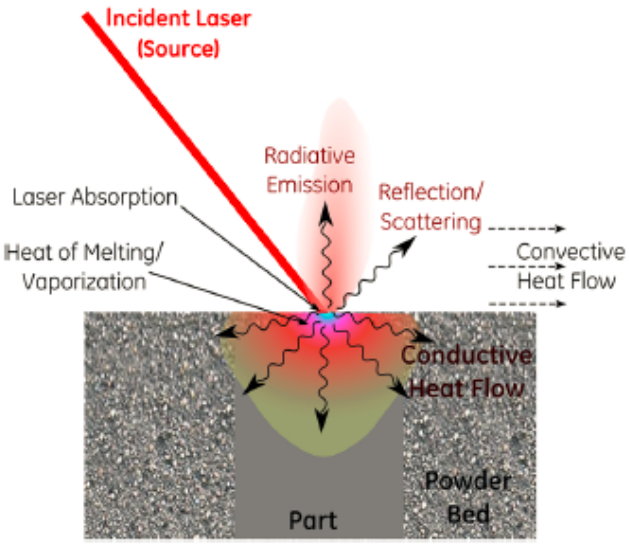

Figure 20: Heat transfer paths in melt pool formation and solidification in a laser melting process (Spears and Gold, 2016).

The powder bed temperature will impact thermal gradients in the heat transfer process, as illustrated, in ultimately influencing internal stresses in finished parts. The physical size of the melt pool is the simplest process signature conceptually. The melt pool will grow or shrink as more or less energy is transferred to the powder bed and/or melt pool. The shape and stability of the melt pool may also change during the process. As the melt pool grows, "satellites" may form as solid powder grains become connected to the edges of the melt pool. Conversely, if too little energy is transferred to the material, a "balling effect", characteristic of an unstable melt pool, may be observed (Kurzynowski et al., 2012).

2.1.5 Summary

An overview of LPBF technology is given in this section; LPBF printing process is sensitive to change in process parameters and can have a significant influence on the outcome of the part. LPBF involves a multi-step process for building a part, thus the sensitivity of the LPBF process makes testing and quality control all the more necessary. Optimal laser powder, scanning speed and hatch distance are essential parameters for each primary track of each layer in order to produce quality parts. The aforementioned shows how much the parameters of the process can impact the production as-well as the material properties.

2.2. TITANIUM ALLOYS FOR BIOMEDICAL APPLICATIONS

2.2.1 Background

Titanium is the fourth most abundant structural metal in the earth crust at a level of ±0.6 %. The incomplete 3d shell enables it to form solid solutions with most substantial elements located in its vicinity in the periodic table (Collings, 1984). Titanium exists in two crystallographic forms. At room temperature, the unalloyed titanium has a hexagonal close-packed (HCP) crystal structure known as alpha phase (Figure 21). At 883 ^{0}C this transforms to a body-centered cubic (BCC) known as beta phase (Henriques, 2009; Yang, 2015). This allotropic behaviour has the capacity to alloy with many elements resulting in titanium alloys that have a wide range of mechanical and corrosion-resistant properties (Seagle, 2018).

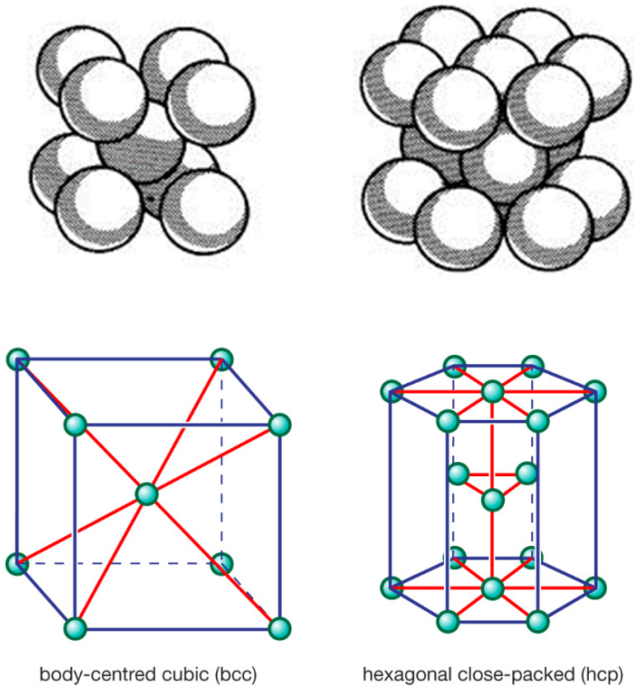

Figure 21: Two crystallographic forms of titanium: beta and alpha phases respectively (Mezzetta, 2016), (Mason, 2018).

The distinction between alpha and beta stabilizers depends on which phase the element is most soluble in. Alloying elements will have an effect on the beta transus temperature (Figure 22) when added to titanium, depending on the nature of these elements and their concentration (Cunha, 2015).

For α-phase stabilization, alloying elements with atoms or electron ratios below 4 are added to titanium, these include aluminium (Al), oxygen (O_2), carbon (C) and nitrogen (N). To stabilize the β-phase, elements having atoms or electron ratios above 4 are used. Stabilizers include vanadium (V), molybdenum (Mo), niobium (Nb).

The beta stabilizers can be divided into two categories according to their behaviour with titanium: β-isomorphous, completely soluble in solid solution, and β-eutectoid, intermetallic phase particles are created. Common elements, as seen in Figure 22**,** can be used as stabilizers. Important elements such as aluminium are used as α-stabilizers, and vanadium and molybdenum as β-isomorphous, while niobium and tantalum also found applications in some alloys β-eutectoid (Donachie, 2000; Cunha, 2015). Aluminium is used as the alpha stabilizer and vanadium as the beta stabilizer. The α-phase alloys have poor plasticity, but also have less tendency to absorb gases while beta-phase alloys provide good mechanical properties, such as high strength and good ductility (Mierzejewska et al., 2019).

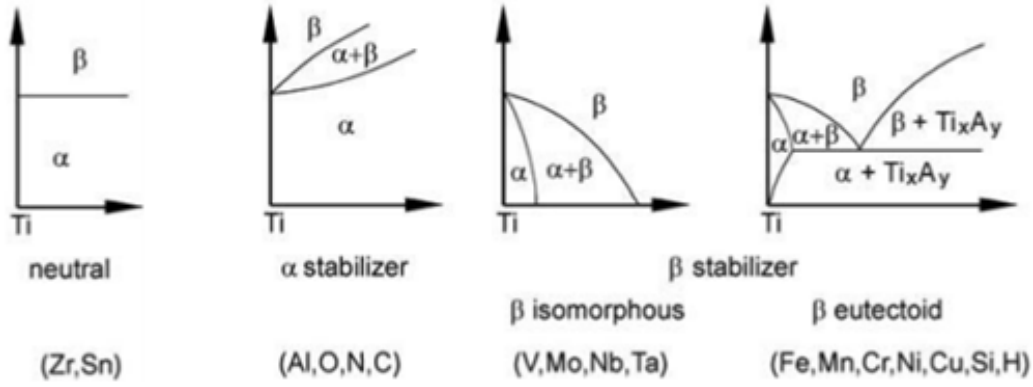

Figure 22: Schematic archetypal titanium binary phase diagram (Cunha, 2015).

According to different alloying additions and phases present in the microstructure, titanium alloys are classified conventionally into three different categories: α alloys, α+β alloys, and β alloys (Yang, 2015). The microstructures are controlled by heat treatment (Figure 23), generally at temperatures in the α-β phase region (Hardie and Ouyang, 1999; Shademan et al., 2004).

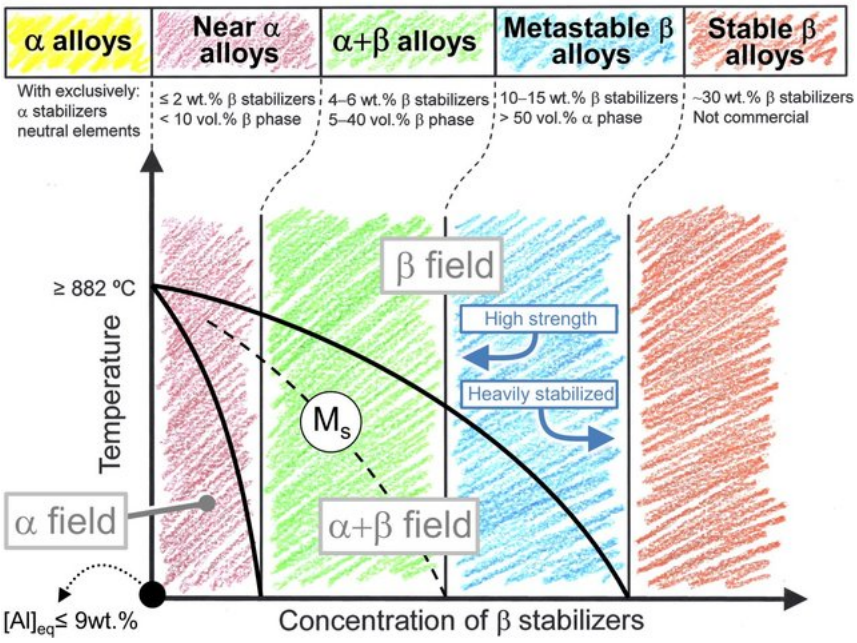

Figure 23: Classification of titanium alloys in the β isomorphous phase diagram (pseudo-binary section). (Barriobero-Vila, 2015).

Titanium alloy microstructures are generally described by the size and the arrangement of their α and β phases. The two extreme cases of phase arrangements are lamellar microstructure (a greater α/β surface area and more oriented colonies), which is generated by cooling from the β-phase field, and equiaxed microstructure (a uniform structure composed of α grains and grain boundaries of β (Polmear, 2006), which results from a recrystallization and globularization process (Leyens and Peter, 2003). Lamellar microstructure exhibits lower strength, lower ductility, and better fatigue propagation resistance (Loier et al., 1985), whereas equiaxed microstructure provides better fatigue initiation resistance but poor propagation resistance. Another kind of structure, bi-modal microstructure, which is considered to be a combination of lamellar and equiaxed microstructure (Figure 24), exhibits well-balanced fatigue properties (Leyens and Peter, 2003). Yang, 2015 and Donachie, 2000 offer in-depth definitions and the steps for a fully developed microstructure according to different temperatures compared to time elapsed.

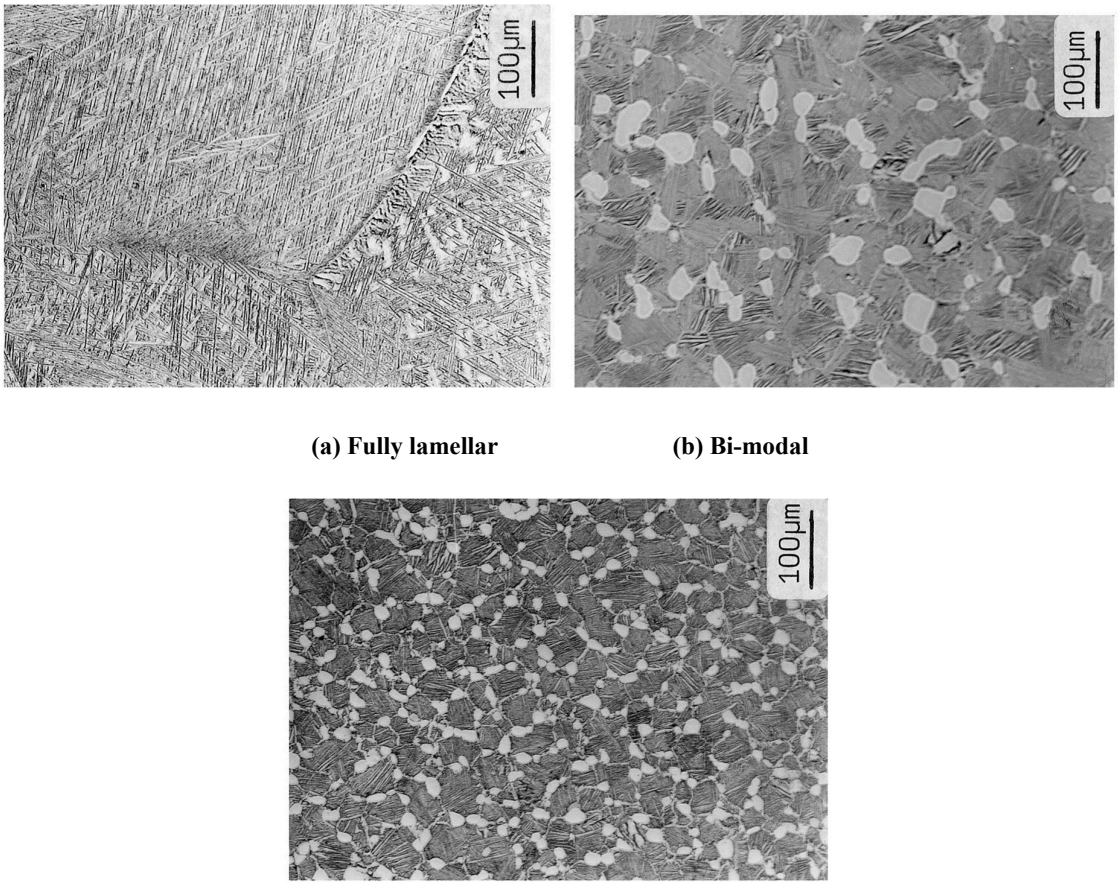

(a) Fully lamellar **(b) Bi-modal**

(c) Fully equiaxed

Figure 24: Different microstructures obtained through certain process routes (Lütjering, 1998).

When the alloys are cooled below the β transus, α phase first nucleates from the grain boundary and then intra-granularly as plates. Due to the close atomic matching along this common plane, the alpha phase thickens relatively perpendicular to this plane and grows faster along the plane where the plates are developed (Figure 25), (Donachie, 2000).

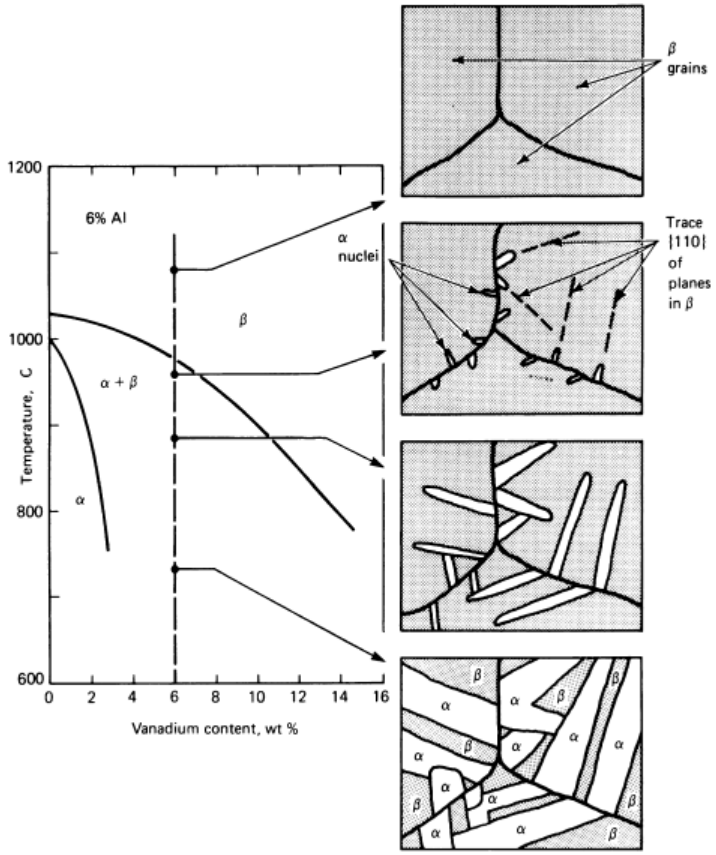

Figure 25: Microstructure of alpha-beta titanium alloys after slowly cooling from above the β transus. The white plates are α, and the dark regions are β (Donachie, 2000).

The α+β alloys contain a limited quantity of β stabilizers and α stabilizers. The addition of α stabilizers is used to strengthen the α phase, while the β stabilizers allow the β phase to be retained at room temperature after cooling from β or α+β phase fields (Yang, 2015). The mechanical properties of α+β alloys depend on the relative amount and distribution of α and β phases (Semiatin et al., 1997). Microstructures can be substantially altered by heat treating them below or above the β-transus. Compositions, sizes, and distribution of phases in these binary alloys can be hardened by heat treatment (Matthew and Donachie, 2001).

Ti6Al4V is temperature dependant, thus with a rise in temperature these properties actually change the physical form and state of the alloy. Titanium α-β alloys are heat treatable and allow for a good mixture of strength and ductility to be obtained through post-processing (Lütjering and Williams, 2007). Figure 26 shows CCT diagram for crystal structure formation subjected to different cooling rates of Ti6Al4V alloy.

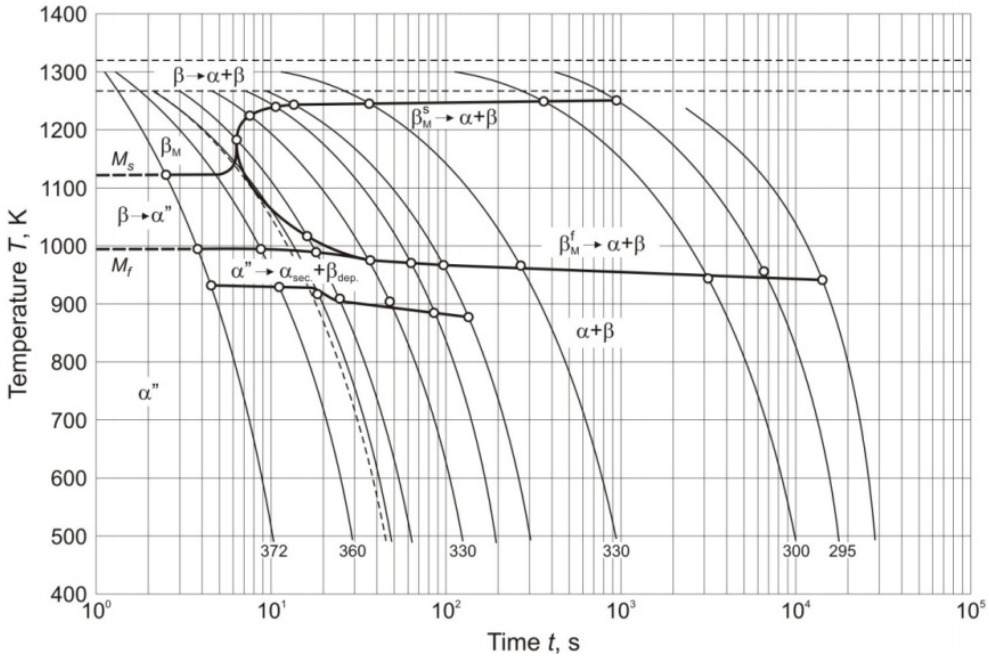

Figure 26: CCT diagram for crystal structure formation subjected to different cooling rates of Ti6Al4V alloy (Sieniawski et al., 2013).

A heat treatment after processing is used to relax stresses and can raise elongation to above 10 % which is required for medical applications according to current material standards (Munsch, 2017). Heating titanium in air results not only in oxidation but also in dissolution of oxygen and nitrogen on the surface layer of the titanium, causing solid solution hardening of the surface. It is important that the heat treatment is done in a controlled atmosphere, using either a vacuum furnace or heat treatment in an inert atmosphere, such as argon, for any heat treatment temperatures above 427 ^{0}C (Donachie, 2000).

Annealing of titanium and its alloys serves primarily to increase fracture toughness, ductility at room temperature, dimensional and thermal stability, and creep resistance. Improvement in more properties is generally obtained at the expense of other properties, and should be selected according to the objective of the treatment (Matthew and Donachie, 2001). During the recrystallization stage, the material is heated above its recrystallization temperature, but below its melting temperature. This causes new grains without pre-existing stresses to form.

Stress relieving is probably the most common heat treatment given to titanium alloys. It is used to decrease the undesirable residual stresses that result from unfused powder particles. Stress relief helps maintain shape stability and also eliminates unfavourable conditions such as loss of compressive yield strength. Stress relieving can be performed without adversely affecting

strength or ductility (Matthew and Donachie, 2001). During stress relief it is crucial that the cooling rate is uniform, especially between 480 to 315 ^{0}C. A recommended procedure for stress relief for Ti6Al4V is a soaking at 480 –650 °C for 1–4 hours (Donachie, 2000).

Ti6Al4V ELI and Ti6Al7Nb have been standardized for biomaterials in ASTM (Akahori and Niinomi, 1998). Common Ti-based alloys in bio-fabrication elastic modulus are compared to one another as well as to bone in Figure 27. Table 2 on page 54 shows the in-depth properties of Ti6Al4V ELI grade 23, while Table 3 on page 62 shows mechanical properties of mandible bone.

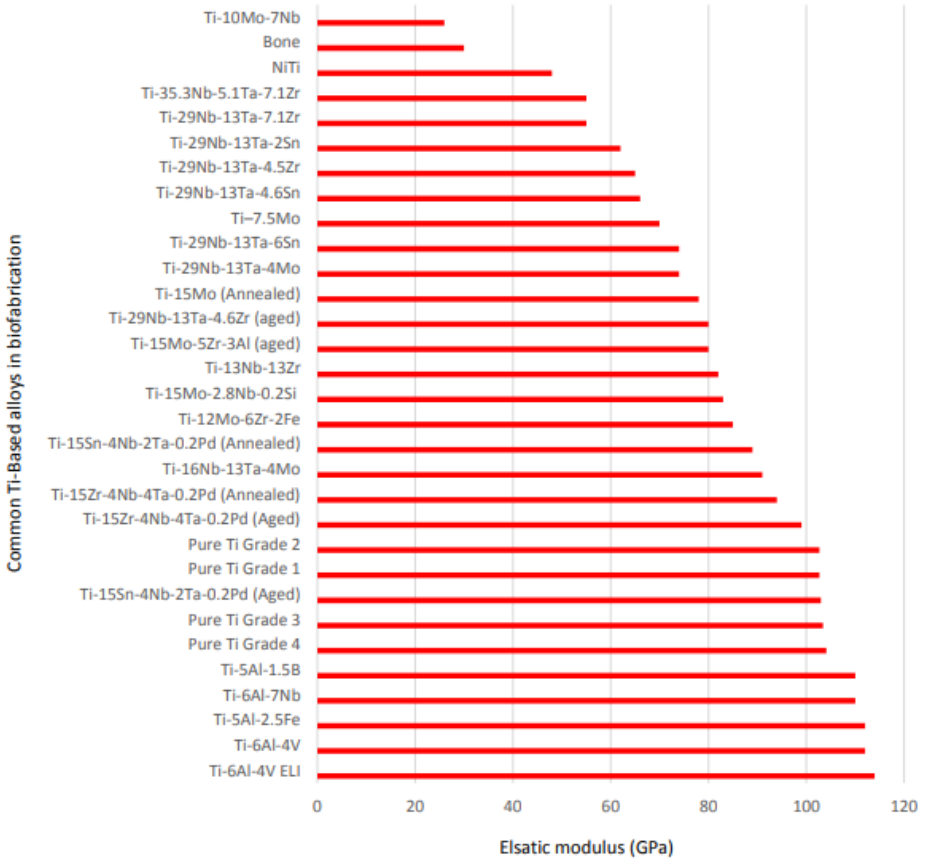

Figure 27: Common Ti-based biomaterial elastic modulus (Okazaki et al., 1998; Niinomi, 2003; Rack and Qazi, 2006; Niinomi et al., 2016).

2.2.2 TI6Al4V conventional alloy

The metallurgy of titanium and its based alloys have been intensely researched over the last 50 years. The unique properties, such as high strength-to-weight ratio, good resistance to corrosive

environments, biocompatibility, bio-adhesion, machinability and availability, makes Ti alloys the material of choice (Albrektsson et al., 2017).

The development of titanium alloys, and more specifically Ti6Al4V (ELI), has accelerated over the past four decades (Leuders et al., 2013). The metal has revolutionized the medical field, especially in biomedical applications, due to the metal's excellent biocompatibility when direct contact with tissue or bone is required. Among the different types of titanium alloys, Ti6Al4V remains the most widely used, due to the excellent mechanical properties (Table 2), and is used extensively in medical devices and serves as a replacement for surgically removed bone due to the rapid acceleration of bone-to-implant growth and healing process (Reade, 2018).

Ti6Al4V (grade 5), known as the "workhorse" of the titanium alloys, is most commonly used in all titanium alloys. The essential difference between Ti6Al4V (grade 23 ELI means extra low interstitials) and Ti6Al4V (grade 5) is the reduction of oxygen content to 0.13 % (maximum) in grade 23. This offers improved ductility and fracture toughness, with some reduction in strength (ASM Aero, 2015; AZoM Materials, 2002).

Titanium 6AI4V alloy is made from 6 % aluminium and 4 % vanadium and is suitably the best metal of choice for medical implants, due to its harmonizing factor with the human body, incredible strength-to-weight ratio, ability to fight corrosion from bodily fluids, non-ferromagnetic properties (safe to examine with MRI), and incredible durability; lasting up to 20 years (Schank, 2018). The mechanical properties of Ti6Al4V alloy are significantly determined by the process used for manufacturing. In this study, the mechanical properties of Ti6Al4V alloy manufactured through LPBF will be examined.

Several superior properties, such as exceptional thermal resistance, high loadbearing capacity and ability to resist corrosion, categorize Ti6Al4V as a super-alloy (Polishetty et al., 2013). Ti6Al4V accounts for roughly 50 % of all titanium alloys production, as it is a frequent choice in both the aerospace and biomedical industry due its high specific strength and low weight (Donachie, 2010). Furthermore, titanium and titanium-based alloys have been widely applied to medical materials, orthopaedic implants and dental implants over the last few decades (Wang et al., 2016).

Modern implants must meet rigorous requirements for materials, and functionality. Implants that replace the tissue of the human body should have biomedical properties comparable to those that are being replaced and should not cause any side effects. Modern medical implants

are regulated and classified in order to ensure safety and effectiveness to the patient (Mierzejewska et al., 2019). The mechanical properties of parts produced using LPBF differ from conventional production. Relevant properties of titanium and its alloys are obtained by a series of operations, or a selection of alloying elements, which have a significant effect on the production of the individual phases (Dobrzanski, 2004). The alloys chemical composition fulfils the standards and norms of a certified medical implant according to ASTM F136 and ISO 5832-3. Applications of titanium has accelerated in a broad spectrum and include implants such as prosheses (hip and knee), trauma fixation (wires, plates, screws), dental implants, cardiac valve prostheses, artificial hearts, and pacemakers, etc.

Table 2: Physical and mechanical properties of wrought grade 23 Ti6Al4V ELI alloy (AZoM, 2013; MatWeb, 2018)

Properties	Value
Beta-transus temperature	980 ^{0}C ± 15 ^{0}C
Density	4430 kg/m^3
Elongation at break	15 %
Fatigue strength	140 MPa
Fracture toughness	100 MPa-m$^{1/2}$
Hardness, Brinell	326
Hardness, Knoop	354
Hardness, Rockwell C	35
Hardness, Vickers	341
Melting point (solidus/liquidus)	1604–1660 ^{0}C (1649 ^{0}C)
Modulus of elasticity	114 GPa
Poisson's ratio	0.342
Shear modulus	44 GPa
Shear strength	550 MPa
Specific heat capacity	0.5263 J/g-^{0}C
Tensile strength, ultimate	860 MPa
Tensile strength, yield	790 MPa
Compressive strength, yield	860 MPa
Thermal conductivity	6.7 W/m-K

2.2.3 LPBF TI6AL4V alloy

AM of metal parts using LPBF is growing exponentially. Confidence in the process can be established via the fundamental understanding of the physics of the process. It is generally accepted that this understanding will be increasingly achieved through modelling and simulation (King et al., 2015).

For parts produced with Ti6Al4V using LPBF, ASTM standards F2924 and F3001-14 assume quite variable elongation of 6–10 %. Minimum tensile properties for Ti6Al4V ELI alloy are similar to wrought annealed material used for surgical implants (Figure 28) (Yadroitsev et al. 2017).

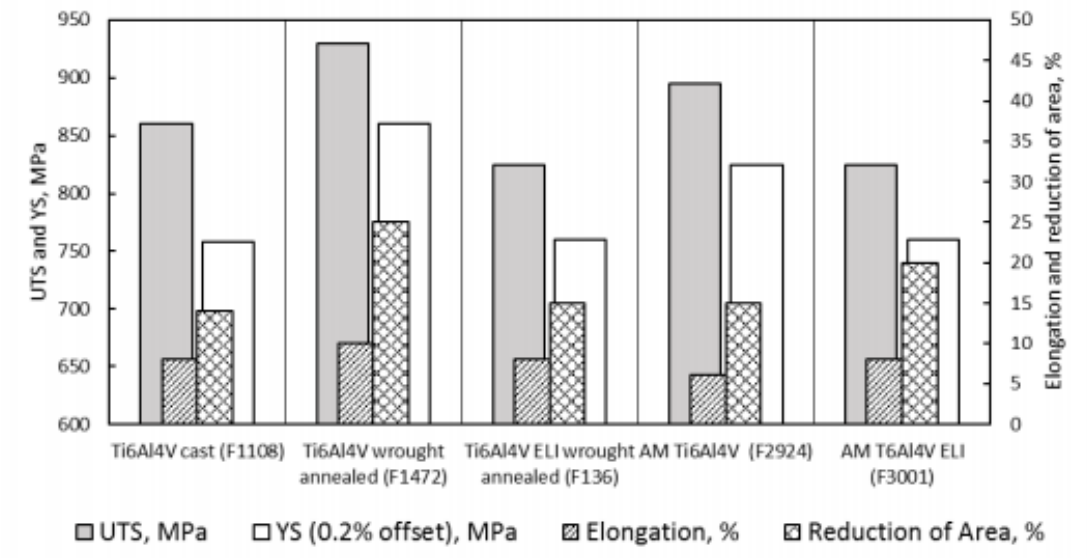

Figure 28: Minimum tensile properties for grade 5 (Ti6Al4V) and grade 23 (Ti6Al4V ELI) alloys for surgical implants (Yadroitsev et al. 2017).

Process-parameters and environment for LPBF influence on the defects, microstructure and related properties of finished parts (Thijs et al., 2010; Bassoli et al. 2018; Kazantseva et al., 2017). The microstructure of as-built Ti6Al4V ELI fabricated by LPBF is shown in Figure 29.

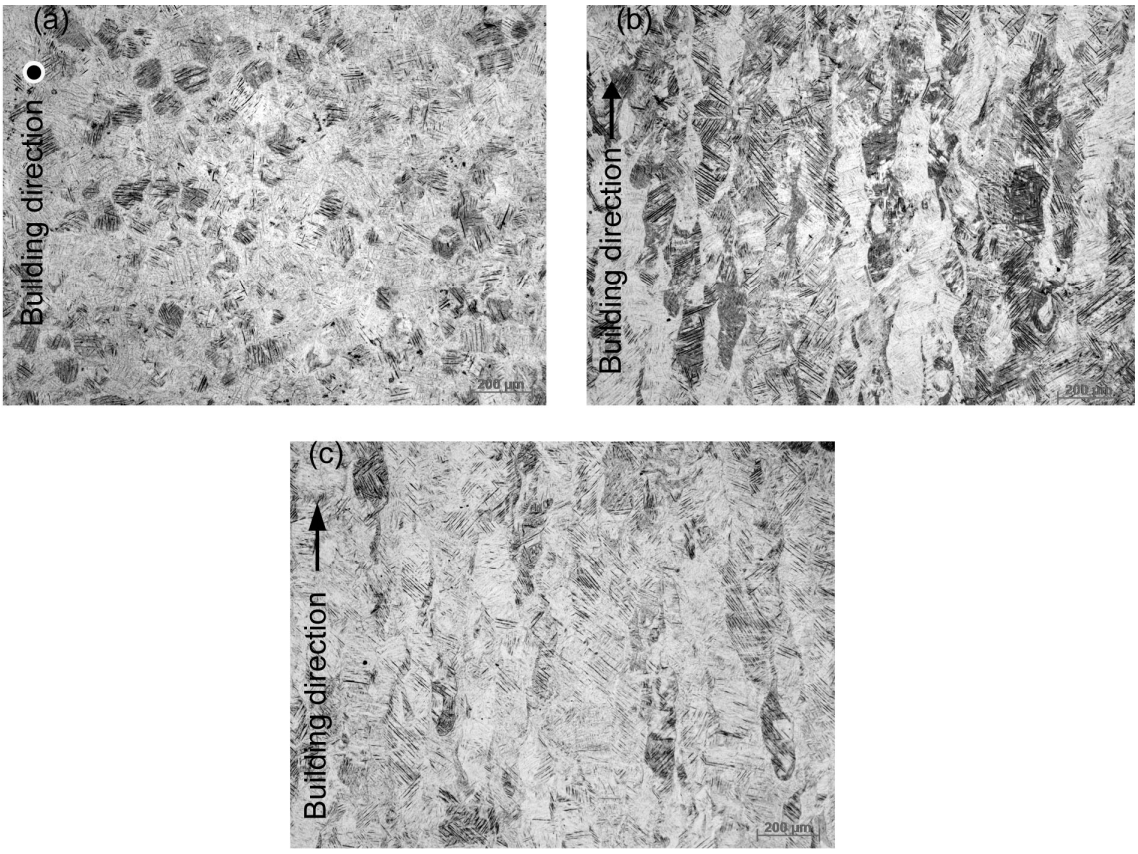

Figure 29: Microstructure of horizontal (a, b) and vertical (c) as-built Ti6Al4V ELI samples at different cross-sections: perpendicular to the building direction (a) and along it (b, c) (Yadroitsev et al., 2017).

Owing to the brittle and anisotropic microstructure, as-built Ti6Al4V alloy has a higher tensile strength compared to the hot-worked material, but a lower ductility dependent on the building orientation (Facchini et al., 2010; Simonelli et al., 2014). This gives it the highest strength-to-weight ratio of any metal suited to medical use. The microstructure of LPBF Ti6Al4V is quite distinctive from that of conventional ways (Baxter et al., 2018; Wang and Li, 2018).

The fast pace of AM technologies is placing it ahead of conventional manufacturing techniques. Unique light-weighting structures can be implemented via AM, which cannot be manufactured by other methods. Additive processes have the potential to transition from a tougher alloy core to a harder outer wear layer without a bond interface, which eliminates delamination concerns. Potentially, materials with unique compositions could be 3D printed, which cannot be cast, extruded or machined (Kardys, 2017).

2.2.4 Summary

Young's modulus, as well as tensile strength, ductility, fatigue life, fretting fatigue life, wear properties, functionalities, etc., should be adjusted to levels that are suitable for structural biomaterials used in implants that replace hard tissue. These factors may be collectively referred to as mechanical biocompatibilities. Many kinds of titanium alloys composed of non-toxic and allergy-free elements are used to satisfy the requirement that when implant devices are implanted to reconstruct disordered bone, prevent bone resorption and enhance good bone remodelling, the Young's moduli of the implants should be close to that of the bone.

2.3. HUMAN MANDIBLE ANATOMY

2.3.1 Mandible anatomy

The mandible, located inferiorly in the facial skeleton, is the largest and strongest bone in the face. It forms the jaw and acts as a receptacle for the lower teeth. The mandible is the only movable stress-bearing bone of the face. The mandible is also the only bone in the cranium that does not articulate with its adjacent skull bones via structures. When the skull is observed purely as a bony structure, there is nothing anatomically holding the mandible and the skull together. The mandible is a singular bone with a distinctive horseshoe shape and is symmetrical on both sides (Bengochea, 2018).

Anatomy plays an important role in the manufacturing and reconstruction of a mandible and the internal working of bodily structures, as revealed by dissection and separation of parts. The mandible (lower jaw) forms the lower part of the skull and along with the maxilla (upper jaw) forms the mouth structure. Movement of the lower jaw opens and closes the mouth and also allows for the chewing of food. Four different pairs of muscles situated on either side of the skull and work in combination to pivot the lower jaw up and down and to allow movement of the jaw from side to side. Loading conditions are factors that determine mandibular bone structure since they play an important role in the modelling and remodelling of bone. During biting and mastication, a combination of sagittal bending, corpus rotation and transverse bending occurs (Levrini et al., 2015).

Reconstruction of mandibular defects should restore the anatomical height and contour of the resected mandible, while optimal restoration of original function involves mastication, deglutition and management of oral section (Wong et al., 2010; Miles et al., 2010; Hayden et al., 2012). Disregarding various forces acting on the mandible after mandibular reconstruction can lead to early screw loosening, plate fracture, bone loss, and failure of reconstruction (Wong et al., 2011).

2.3.1.1 Mandible bone

Bone can be seen as an open cell composite material composed of osteogenic cells, extracellular matrix (ECM) proteins, growth factors, mineral calcium in the form of calcium hydroxyapatite, and a complex vascular system. Bone consists of cells that make up 10 % of the total volume and include osteoprogenitor cells of mesenchymal origin, namely osteocytes and osteoblasts and bone-resorptive cells of hematopoietic origin, namely osteoclasts (Polo-

Corrales et al., 2014). Osteoblasts can either become embedded in the bone (building the bone) as osteocytes, transforming into inactive osteoblasts and become bone-lining cells, or undergo programmed cell death (Jayakumar and Di Silvio, 2010). Osteocytes embedded in the bone matrix are the most abundant cell type of bone-forming networks. Through this network, osteoclasts function as stress and strain sensors; signals that are important for maintaining bone structures (Franz-Odendaal et al., 2006) Osteoclasts are large cells that attach to bone matrix through a brush border and solubilize its mineral content through acidification. Cortical bone turnover rate (remodelling with healthier bone and calcium) is smaller than that of trabecular bone, but adequate to maintain biomechanical strength of the tissue. The rate of trabecular bone turnover is higher, more than required for the maintenance of the mechanical strength of cortical bone, indicating that is more important for mineral metabolism (Buck and Dumanian, 2012). The lower jaw consists of no more than five individual parts that intramembranous ossify together (Figure 30): ramus, body, and the alveolar process.

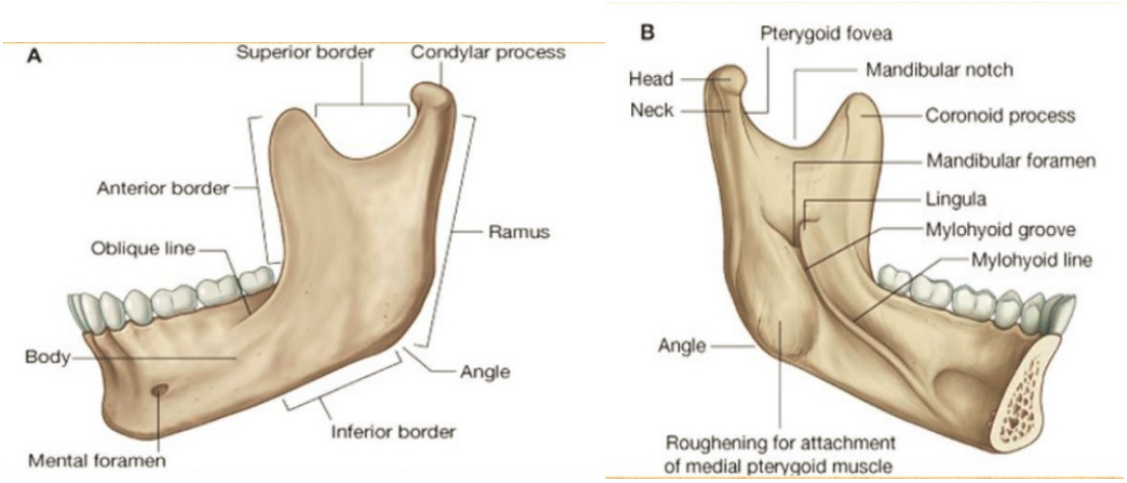

Figure 30: Different anatomical segments of the lower jaw (Singh, 2015).

The alveolar of the mandible extends superiorly from the body and consists of two bony plates, including a thick buccal part and a thin lingual part (Figure 31). The alveolar bone and periodontium support the teeth, but neither has a physiological function once the teeth are lost, and are therefore resorbed. Alveolar bone changes shape significantly with tooth loss, in both the horizontal and vertical planes, but the overall pattern of resorption is largely predictable (Matthew, 2007).

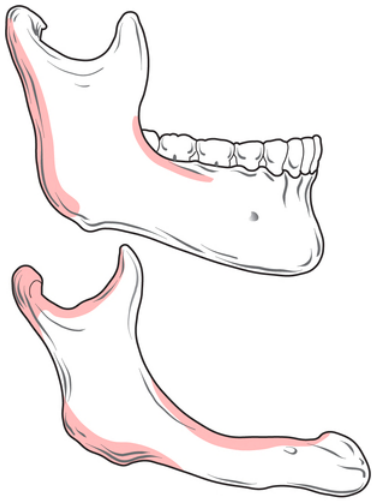

Figure 31: Mandible with and without the alveolar ridge (Matthew, 2007).

Cortical bone represents the outer compact layer of bone as well as the inferior border of the mandible. Cancellous bone, also called trabecular bone, is found inside, in between the compact bone and is filled with small pockets of bone marrow (Figure 32). The orthotropy ratio is smaller than that for long bones, which approaches the mandible structure to isotropic material (Milewski and Kromka-Szydek, 2010). The mandible is composed of a cortical structure which may account for up to 79–89 % of the entire bone (Drozdzowska et al., 2002). It can be assumed that the model of the mandible is made up entirely of isotropic material (cortical bone), and the resulting stress distribution depends on the geometry of the mandible (Miodowska et al., 2016).

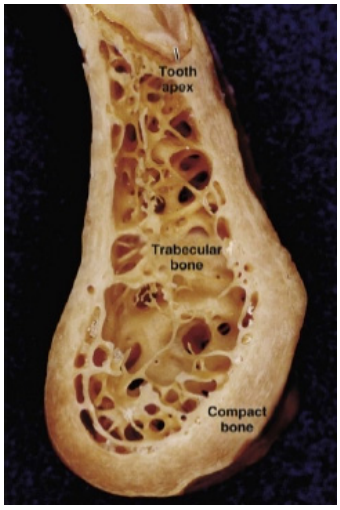

Figure 32: Body of the mandible, the outer compact layer and the inner supporting network (Nanci, 2017).

Fractures of the mandible are common in patients who sustain facial trauma; most mandibular fractures are seen to occur in male patients, and 35 % of fractures occur between the ages of 20 to 30 years (Nyeah, 2016). In about 60 % of cases, the break occurs in two places. The most common areas (Figure 33) of fracture is at the condyle (36 %), body (21 %), angle (20 %), and symphysis (14 %) (Murray, 2013; Passi et al., 2017).

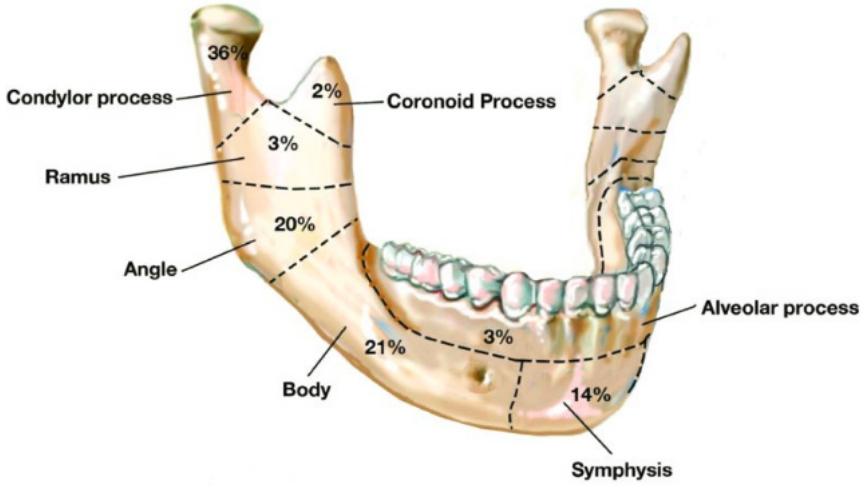

Figure 33: Percentage fracture regions (Back to post: Mandibular 2017; Mandibular fracture, 2018).

Treatment of these injuries is important to maintain proper speech, swallowing, and masticatory function of the lower jaw. Treatment of mandibular fractures involves an optimal environment for bone healing to occur; adequate blood supply, immobilization, and proper alignment of fracture segment (Koshy et al., 2010).

The vascularized free fibular flap (FFF) is the most commonly used flap in the head and neck for bony reconstruction, although other vascularized bone flaps, such as the iliac crest, scapula and radial forearm flaps commonly used in the head and neck also provide good bone-to-implant fixation. The vascularized free composite flap contains bone and muscle with or without skin and provides reliable single-stage reconstruction with excellent functional and aesthetic results (van Zyl and Fagan, 2017).

The ability to create anatomical landmarks as geometrical elements (Figure 34) on 3D human bone models has a significant role and a vast potential for bone reconstruction after innate defects, illnesses, and traumas. Vitkovic et al., 2015 define anatomical landmarks important for implant design. These anatomical landmark points are an important aspect in the mandible geometry (Arsic et al., 2010). Different regions (cortical and trabecular) of bone are

distinguished in order to attribute different mechanical properties within the subsequent definition of the finite element model.

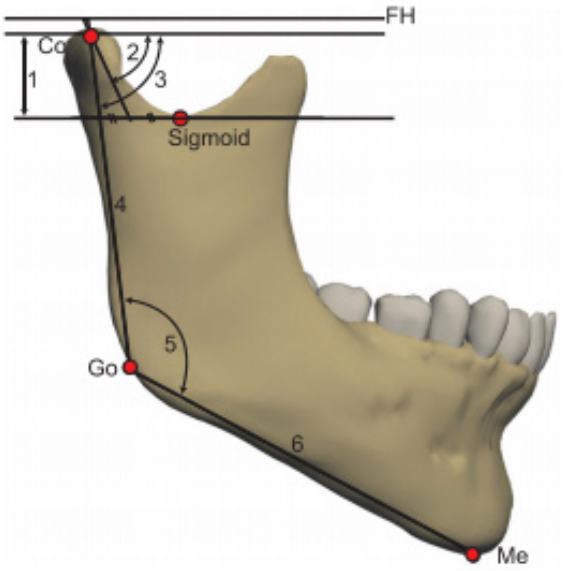

Figure 34: Lateral view of the mandible shows ramal and condylar landmarks and parameters: FH, Frankfort horizontal plane; Co, condylion; Go, gonion; Me, menton; 1, condylar height; 2, condylar anteroposterior inclination; 3, ramal anteroposterior inclination; 4, ramal length; 5, gonial angle; 6, mandibular body length (Bayome et al., 2013).

2.3.2 Mandible bone mechanical properties

Hardness is one of the most important parameters for comparing properties of material. Mechanical properties of bone and Ti6Al4V are shown in (Table 3 In relation to the material properties, the cortical and cancellous bone can be taken as homogeneous and isentropic with different properties, this is due to that both the bone are significantly different in strength (Ilavarasi and Anburajan, 2011; Jedrusik-Paw1owska et al., 2013).

Bone is a porous tissue material, and introducing a porous material allows a physiological rational use for the replacement of bone fractures due to trauma or clinical conditions. Introducing pores into a material structure reduces the stiffness value to close to that of a normal bone, which can in addition provide a good load transfer and stimulate the form of new bones (Griss and Heimke, 1976). The porous structure will allow new bone tissue to grow into the structure, providing adequate biological fixation (Figure 35).

Table 3: Mechanical properties of bone and Ti6Al4V (Nouri et al., 2010; AZoM, 2013; MatWeb, 2018)

	Cortical bone*		Cancellous bone*	Ti6Al4V *
	Longitudinal direction	Transverse direction		
Strength, tension, MPa	79–151	51–56		790
Strength, compression, MPa	131–224	106–133	2–5	860
Elastic moduli, GPa	17–20	6–13	0.76–4	114
Apparent density,g/cm^3	1.99		0.05–1.0	4.43
Poisson's ratio	-	-	-	0.342

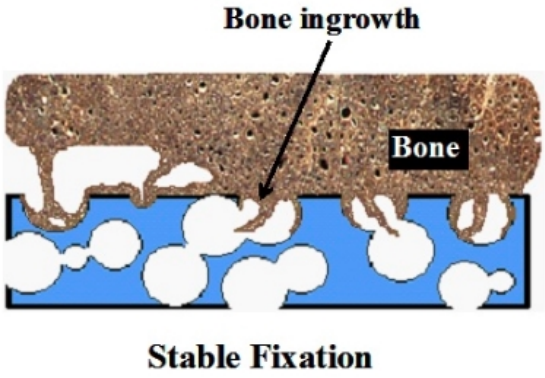

Figure 35: Bone ingrowth into a porous scaffold (Nouri et al., 2010).

The force-bearing material requires high elastic modulus with low deflection. As the elastic modulus of a material increases, the fracture resistance decreases. It is preferable/desirable that the biomaterial elastic modulus is similar to bone (Kokubo, 2008). It is helpful to evaluate the serviceability, performance and long-term clinical success of biomaterials. It is reported that high fracture toughness material improves clinical performance and reliability as compared to low fracture toughness (Fischer and Marx, 2002). Elastic modulus physically represents the stiffness of a material within the elastic range when tensile or compressive loads are applied. It is clinically important because it indicates that the selected biomaterial has similar deformable properties as the material it will replace (Figure 36).

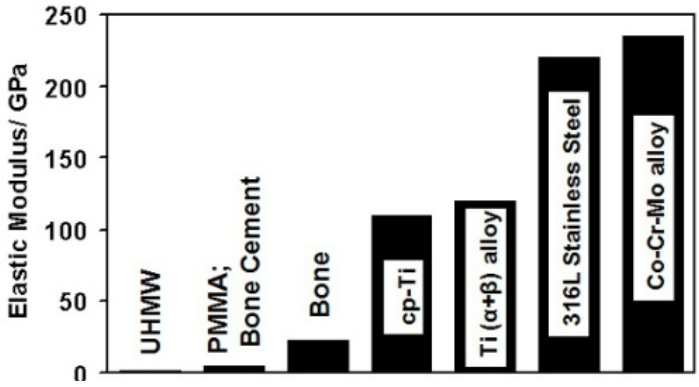

Figure 36: Elastic modulus of bone in comparison with biomedical titanium alloys (Niinomi et al., 2006).

2.3.1.2 Mandibular muscles

During mastication (action of chewing food), a rhythmic and repetitive motion of the mandible with respect to the maxilla is carried out. The motion of the mandible during mastication is a three-dimensional, complex motion, which has been described as having the shape of a teardrop (Koolstra, 2002). During this action of feeding/chewing, all the muscles of mastication, including the medial and lateral pterygoid muscles, temporal muscle, and masseter muscles attached to it contribute to the process of chewing food (Bengochea, 2018). Muscles that power the jaw movements during chewing are known as the muscles of mastication (Figure 37) or masticator muscles, and are classified as: jaw elevators, and jaw depressors (Masticatory force, 2018).

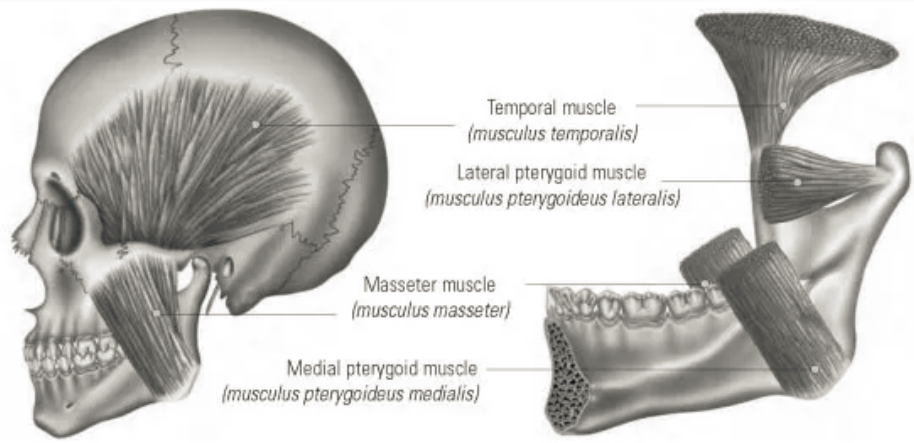

Figure 37: Maxillofacial muscles of mastication (Masticatory muscles, 2017; Weickenmeier et al., 2017).

Emin (2017) visually defines the origin of muscle attachment to the mandibular bone (Figure 38). The origin point of the temporalis muscle is along the entire rim of the temporal fossa of

the skull and insertion point is the coronoid process of the mandible. The masseter muscle is a very thick muscle made up of two parts, the origin point of the outer masseter muscle is along the zygomatic arch and its insertion point is on the surface of the ramus of the mandible. The origin point of the inner masseter muscle is from the rear of the zygomatic arch and its insertion point is on the upper surface of the ramus of the mandible. The pterygoid muscle is made up of two muscles; the lateral pterygoid and the medial pterygoid which are located on the inside of the ramus of the mandible and work in tandem with the masseter muscle to assist in chewing, jaw rotation, side-to-side movement of the mouth, and the protection of the lower jaw. The lateral pterygoid muscle is located higher than the medial pterygoid muscle.

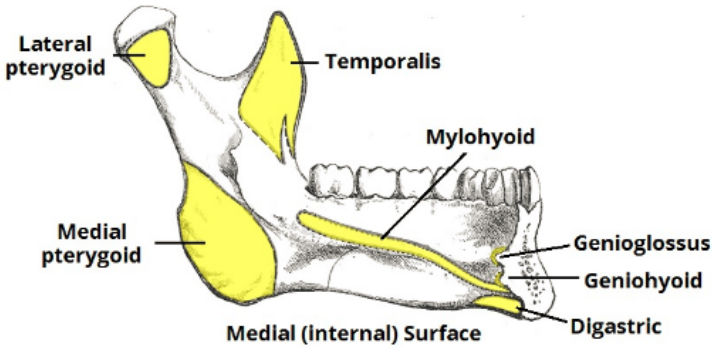

(a)

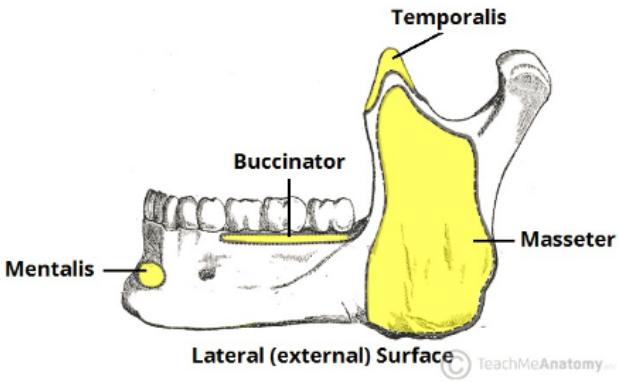

(b)

Figure 38: Muscular attachment of the mandible; (a) internal or medial view of the left side mandible, and (b) left lateral or side view (Emin, 2017).

There is a considerable variation in the arrangement of the fibres of certain muscles with reference to the tendons to which they attach to. For some muscles, the fibres are parallel and run directly from their origin to their insertion (Gray, 2018). The masticatory muscles are composed of fibres showing rather heterogeneous activity (van Eijden et al., 1996; Blanksma

et al., 1997), therefore, their functionality cannot be captured by groups of parallel vector in only one direction.

Our bodies have different types of tissues that are used to connect all of our parts. Bones are connected to other bones through tissues called “ligaments”. Muscles are connected to bones by tendons (Figure 39). Tendons are very strong, and are built from long strands of protein and are not very stretchy, thus when muscles pull, they pull too and they move the bones (Griffin, 2018).

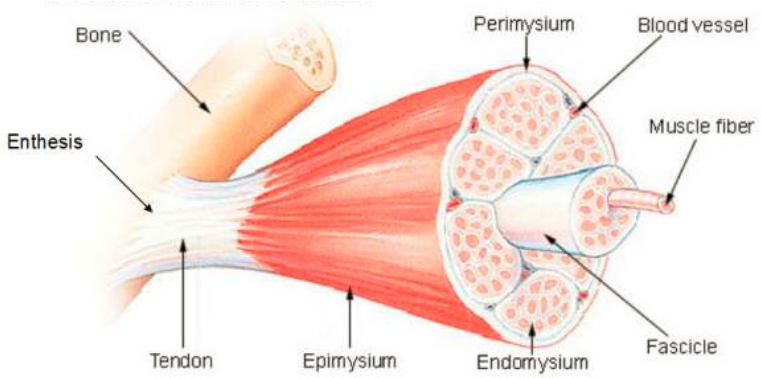

Figure 39: Muscle structure, showing an indirect attachment (Muscle Enthesis, 2013).

There are two types of muscle attachments (enthesis) to the bone (Muscle Enthesis, 2013): Direct attachment: A direct attachment is where the muscle quite literally inserts directly to the bone. A common site for this configuration is the abdominal wall muscle that may attach directly to the brim of the pelvis. Indirect attachment: An indirect attachment occurs where the muscle forms a tough elastic fibrous band, termed a tendon, which then attaches to the bone.

2.3.3 Mandible biomechanics

The energy that moves the mandible and allows functioning of the masticatory system is provided by muscles. The mandible forces can be assumed to be symmetrical and with equal magnitude on both the right and left side (Choi et al., 2005). Muscles are coherent structures with inhomogeneous but continuous fibre orientation (Schumacher, 1961).

The lack of bone continuity results in the mandible moving upwards and paracentrically due to the action of the stomatognathic system muscles, and leads to significant defects, both functional (speaking and chewing) and aesthetic (face deformation). Therefore, reconstruction

using bone graft must be performed (Dabrowski et al., 2010). One of the most important clinical problems is the size of the removed part of the mandible its location. Maxillofacial surgery autogenous grafts from the iliac crest stabilized with titanium, reconstructive plates are predominantly used (Miodowska et al., 2016).

Forces applied to the mandible cause various zones of tension and compression (Figure 40), depending on the region where the bite force is applied. The superior portion (top half) of the mandible is designated as the tension zone and the inferior portion (bottom half) is designated as the compression zone. The mandible is a hoop of bone that deforms with movement based on the origin and insertion of the muscles of mastication (Markad, 2014).

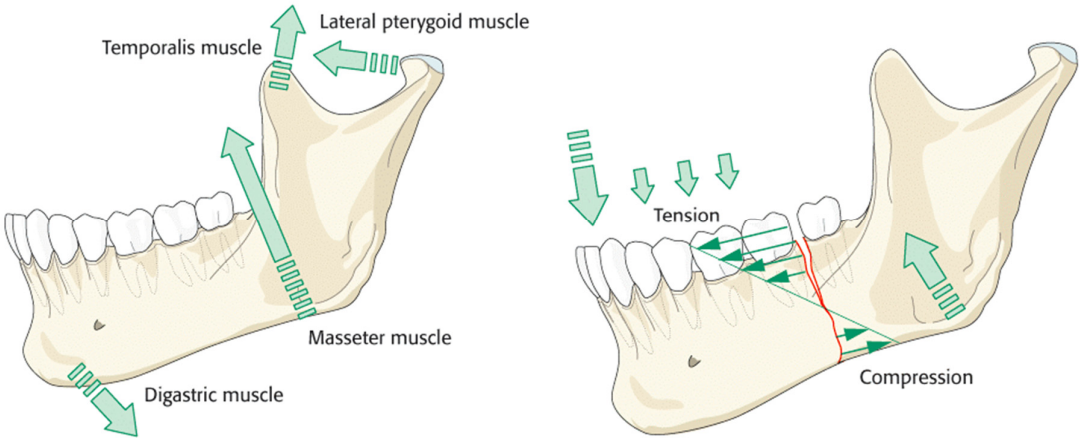

Figure 40: Mandibular muscle force direction (a), and tension and compression zones (b) (Markad, 2014).

The mandible is strongest in the midline (symphysis) and weakest at both ends (condyles). Therefore, the most common area of fracture in the mandible is the condylar region. A blow to the anterior mandibular body is the most common reason for condylar fracture. The force is transmitted from the body of the mandible to the condyle that is trapped in the glenoid fossa. Commonly, a blow to the ipsilateral mandible causes a contralateral fracture in the condylar region (Markad, 2014). The motion of the mandible during the mastication cycle is a three-dimensional complex motion, and the stage of mastication determines the amplitude of the anterior and lateral movement (Faulkner et al., 1987). Bite force can provide useful data for evaluating jaw muscle functionality and activity. Loadings are thought to be factors that determine mandibular bone structure since they play an important role in the modelling and remodelling of bone. During biting and mastication a combination of sagittal bending (Figure

41), corpus and transverse bending occurs (Levrini et al., 2015). Faulkner et al., 1987 and Commisson et al., 2015 show the muscle forces' magnitude and direction during mastication.

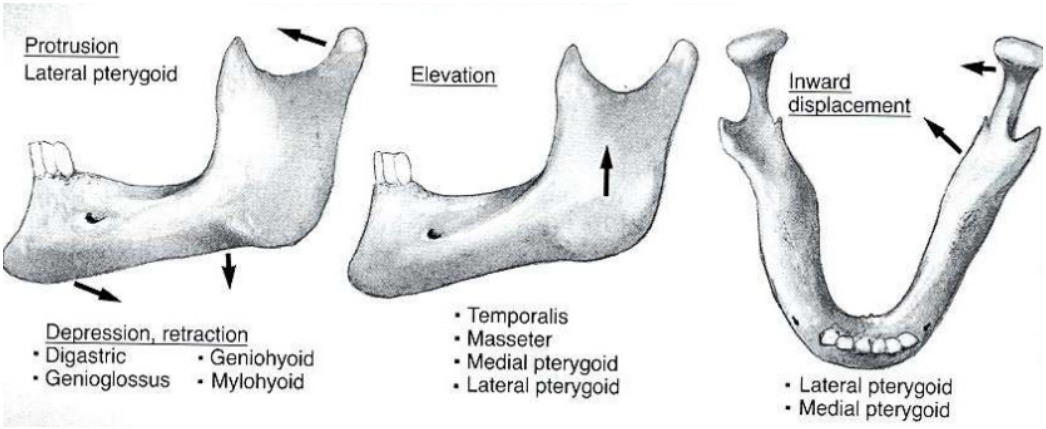

Figure 41: Mandibular force directions (Stierman, 2000).

The jaw moves through contractions of the masticatory muscles. Each muscle contraction is associated with a force which is expressed by three independent variables: its magnitude, its point of application, and its orientation. The last variables are dependent of the muscles line of action, defined by the geometry of the system. Each muscle can produce a translation of the lower jaw along its line of action, and a rotation about an axis perpendicular to it and running through the jaw's centre of gravity (Koolstra, 2002). Pandula, 2011 states that mastication forces (Table 4) are the forces exerted during mastication with variations in region, person, age, sex, food and race. The muscles of mastication are the main cause for these forces, as they contract and relax leading to the production of force for mastication. The average maximum sustainable biting force that is generated by the mastication organ muscles is about 756 N.

Table 4: Numerical data and magnitude of the mastication muscles (Kijak et al., 2015)

	Muscle name	F_{MAX} (N)	Muscle force angle orientation (α)
Short face	Massetter	217.7	−8
	Medial pterygoid	148	−13
	Lateral pterygoid	150.8	−97
	Temporalis	210.7	27
Normal face	Massetter	166.9	−19
	Medial pterygoid	113	−17
	Lateral pterygoid	145.6	−97
	Temporalis	177.4	27
Long face	Massetter	120	−17
	Medial pterygoid	89.9	−18
	Lateral pterygoid	131.9	−99
	Temporalis	155	27

The face is filled with air cavities, soft tissue spots, arteries, and nerves as well as individual variations that need to be considered. Stress shielding is solved by matching the stiffness of the orthopaedic implant to the original bone being simulated or replaced.

2.3.4. Summary

Biological biocompatibility refers to chemical reactions with living tissue, and is expressed by indications such as toxicity, allergy and fusing between biomaterials and living tissue. Ti6Al4V alloys is biocompatible material.

Each person's physique and bone structure is different, meaning that chewing loads can vary in both magnitude and direction. When designing a mandibular implant, the stress and strain distribution as well as the capability to absorb the chewing load should be used to evaluate the design. Maximum stresses in designed implant must be lower than the yield strength of used material.

2.4. FINITE ELEMENT ANALYSIS

Application of the finite element stress analysis technique to the biomechanical investigation of the oral system, such as human teeth, periodontal ligament, implant designs and mandibular bone modeling, was initiated in the early 1970s (Choi et al., 2005).

In FEA, the accuracy of the FEA results and requested computing time are determined by the mesh density (element density). According to FEA theory, the FE models with fine mesh (small element size) yield to highly accurate results but may take longer computing time. FE models with coarse mesh (large element size) may lead to less accurate results but do save more computing time (Liu, 2013). Small element size will increase the FE model's complexity which is only used when high accuracy is required. Large element size, however, will reduce the FE model's size and is extensively used in simplified models, providing a quick and rough estimation of design (Liu, 2013). Due to its importance, in generating FEA models, the foremost problem is to choose appropriate element size so that the created models will yield accurate FEA results while saving as much computing time as possible (Liu, 2013). FEA makes it possible for the designer to identify an implant's weakness before the manufacturing commences and allows for pre-manufactured and pre-surgery modification to the initial design in order to optimize it in terms of strength and material used. An AM design loop flow chart for medical implants is shown in (Figure 42).

Mandible model assembly is an important aspect in ensuring that the implant and the section of the bone affected fit perfectly. Therefore, a good fixation with the different properties of bone ensures there is no friction on the implant-to-bone fixation. Scaffolding tissue engineering (TE) aims to regenerate damaged tissue by combining cells from the body with highly porous scaffold biomaterial, and acts as a template for tissue regeneration, guiding the growth of new tissue (O'Brien, 2011).

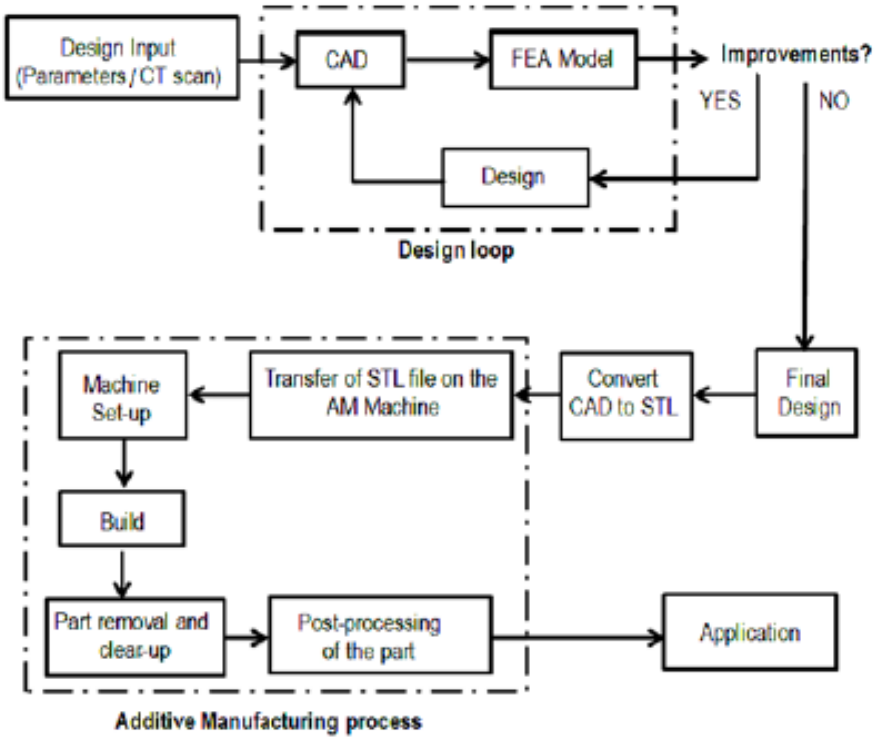

Figure 42: AM design loop flow chart for medical implants (Al-Ahmati et al., 2015; Monaheng, 2017).

FEM analysis of stresses and strains distribution in the mandible and around implants placed in the resected part is an important issue in dental engineering. The load scheme assuming the muscle action is adopted as the closest to the physiological conditions of the stomatognathic system work (Miodowska et al., 2016).

CAD systems offer solutions for the planning of the maxillofacial reconstruction surgery in relation with the aesthetic outcome and the final prosthetic and functional rehabilitation (Tarsitano et al., 2014). An accurate CAD model is based on a high-resolution CT scan of the mandibular bone geometry. The CAD model is designed prior to the FEA and manufacturing process. A CT scan is done to achieve a 3D visualization of the patient mandible, and the affected area can, therefore, be removed and replaced with a scaffold (titanium implant) (McCollough, 2018).

By definition, a Standard Triangle Language (STL) model is a completely closed boundary representation constructed entirely of triangular facets, the sizes of which are determined by tolerance applied to an original surface or solid model. STL format uses triangles; this triangular mesh is most often derived from the surface, and only the surface of a 3D CAD

designed object. Mesh can also be derived from “point clouds” generated through laser scanning (STL, 2011).

The surface normal of each triangle is explicitly defined as a vector, which helps improve processing speed for rapid prototyping but mostly just adds unnecessary data for three-axis machining applications (Beard, 1997). The number of triangles is primarily a function of the size of the surface (Figure 43) and the resolution of the tessellation. The higher the resolution, the greater the number of triangles and the closer the approximation is to a true curved surface.

Figure 43: Series of linked triangles to recreate the surface geometry of a solid perfect sphere (Giang, 2018).

A rule of thumb for maximum resolution and good 3D visual effect and printing results, is to export with a $1/20^{th}$ of the 3D printed-layer thickness and never below 0.001 mm (1micron) chord height and a 15 degree angular tolerance. This will result in an STL file with ideal accuracy for most 3D-printing applications (Giang, 2018)

2.4.1 Mesh generation

FEM is suitable for structures that go beyond a simple analytical formula representable geometry. The geometry is meshed, that is, divided into small parts. These parts are called “finite elements” (Thieme, 2016). The mesh is also used to represent the solution field to the physics being solved (Frei, 2013). By defining a geometric design space, FE may be used to calculate an optimum component shape. Often, FEM begins with the import of CAD geometry into a FEM pre-processor, and with the meshing of the geometry (Thieme, 2016). Different element types (Figure 44) can be used.

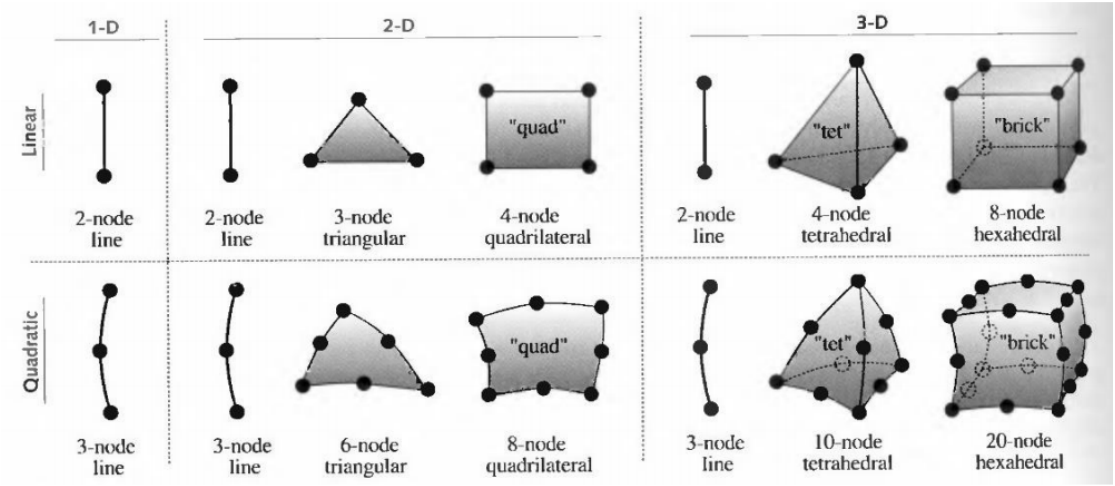

Figure 44: Most commonly used element types (Norton, 2006; Thieme, 2016).

Two types of element shapes are commonly used for mesh generation: tetrahedral and hexahedral (Figure 45). Tetrahedral meshing is highly automated, and is good at predicting stresses with sufficient mesh refinement, while hexahedral elements have a consistently predicted reasonable force vs loading (stiffness) conditions, material incompressibility in friction and frictionless contacts. Tetrahedral and prisms are recommended when there are frictionless contact conditions and when the material incompressibility conditions can be relaxed to a reasonable degree of assumption (Srinivas, 2017).

Hexahedral meshing commonly requires user intervention and is effort intensive in terms of partitioning. Hexahedral elements are generally preferred over tetrahedral elements due to their superior performance in terms of their convergence rate and accuracy of the solution (Srinivas, 2017). Modified second-order tetrahedral elements (C3D10, C3D10M, C3D10MH) all mitigate the problems associated with linear tetrahedral elements; therefore, they offer a good convergence rate with a minimum of shear or volumetric locking.

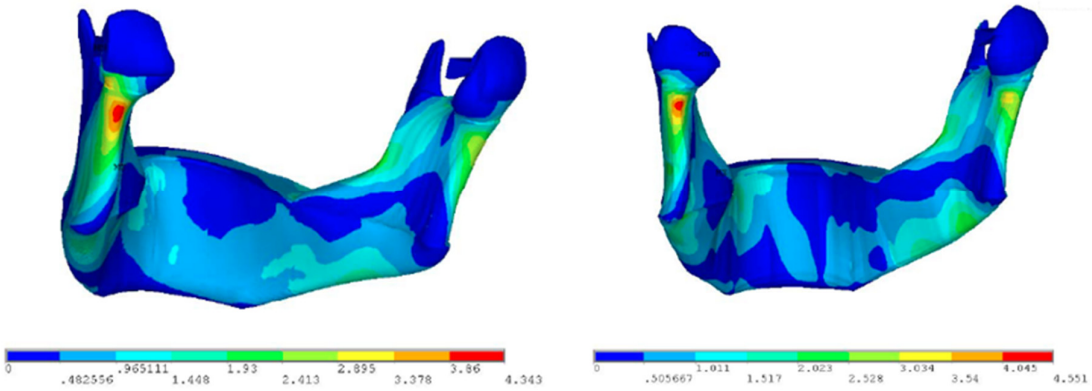

(a) **(b)**

Figure 45: Von Mises equivalent stress (MPa) on the mandible and TMJ: tetrahedral (a) and hexahedral (b) models (Armentani et al., 2010).

The results based on tetrahedral and hexahedral models show a level of discrepancy and minimum legend variation that is not such as to affect future work.

In areas where accurate stresses are needed, elements should be of good quality. The key for adaptive mesh generation is to refine the mesh at places where errors are too large and the coarse mesh at places where the mesh size is too dense.

Some FEM software preferentially inserts smaller elements around a hole and allows a manually smaller mesh input (Figure 46). This should be considered important as seen by stresses around a defect (fracture, pores, etc.) will be higher. Therefore, it is important to use a combination of adaptive mesh refinement, engineering judgement, and experience to find a suitable mesh (Frei, 2013).

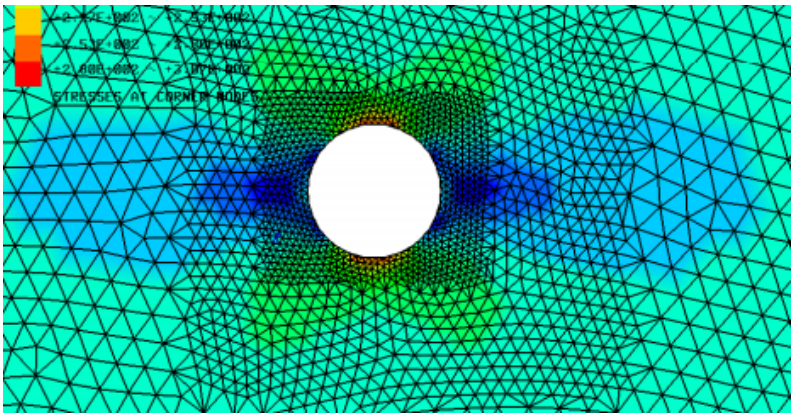

(a)

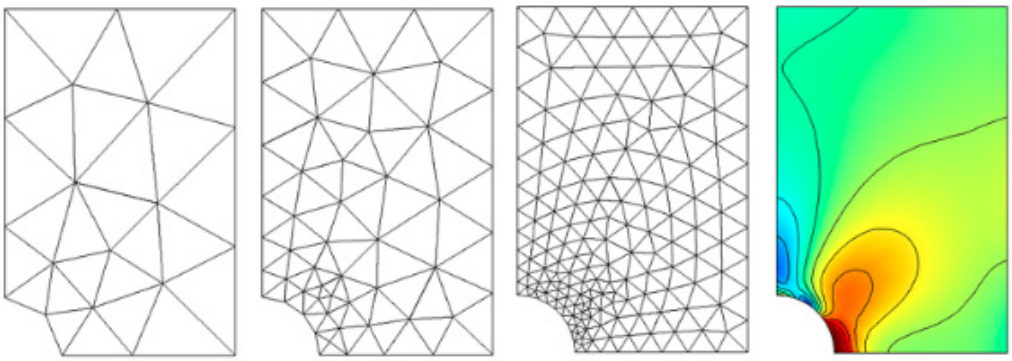

(b)

Figure 46: Different mesh shape and size calculating the stress and displacement: Mesh refinement around a hole (Neupane, 2014) (a), and mesh refinement at critical area (b) (Frei, 2013).

2.4.2 FEA of mastication

FEA is applied in engineering and other fields as a computational tool for performing engineering (stress/deflection) analysis. It includes the use of mesh generation techniques for dividing a complex problem into small elements, as well as the use of software program coded with FEM algorithm. In applying FEA, the complex problem is usually a physical system with the underlying physics as the Euler-Bernoulli beam equation, the heat equation, or the Navier-Stokes equation expressed in either PDE or integrated equations while the divided small elements of the complex problem represent different areas in the physical system (Abadzhiev et al., 2017).

Accurate three-dimensional modelling will enable the clinician to best access the form and engineering requirements of hardware that is used to treat mandibular fractures. Not only can

surgical planning be refined with this technology, it can also be used to study various aspects of facial bone osteotomies, such as post-operative functional change and stability of the orthognathic movement (Choi et al., 2005).

FEA that have simulated masticatory loading of the human mandible differs significantly with regard to their basic input variables such as material properties, constraints, and applied forces (Groning et al., 2012).

In maxillofacial reconstruction surgery, the appropriate design and geometrical standards are important functions for a successful implant application. With conventional reconstruction methods (manually bending plates) of the mandible such as bone grafting restoration of the jaw geometry, jaw relationship, and condylar position are difficult to maintain (Hung, 2011).

The surface triangle mesh contains several thousand small triangles; a mesh simplification is done to reduce the numbers of triangles. A multi-resolution model for reduction is used to re-insert the small triangles at the location where the implants are inserted into the mandible (Futterling et al., 2001). How to simulate muscle force in a realistic way is probably the most challenging part of an FEA (Figure 47). Muscular load actions are shown in Table 5.

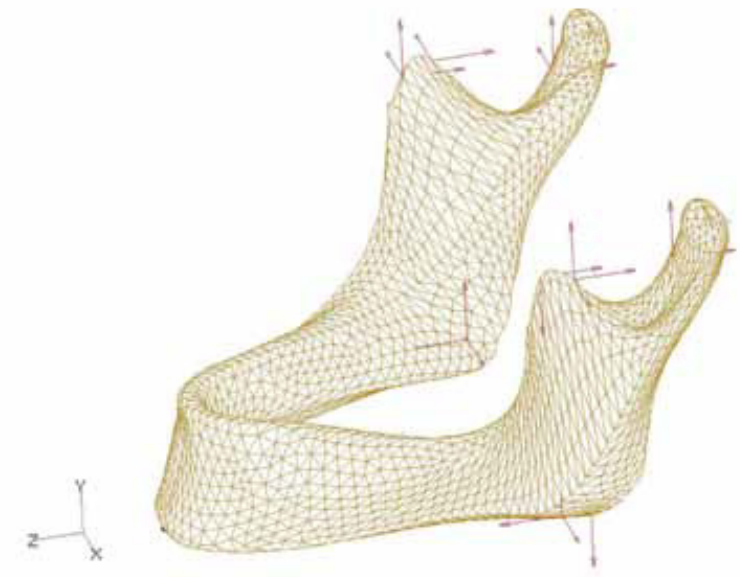

Figure 47: Mandible with mesh and muscle forces (Levrini et al., 2015).

Table 5: Muscular load action (Ramos et al., 2011)

Muscle action	Load (N)		
	X	Y	Z
Deep masseter	7.776	127.23	22.68
Superficial masseter	12.873	183.50	12.11
Medial pterygoid	140.380	237.80	−77.30
Temporalis	0.064	0.37	−0.13
Medial temporal	0.970	5.68	−7.44

The influence of masticatory muscle action on the development of craniofacial morphology has received considerable attention (Pepicelli et al., 2005). Since bone adapts to loads by remodelling to reach optimal form to withstand specific loading (Kiliaridis, 1995), it has been hypothesized that craniofacial skeletal form is largely determined by mechanical loading.

Studies show that the mandibular shape varies to a certain extent as a function of the force applied to it by the temporalis and the masseter muscles (Gateno et al., 2015). The size and shape of the jaw should reflect the muscle size and activity (Proffit et al., 2014).

When reconstructing a mandible due to fractures (any stage, 1, 2 or 3) or resection, it is important for the stress-strain distribution to be as close as possible to a normal/healthy mandible bone (Figure 48). It is expected that the bone will remodel in response to this healthy loading pattern, allowing the reconstructed mandible to become stronger, thereby providing better support for dental implants (Moghaddam et al., 2017).

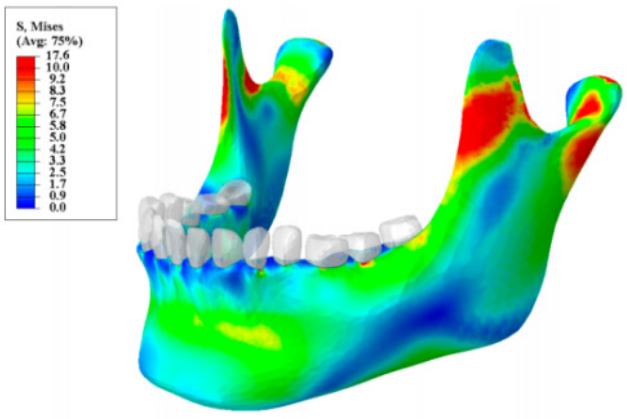

Figure 48: Von Mises stress distribution for a normal mandible (Moghaddam et al., 2017).

The yield strength is expressed by the point dividing the elastic strain region and the plastic strain region of the stress-strain curve. Beyond the yield point, the bone tissue will not return to its original shape if the load is released (van Eijden, 2000). Mandibular parameters are shown in Table 6.

Table 6: Analysis of mandibular parameters (Alvarez-Arenal et al., 2009; Bayome et al., 2013; Ozturk et al., 2013; Lopez et al., 2017)

Variable		
Ramal length (mm)	Gonial angle (^{0})	Mandibular body length (mm)
57.57 ± 5.82	115.46 ± 3.96	87.98 ± 4.98
62.30	115.47	71.42
59.28	127.55	73.07

The average von Mises stress in different zones of the normal mandible is compared to a reconstructed mandible (Figure 49). The results show good agreement with each other (the maximum discrepancy of 4.6 % on the condyle zone).

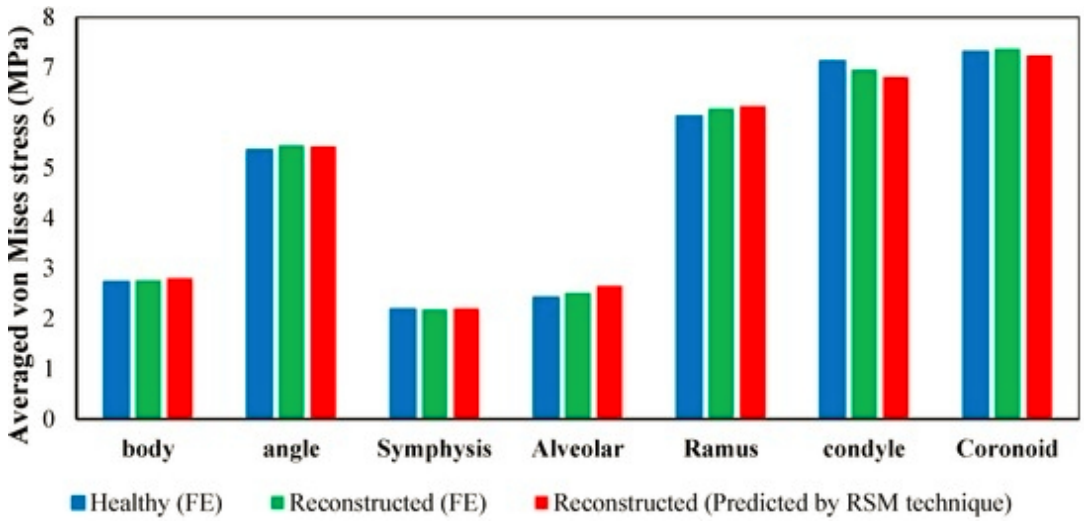

Figure 49: Average von Mises stress in different regions obtained from FEA of a normal mandible and of a reconstructed adult mandible (Moghaddam et al., 2017).

2.4.3 Summary

Sustainability in an exponentially growing biomedical field is an important factor ensuring a functional part can accommodate a resected area's functions. FEA allows a virtual contribution to either simulate geometric functional analysis of a resected area, or an integrity analysis of internal porosity contributing to the mechanical properties. FEA can be used as an alternative method to validate any experimental testing with cost efficiency and time efficiency commencing in accurate experimental testing, and knowledge of what to expect from experimental results.

CHAPTER 3: MATERIALS AND METHODS

3.1 EOSINT M 280

Ti6Al4V samples were produced by the EOSINT M 280 machine (EOS GmbH) equipped with an ytterbium fibre laser operating at 1075 nm wavelength (IPG Photonics Corp.) (Figure 50). The laser beam has a TEM_{00} Gaussian profile and 80 µm spot diameter. Original EOS parameter set Ti64_Performance 2.0 recommended for 30 µm powder layer thickness was used. A back-and-forth scanning by strips (5 mm) with the hatch distance of 100 µm was applied for manufacturing of specimens in accordance with standard process parameters. The substrate and powder material were similar in chemical composition. Argon was used as the protective atmosphere.

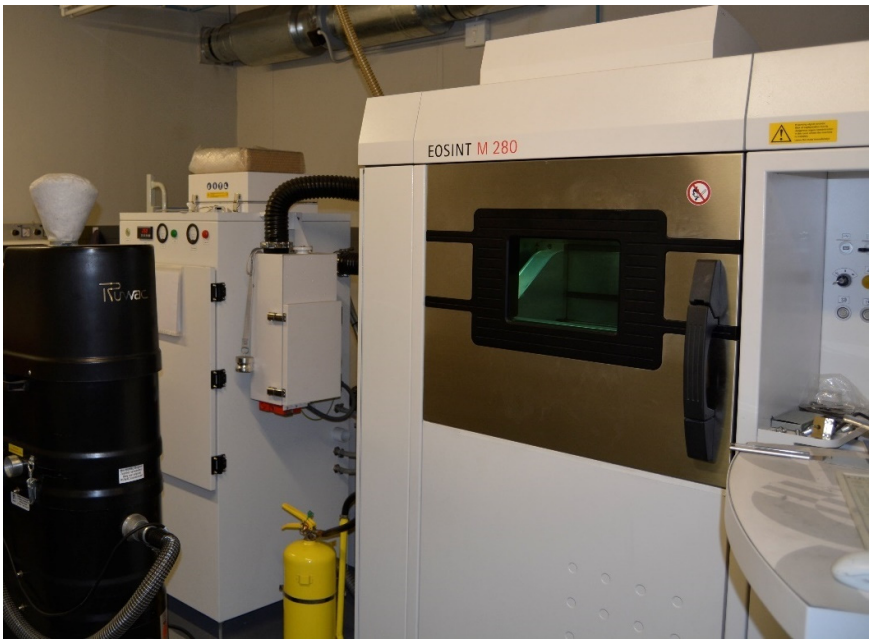

Figure 50: EOSINT M 280 system used to produce Ti6Al4V samples.

The procedure for manufacturing on the EOSINT M 280 system was as follows:

1. Clean Ti6Al4V substrate with ethanol;
2. Install substrate via all allen bolts into the EOSINT M 280 build chamber;
3. Level the platform and substrate using the EOSINT M 280 interface and a feeler gauge;
4. Ensure re-coater blade is damage-free;
5. Deploy powder into hopper (utilizing PPE at all times);
6. Compact the powder;

7. Level powder;
8. Ensure re-coater arm path over the substrate is collision-free (clearance 0.03 mm < 0 mm);
9. Install duct in front of building chamber;
10. Flood chamber with argon until oxygen content is below 0.01 %; and
11. Commence automatic LPBF start process through the EOS interface.

Ti6Al4V parts were produced in accordance with the CRPM ISO 13485 certification for 3D printing of medical devices.

3.2 Ti6Al4V (ELI) POWDER

Ti6Al4V ELI (extra low interstitials) powder was supplied by L.P.W. Technology Ltd. Powder had spherical particles with equivalent diameters (weighted by volume) d_{10} = 23 µm, d_{50} = 33 µm, d_{90} = 46 µm. A chemical composition of the Ti6Al4V (ELI) powder is shown in Table 7. Chemical composition of powder was in accordance with ASTM F136 and ASTM F3001 standards.

Table 7: Chemical composition of Ti6Al4V powder (wt.%)

N	C	H	Fe	O	Al	V	Ti
ASTM F136-13 for Ti grade 23 for surgical implant applications							
≤0.030	≤0.080	≤0.0125	≤0.25	≤0.13	5.5–6.5	3.5–4.5	Balance
Employed powder							
0.01	0.01	0.002	0.20	0.09	6.26	4.1	Balance

3.3 SPECIMENS DESIGN

3.3.1. Anatomy analysis

The face is filled with air cavities, soft tissue spots, arteries, and nerves as well as individual variations that need to be considered. The mandible is the only movable stress-bearing bone of the face and disregarding the forces acting on the mandible can lead to reconstruction failure (Wong et al., 2011). The following anatomical factors influence the stability of an implant and screws: bone characteristics (bone density, bone depth, cortical bone thickness), soft tissue, and the proximity of specific anatomical structures (nerves, roots, vessels, nasal cavities). Geometry and mechanical properties of the mandible are complex and depend on many factors (Table 8 and Table 9). (Baek et al., 2012). By researching the anatomy of a human mandible,

one can incorporate anatomical functions and properties (mandible geometry, mandibular length, muscle attachments, shape and size of bone properties, porous structures, etc.) into a sustainable design structure, assuring great osseo-integration, muscle attachment, and implant-to-bone fixation.

Table 8: Different mandibular bone material properties (Correia et al., 2008; Mariano et al., 2012; El-Anwar and Mohammed, 2014; Iranmanesh et al., 2014)

	Cortical bone	Cancellous bone
Young's modulus (GPa)	13.6–15	0.24–1.85
Poisson's ratio	0.3	0.3–0.45

Table 9: Measurement of the mandible body (Klinge et al., 2017; Tunis et al., 2017; Lopez et al., 2017)

Normal age group mean value			
	Height	W1	W2
LO-MOL-R	26.8±2.6	13.0±1.9	11.0±1.6
LO-PRE-R	30.7±2.8	10.4±2.1	10.0±1.8
LO-MID	32.3±3.0	7.3±1.6	13.5±2.4
LO-PRE-L	30.7±3.0	10.4±2.0	10.2±1.7
LO-MOL-L	26.6±2.8	13.3±1.9	11.0±1.7
Mandible parameters			
Ramal length (mm)		59.28	
Gonial angle (^{0})		127.55	
Mandibular body length (mm)		73.07	

(±SD-Standard deviation; W1-coronal width; W2-apical width; LO-MOL-R lower molar right; LO-PRE-R lower premolar right; LO-MID lower midline; LO-PRE-L lower premolar left; LO-MOL-L lower molar left)

Kim and Park, 2011 explain in tabular form the difference in bone thicknesses between men and women in the mandible buccal and lingual areas as well as different sections of the mandible. They also show the mandible in transaxial slices, whereas Gonzalez, 2008 and de Souza Fernandes et al., 2010 show slices from an axial view. These two articles may serve as a reference to distinguish between different perspectives.

Kijak et al., 2015 characterized in depth the different muscle lines of action along with the force these muscles exert during a mastication cycle. Figure 51 shows the basic method of

muscle placement when designing a sample with precise replica of different muscle magnitude and line of action.

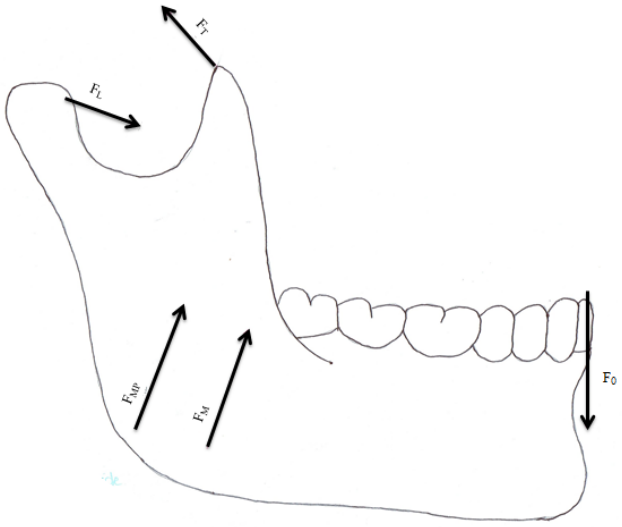

Figure 51: Schematic diagram reflecting the muscle positioning on the mandible bone: F_M: Masticator/Masseter, F_0: Applied force, F_{MP}: Medial pterygoid, F_L: Lateral pterygoid, and F_T: Temporalis (Kijak et al., 2015).

Mandibular size and shape play a tremendous role in the final design of a sample with mandibular similarities for optimal experimental values.

3.3.2. Ti6Al4V ELI samples

Various sources (Gonzalez, 2008; de Souza et al., 2010; Kim and Park, 2011) show different mandible cortical bone thickness, body height and width, and elastic modulus which result in thinner implants. Model tests of the mastication cycle are very often conducted on flat sample specimens. By reducing the spatial structure to a flat sample, one can assume a symmetrical mandible load with active and passive forces. Anchoring reinforcement is one of the major factors underlying a successful replacement of a reconstructed mandible and should therefore be implemented when an implant is designed. Mandible reconstruction should strive to restore bony contours and work towards the restoration of mastication (Walton et al., 2010).

A research into AM porosity shows that a variety of shapes may occur and they may be elongated like ellipses in many cases (see Appendix 5). Taking into account peculiarities of LPBF manufacturing of fine features (Kouprianoff, 2017), small rectangular geometry pores were

chosen for design and testing purposes. In reality, the sample's surface roughness in microscopic view will be rough with small implicit spikes or ridges superior to the rest of the sample surface and can contribute and result in small errors. A smooth surface area was considered when calculating the contact area of a cylinder.

Du Plessis et al., 2016b show that the directionality of defects observed may be helpful to interpret quality issues of AM of metal components and help designers or engineers to select the building orientation wisely. It was found, according to previous research done by (Yadroitsau et al., 2018), that a defect of 200 µm had no significant effect on material properties of the specified samples, and Kouprianoff, 2017 showed that a layer-induced defect of 180 µm thickness had partially fused areas together.

Before any AM commenced, samples were designed with CAD. Samples were designed 100 mm in length, 15 mm in width and a thickness of 2.5 mm. The induced artificial defects were fabricated by leaving cavities in the CAD file while keeping processing parameters constant. Artificial defects were inserted at various depths of the implant to mimic pores. The defects were set in the centre, 2 mm from the side, and 500 µm from the top and bottom respectively, representing four independent cases.

Six additional reference solid samples (RS) were manufactured. According to above references, defect height (thickness) was 210 µm (Set AD1) and 420 µm (Set AD2) to find critical porosity in implants (Table 10). Length of all defects was 1 mm (Figure 52).

Table 10: Samples classification

Description	Top view	Side view	Width	Thickness	Designation	Quantity
AD*x*.1	2 mm from the side	middle	300 µm	210 µm	AD 1.1 A-C	3
			500 µm	420 µm	AD 2.1 A-C	3
AD*x*.2	middle	500 µm from bottom	300 µm	210 µm	AD 1.2 (A-C)	3
			500 µm	420 µm	AD 2.2 (A-C)	3
AD*x*.3	middle	middle	300 µm	210 µm	AD 1.3 (A-C)	3
			500 µm	420 µm	AD 2.3 (A-C)	3
AD*x*.4	middle	500 µm from top	300 µm	210 µm	AD 1.4 (A-C)	3
			500 µm	420 µm	AD 2.4 (A-C)	3
Reference sample					RS	6

Solidworks 2017 design software was used in this study and converted to STL file format via the Solidworks platform. The STL files were then imported into Magics software (Materialise), which is purpose-made AM software, and the final step in communication to the EOSINT M

280 machine, and then placed on a virtual substrate within the software. The final supports were then added and processing and manufacturing could commence (Figure 53).

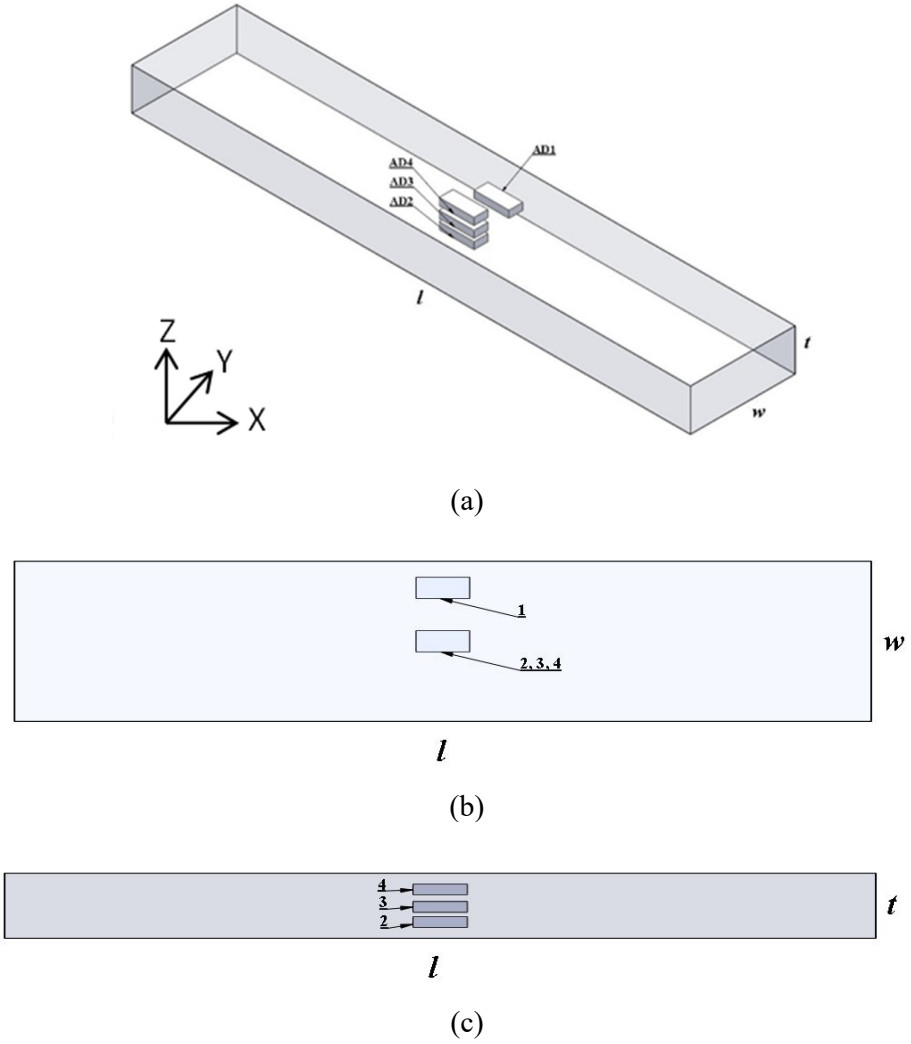

Figure 52: 3D view of Ti6Al4V ELI sample with combined artificial defect placement classification (a); top view (b) and side view (c).

The samples were built on a Ti6Al4V substrate with recommended EOS standard process parameters. Samples were manufactured at a depth of 16 mm vertically instead of 15 mm to facilitate separation with the wire cutter. Domes for identification were placed on the right side of the sample correlating with a respective pore. A 0.8 mm wire cutter was used to remove the samples from the substrate and machined to the required 15 mm.

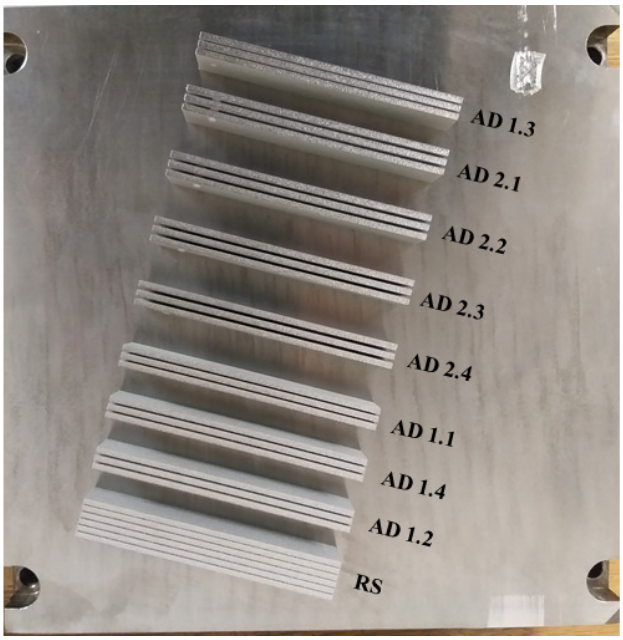

Figure 53: Ti6Al4V vertically produced samples with titanium substrate.

3.4 DESIGN OF EXPERIMENTS

Taking the geometry of samples into account, loadings and pre-calculated stresses for under mastication LPBF Ti6Al4V ELI samples were experimentally tested at 800 N, 900 N and 1500 N. The design of the experiments is presented in Figure 54:

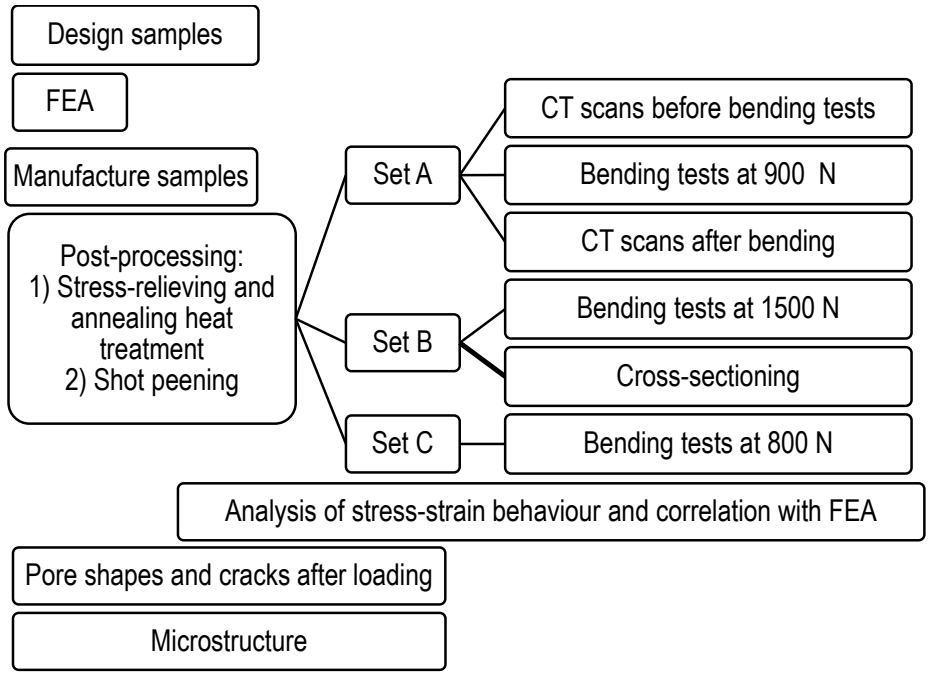

Figure 54: Flow chart of experiments with LPBF Ti6Al4V samples.

3.5 POST-PROCESSING

3.5.1 Heat treatment

For certified implants, post-printing treatment is extremely important. The annealing stage alters the physical and sometimes chemical properties of a material to increase the ductility and reduce its hardening, allowing a long-lasting implant. LPBF Ti6Al4V samples were stress-relieved in vacuum furnace system SS1224-13, installed at CUT for three hours at 650 °C and furnace cooled (Figure 55).

(a)

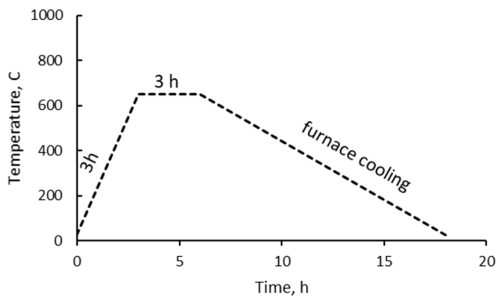

(b)

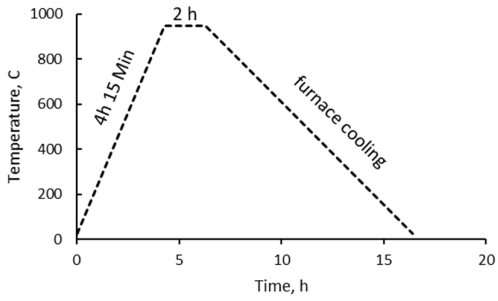

(c)

Figure 55: Vacuum furnace (a) and heat treatment procedure for Ti6Al4V ELI samples: stress-relieving (b) and annealing in vacuum furnace (c).

Maximum temperature during the stress-relieving stage did not exceed the β transus of the material; no recrystallization takes place and therefore no material properties are adversely affected or improved, except that the crystal structure adjusts in such a way that residual stress

is eliminated. Samples were separated from the base plate and soaked at 941 °C for two hours (Figure 55c) in accordance with SAE AMS 2801:2003 standard to improve ductility and enhance fatigue resistance.

3.5.2 Shot peening

The fatigue strength of as-built AM metals is weaker than that of the bulk equivalent (Sato et al., 2016; Soyama et al., 2018). It has been reported that the fatigue life of AM Ti6Al4V decreases as the maximum surface roughness increases (Chan et al., 2013). For implants, a high strength and lifetime are extremely important, so it was decided to use the shot-peening process to decrease surface roughness and introduce compressive stress to the surfaces of Ti6Al4V ELI samples. Shot peening is a mechanical surface procedure that can enhance the fatigue strength by creating residual compressive stresses on the surface and improve the surface finish of the component. In the process, hard beads (made from steel, ceramic or glass) accelerated by compressed air impact the treated material and affect the surface. The surface quality has a significant influence on the fatigue life of the α-β Ti6Al4V alloy (Belan et al., 2019).

Due to the vertical building direction and taking the powder layers into consideration, the load will be perpendicular to the powder layer when orientated for three-point bending. Yadroitsev et al. (2018) showed that the process parameters used resulted in the lateral surfaces of the Ti6Al4V LPBF samples having a higher roughness than the top surface. Rz values were about 120 µm, which is quite high and can influence the mechanical properties. As indicated by Zebrowski et al. (2019), mechanical properties of 3D printed Ti-alloy implants were most favourable in the cases where surfaces were modified with steel shot, but for better biocompatibility, processing with ceramic balls was the most preferred method. For the present study, samples were shot peened using steel beads. Shot peening was done in a Peenmatic PM 750S blast cabinet with a 6 mm diameter blasting nozzle and stainless steel beads that were accelerated under a pressure of 3.7 bar to impact the surfaces of the test pieces. Shot peening was applied for about 10 minutes per surface. The size of the stainless steel beads was near 500 µm (Figure 56).

(a) (b)

Figure 56: Blast cabinet (a) and stainless steel beads (b) used for shot peening.

3.6 PHYSICAL TESTS

3.6.1 Three-point bending

Three-point bending (TPB) is one of the most common material testing methods to study the mechanical performance of materials with structural applications (Arrese and Mujika, 2008). This experimental procedure exerts compression and tensile forces on the sample under bending (Figure 57). Samples can show either failure caused by the compression force or tensile force. In a TPB test, the convex side of a plate sample is placed in tension, and the outer material is subjected to maximum stress and strain. Failure will occur when the strain or elongation exceeds the material's limits.

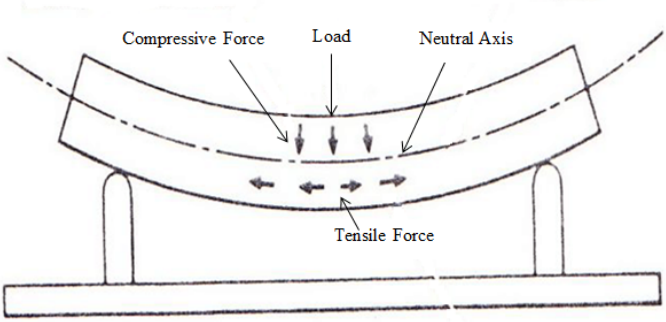

Figure 57: Forces involved in TPB.

TPB tests were done by a MTS Criterion machine (Figure 58), which is recommended to test in accordance with the multi-input devices (load frames). The properties of tool steel T10 were used for calculations. At a maximum loading capacity of maximum 30 kN, the MTS system is ideal to replicate a downwards bite force of the mandible. Samples were subjected to destructive testing allowing thorough investigation of the deformation of the sample when an artificial defect is introduced.

(a)

(b)

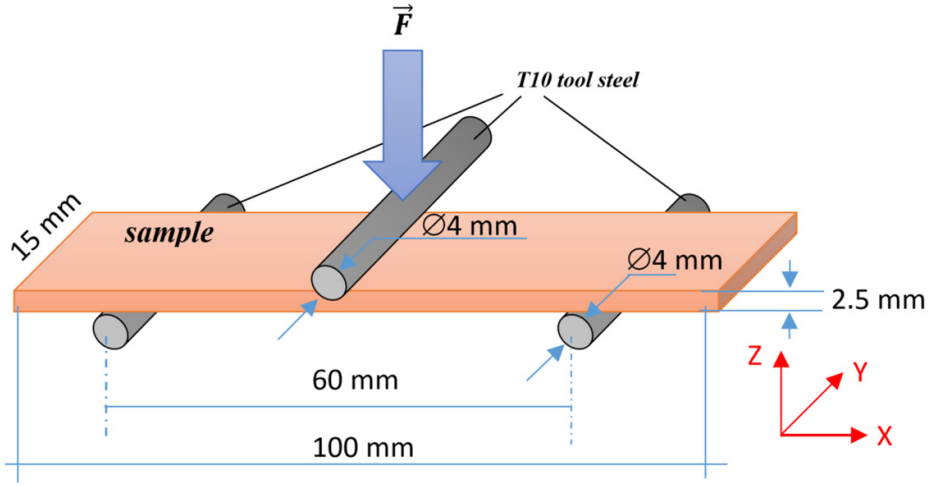

(c)

Figure 58: MTS Criterion model 43: loading frame (a) and adjustable TPB fixtures (b) and basic MTS setup for testing samples (c).

The frictionless contact between the sample and the supports during bending depicts situations of sample thickness to rotate inwards during bending. The amount of deformation (strain) with compressive loading (stress) will reveal the distinctive material property and when different artificial defects are introduced. Experimental data was analyzed by stress-strain plot graphs**,** indicating failure of samples subjected to different design conditions. This verification method allows for defects to be simulated in a controlled environment thereby answering related questions whether a certain size defect will impact the performance of a mandibular implant.

Various authors indicate maximum mouth opening and closing velocities (Karlsson and Carlsson, 1990), but it can be concluded that when grinding the teeth, the velocity and force exerted will vary. Therefore, replicating the grinding of teeth at a constant low speed was chosen to conduct the test to achieve accurate results. If the sample is sufficiently brittle and the force required within the limit of the load cell, fracture will occur. TPB tests with a support span of 60 mm were conducted at room temperature, first deforming it elastically then plastically (Figure 58c). Samples were selected and subjected to a series of loads, replicating worst-case implant failure, and it was recommended that the load end point varies between 800 N–1500 N (higher than maximum bite force). An important parameter is the speed at which the machine would perform a downward force. The loading nose and support must have cylindrical surfaces. In order to avoid excessive indentation or failure due to stress concentration directly under the nose, the radii of the loading nose and supports must be 2.0 mm. This is specified to simulate muscle attachment, and/or teeth force when biting down.

If there were no defects at all (a perfectly homogeneous sample), the flexural and tensile strengths of the sample would be the same. However, this is not common in practice as AM parts can have random voids, cracks or other defects that cause a stress concentration weakening the sample in a localised area. Bending strengths are generally higher than tensile strengths. In some more unusual cases, if a sample has a surface with a large number of flaws (due to rust spots or scratches), this will cause the tensile strength to be higher than the bending strength.

The main advantage of TPB is the ease of preparation and testing, although this method of testing is sensitive to loading geometry and strain rate. The bending moment varies linearly from the end where it is zero, and the absolute value at the centre is where the risk of rupture is most important.

Preparation of the MTS Criterion model 43 *(MTS Criterion Series 40 product manual for visual description)*:

- Place TPB fixtures on the top and base adapter. Fasten and secure both fixtures through the use of a pin and clamping tool for centre bending;
- Ensure a radius of 2 mm for the top (loading nose) and bottom (supports) fixtures are used;
- Adjust bottom (supports) fixture to a 60 mm span length;
- Adjust sample positioning with centring device on bottom (support) fixture to ensure centre loading;
- Switch on computer and open the program;
- Switch on MTS machine at the power switch;
- Measure the sample's width and thickness, and indicate the sample centre;
- Add necessary inputs into program;
- Place a sample on the bottom (supports) fixture against positioning pins;
- Enable handset (indicator is lit), by pressing the interlock button to move the crosshead up or down, either with the up and down arrows, or thumb-wheel for finer adjustments until the loading nose touches the sample's centre line;
- Zero signal the force on the program;
- Start the process until required bending is reached; and
- Repeat last five steps until all samples are bent.

For the MTS machine setup, the speed of loading was set 1 mm/min to ensure an accurate loading-displacement curve. If L is considered the total length of the beam, and the maximum bite force considered to be F=756 N for normal mastication. For testing purposes, a force of F=900 N was used for Set A Ti6Al4V samples.

3.6.2 Surface roughness testing

Surface roughness defines a surface texture. It is quantified by the deviations in the direction of the normal vector of a real surface from its ideal form. If these deviations are large, the surface is rough; if they are small, the surface is smooth. The surface roughness was measured using a Mitutoyo SJ-210 surface roughness tester which fulfils ISO 1997 requirements (Figure 59).

Figure 59: Mitutoyo SJ-210 surface roughness tester.

The parameters used for the measurements are as follows:

- Four randomly selected samples were tested;
- Distance of measurement: 5 mm;
- Speed of detector: 0.5 mm/s;
- One direction of measurement at 0˚ (longitudinal);
- Three measurements minimum along the longitudinal direction.

The device was completely stationary when the tests were conducted.

3.6.3 Micro CT-scans

CT scanning is currently the only diagnostic imaging technique that can determine the structure, density and assembly of the bones (Watzek and Ulm, 2002; Quirynen et al., 2003; Norton and Gamble, 2001; Shahlaie et al., 2003), as well as non-destructive testing of physical objects. As indicated by du Plessis et al. (2018), such X-ray techniques as 2D digital radiography and 3D micro-computed tomography (microCT) are very useful to analyze parts without destroying them. MicroCT works by acquiring X-ray absorption images from many

angles around the object, followed by reconstruction to produce a 3D representation of the object, including its interior. It is also known as X-ray tomography, CT scanning or X-ray microscopy (XRM). In this work, artificially induced defects in Ti6Al4V ELI samples were found by microCT, which would be very difficult to detect by other non-destructive testing methods because the artificial defects are entirely contained inside the object and not connected to the surface. A microCT scanning allows accurate images of possible or induced defects.

The samples (Set A) were CT scanned at the University of Stellenbosch CT scanner facility (du Plessis et al., 2016 c) using a General Electric Nanotom S system set to optimum parameters. NanoCT scans settings of 150 kV, 130 uA, with 0.5 mm beam filter were used, with image acquisition of 500 ms per image, 3 000 step positions in a full 360° rotation. At each step position, the first image is discarded and two subsequent images averaged. The samples were scanned at 10 µm. Visualization and analysis were performed by Volume Graphics VGStudioMax 3.3 software (du Plessis et al., 2015; 2016a).

3.7. MICROSCOPY ANALYSIS

To analyze changes in microstructure and appearance of cracks after loading, samples were cut at lengths mimicking that of the µCT scan length of 10 mm on both sides of the centre line (Figure 60) with a 0.8 mm diameter wire cutter.

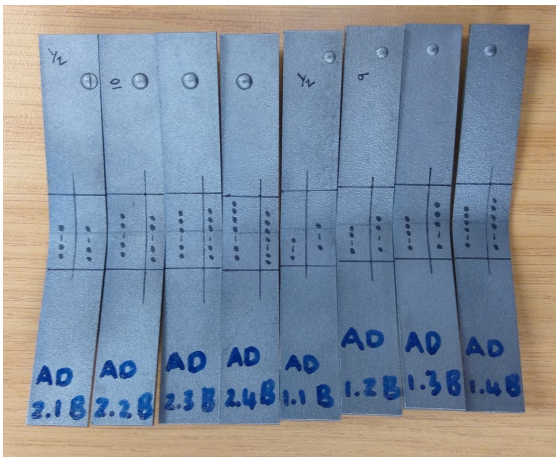

Figure 60: Ti6Al4V samples tested up to 1.5 kN.

Samples were set in resin with a CitoPress-1 hot mounting press, Figure 61 (a), Thereafter, a grinding and polishing procedure was followed using a Tegramin-25 polishing machine from

Struers (Figure 61 (b) to expose pores, and lastly, etched to see the microstructures' behaviour after bending.

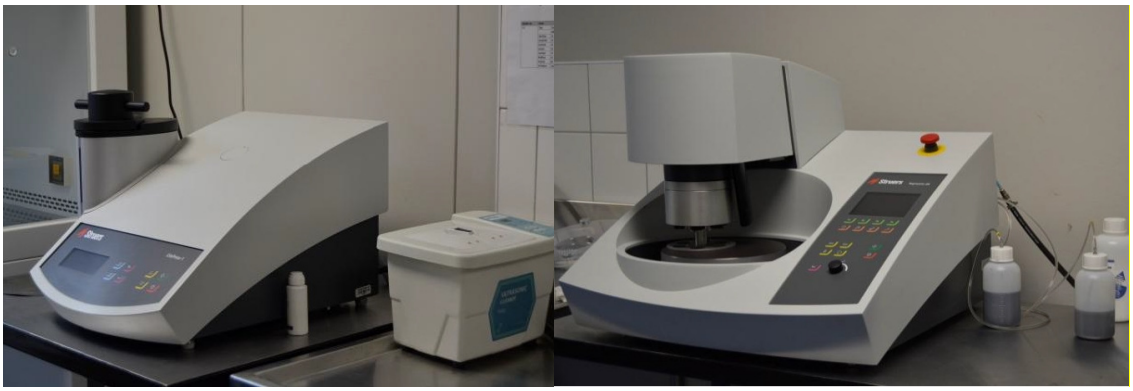

(a) **(b)**

Figure 61: CitoPress-1 hot mounting press (a) and Tegramin-25 polishing machine (b).

Cross-sectioning was conducted after the samples were loaded in the TPB setup. Samples were ground and polished according to Struers recommendations (Struers, 2020) and visually inspected under an optical microscope until the pores were reached.

3.8. NUMERICAL SIMULATIONS

3.8.1 Stress-strain calculations

The bending stress is highest in the area of loading and in the bottom part and gradually decreases as it moves closer and closer to the neutral axis. It is zero at the neutral axis. The bending stress increases in the reverse direction as the distance increases from the neutral axis. In Figure 57, arrows indicate the magnitudes of bending stress at different layers of a section above and below the neutral axis. Under three-point loading, these shear stresses do not vary across the span length but do vary parabolically through the thickness (Adams, 2017; Tec-science, 2018). For a flexural loading, all three fundamental stresses are present (tensile, compressive and shear). TPB is preferred to allow the sample to move freely at the supports when loaded as this method is used to simulate a mandibular implant. Depending on the material strength properties, the initiation of the material failure is imposed by one of these stresses reaching its limiting value or by their combined effect (Sauvage et al., 2017). Values of elastic modulus and Poisson's ratio used in numerical simulations are shown in Table 11.

Table 11: Ti6Al4V grade 23 and T10 tool steel used for MTS setup

Description	Ti6Al4V	T10 tool steel	Al alloy
Poisson's ratio	0.342	0.275	0.33
Elastic modulus	114 GPa	210 GPa	70 GPa

The second moment of area I_x (also known as area moment of inertia, the moment of inertia of plane area and the second moment of inertia) is used to predict the resistance of samples to bending and deflection because the deflection o depends not only on the load, but also on the geometry of the beam's cross-section (see Appendix 1). Samples that have higher second moment of area are stiffer and they are more resistant to bending. This parameter is very important for implants that must be flexible in one direction and rigid in other directions. According to Monaheng (2017), with a factor of safety (FoS) of 2.8, the recommended minimum thickness of Ti6Al4V was found to be 2 mm, taking into account that mandible bone elastic modulus is 21 GPa with a thickness of 3.8 mm. Therefore, the 2.5 mm thickness of the Ti6Al4V samples is appropriate with respect to mandible cortical bone. The theory and calculations on the second moment of area (Equation 1), maximum deflection (Equation 9) and slope of the beam (Equation 10) are shown in Appendix 1.

Another important characteristic is the contact area: it should be wide enough so as not initiate any cracks in the material being tested. Thus, the loading nose must be chosen to represent muscular attachment at a certain area of contact. The contact area can be calculated (Equation 12), as well as measured after bending (Figure 75).

3.8.2 FEA procedure

In TPB, there is compressive stress along the top surface and tensile stress along the bottom surface. The stress concentrations are usually observed at the loading and the supporting pins. Numerical calculations estimate the potential damage to the beam when subjected to TPB when holes are placed in different parts on the beam. It is clear that there is a stress concentration at the point where the force is applied. Boundary conditions (BC) in each variant were similarly defined in the form of simply supported constraints that blocked appropriate kinematic degrees of freedom for both the beam edges (span length). In the FE model, the bending was realized

by applying the concentrated load at the beam middle span. Here, the load was applied perpendicular to the layer plane.

Numerical simulation is used as a platform where experimental results validate the process of FEA; therefore, a finer mesh, at least 3 times smaller than the artificial defects, was used for optimal result validation. Aluminium samples with 1 mm bore holes introduced allows a simple mesh for accurate and fast results. Hexahedral mesh of 0.05 mm for the whole sample was used for the FEA (Figure 62).

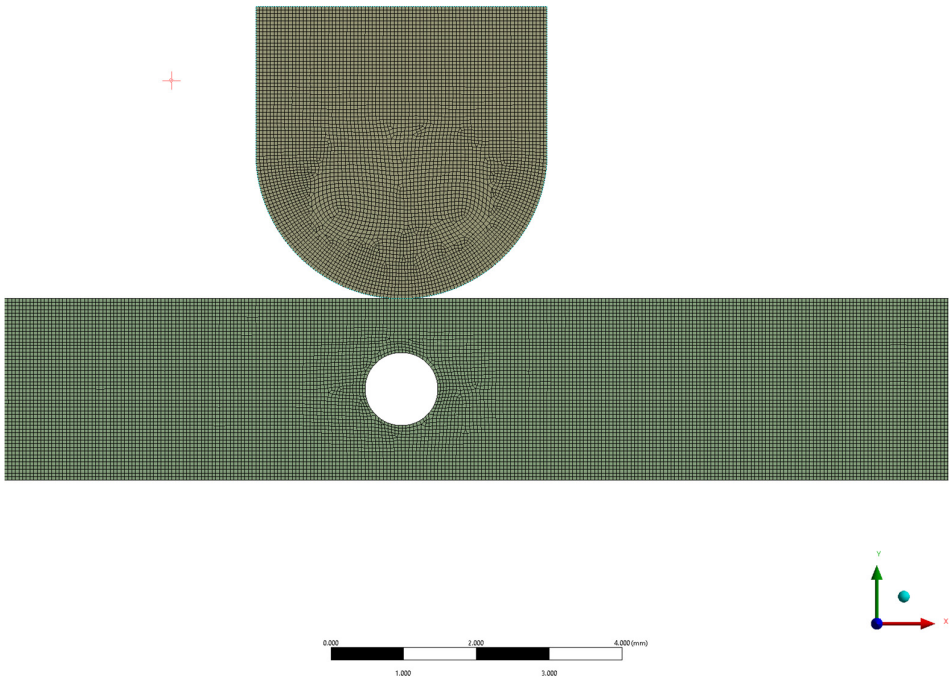

Figure 62: Hexahedral mesh of 0.05 mm for FEA of Al alloy samples.

For Ti6Al4V samples, the smallest dimension from the artificial defect is the height of the artificial defect, which is 210 µm, thus the overall mesh size around this defect will be 70 µm. This method was used for all defects with artificially induced pores. It is important that the elements of the mesh conform very well to the geometry of the part, thereby representing a good approximation of the part geometry. The mesh transitioned from a fine tetrahedral mesh size of 70 µm around the artificial defects to a coarse hex-dominant mesh of 200 µm for the rest of the sample (Figure 63).

Tetrahedral meshing is highly automated and good at predicting stresses with sufficient mesh refinement (Srinivas, 2017). As research indicates, stresses (fractures, pores, etc.) around a defect will be higher, thus a combination of adoptive mesh refinement is used. From a physical

point of view, the model can be refined only in particular regions of interest and further have a transition zone from fine to coarse mesh (Figure 63). Smaller elements around a hole or defect were used and gradually increased to the required mesh size.

Taking into account the experimental loading conditions, the punch, the specimen, and supports were set as ideal elastic plastic bodies. ANSYS was used to construct the finite element of TPB static-load simulation. This software ensures accurate, consistent, traceable materials information, and provides tools to support desired design and research.

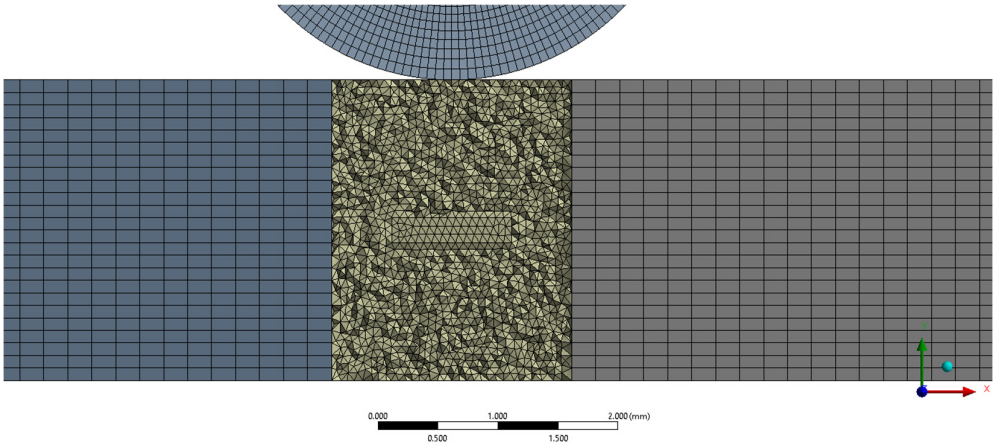

Figure 63: ANSYS mesh transition from fine to coarse.

3.9. PRELIMINARY TESTS WITH Al ALLOY

In order to verify the FEA model, aluminium alloy 6082 T6 samples corresponding with Ti6Al4V designed samples were tested. This alloy is the most commonly used for machining. Aluminium bulk samples underwent cross-sectioning, polishing, hardness testing and energy dispersive X-Ray spectroscopy by SEM (Table 12). The microstructure of the alloy was homogenous (Figure 64): the dark particles contain Si and Al; bright particles contain Mn, Fe and Cr. Darker and brighter areas of the matrix have identical chemical composition but different density of fine dispersed particles (Jíša et al., 2010).

Table 12: Chemical composition of Al 6000 alloys

Elements	Al 6000 alloy (MatWeb, 2018)	Average values from EDS analysis (wt. %)
Aluminum, Al	91.7–99.6 %	balance
Bismuth, Bi	0.150–1.50 %	
Boron, B	0.00300– 0.0600 %	
Chromium, Cr	0.0300–0.400 %	0.05
Copper, Cu	0.0100–1.20 %	
Cr + Mn	0.120–0.500 %	
Iron, Fe	0.0400–1.00 %	0.23
Lead, Pb	0.00300–2.00 %	
Magnesium, Mg	0.200–3.00 %	0.46
Manganese, Mn	0.0200–1.40 %	0.81
Nickel, Ni	0.0500–0.200 %	
Oxygen, O	0.0500–0.500 %	
Silicon, Si	0.200–1.80 %	0.7
Strontium, Sr	0.0005 %	
Tin, Sn	0.0500–2.00 %	
Titanium, Ti	0.0100–0.250 %	
Vanadium, V	0.0500–0.300 %	
Zinc, Zn	0.0300–2.40 %	0.11
Zirconium, Zr	0.0500–0.200 %	
Zr+Ti	0.150–0.200 %	

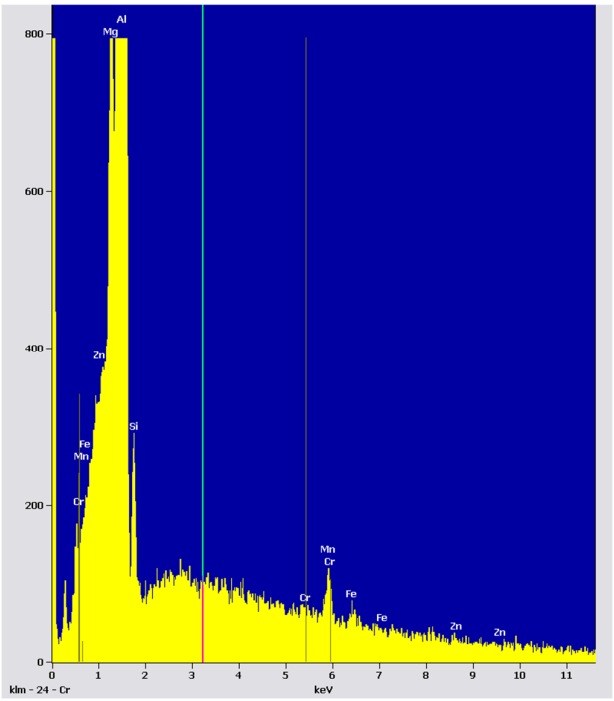

(a)

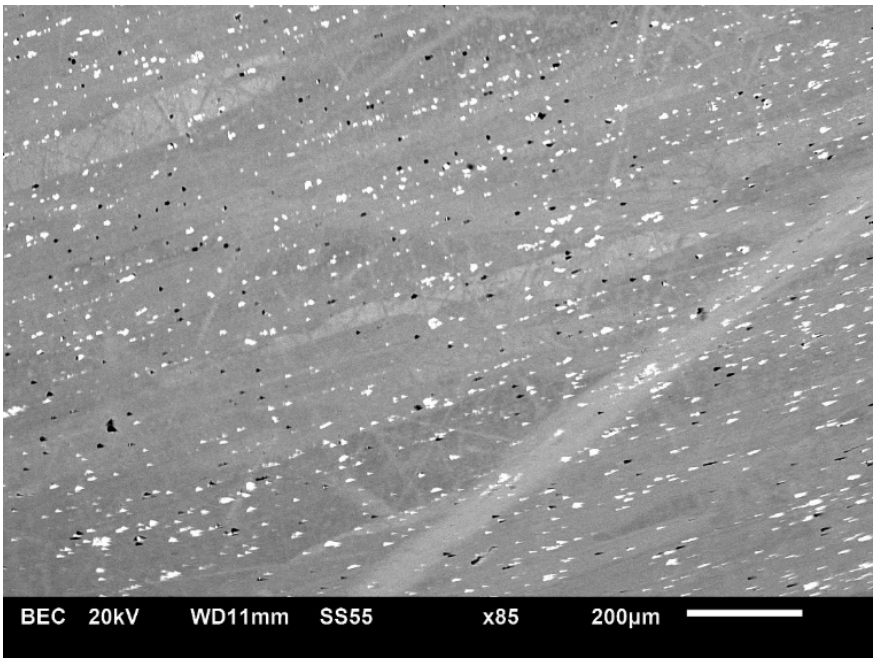

(b)

Figure 64: EDS spectrum (a) and corresponding BSE image of Al alloy (b).

Table 13: Mechanical properties of Al 6000 alloys

Mechanical Properties (MatWeb, 2018)	
Hardness, Vickers	35.0–149
Tensile strength, ultimate	89.6–565 MPa
Tensile strength, yield	40.0–517 MPa
Compressive strength, yield	365–490 MPa
Elongation at break	1.00–35.0 %
Modulus of elasticity	67.0–140 GPa
Compressive modulus	96.0–121 GPa
Ultimate bearing strength	228–1080 MPa
Bearing yield strength	103–1100 MPa
Poisson's ratio	0.296–0.330
Fatigue strength	55.0–517 MPa
Machinability	30.0–90.0 %
Shear modulus	25.8–53.8 GPa
Shear strength	60.0–331 MPa

In order to test catastrophic failure in a sample, a representation of defects in the form of 1 mm bore holes were used and placed at various prescribed locations to the centre (Figure 65).

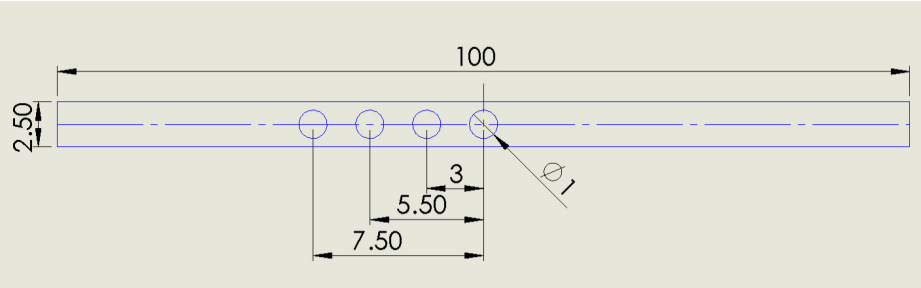

Figure 65: Sketch of the location of drill holes in Al samples.

Two testing methods for samples Set 1 and Set 2 were used to see whether both stress-strain and load-displacement graphs' results corresponded for incremental loading 400 N–500 N (Set 1) or one total loading cycle until failure (Set 2), see Table 14. The MTS images of the preliminary Al samples were tested in such a way so as to compare the accuracy of the machine and the durability of the samples. The following steps were used and inserted in corresponding images and tables in Appendix 2. After each loading, samples were analyzed by optical microscope.

Table 14: Aluminium samples' classification for preliminary test*

Description	Label	Loading
Solid block	Al 1A	Incremental loading: 400 N-430 N-460 N-500 N
	Al 1B	directly until failure
Centre pore	Al 2A	Incremental loading: 400 N-430 N-460 N-500 N
	Al 2B	directly until failure
3 mm offset	Al 3A	Incremental loading: 400 N-430 N-460 N-500 N
	Al 3B	directly until failure
5.5 mm offset	Al 4A	Incremental loading: 400 N-430 N-460 N-500 N
	Al4B	directly until failure
7.5 mm offset	Al 5A	Incremental loading: 400 N-430 N-460 N-500 N
	Al 5B	directly until failure
Samples for microhardness testing	Al 6A	Incremental loading: 400 N-430 N-460 N-500 N
	Al 6B	directly until failure

Set 1*: *Al 1A, Al 2A, Al 3A, Al 4A, Al 5A;* ***Set 2**: Al 1B, Al 2B, Al 3B, Al 4B, Al 5B.*

Preliminary tests were conducted in the following manner:

- FEA analysis in accordance with experimental setup, with only downwards-simulated forces of 400 N, 430 N, and 550 N respectively;
- Both sets 1 and 2 were visually inspected under an optic microscope;

- A force of 400 N was used for both Set 1 and Set 2 respectively and analyzed afterwards with an optic microscope;
- Individual forces of 430 N, 460 N, and 550 N were used for Set 1 only and analyzed after each loading increment under an optic microscope;
- A force of 550 N was used for Set 2, and again analysed under an optic microscope;
- FEA, visual inspection, and MTS data analysis was used for results.

3.10 SUMMARY

Anatomical data showed a regular mandible body length to be about 73 mm with a cross-sectional thickness of about 16 mm; therefore, a sample length of 100 mm was chosen which included a fixation of more or less 20 mm. The area calculated on the exposed artificial defect length is 60 mm which represents the mandible body length.

When the stress concentration is observed from various angles it can be concluded that within this danger area (closer to the applied load), artificial pores will have an effect on the mechanical properties of an implant, as seen in the preliminary test. The artificial defects were strategically placed close to the contact area to ensure optimal results for a worst-case scenario.

The normal procedure for a qualified medical implant was used as guideline to treat the samples. The specimens produced on the baseplate of the EOSINT M 280 system were stress-relieved with the baseplate in a vacuum furnace then removed from the substrate using an 0.8 mm diameter wire cutter. The samples' surface roughness accuracy was measured, then samples were annealed in vacuum and shot peened. MicroCT scans were used to locate any extra induced pores and visually define the internal structure of the samples. The samples were bent to the required force and compared to the numerical simulations. Samples were cross-sectioned to inspect the internal defect displacement and other defects.

CHAPTER 4: RESULTS AND DISCUSSION

4.1 PRELIMINARY TESTS WITH Al ALLOY

The design and methods used for the preliminary studies were tailored to address the specific issues and questions to be answered. The preliminary study was relatively short term and inexpensive in comparison to the main LPBF Ti6Al4V ELI samples tests. The main experimental test started soon after the preliminary study, so avoiding the situation of changing between the two.

Preliminary studies were examined to provide local up-to-date data, in order that through literature and trial and error the optimal sample size required for conducting the titanium experimental procedures could be determined. Although material properties differed from the titanium experimental study, they were used as a guideline when comparing FEA and experimental results. Schema for FEA and experimental tests with Al samples and the sketches for the drill hole locations are shown in Figure 65. Using Solidworks, five beam pairs were generated with various hole placements. Numerical analysis was performed using an ANSYS commercial software package.

Boundary conditions in each set were defined in the form of simply supported constraints that blocked appropriate kinematic degrees of freedom for both the beam edges. The pinned supports were fully constrained.

4.1.1 Numerical simulation analysis of Al samples

The results showed that the solid aluminium sample stayed within the elastic range where a loading force of 430 N was applied. This statement was not the case when the load was increased to 550 N: the sample exceeded the yield strength (YS) and reached ultimate tensile strength (UTS), Figure 66. The von Mises stress was at maximum value at the tensile side, increasing in magnitude as the loading increased.

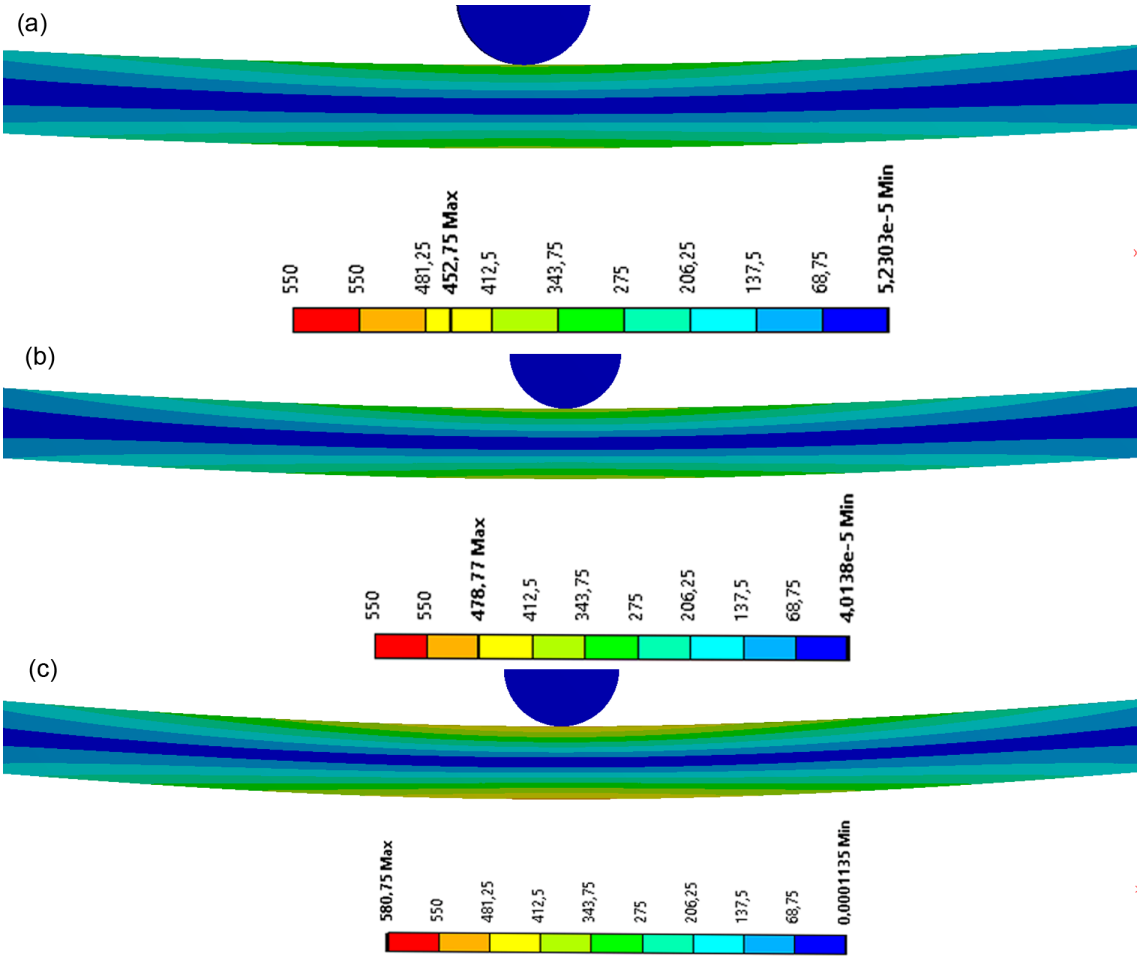

Figure 66: Von Mises stress (MPa) distribution in solid test samples: 400 N (a), 430 N (b) and 550 N (c).

For samples with holes, the results showed that the maximum von Mises stress was located under the loading nose and at the bottom side of the sample (tensile stress) (Figure 67). The samples showed no signs of deformation at an early and low loading. However, as soon as the load increased to 430 N, the samples were on the verge of not only deformation but failure.

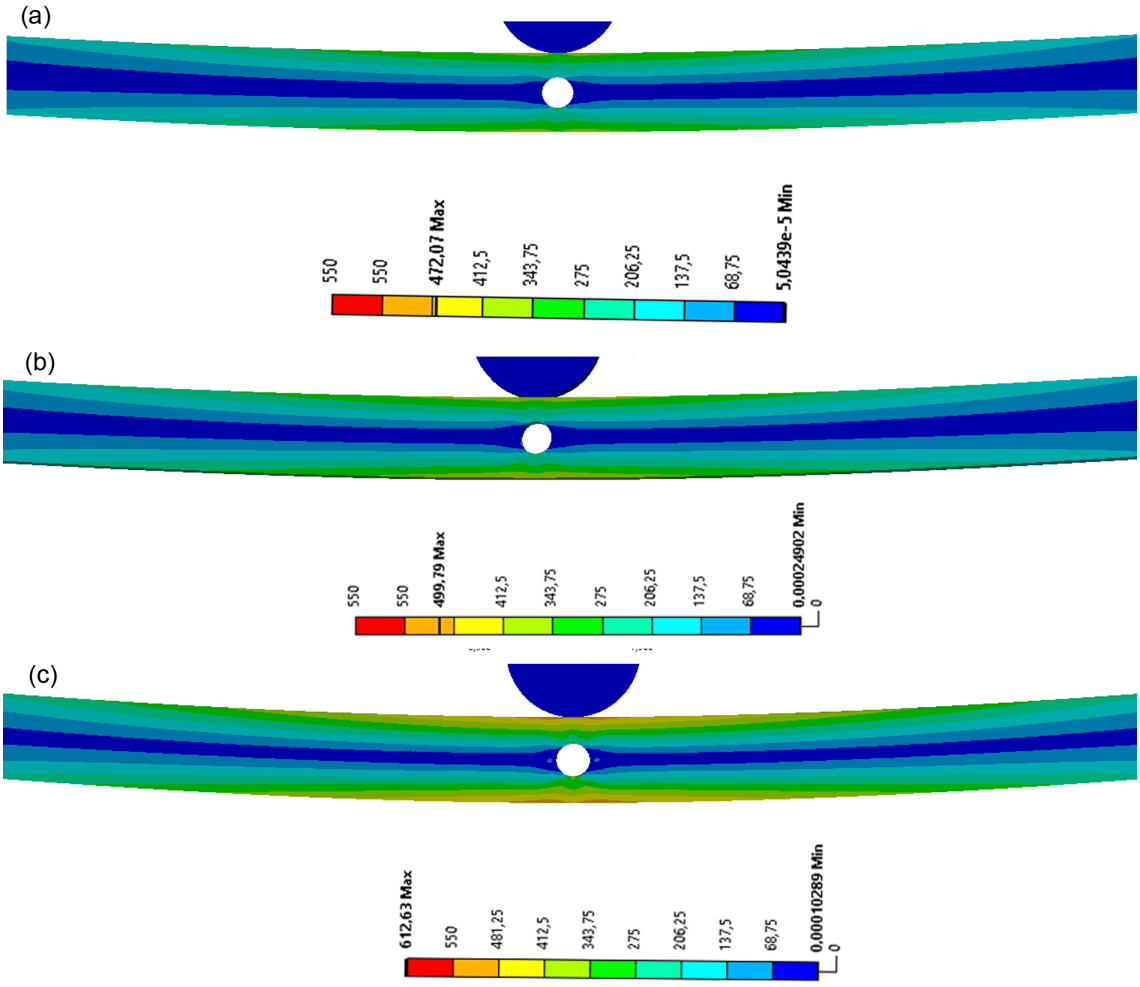

Figure 67: Von Mises stress (MPa) distribution in test samples with centre hole: 400 N (a), 430 N (b) and 550 N (c).

With off-centre holes, stress distribution started to be non-symmetrical and high-stressed areas moved from the centre to the side. With lower loading, signs of failure were noticed. Signs of fracture did occur at a 430 N load, although the sample was still within elastic range. As soon as the loading exceeded the 430 N forces, maximum von Mises stress increased with the loading and stress also increased around the hole (Figure 68).

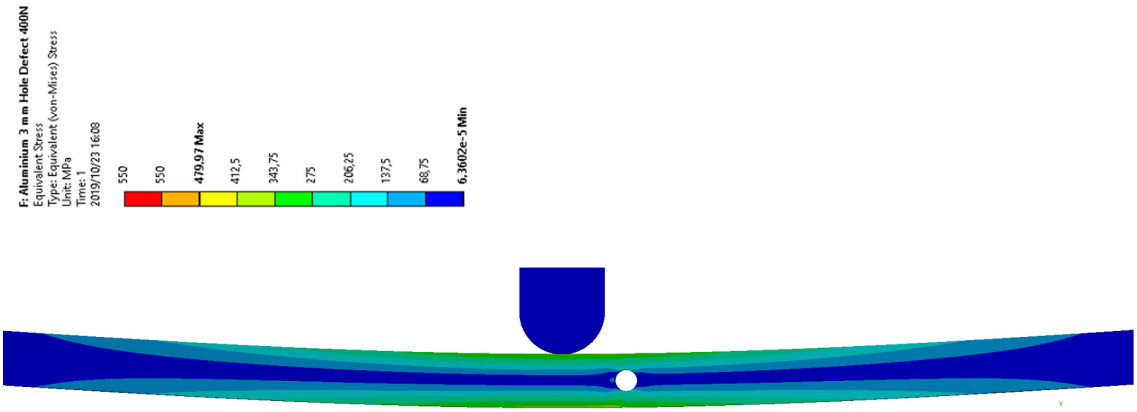

(a)

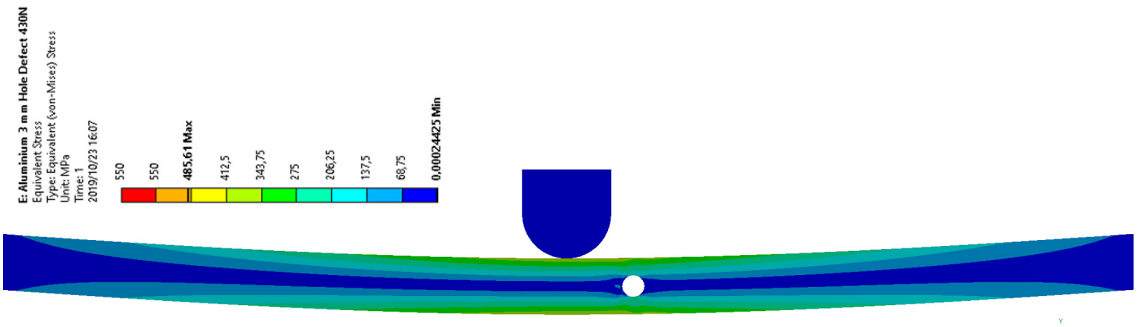

(b)

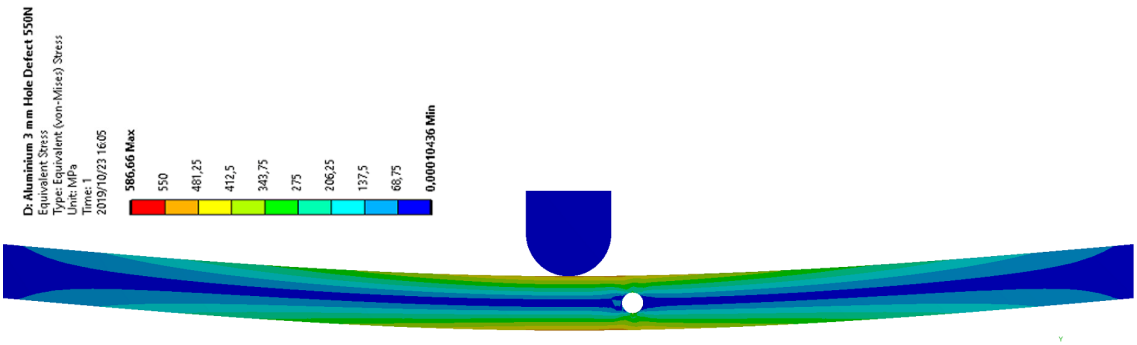

(c)

Figure 68: Von Mises stress (MPa) distribution in 3 mm offset test samples: 400 N (a), 430 N (b) and 550 N (c).

Non-symmetrical stress was the case for larger off-centre hole placement. Higher stress can be seen in the neutral plane around the hole, and increasing in value as the load increased. It can be seen that smaller loading affected the sample within the elastic range. As soon as the load increased to 550 N, the sample succumbed to plastic deformation (Figure 69).

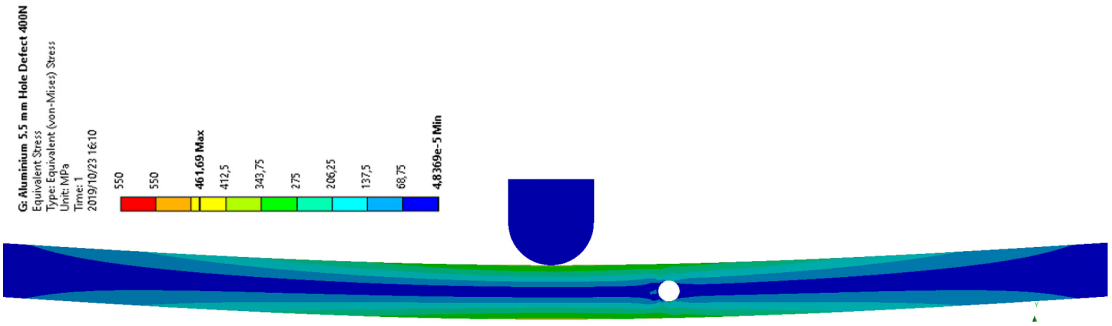

(a)

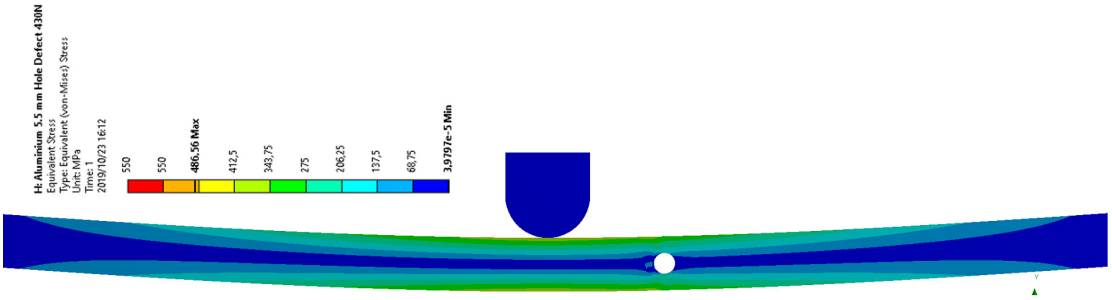

(b)

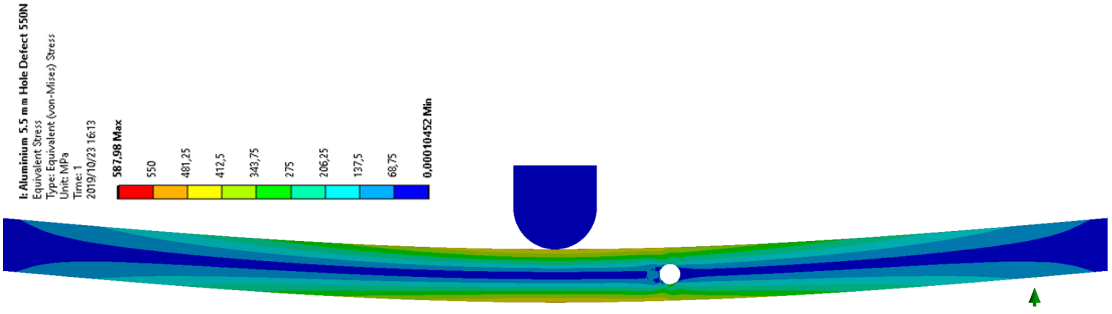

(c)

Figure 69: Von Mises stress (MPa) distribution in 5.5 mm offset test samples: 400 N (a), 430 N (b) and 550 N (c).

Similarities between Figure 70 and 69 for all loading values were observed. Furthermore, results were closely related to that of the solid sample. Samples can be seen with stress increasing around the hole as the load increased.

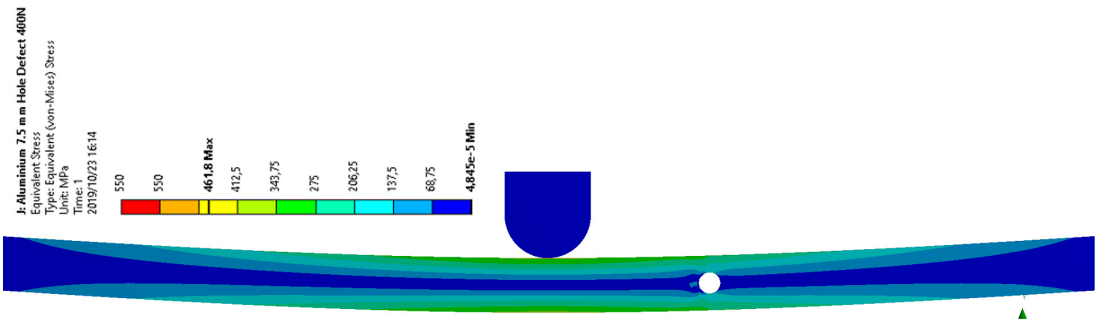

(a)

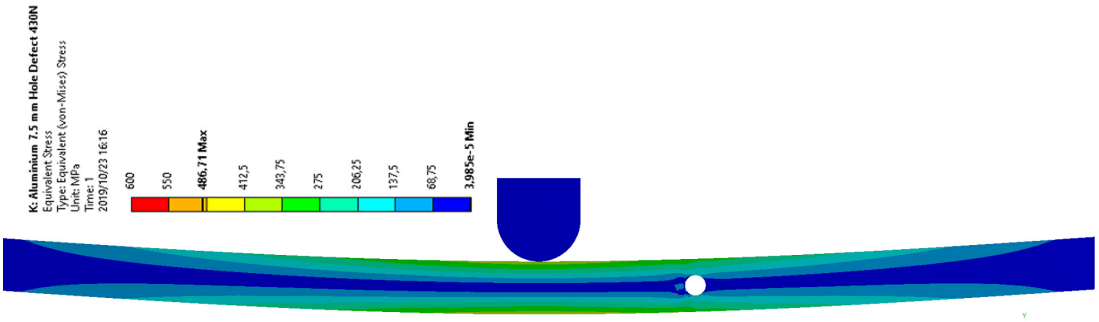

(b)

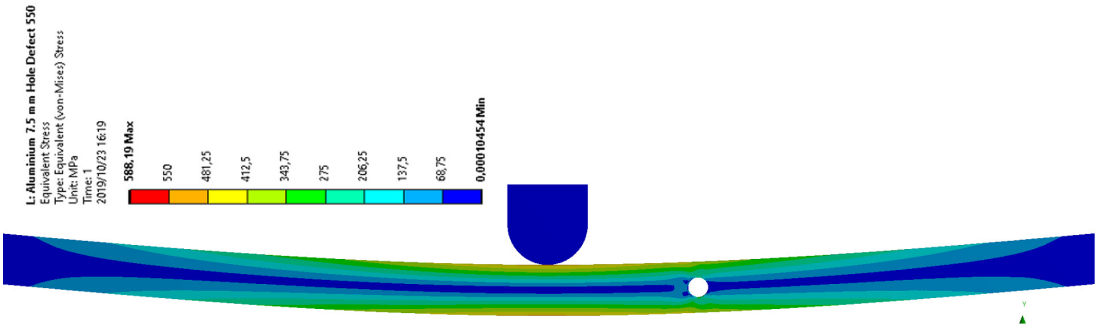

(c)

Figure 70: Von Mises stress (MPa) distribution in 7.5 mm offset test samples: 400 N (a), 430 N (b) and 550 N (c).

For each simulation, the reference sample showed the least induced stress as there were no internal geometry changes. Anomalies were the case for most simulated samples, but in reality the sample with a hole or impurity closer to the point of application should show the most induced stress while decreasing as the distance from the contact area increases.

As expected, there is a neutral plane in the middle of the beam; the values are anti-symmetric relative to the stress direction (compression and tension). Since the simulated beam was from homogenous isotropic material, the stresses for the incremental loading and full-cycle loading showed similar behaviour (Appendix 2). FEA shows that the maximum stresses were located in the contact area and at the outside surface of the beam. The stresses increased causing the material to yield, resulting in an increased contact area, which then caused the stresses to decrease.

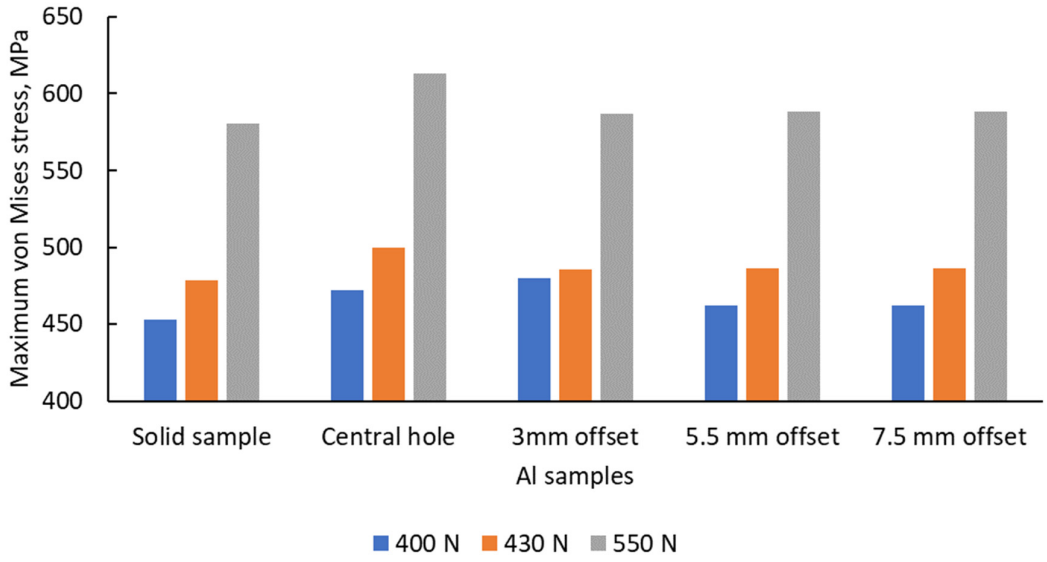

Figure 71: Maximum von Mises stress calculated by FEA.

Introducing holes off-centre leads to non-symmetrical compression and tensile stress distribution. Thus, different deformation behaviour will surface in different samples, and different strain around the holes will be observed. Therefore, FEA of the TPB test method needs to be judged by experimental evidence in order to validate the results obtained and to give recommendations for its application.

4.1.2 Visual inspection

Aluminium samples from Set 1 (Table 14) showed that the first incremental load of 400 N force exerted on these samples initiated a fracture only around the centre drill hole of Al 2A but did not resemble the same features for samples Al 3A, Al 4A, and Al 5A (Figure 72).

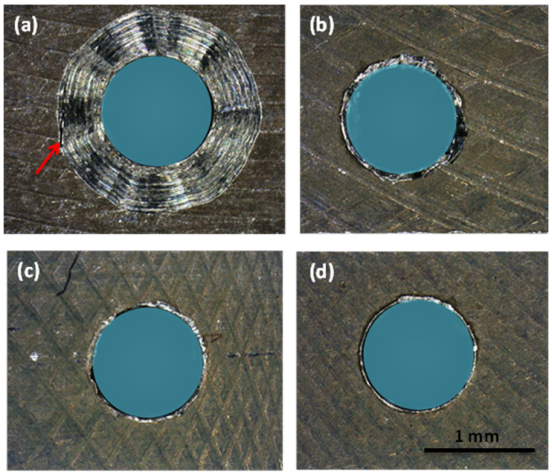

Figure 72: Set 1 optical microscope analysis after individual 400 N downwards force; Al 2A (a), Al 3A (b), Al 4A (c) and Al 5A (d). Crack is indicated with red arrow.

Increasing the downwards force to 430 N (Figure 73) finally resulted in complete failure of Al 2A (Figure 75) and initiated a crack in Al 3A (Figure 74), which showed failure shortly afterwards.

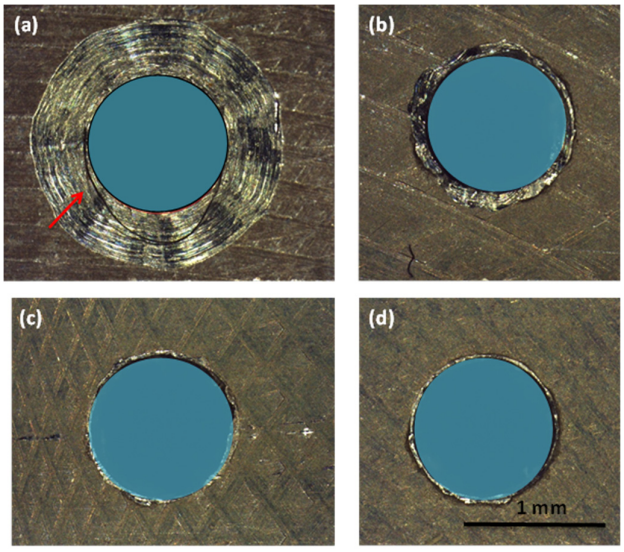

Figure 73: Set 1 optical microscope analysis after individual 430 N downwards force; Al 2A (a), Al 3A (b), Al 4A (c) and Al 5A (d). Crack is indicated with red arrow.

Within these three independent forces, no changes were seen in samples Al 4A and Al 5A, respectively (Figure 74 c, d). Sample Al 2A was broken and deformed and a crack was found in sample Al 3A, as seen in Figure 74. Fracture was found on the tensile side, while more crack initiation was found to start on the compression side.

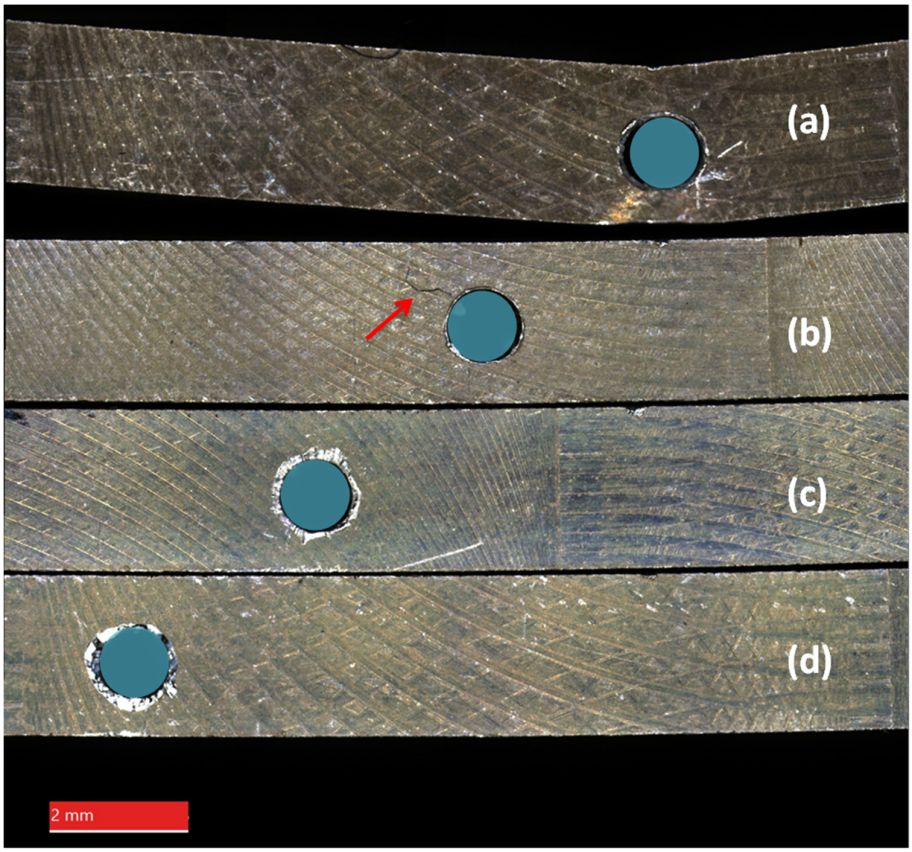

Figure 74: Digital microscope photos after 460 N loading; Al 2A (a), Al 3A (b), Al 4A (c) and Al 5A (d) from Set 1. Crack is indicated with red arrow.

Failure assessment allowed for an estimation of the potential failure initiation of the beam subjected to a TPB test. When the samples experienced compressive stress, the bottom tensile stresses caused cracks or fractures, since the compressive stress for Al alloys is higher than the ultimate tensile stress (Figure 75). Some stresses could have been unintentionally introduced during the drilling of holes that led to cracks during high loading at bending.

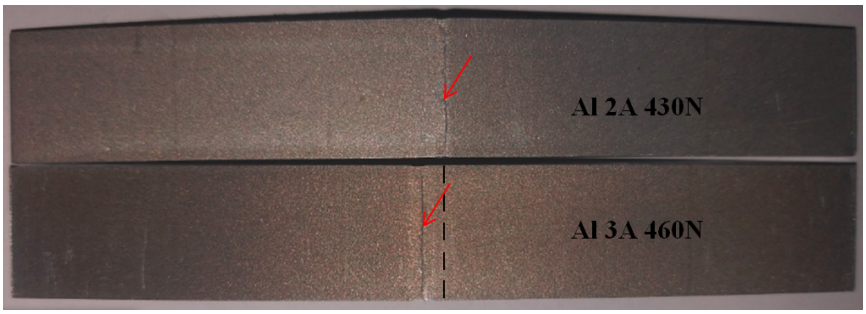

Figure 75: Al 2A and Al 3A fracture at their respective loading force on the bottom side of samples.

Contact area caused by a smaller loading nose radius can be identified denting the top surface of the samples (Figure 76). The reason this factor is of importance, especially when considering the testing of titanium, is to understand the behaviour exerted on the tested samples. Digital microscope images revealed an average contact area of 87.7±18 µm. Literature suggests that an appropriate punch radius is in the range of 2.5 to 3.0 mm (Hou et al., 2016). The radius of the loading nose did not initiate any fractures leading to failure. By visually inspecting the contact area, an average experimental value and a calculated value could be compared (Table 15).

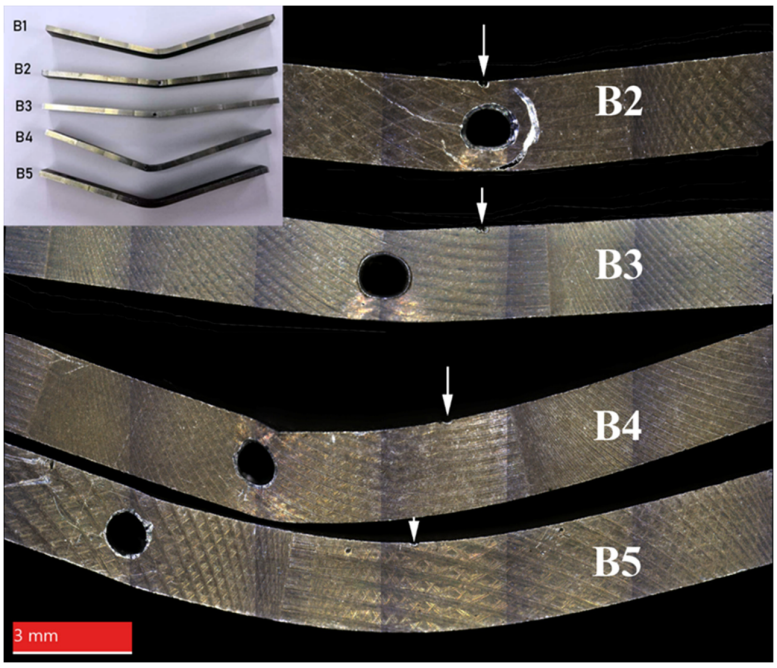

Figure 76: Set 2 optical microscope analysis for 550 N downwards force. Loading direction is indicated with white arrow.

It can be concluded that up to an offset of 3 mm from the point of contact, significant features, such as fractures, fatigue or catastrophic failure will occur, and furthermore, deformation may alter the integrity of an alloy's capability to perform to its required standard (Figure 76).

4.1.3 Analysis of stress-strain behaviour

At the initial stage, FEA of the TPB test estimated the deformed mode shapes (pattern of structural deflection) of the beam geometry subjected to flexural loading. Structural displacements were displayed in the direction coincident with the loading plane. Such analysis indicated considerably different deformed mode shapes depending on the beam geometry. Table 15 shows the theoretical calculations for sample Al 1B. High contact stresses indicate sample damage above 460 N loading forces. Maximum deflection at 400 N must be near 1.3 mm.

Table 15: Theoretical values for solid Al sample

	400 N	430 N	460 N	550 N
Modulus of elasticity, GPa.	70			
Second moment of area, m^4	0.019531×10^{-9}			
Contact modulus, Pa	17.132×10^{-12}			
Total contact area, µm	68.2	70.7	73.2	80.0
Contact stress MPa	498	516	534	584
Maximum deflection, mm.	1.3	1.4	1.5	1.8
Max slope: Radians, 10^{-3} ° Degree, ^{0}	65.8 3.8	70.8 4.1	75.7 4.3	90.5 5.2

Figure 77 represents the general features of individual sample's reaction when tested with an end goal of 550 N. A failure in sample Al 2B and Al 3B was noted. Deviations between samples Al 1B, Al 4B, and Al 5B were because of internal structural damage or weak points along the axis of the sample at such a distance that it did not cause failure but clear reduction in elastic modulus.

For sample Al 1B at 400 N, the displacement was predicted at 1.32 mm (Table 15). Experimental results showed a displacement at the same load of 1.62 mm. Therefore, it seems that the actual elastic modulus of Al alloy was lower than 70GPa that was used for simulations.

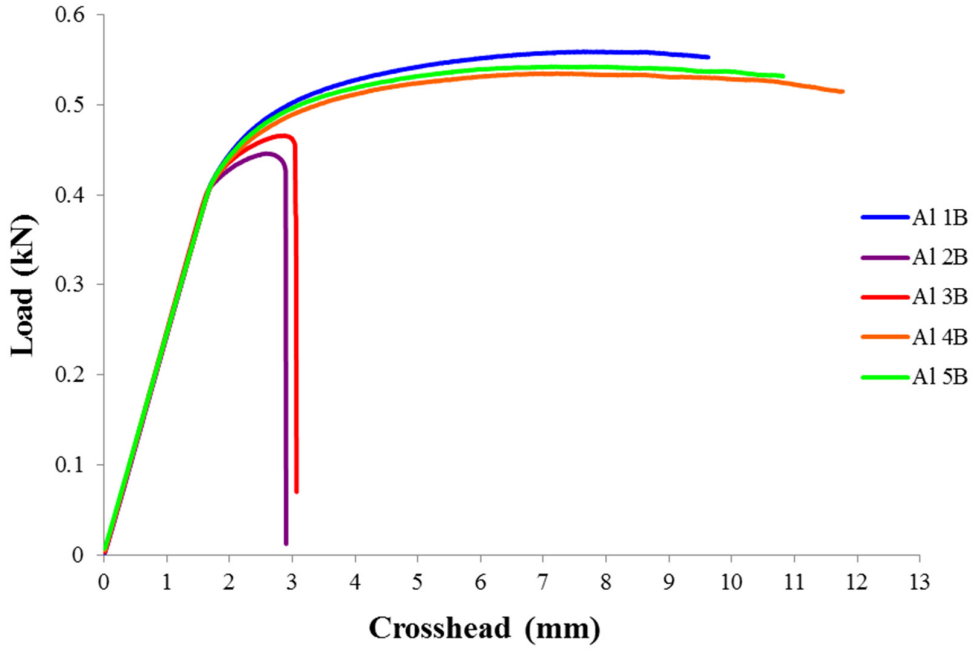

Figure 77: Load-displacement curve for Al samples Set 2.

A full-cycle loading showed complete failure as the maximum von Mises stress exceeded the UTS: this failure can be seen in Figure 77. According to FE simulation, the fracture mode of the Al samples corroborate with the experimental results, and the fracture mode of the Al samples was consistent with the FE (Figure 78). FEA predicted non-symmetrical fracture of samples with holes less than 3 mm offset from the contact area and this was confirmed experimentally. Modulus of elasticity at bending E_b of 56.3 GPa was obtained using experimental data as recommended by ASTM standard D70-03 (see Appendix A1.4). It must be noted that all measurements were performed without an extensometer so the machine compliance correction must be done for actual deflection occurring under loading.

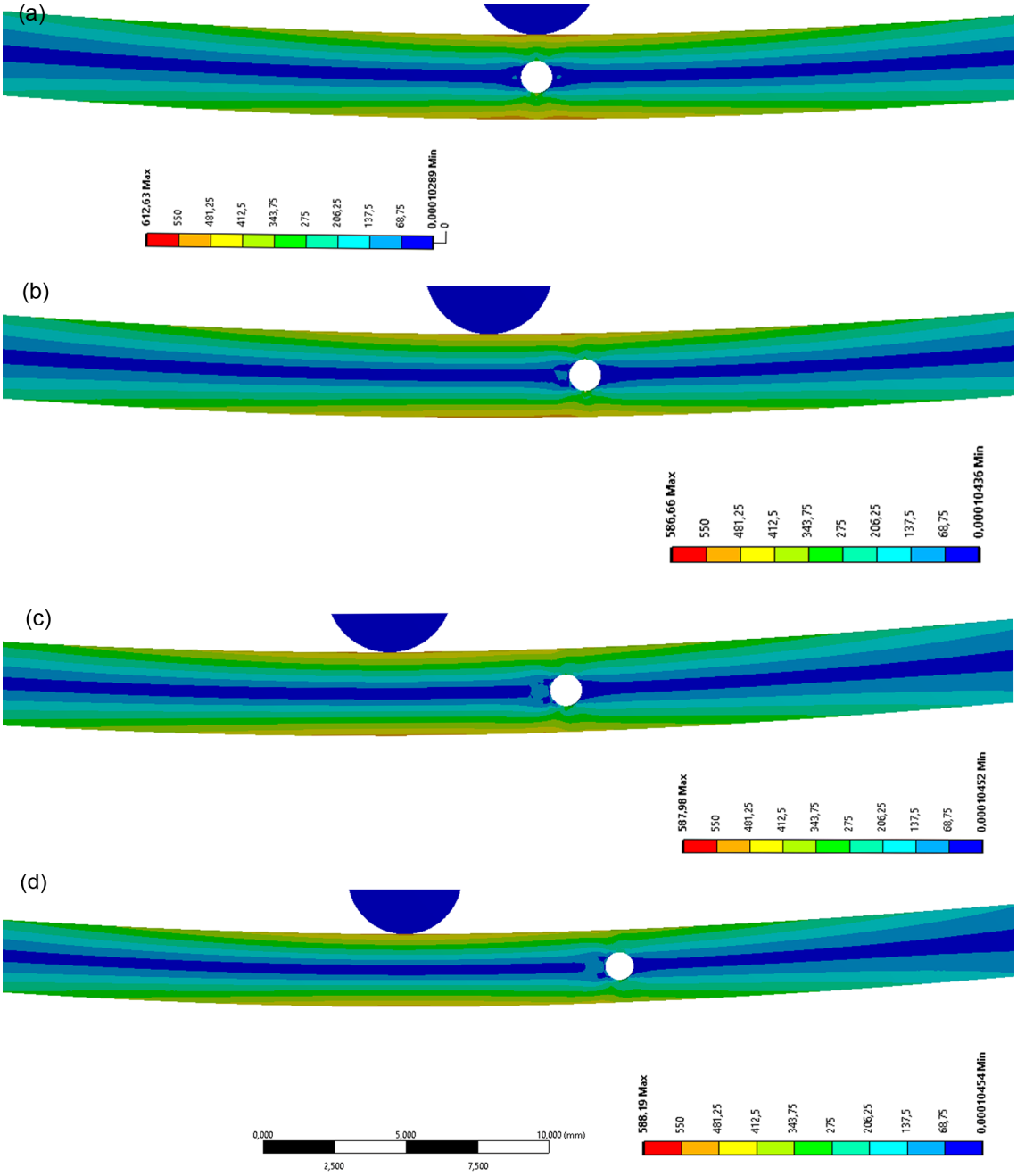

Figure 78: Von Mises stress (MPa) distribution at 550 N loading representing Al Set 2 samples: central hole (a), 3 mm offset hole (b), 5.5 mm offset (c), and 7.5 mm offset (d).

Table 16 shows flexural stress at break for Set 2 and can also be compared with values obtained from FEA. Samples Al 2B and Al 3B broke very close to the yielding and maximal flexural stress was equal to flexural stress at break. The other samples broke after 3 % strain limit.

Table 16: Mechanical properties with maximum recorded loading of Set 2 samples

Sample	Maximum bending load, N	Maximum deflection – (crosshead), mm	Maximum flexural stress, MPa	Maximum flexural strain, (mm/mm)
AL 1B	559.0	7.5	537	31.4
AL 2B	445.8	2.6	428	10.8
AL 3B	465.9	2.9	447	11.9
AL 4B	534.1	7.2	514	30.0
AL 5B	542.4	7.1	521	29.7

4.1.4 Summary

The aluminium samples showed catastrophic failure with defects closer to the point of contact and only internal deformation further away from the contact area. The experiment was repeated twice, one with incremental loading Set 1 and one with full-cycle loading Set 2. Both sets showed similar results when compared to FEA. Chemical analysis played an important role ensuring the correct mechanical inputs were used for FEA. Three approaches were used, namely FEA, MTS three point bending (experimental), and theoretical calculations.

The preliminary test served as a pilot for the actual titanium tests. Thus, artificial defects in LPBF Ti6Al4V samples were carefully introduced to medical-graded titanium samples in a region close to the area of loading. FEA should be able to be compared with multiple experimental results. Experimental loading force should be sufficient and of such that it exceeds maximum mastication force, resulting in optimal data for analysis.

4.2 Ti6Al4V ELI SAMPLE TESTS

Ensuring additively manufactured metal-based components are free of major defects is crucial to fulfilling medical requirements for clinical applications. Random porosity, high surface roughness and deformation during processing are currently the main drawbacks in LPBF parts. The prediction of defective samples' mechanical properties with numerical simulations is extremely important to understand the effect of these defects. A step-by-step systematic approach to determining defects in LPBF and their influence on mechanical properties was done in the current research. In Appendix 5, different types of mandible reconstruction by LPBF and porosity in LPBF parts were investigated. On the basis of this research, defects in LPBF Ti6Al4V ELI samples were introduced.

The maximum stress that was found in mandibular bone is 79–151 MPa, while solid Ti6Al4V material has tensile yield strength of 864–933 MPa (Ilavarasi and Anburajan, 2011; Morgan et al., 2018). In the case of an inappropriate design or an unforeseen loading event, breakage of the metal component might occur. TPB tests are a common tool used to characterize bone material properties. TPB has a number of limitations, for example, local deformations are likely to occur at the point of contact with the loading nose and supports, due to stress concentrations (Albert et al., 2012). Local deformation can result in an overestimation of beam deflection at mid-span.

As-built samples had roughness of Ra=18±2.0 µm and Rz=102±9.6 µm (Appendix 3). As-built samples were rough because the tested surface was created by a consequence of layers, since samples were manufactured in vertical direction (Figure 53). After shot peening, the surface roughness had been improved: Ra = 5±0.8 µm and Rz = 34±4.8 µm. It can be concluded that the shot peening reduced the surface roughness significantly. However, it must be kept in mind that the placement, function, and overall performance of the part play a big role in what surface roughness is required for the specific tasks.

4.2.1 Numerical simulation analysis of Ti6Al4V ELI samples

Numerical simulations were set at a range between two independent experimental loading conditions. As seen from preliminary tests, optimal results would be obtained which closely resemble FEA and experimental tests, thus the focus and conclusion will be drawn mainly between a 900 N-1000 N force. FEA simulations were conducted as a frictionless action, although in experimental testing, some form of movement between the sample and supports did occur, which in reality can cause small variations in the deflection and stresses obtained from the numerical simulations and experimental results. The FEA loop began with the FEA inputs (mesh, loads, boundary conditions, and material properties) which resembled experimental models as closely as possible.

Mechanical properties from Table 2 were used to possibly match data obtained in TPB tests (stretching, compression). Mesh parameters were fixed for all samples using a fine tetrahedral mesh size of 70 µm at the centre and transitioning into a coarse hex dominant mesh of 200 µm for the rest of the sample. Presenting comparative FEA of beam deflection for various beam internal geometries can give composite manufacturers important insights.

Von Mises stress definition indicates that it is used to predict yielding of materials under complex loading. If the sample is to remain elastic under loading, the maximum value of the von Mises stress from the FEA model needs to remain below the yield value (Table 17). If the maximum von Mises stress from the FEA is greater than the yield value, plastic strains will develop. This may not cause the sample to fail; however, incremental analysis on how the stresses redistribute due to plasticity can be examined and in this manner, the limit load for the sample may be found.

Focusing on reference sample 2 (optimal conditions) for medical titanium implants and for explanatory reasons, it was found that the maximum von Mises stress obtained through FEA exceeded the point of yield stress (Table 2). By referring to mandibular movement, a static occlusion was simulated, and it can be presumed that for cyclic loading, under the same conditions over a period of time, the sample will eventually show some form of failure which may cause sample failure.

Table 17: Maximum von Mises stress found by FE simulations at 1 kN for TPB

Sample identification	Von Mises stress σ_v (MPa)
AD 1.1 A	947
AD 1.2 A	947
AD 1.3 A	947
AD 1.4 A	958
AD 2.1 A	948
AD 2.2 A	948
AD 2.3 A	950
AD 2.4 A	957
RS 2	932

Numerical simulations showed that the reference sample did not succumb to failure, nor did samples with artificial defects. By comparing FEA stresses obtained from AD 1 (Figure 79) and AD 2 (Figure 80), similarities were seen between corresponding pore placements despite their size difference.

Further analysis shows that artificial defects closer to the point of contact with loading nose showed high stress. This is due to the stress concentration caused by the compression force and tensile force (Figure 57). The placements of the artificial defects impact the capability of the samples to withstand the subjected force and are forced to yield (Figure 79, Figure 80). Furthermore, a safety factor (S.F.) can be introduced to locate the yield point through FEA. This method allows precise and safety measurement in designing and simulating specific geometries for different outcomes within the safety region. Monaheng (2017) calculated a suitable S.F. of 2.8 for the required thickness of the mandibular implant.

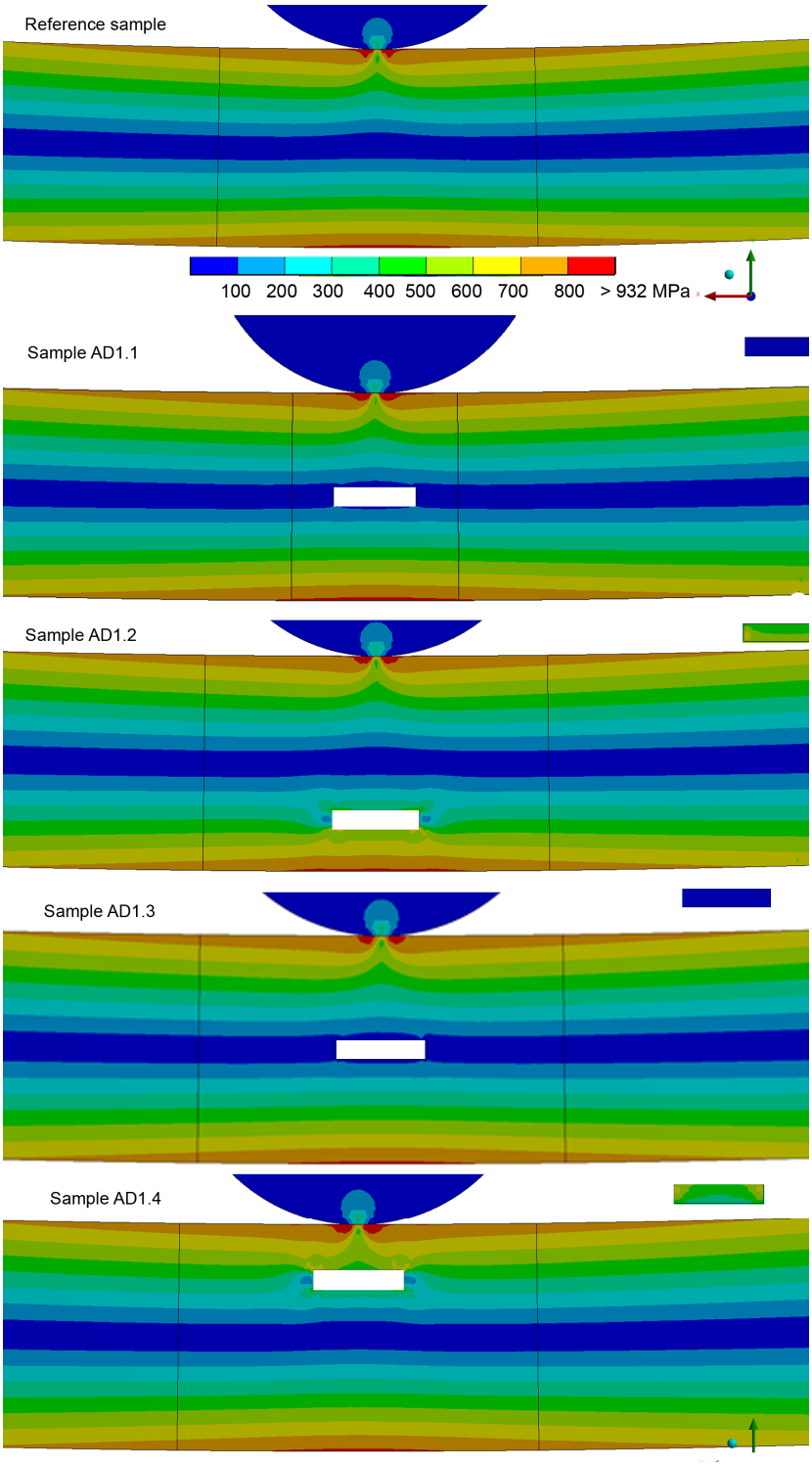

Figure 79: Von Mises stress distribution for a reference solid sample (RS) and AD1.1–AD1.4 (e) samples for 1 kN bending simulations - cross-sections in the middle of the samples.

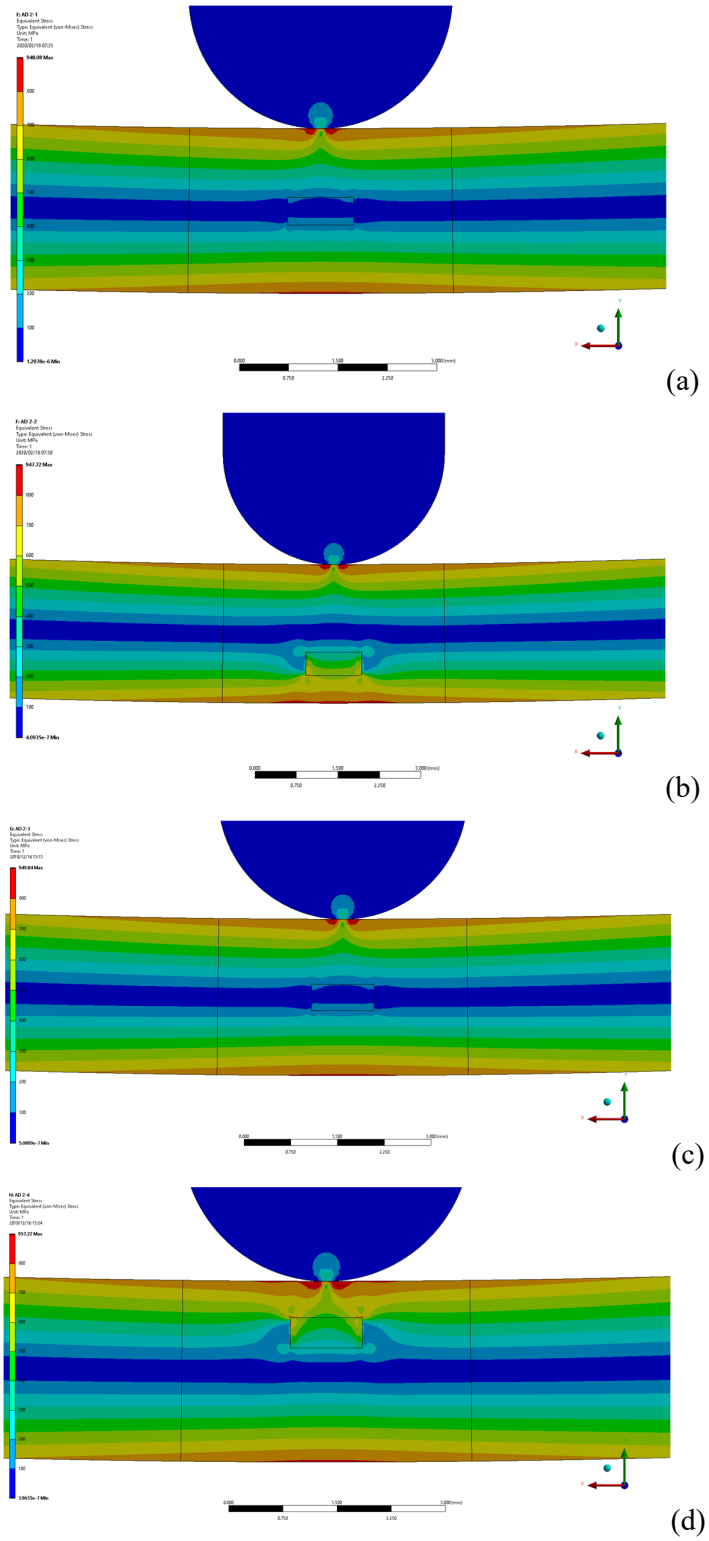

Figure 80: Von Mises stress distribution for AD2.1–AD2.4 (a-d) samples for 1 kN bending simulations - cross-sections in the middle of the samples.

Once FEA results are obtained, they should be analyzed using engineering principles and should an unacceptable mismatch occur, the FEA inputs should be modified. However, should similarity be the outcome, the results can be used to evaluate whether the required mechanical properties are achieved before the final implant design is approved.

The histogram (Figure 81) indicates high stress for artificial defects with pore size 1000 × 500 × 420µm. The maximum stress was located at the farthest surface from the neutral axis (it can be top or bottom), Figure 79–Figure 80. At some location along the vertical axis of the beam, the stress will be zero; this location is the centroid or neutral axis of the cross-section. Due to irregularities, there is an increase in the intensity of stresses in the sample. Sharp internal corners and high loading will cause an increase in stress concentration, as well as failure via a propagating crack, when a concentrated stress exceeds the material's theoretical cohesive strength.

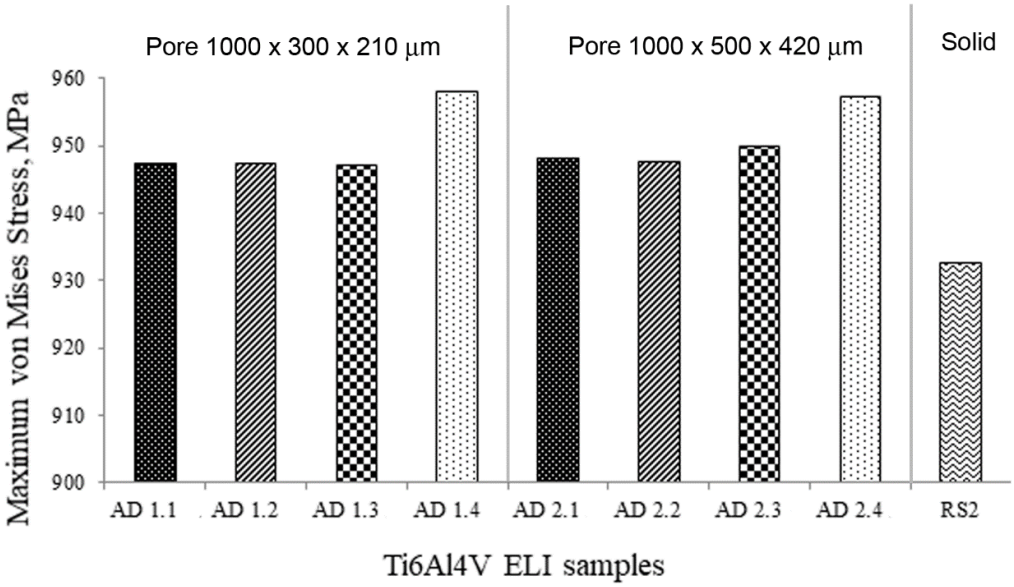

Figure 81: Maximum von Mises stress for different Ti6Al4V ELI samples calculated by FEA at 1 kN bending tests.

Validation of FEA depends on a proper resemblance between FEA and the experimental setup. Therefore, FEA should be integrated well within the computational design process of medical implant (Figure 42).

4.2.2 Porosity analysis

4.2.2.1 Reference sample

The use of X-ray tomography to visualize porosity in parts (non-destructively) prior to mechanical testing allows an indepth understanding of the effect on the mechanical properties of the part. This provides the possibility to differentiate between critical defects and harmless pores, and thereby build confidence in AM processes. Defects in LPBF include unintended porosity, rough surfaces and deviations from design, which can have different root causes and can vary significantly among samples (Appendix 5). These different types of pores typically have different sizes, shapes and 3D distributions that can be noted in the reference sample. All these types of defects have effects on the mechanical properties of a final part. Two main types of porosity are known to occur (Sharratt, 2015). Lack-of-fusion defects have shown to be irregular in shape, and in contrast, gas entrapment porosity is very spherical. The results of recent studies all indicate that the porosity structure may depend on the build direction (Ziółkowski et al., 2014). All these examples show irregular porosity shapes indicating lack of fusion as the cause. Generally, the average porosity in parts built to good specifications is > 99.5 % dense, that is, 0.5 % porosity or less (du Plessis et al., 2016 b).

Directionality of the defects observed may assist to interpret the quality standard of AM metal components and help engineers and designers to wisely select building orientation when producing complex parts using LPBF methods. Careful microCT analysis of the reference sample showed that most estimated pores had elongated shapes, the pores were small and randomly distributed in the sample. The largest pore, at 130 μm, was elongated parallel with the building direction and can possibly be classified as an interlayer pore (Figure 82). For optimal conditions the reference sample showed to be 99.99% dense. Therefore, <0.01 % porosity was calculated before bending. Defect volume ratio of 0.0015%, and 0.0019% before and after bending respectively, indicating no new defects noted by CT scanning.

It is increasingly becoming clear that small pores will always be present in LPBF parts, varying in distribution and morphology depending on the system used, the powder used and the process parameter. Very often smaller pores will have an influence on the mechanical properties of a part, compared to larger pores, for example, when they are near the surface (Malefane et al., 2018). This is an important general result which builds confidence in the capability of LPBF parts. Despite smaller pores, mechanical properties can be excellent, thus the critical factors affecting the mechanical properties shift towards microstructure, surface roughness and part

geometry, irrespective of the material type. Larger pores start to play a significant role affecting the mechanical properties leading to premature failure.

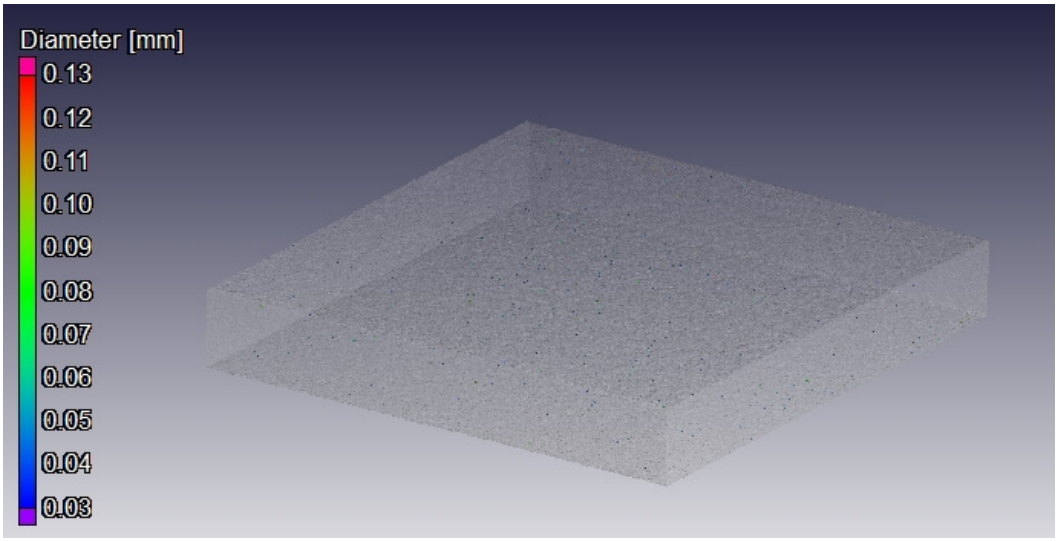

(a)

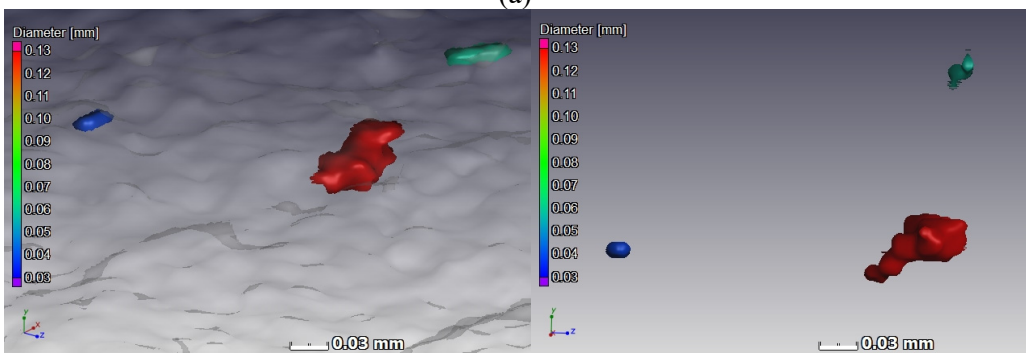

(b)

Figure 82: CT scans reconstruction of pore in reference (RS) sample: ROI of 2 cm (a) and shape of the biggest pore (b).

4.2.2.2 Artificially introduced defects

The vertical building direction showed the artificial defect to be flat at the bottom surface with few sharp edges projecting outwards, but rough outer surfaces were noted as the building continued. This can be due to the sintered powder, after annealing, contouring parameters, as well as the heat transfer when the laser passed the unfused parts (Figure 83–Figure 84).

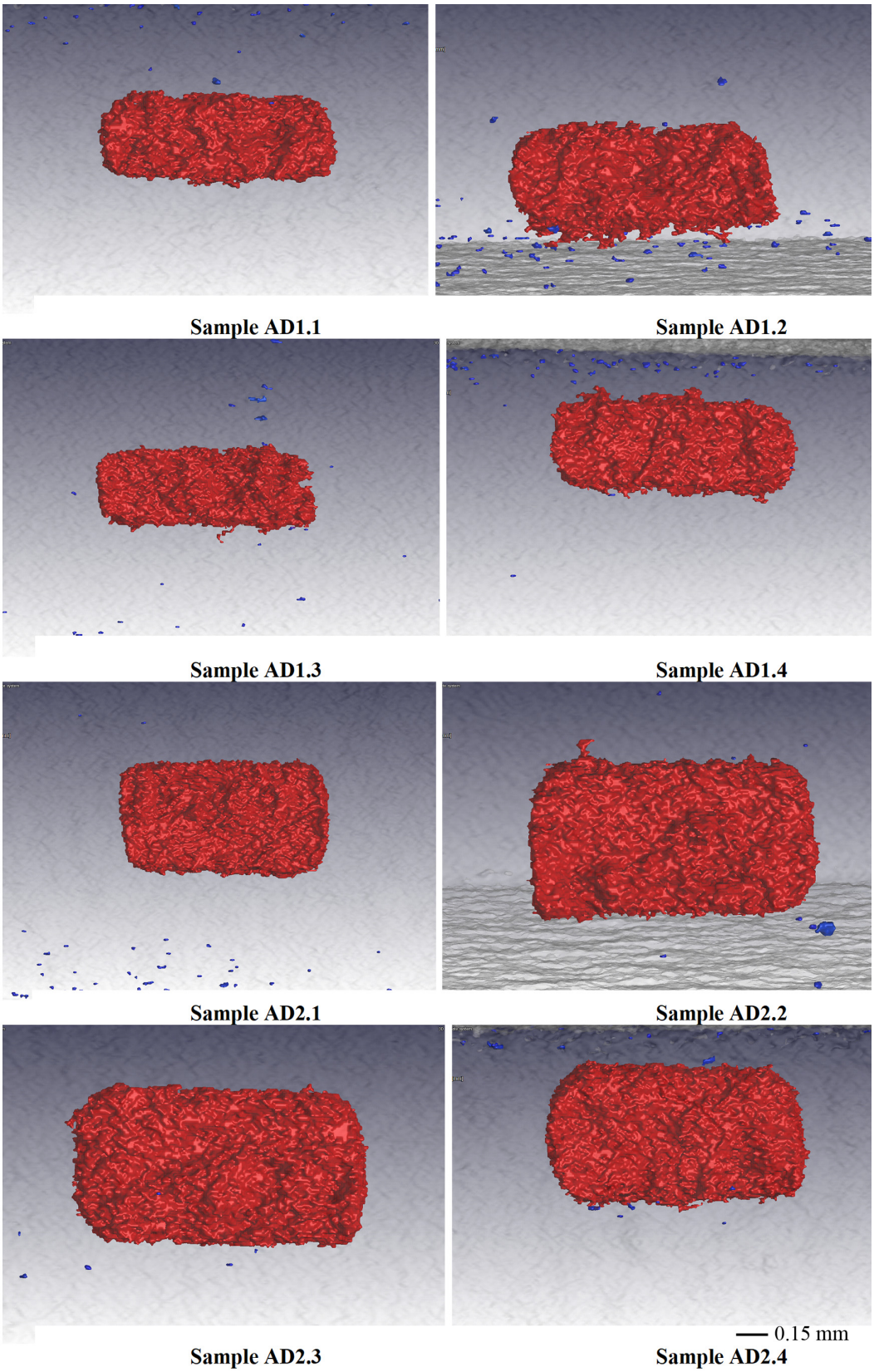

Figure 83: Reconstruction of Ti6Al4V ELI pore before bending.

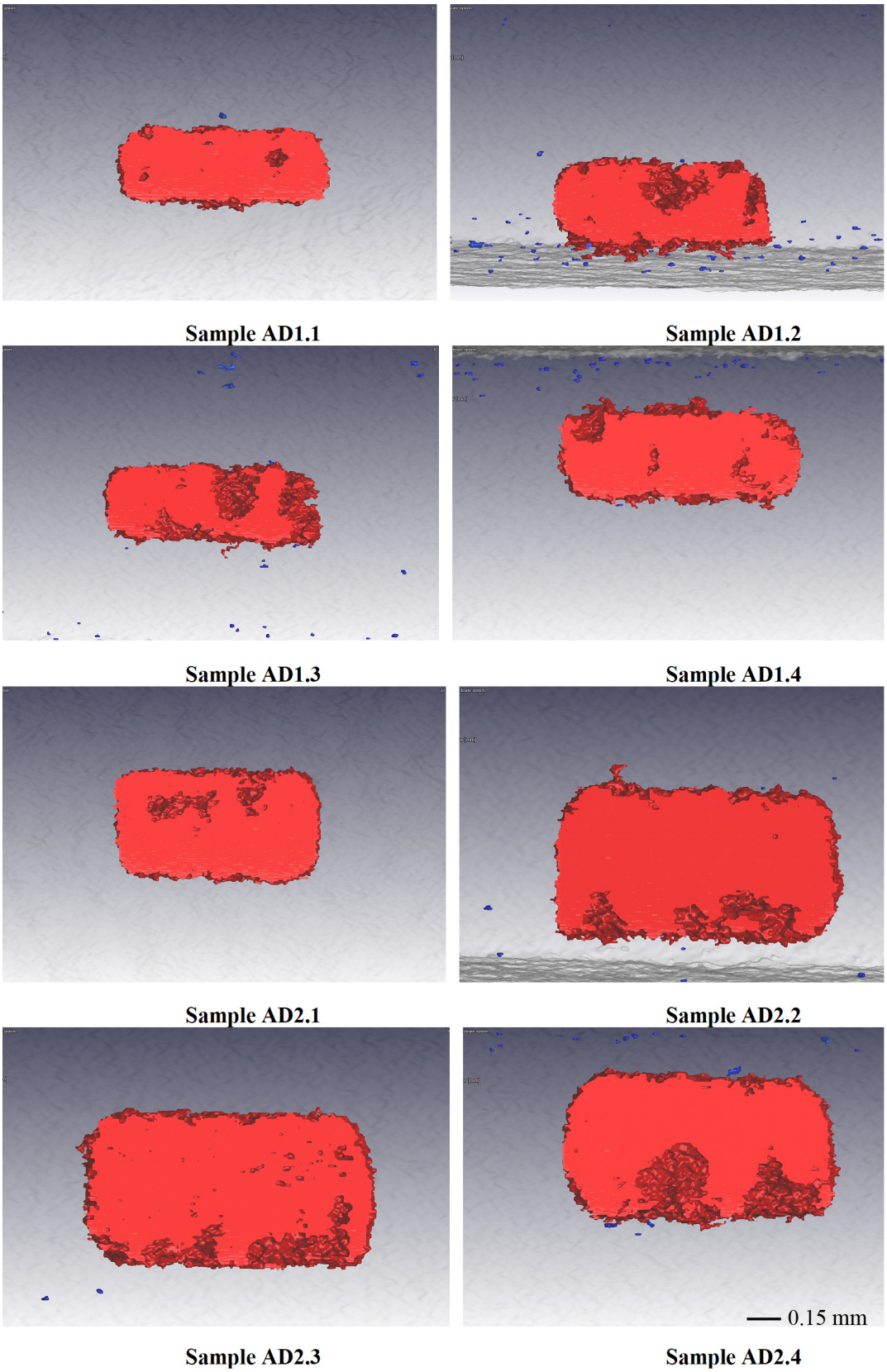

Figure 84: Cross-sectional front view reconstruction of Ti6Al4V ELI sample before bending.

Sintered powder is visible inside the designed voids (Figure 84) because samples were annealed for three hours at 941 °C. Pores were fairly irregular in shape in comparison with sharp rectangular edges, as seen in the design. This adds to the irregular and randomly distributed spectrum for complex shapes.

4.2.3 Experimental stress and strain behaviour

Ti6Al4V ELI theoretical comparison of reference sample are shown (Table 18) for different loading conditions. Contact stress ranges between 836–887 MPa.

Table 18: Theoretical values for solid Ti6Al4V ELI samples (RS) for used for setup

Load	800 N	900 N
Modulus of elasticity, GPa	114	
Second moment of area, m^4	0.01953×10^{-9}	
Contact modulus, Pa	12.148×10^{-12}	
Total contact area, μm	81.2	86.2
Contact stress MPa	836	887
Max slope: Degree, ^{0}	4.6	5.2
Max deflection, mm	1.6	1.8

In TPB tests, fractures are assumed to occur at the midpoint between the supports, which may not be exactly true (Albert et al., 2012). This statement may depend on any internal or external defects that create notches, altering the mechanical integrity of the specimen, causing more stresses to focus on this area. The major concern is whether fracture could occur at the interface between the stacked layers around the artificial defect. In the bending test, the loading head pressed against the top surface. Boundary conditions (BC) in each variant were similarly defined in the form of simply supported constraints that blocked appropriate kinematic degrees of freedom for both the beam edges. In the same way, as it was observed from the FEA results, the experimental results presented in Figure 85–Figure 88 also illustrate that there is a direct relationship between the applied load and the strain (crosshead) induced in the sample. All sample results were plotted in terms of applied load versus centre displacement under the crosshead of the MTS machine. All samples had the same span length (60 mm), thus making it possible to superimpose the load-displacement plots for each group of samples. This allows a more accurate comparison of the resulting curves. All of the tests were carried out at room temperature.

The load spectrum was applied on the sample and results recorded for all samples with independent loading. It must be noted that the MTS machine was not equipped with a displacement sensor, only the crosshead motion was taken into account for stress-strain calculations. Thus, an approximate measurement of strain and stiffness was obtained by measuring the crosshead displacement of the test frame. As recommended in literature, the strains determined using the crosshead displacement need to be considered and should only be used for qualitative purpose (Broughton, 2012). Due to the mastication force (756 N), an over-estimation of experimental loading (900 N) for the samples showed exceptional results even with artificial defects areas higher than most literature experiments conducted in the past. Optimal loading spectrum where the material values under bending falls within the border line of the elastic limit was presumed acceptable. For FEA validation purposes, it was necessary to determine the specific strain value from the tests that represent the specific placement of artificial defects and to interpret the strain distribution from experimental data. Loading plots (Figure 85) of reference solid samples show each loading pattern at a common loading force.

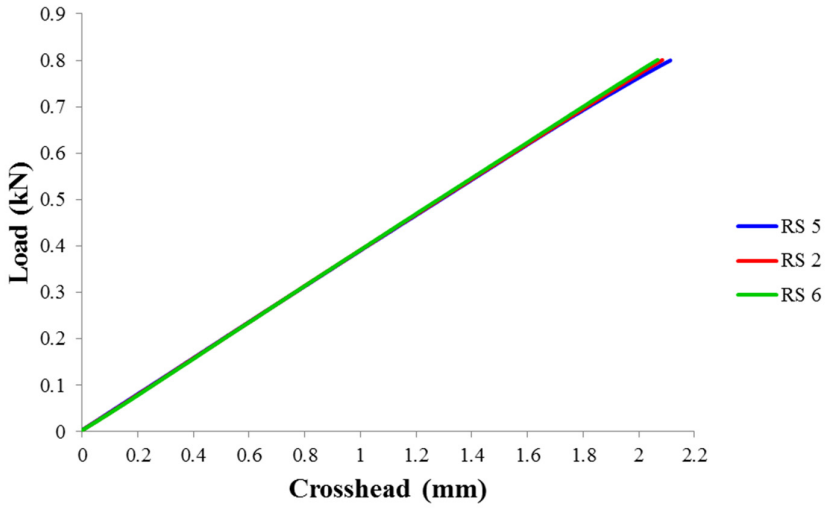

Figure 85: Load-deflection curves for reference samples loaded up to 800 N.

While plotting the reference samples a number of questions arise: Does the EOS machine's printing capabilities meet all necessary standards? Do the MTS bending forces align with different samples when tested incrementally or fully loaded? Looking at the integrity of the reference samples, they should be produced in a manner that all data to any required point should be identical with no delamination observed before reaching the required load. Figure 86 gives a clear indication of when the loading nose and the samples do not touch before bending starts. The line graph shows a zero increase in load as the measurements are recorded, but does

include the downwards movement of the loading nose until the sample causes resistance to the loading nose and the line graph starts to give valid and usable data. Furthermore, the loading nose was set to touch the sample and cleared manually on the program to start the recorded data at zero.

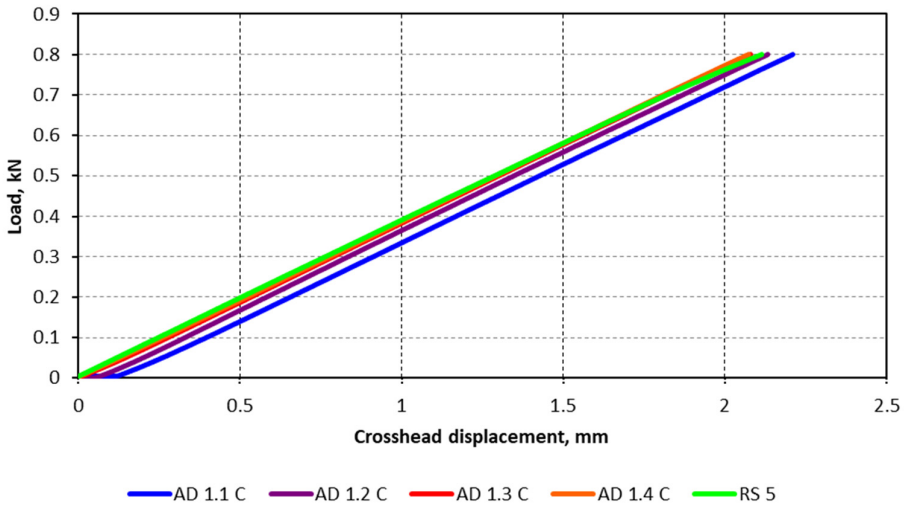

(a)

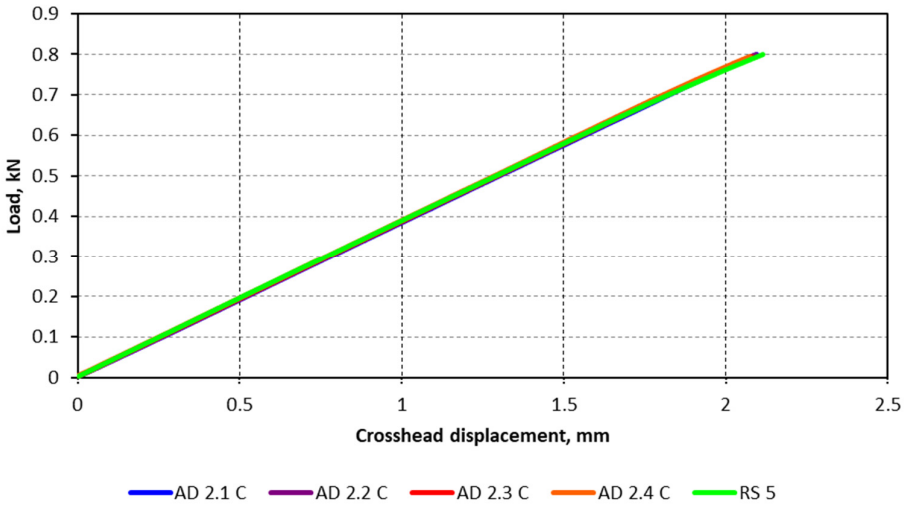

(b)

Figure 86: Load-deflection curves for Set C with different artificial defects: AD1 (a) and AD2 (b). Maximum loading was 800 N.

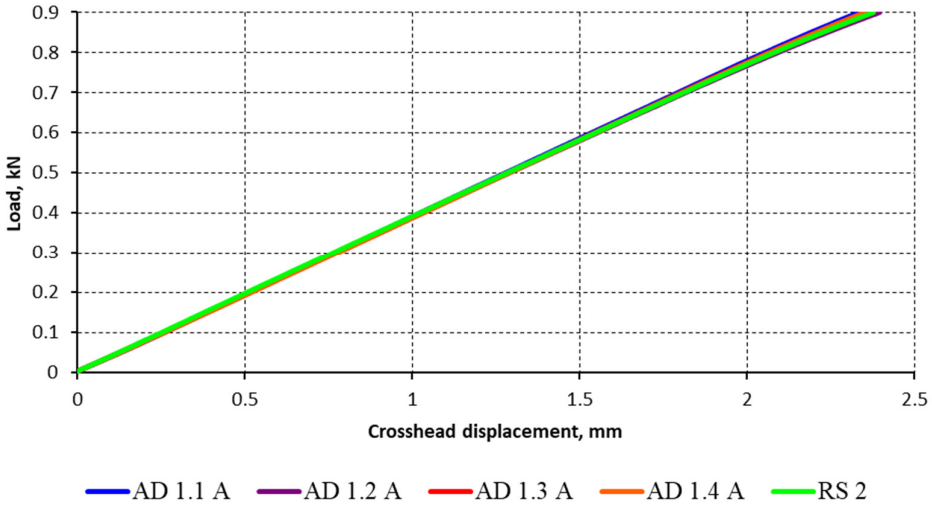

(a)

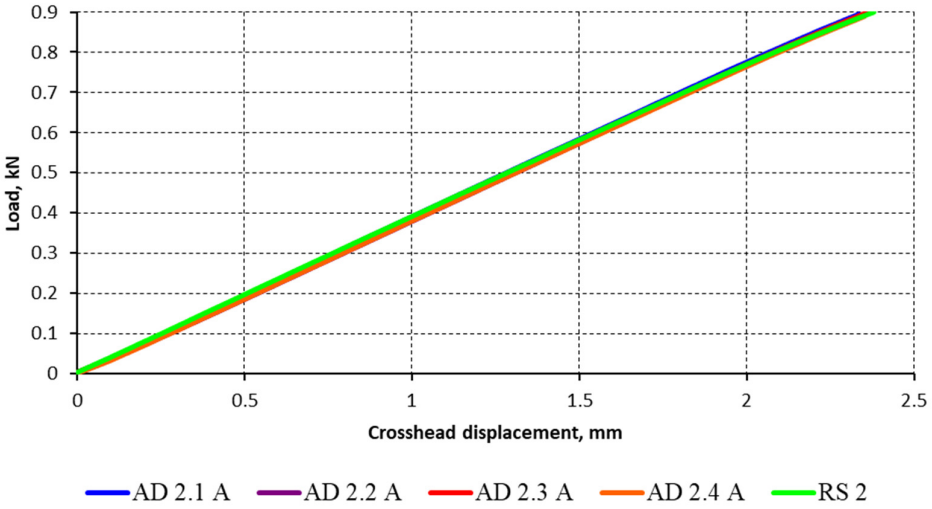

(b)

Figure 87: Load-deflection curves for Set A with different artificial defects: AD1 (a) and AD2 (b). Maximum loading was 900 N.

Results indicate that up to a load of 900 N no difference in stress-strain behaviour was noted on samples whether they had artificial defects or not, (Figure 85–Figure 88).

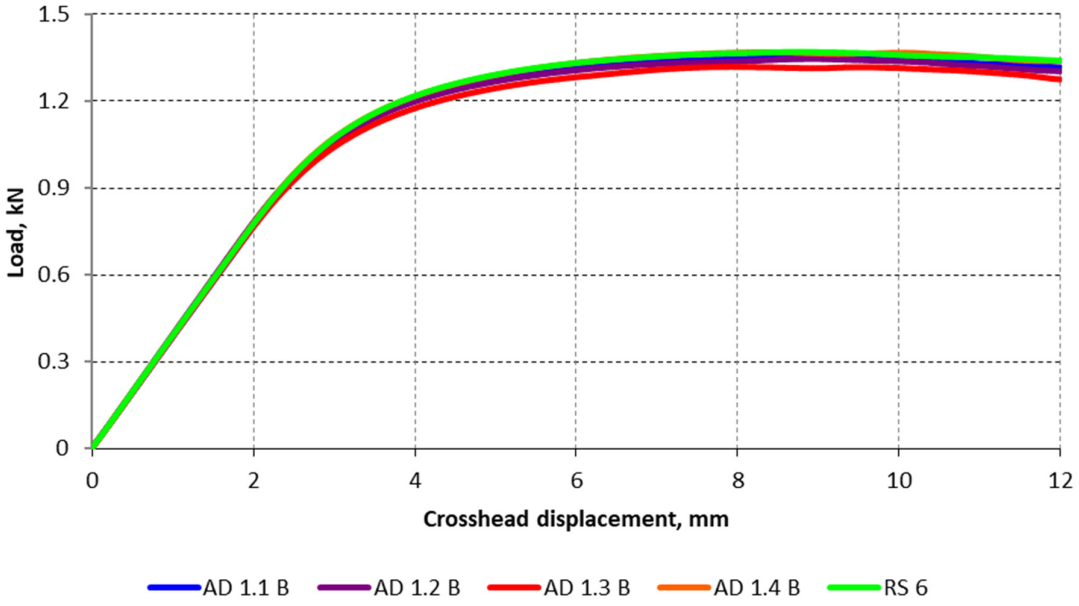

(a)

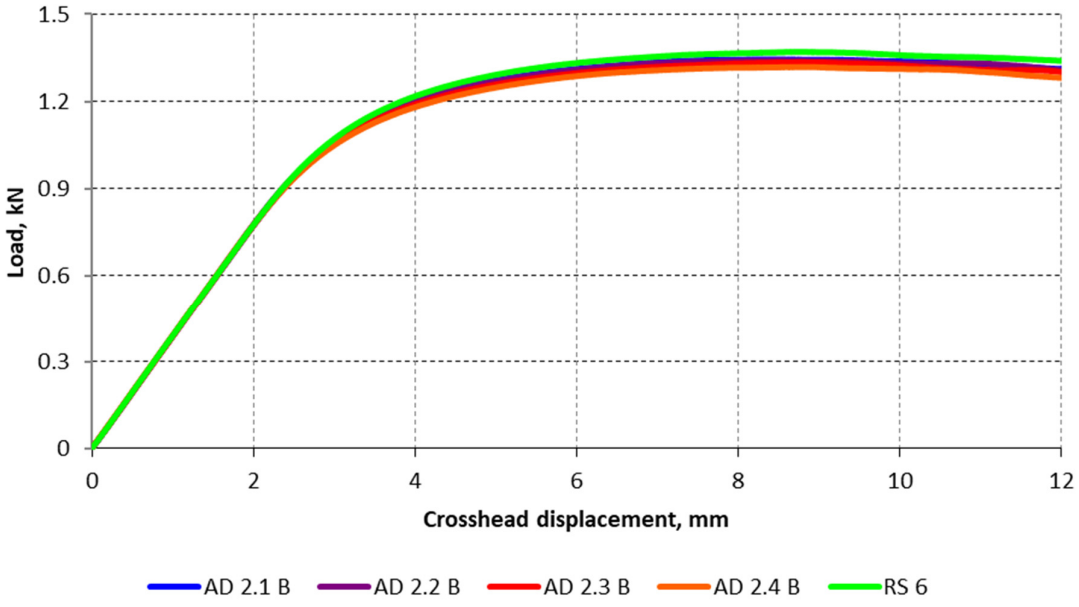

(b)

Figure 88: Load-deflection curves for Set B with different artificial defects: AD1 (a) and AD2 (b). Maximum loading was 1.5 kN.

Table 19 is used for direct comparison of FEA and data points obtained from MTS results. Experimental results show that samples had similar stress-strain behaviour in bending tests up to 1 kN loading.

Table 19: Experimental and FE results for TPB tests

	Experimental results					Numerical results
	Maximum load (kN)	Crosshead (mm)	Flexural stress (MPa)	Flexural strain (mm/mm)	Flexural modulus (MPa) *	Von Mises stress (MPa) at 1 kN loading
AD1.1B	1.351	8.552	1407	0.00540	101	947.4
AD1.2B	1.347	8.867	1403	0.00539	101	954.8
AD1.3B	1.320	7.808	1375	0.00528	100	947.1
AD1.4B	1.369	8.245	1426	0.00548	101	958.1
AD2.1B	1.345	8.531	1401	0.00538	100	948.0
AD2.2B	1.341	8.582	1397	0.00537	100	947.7
AD2.3B	1.335	8.832	1391	0.00534	100	949.8
AD2.4B	1.319	8.920	1374	0.00528	100	957.2
RS6	1.370	8.535	1427	0.00548	100	932.5

* See Appendix 4, calculated from experimental data for Sets A–C.

Samples from Set B and reference sample 6 were tested until plastic deformation. This was used as guide or to superimpose samples with internal artificial defects leading to non-uniform curvature (Figure 88). Samples subjected to a 1500 N force showed no visible fractures nor failure. On closer inspection, the samples did not reach the input 1500 N loading force, indicating yielding before this value. The curves were divided into regions: the linear region, in appearance, explains the elastic behaviour of the material. The second region, after the load reached a peak value, gradually decreased in load and increased in displacement, which is due the material reaching its yield point. No sudden drop in load indicates zero fractures. When a material was plastically deformed, there was no longer a linear relationship between stress and strain as there is for elastic deformations.

4.2.4 Analysis of artificial porosity after testing

The CT scan data provides accurate input regarding porosity distribution and magnitude that may be of concern in future functioning. Complex-shaped design, like irregular bone geometries, can lead to an increase in size or sharpness of porosity. These complex geometries will be greatly deformed in comparison with non-complex geometries. Pre-bending images show clear form of the artificial defects with somewhat round edges projecting small clumps of fused powder outwards; this may be due to the heat transitioning around the artificial design from the laser as it passes the contour lines programmed by the EOS machine. Shape and size of the artificial defects are rough and fairly irregular in shape (Figure 89). There was concern

that the sharp edges of the artificial defect could have initiated fractures, but no sign of any fractures were noted, only an increased amount of pores around the artificial defect. When the pre-bending and post-bending samples were analyzed, similar results were obtained. One point to be noted regarding the samples integrity is that smaller defects formed around the artificial defects. Pores along the top and bottom surfaces (from loading direction) after bending were noted (Figure 90). Some larger pores are known to rise from small grouping pores in one location.

When pre-bending is reviewed against post-bending, it can be seen that although small defects along the compressive and tensile surface were noted, it played no role in fracture of the sample, although it resulted in an increased number of pores on the same compressive and tensile surface due to the compression force. As mentioned, larger pores are known to arise from small groupings of interlayer pores. Given the location of this number of smaller pores close to the surface, futuristic failure is a possibility when, for example, the sample is subjected to cyclic loading within the elastic range. This phenomenon of smaller surface pores leading to larger pores can be somewhat explained by the four “corner edges” of the “rectangular-shaped” artificial defect. From the post-bending images, small projections outwards of these “corner edges” can be seen

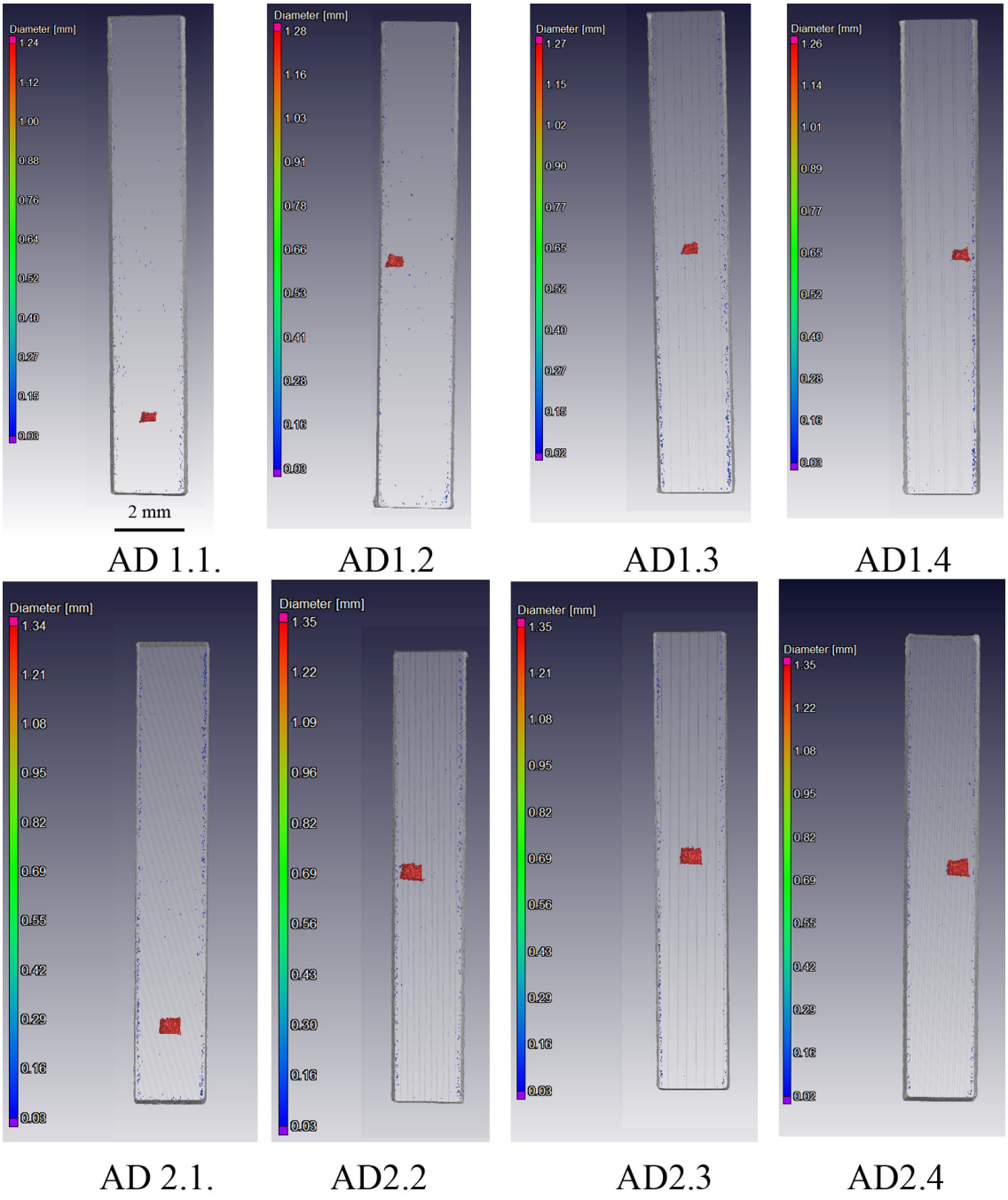

Figure 89: CT scan reconstructions of cavities in LPBF Ti6Al4V ELI samples after testing.

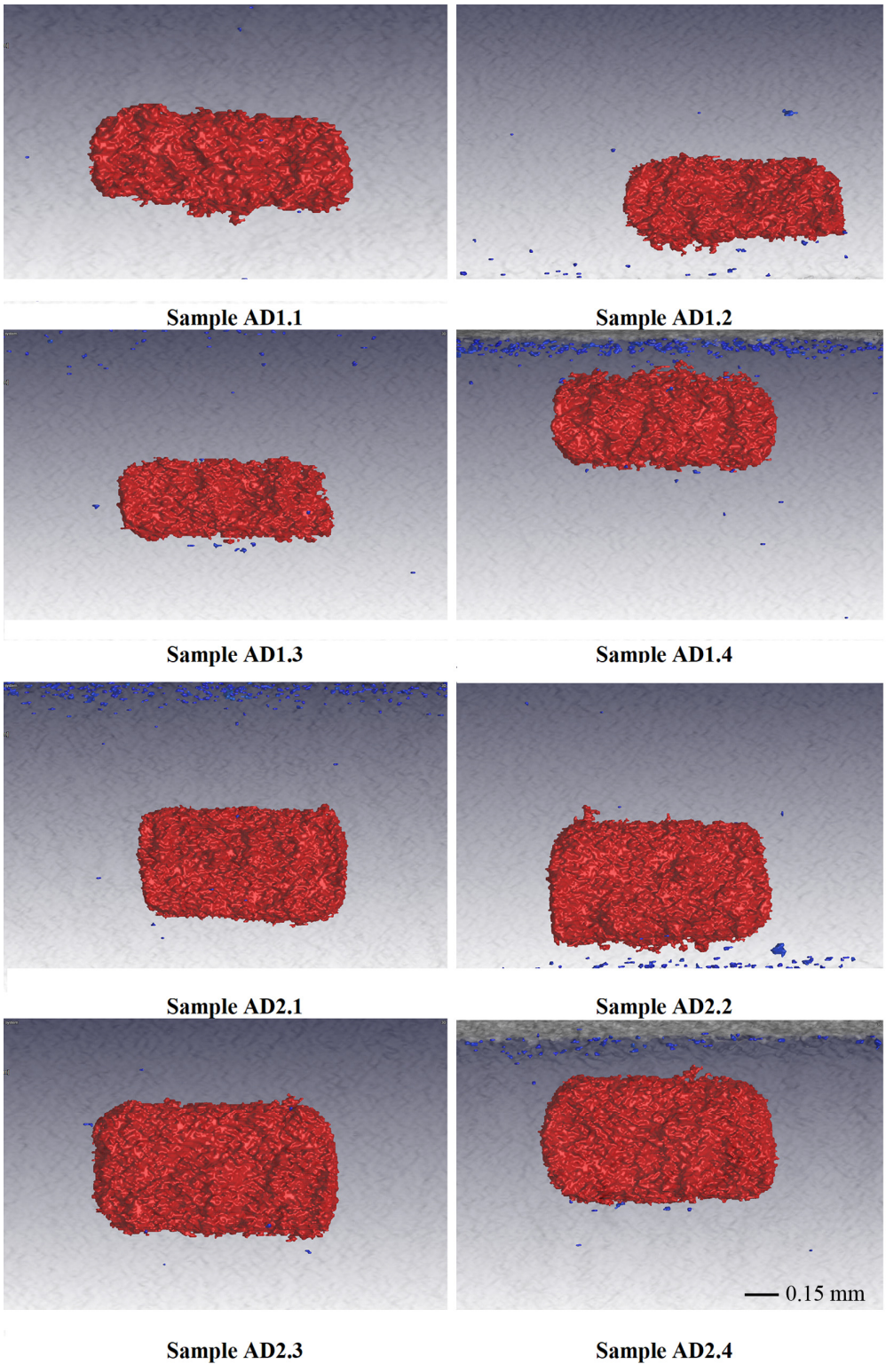

Figure 90: Reconstruction of Ti6Al4V ELI pore extraction after bending.

4.3 DESTRUCTIVE TESTING

Most frequently, failure takes place as a result of high tensile stresses at the surface or around notches (Hsu et al., 2010). Sul et al., 2002 state that the surface layer may lead to small, superficial microcracks followed by fast re-passivation. This effect takes place continuously and may even be promoted by the corrosive environment (oxidative wear). According to previous studies, a notable increase in fatigue strength can be found after shot peening relative to untreated (as-built) specimens. This can be associated with the introduction of high-compression stresses at the surface. Shot peening increases the high-cycle fatigue strength of implants without changing their design or material. The beads strike and deform the substrate at the surface, introducing compressive residual stresses.

Although samples were shot peened, the surface still remained rough (Figure 91). In places where pores were present (artificially introduced), new necks formed and served as bonds for powder particles. During annealing, the loose powder fused together causing necking, also fusing to the rough edges of the internal defect (Figure 92). The cross-sectioning does not show any microfractures around the artificial defect, neither were surface or internal fractures noted at the surrounding material.

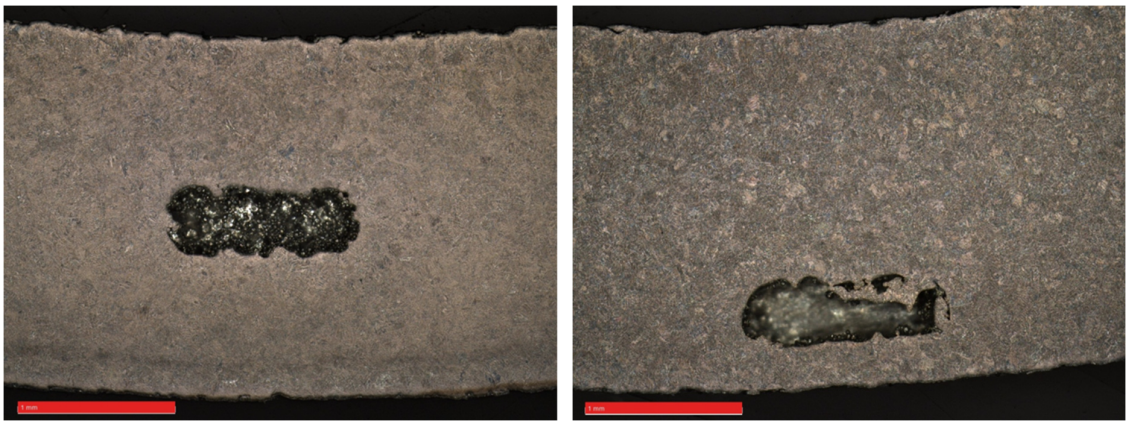

(a) **(b)**

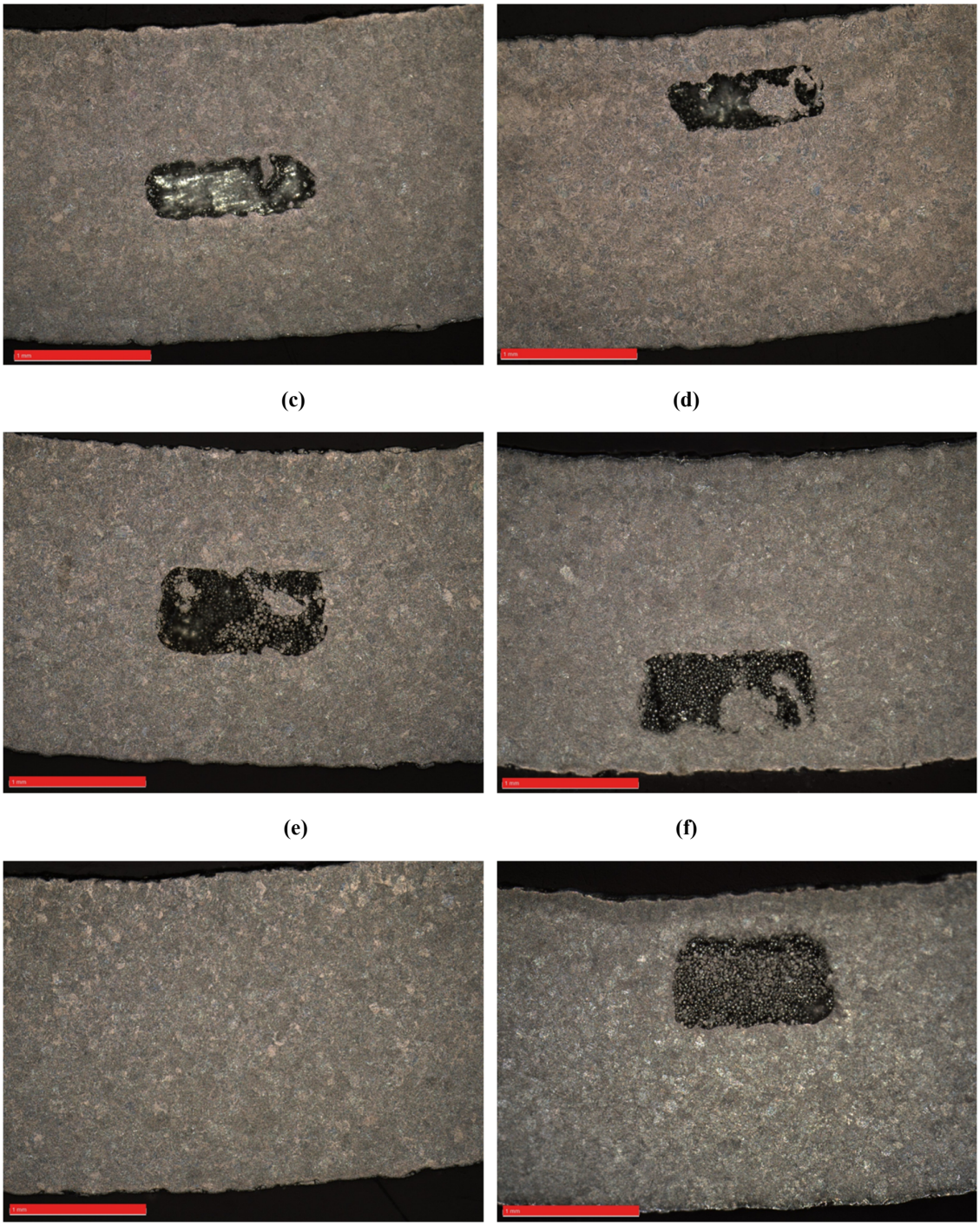

Figure 91: Microscope view of designed artificial defects and microstructure; AD1.1B (a), AD1.2B (b), AD1.3B (c), AD1.B (d), AD2.1B (e), AD2.2B (f), AD2.3B (g), and AD2.4B (h).

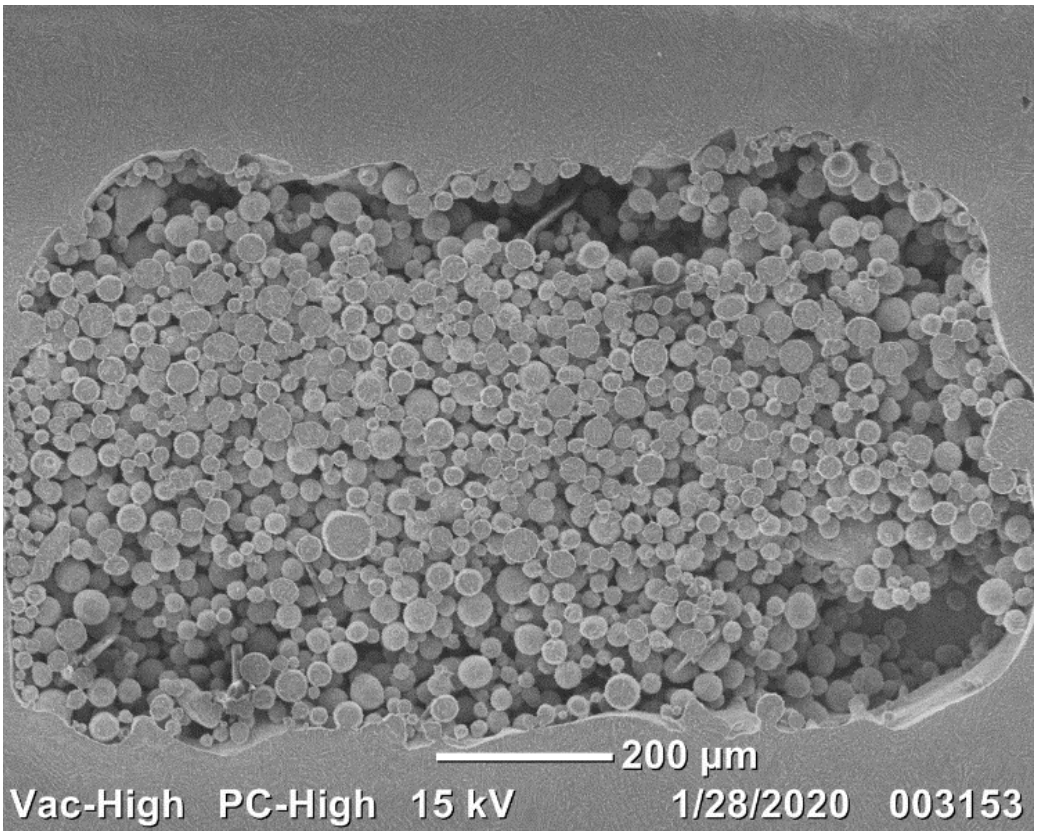

Figure 92: SEM image of powder sintering after annealing in AD 1.1B sample.

4.4 BENDING PROPERTIES OF LPBF Ti6Al4V ELI SAMPLES

Shunmugavela et al. (2015) found that LPBF rods have higher yield strength and ultimate tensile strength compared to their wrought counterparts. But LPBF as-built parts lacked significantly in ductility, unlike the wrought part. This difference in their material behaviour can be explained in the difference in microstructure, as titanium alloy's mechanical properties are strongly influenced by its microstructure. In the wrought Ti6Al4V, the size of the equiaxed α grains determines the mechanical property, whereas in SLM Ti6Al4V, the colony size and size of the α laths determine its property. Yadroitsev et al., 2018 showed that fatigue properties revealed a correlation between the number of cycles to failure and the surface roughness and heat treatment. Samples with a rougher surface demonstrated a decreased number of cycles to failure. Post-processing is an essential stage in AM. Samples that were stress relieved and annealed will exhibit lower UTS when compared to as-built samples. Stress-relieved samples have been found to have a decrease in UTS by 6–8 % from the initial as-built level, although the yield strength (YS) after stress-relieving heat treatment did not change in comparison with

as-built samples. Literature suggests that with regard to mechanical properties, there seems to be a slight gain in ductility of the specimens once stress relieved when compared to as-built samples. Annealing led to significantly improved ductility of LPBF Ti6Al4V.

The flexural modulus is inversely related to deflection. Higher flexural modulus will result in a stiffer material. In the cases investigated, all samples had similar experimental flexural modulus – about 100 GPa. It must be noted that samples were heat treated (annealed).

Numerical simulation showed that samples with artificial defects closer to the point of contact would experience the maximum stress (Figure 92c). On closer inspection of sample AD 2.4, a maximum load of 1319 N with a displacement of 8.9 mm was recorded. The recorded load, in comparison with other samples, is the smallest in value, yet the sample exerted the largest amount of deflection (Figure 92 b). This phenomenon is due to the sample structural integrity.

Ilavarasi and Mariamichael, 2011; Morgan et al., 2018 found that for mandibular bone von Mises stress of 128.6 MPa. Present experimental results showed that values higher than that for bone was found for all samples. Bone tissue is an anisotropic material, although in general, bone tissue may lead to higher loads in the longitudinal direction and a lesser quantity of load when applied over the bone surface.

Pores with magnitudes 1000×300×210 μm and 1000×500×420 μm were not an influencing factor in the mechanical outcome for a static load for Ti6Al4V ELI samples. It should be noted that for this study a magnitude of 756 N, representing a maximum biting force, was compared to a static loading simulation. Results showed compelling evidence that although all samples reached yield, the samples neither showed any sign of fracture on the surface nor around the internal artificial defect nor within the microstructure grains of the samples. However, different outcomes could be found when testing cyclic loading with the same frame of parameters.

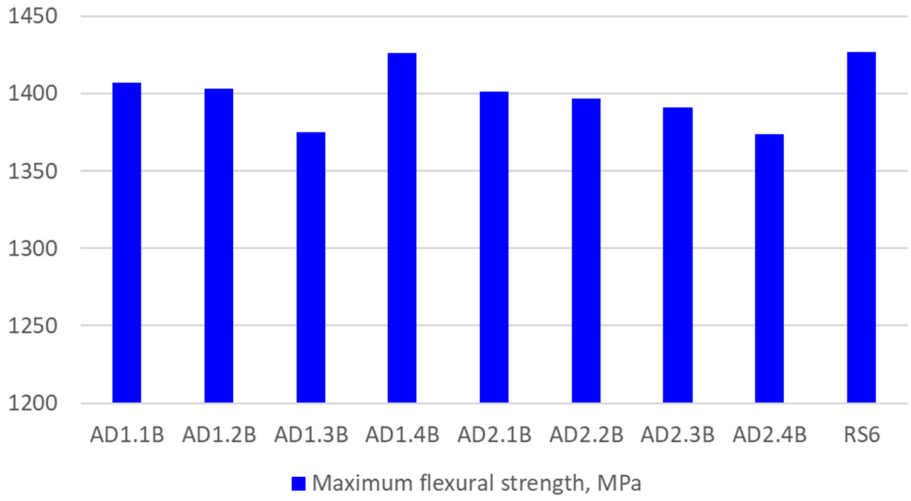

(a)

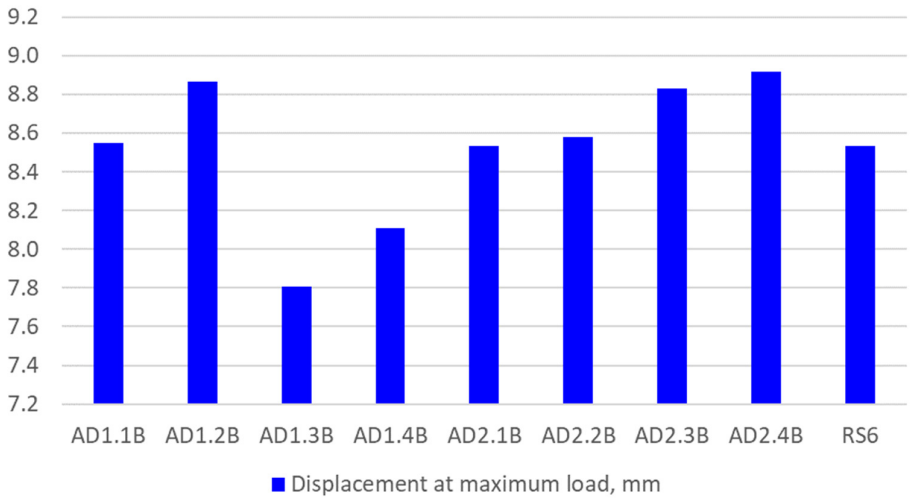

(b)

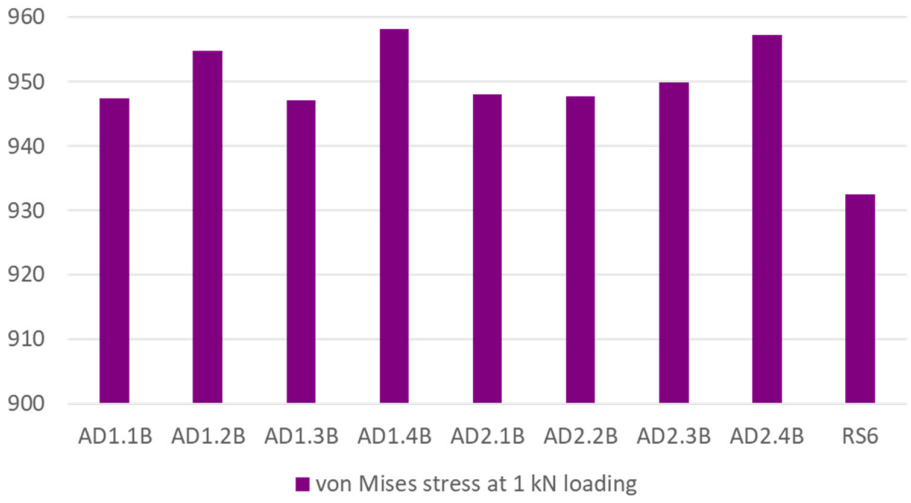

(c)

Figure 93: Maximum flexural strength (a) and displacement at maximum load (b) for Set B samples and maximum von Mises strength at 1 kN loading (c).

CHAPTER 5: Conclusion and future work

The need for new implants, treatments and prostheses as well as prolonging the lifespan of implants has increased. Laser powder bed fusion is very suitable technology for manufacturing customized implants for bone replacements. The aim of this study was to understand critical size and shape of defects influencing the mechanical performance of additively manufactured mandibular implants through LPBF. This is considered highly important and studied widely due to the importance of improving the quality of additively manufactured parts and ensuring their reliability for applications such as medical implants.

During LPBF process, different types of defects such as, unintended porosity, rough surfaces and deviations from design, which can have different root causes and can, vary significantly among samples. Powder material properties, non-uniform delivery of the powder layer, deformation during manufacturing, deviations from optimal process-parameters caused by changes in the laser beam, the optical components and the scanning system operation, may result in lack of fusion pores, metallurgical pores, keyhole pores, etc. Specifically lack of fusion pores are more irregular and have been shown to be more detrimental to mechanical properties than other forms of porosity, so special care must be taken to ensure no lack of fusion occurs. These defects affect the mechanical properties of the parts. The presence of the defects, shape, distribution and location relative to the applied pressure will decrease the strength of the part, thus simulation of such defects allows one to predict the deformation behaviour of the metal under stress. This is especially important for mandibular implants undergoing constant stresses.

The objectives for this study were as follows:

- Biomedical investigation of human mandible functioning;
- Analysis of critical points for different types of mandible reconstruction;
- Analysis of porosity in LPBF mandible implants;
- Production and exact treatment of samples for certified mandible implant;
- Experimental testing of Ti6Al4V ELI samples with prescribed sample size, pore size and shape, and loading;
- Numerical simulation and validation data compiled from numerical simulation with mechanical testing.

Briefly touching on the aforementioned:

- LPBF process and its capabilities were studied;

- Ti6Al4V alloy influence on a biomedical application was described;
- Properties of Ti6Al4V alloy microstructure was described;
- Human mandible anatomy was studied;
- FEA was described;
- Ti6Al4V ELI powder was described;
- Preliminary tests were conducted before any experimental tests with L=PBF samples. Aluminium alloy was used as a pilot test with TBA and FEA;
- Defects size, shape, and location in normal LPBF printing parameters were studied and incorporated into the titanium sample design;
- As-built and shot peened Ti6Al4V samples' surface roughness were described;
- Maximum mastication load was used as benchmark when samples were simulated in ANSYS. Loads used for simulation, to determine whether the implant with artificial defects would withstand the forces exerted, exceeded the mastication force (safety factor).

Complex-shape production often results in porosity near critical load bearing sections, thus careful anatomical inputs are included in both experimental and numerical assessments, resulting in more effective implants for future encounters in implants subjected to defects. The current results are found by optimal manufacturing process well developed and validated over a number of years, in combination with optimal heat treatment. The reliability of the experimental data is provided by the use of modern research methods. The results obtain open new scientific knowledge in the field of creation and medical applications of biocompatible titanium alloys. MicroCT-simulation holds particular promise to be applied to more complex parts to predict their mechanical performance. This is extremely important for complex parts where pore location can more strongly affect the strength properties leading to possible premature failure in such parts. Vertical defects following the build direction can be preferentially formed and may be a general result for all types of defects and internal cavities in such parts. The directionality of defects observed may be useful to interpret quality issues of additive manufacturing of metal components and help designers or engineers to select the building orientation when producing complex LPBF parts.

The work involves an investigation of the influence of manufacturing flaws, particularly porosity, on the mechanical performance of additively manufactured biomedical titanium used for facial implants. Creating artificial pores or defects in L-PBF parts and subjecting these parts to mechanical tests to reveal the effect of specific defect types found in LPBF implants were

done. The influence of these artificial defects on the mechanical properties and integrity of the samples was determined through TPB and inspection with the aid of FEA, microCT analysis and destructive testing. Results indicate that defects of 1000 µm×300 µm×210 µm and 1000 µm×500 µm×420 µm in size at various depths to the neutral axis of the sample had no significant outcome to the mechanical performance of the samples when tested statically in 3-point bending. Samples were tested statically at loading of 800, 900 and 1500 N, representing a maximum biting force. Most importantly, they could all reach maximum predicted mandibular bite force without failure. Ti6Al4V ELI sintered powder was visible inside designed voids due to post processing. Pores were fairly irregular shaped in comparison with sharp rectangular edges as in simulated defects. This adds to the irregular and randomly distributed spectrum for complex shapes. The use of artificially designed defects for test parts is useful for relating mechanical properties to specific pore types and sizes.

While these results are very promising, implants are subjected to cyclic loads and fatigue performance is therefore critical and remains to be investigated – especially in the context of mandibular implants. It opens the possibility of various investigations to follow that can include the following in combination; process parameters, post processing, fatigue properties, non-destructive testing methods such as X-tomography, complex-geometry parts, critical pore size and location also the influence of a corrosive medium on fatigue strength during cyclic loading can be investigated.

REFERENCES

Abadzhiev, M., Todorov, G., and Kamberov, K., 2017. Mandibular flexure – a reason for chronic pain syndrome in edentulous patient restored with fixed ZrO2 construction over implants, inserted in natural bone and bone graft area. Case report. *Journal of IMAB*, 23(1), pp. 1432-1440.

Adams, D., 2017. Can flexure testing provide estimates of composite strength properties? Available at: www.compositesworld.com/articles/can-flexure-testing-provide-estimates-of-composite-strength-properties. Accessed: Dec. 2019.

Akahori, T., and Niinomi, M., 1998. Fracture characteristics of fatigued Ti-6Al-4V ELI as an implant material. *Material Science and Engineering:* A, 243(1), pp. 237-243.

Al-Ahmari, A., Nasr, E.A., Moiduddin, K., Anwar, S., Al Kindi, M., and Kamrani, A., 2015. A comparative study on the customized design of mandibular reconstruction plates using finite element method. *Advances in Mechanical Engineering*, 7(7), pp. 1-11.

Al-Ali, M.A., Al-Ali, M.A., Takezawa, A., and Kitamura, M., 2017. Topology optimization and fatigue analysis of temporomandibular joint prosthesis. *World Journal of Mechanics*, 7, pp. 323-339.

Albert, C., Jameson, J.R., and Harris, G.F., 2012. Design and validation of bending test method for characterization of miniature pediatric cortical bone specimens. *Journal of Engineering in Medicine*. 227(2), pp. 105-113.

Albrektsson, T., Chrcanovic, B., Ostman, P.O., and Sennerby, L., 2017. Initial and long-term crestal bone responses to modern dental implants. *Periodontology*, 73, 1, pp. 41-50.

Al-Makky, M., and Mahmoud, D., 2016. *The importance of additive manufacturing progress in industrial applications. Proceedings of the 17th International AMME Conference, 19-21 April 2016, Cairo, Egypt, pp. 1-15.*

Alvarez-Arenal, A., Lasheras, F.S., Fernández, E.M., and González, I., 2009. A jaw model for the study of the mandibular flexure taking into account the anisotropy of the bone. *Mathematical and Computer Modelling*, 50, pp. 695-704.

Anam, M.D.A., Dilip, J.J.S., Pal, D., and Stucker, B., 2014. *Effect of scan pattern on the microstructural evolution of Inconel 625 during selective laser melting*, Annual International Solid Freeform Fabrication Symposium SFF 2014, Austin, U.S.A., pp. 363-376.

Arisoy, Y.M., Criales, L.E., Ozel, T., Lane, B., Moylan, S., and Donmez, A., 2017. Influence of scan strategy and process parameters on microstructure and its optimization in additively manufactured nickel alloy 625 via laser powder bed fusion. *The International Journal of Advance Manufacturing Technology.* 90(5-8), pp. 1393-1417.

Armentani, E., Caputo, F., and Citarella, R., 2010. FEM sensitivity analyses on the stress levels in a human mandible with a varying ATM modelling complexity. *The Open Mechanical Engineering Journal*, 4, pp. 8-15.

Arrese, A., and Mujika, F., 2008. Influence of bending rotations on three and four-point bend end notched flexure tests. *Engineering Fracture Mechanics*, 75(14), pp. 4234-4246.

Arsic, S., Peric, P., Stojkovic, M., LLic, D., Stojanovic, M., and Vucic, S., 2010. Comparative analysis of linear morphometric parameters of the humane mandibula obtained by direct and indirect measurement. *Vojnosanitetski Pregled*, 67(10), pp. 839-846.

ASM Aero, 2015. ASM Aerospace specification metals, Inc. Available at: http://www.asm.matweb.com/search/SpecificMaterial.asp?bassnum=mtp642. Accessed: Nov 2018.

ASTM D790-03., 2003. Standard test method for flexural properties of unreinforced and reinforced plastics and electrical insulation materials. ASTM International, pp. 1-11.

ASTM F136-13. Standard specification for wrought Titanium-6Aluminum-4Vanadium ELI (Extra Low Interstitial) alloy for surgical implant applications (UNS R56401). ASTM International, West Conshohocken, PA, 2013.

ASTM F2792-12a, Standard terminology for additive manufacturing technologies. ASTM International, Available at: http://www.astm.org/Standards/F2792.htm, 3 p. Accessed: June 2018.

Aumund-Kopp, C., and Riou, A., 2015. Introduction to additive manufacturing technology. 1st ed. *European Powder Metallurgy Association*, 41 p.

Aversa, A., Lorusso, M., Trevisan, F., Ambrosio, E.P., Calignano, F., Manfredi, D., Biamino, S., Fino, P., Lombardi, M., and Pavese, M., 2017. Effect of process and post-process conditions on the mechanical properties of an A357 alloy produced via laser powder bed fusion. *Metals,* (2075-4701), 7(2), pp. 1-9.

AZoM Materials., 2013. Titanium Alloy- Ti6Al4V Grade 5. U.S Titanium Industry Inc. Available at: http://www.azom.com/article.aspx?ArticleID=9365. Accessed: July 2019.

Bacchewar, P.B., Singhal, S.K., and Pandey, P.M., 2007. Statistical modeling and optimization of surface roughness in selective laser sintering process. *Proceedings of the IMechE, Part B: Journal of Engineering Manufacture*, 221(1), pp. 35-52.

Baek, S.H., Cha, H.S., Cha, J.Y., and Moon, Y.S., 2012. Three-dimensional finite element analysis of the deformation of the human mandible: A preliminary study from the perspective of orthodontic mini-implant stability. *Korean Journal of Orthodontics*, 42(4), pp. 159-168.

Barriobero-Vila P., Phase transformation kinetics during continuous heating of α+β and metastable β titanium alloys. PhD thesis, Vienna University of Technology, 88 p.

Bassoli, E., Sola, A., Celesti, M., Calcagnile, S., and Cavallini, C., 2018. Development of laser-based powder bed fusion process parameters and scanning strategy for new metal alloy grades: A holistic method formulation. *Materials*, 11(2356), pp. 1-16.

Baxter, C., Cyr, E., Odeshi, A., and Mohammadi, M., 2018. Constitutive models for the dynamic behaviour of direct metal laser sintered AlSi10Mg_200C under high strain rate shock loading. *Material Science and Engineering: A*, 731, pp. 296-308.

Bayome, M., Park, J.H., and Kook, Y.A., 2013. New three-dimensional cephalometric analyses among adults with a skeletal Class I pattern and normal occlusion. *The Korean Journal of Orthodontics*, 43(2), pp. 62-73.

Beard, T., 1997. Machining from STL additive manufacturing, Available at: http://www.additivemanufacturing.media/articles/machining-from-stl-file., Accessed: Nov 2018.

Belan, J., Kuchariková, L., Tillová, E., and Chalupová, M., 2019. Three-point bending fatigue test of Tial6v4 titanium alloy at room temperature. *Advances in Materials Science and Engineering*, pp. 11.

Bengochea, K., 2018. Mandible- what to learn about it. KenHub, Available at: http://www.kenhub.com/en/library/anatomy/the-mandible. Accessed: July 2018.

Blanksma, N.G., van Eijden, T.M., van Ruijven, L.J., and Weijs, W.A., 1997. Electromyographic heterogeneity in the human temporalis and masseter muscle during dynamic tasks guided by visual feedback. *Journal of Dental Research*, 76(1), pp. 542-551.

Bose, S., Ke, D., Sahasrabudhe, H., and Bandyopadhyay, A., 2018. Additive manufacturing of biomaterials. *Progress in Materials Science*, 93, pp. 45-111.

Brika, S.E., Zhao, Y.F., Brochu, M., and Mezzetta, J., 2017. Multi-objective build orientation optimization for powder bed fusion by laser. *Industrial Engineering & Management*, 6(4), pp. 9.

Broughton, W., 2012. Testing the mechanical, thermal and chemical properties of adhesives for marine environments. In: Adhesives in Marine Engineering, Woodhead Publishing Series in Welding and Other Joining Technologies, pp. 99-154.

Brusa, E., Sesan, R., and Ossol, E., 2017. Numerical modelling and testing of mechanical behaviour of AM Titanium alloy bracket for aerospace applications. *Procedia Structural Integrity*, 5, pp. 753-760.

Buck, D.W II., and Dumanian, G.A., 2012. Bone biology and physiology: Part 1. The fundamentals. *Plastic and Reconstructive surgery,* 129(6), pp. 1314-1320.

Carter, L.N., Martin, C.; Withers, P.J., and Attallah, M.M., 2014. The influence of the laser scan strategy on grain structure and cracking behaviour in SLM powder-bed fabricated nickel superalloy. *Journal of Alloys and Compounds*, 615, pp. 338-347.

Chakravorty, D., 2018. 3D printing support structures – all you need to know. Support structures simplified. https://all3dp.com/1/3d-printing-support-structures/ Accessed: June 2020.

Chan, K.S., Koike, M., Mason, R.L., and Okabe, T., 2013. Fatigue life of titanium alloys fabricated by additive layer manufacturing techniques for dental implants. *Metall and Mat Trans A*, 44, pp. 1010-1022.

Choi, A.H., Ben-Nissan, B., and Conway, R.C., 2005. Three-dimensional modelling and finite element analysis of the human mandible during clenching. *Australian Dental Journal*, 50(1), pp. 44-48.

Choi, A.H., Ben-Nissan, B., and Conway, R.C., 2005. Three-dimensional modelling and finite element analysis of the human mandible during clenching. *Australian Dental Journal*, 50(1), pp. 42-48.

Collings, E.W., 1984. The physical metallurgy of titanium alloys. *American Society for Metals*, Metals Park, OH.

Commisson, M.S., Martınez-Reina, J., Ojeda, J., and Mayo, J., 2015. Finite element analysis of the human mastication cycle. *Journal of the Mechanical Behaviour of Biomedical Materials*, University of Seville, Spain, 41, pp. 23-35.

Concept Laser, 2015. Concept Laser online. Available at: http://www.concept-laser.de/en/technology/lasercusingr.html. Accessed: July 2018.

Correia, A., Piloto, P., Reis Campos, J.C., Vaz, M., 2008. Finite element analysis of the mechanical behavior of a partially edentulous mandible as a function of cancellous bone density. *Revista Odonto Ciência*, 24(1), pp. 22-27.

Criales, L.E., Arisoy, Y.M., and Özel, T., 2016. Sensitivity analysis of material and process parameters in finite element modeling of selective laser melting of Inconel 625. *International Journal of Advance Manufacturing Technology*, 86(9-12), pp. 2653-2666.

Cunha, A., 2015. Multiscale femtosecond laser surface texturing of titanium and titanium alloys for dental and orthopaedic implants. *The Pontifical Catholic University of Rio Grande do Sul*, pp. 1-250.

Dabrowski, J., Przybysz, J., Pietka, T., and Domanski, W., 2010. Titanium reconstructive plates in the reconstruction of mandibular continuity. *Dental Journal*, 63, pp. 663-671.

Das, S., 2003. Physical aspects of process control in selective laser sintering of metals. *Advance Engineering Material*, 5, pp. 701-711.

Dawes, J., Bowerman, R., and Trepleton, R., 2015. Introduction to the additive manufacturing powder metallurgy supply chain. *Johnson Matthey Technology Review*, 59(3), pp. 243-256.

de Souza Fernandes, A.C., de Quadros Uzeda-Gonzalez, S., Mascarenhas, .M.L,, Machado, L.A., and de Moraes, M., 2010. Direct and tomographic dimensional analysis of the inter-radicular distance and thickness of the vestibular cortical bone in the parasymphyseal region of adult human mandibles. *British Journal of Oral and Maxillofacial Surgery*, 50(4), pp. 350-355.

Dobrzanski, L.A., 2004. Metallic materials engineering, Publishing House WNT, Warsaw.

Donachie, M.J., 2000. Titanium: A technical guide. Materials Park, Ohio, second edition, ASM International, Technology & Engineering, pp. 1-369.

Donachie, M.J., 2010. Titanium: A technical guide. Materials Park, Ohio: ASM International, Technology & Engineering, pp. 22.

Dormehl, L., 2019. The brief building history of 3D printing. Digital Trends, Online: http://www.digitaltrends.com/cool-tech/history-of-3d-printing-milestones/.

Drotsky, J.G., 2011. Strength of materials for technicians, 4th edition. Pearson Education South Africa (Pty) Ltd, Forest Drive, Pinelands, Cape Town, chapters 6 & 14.

Drozdzowska, B., Michno, M., and Michno, A., 2002. The relationship between mandibular bone mass and skeletal osteopenia/osteoporosis (*Związek masy kostnej żuchwy ze stanem mineralizacji szkieletu na podstawie piśmiennictwa*). *Nowa Stomatologia,* 3, pp. 127-130.

du Plessis, A., and Rossouw, P., 2015. Investigation of porosity changes in cast Ti6Al4V rods after hot isostatic pressing. *Journal of Materials Engineering and Performance*, 24(8), pp. 3137-3141.

du Plessis, A., Broeckhoven, C., Yadroitsava, I., Yadroitsev, I., Hands, C.H., Kunju, R., and Bhate, D., 2019. Beautiful and Functional: A review of biomimetic design in additive manufacturing. *Additive Manufacturing*, 27, pp. 408-427.

du Plessis, A., le Roux, S.G., Booysen, G., and Els, J., 2016, a. Quality control of a laser additive manufactured medical implant by X-ray tomography. *3D Printing and Additive Manufacturing*, 3(3), pp. 175-182.

du Plessis, A., le Roux, S.G., Booysen, G., and Els, J., 2016, b. Directionality of cavities and porosity formation in powder-bed laser additive manufacturing of metal components investigated using X-ray tomography. *3D Printing and Additive Manufacturing*, 3(1), pp. 48-55.

du Plessis, A., le Roux, S.G., Booysen, G., and Guelpa, A., 2016, c. The CT Scanner Facility at Stellenbosch University: An open access X-ray computed tomography laboratory. *Nuclear Instruments and Methods in Physics Research B*. 384, pp. 42-49.

Dunbar, A.J., 2016. Analysis of the laser powder bed fusion additive manufacturing process through experimental measurement and finite element modelling. *PhD thesis, The Pennsylvania State University*, U.S,A., 158 p.

El-Anwar, M.I., and Mohammed, M.S., 2014. Comparison between two low profile attachments for implant mandibular overdentures. *Journal of Genetic Engineering and Biotechnology*, 12(1), pp. 45-53.

Emin, A., 2017. The mandible-structure-attachments-fractures. TeachMeAnatomy. Available at: http://www.teachmeanatomy.info/head/osteology/mandible/. 9 p, Accessed: July 2018.

English, C.L., Tewari, S.K., and Abbott, D.H., 2011. An overview of Ni Base additive fabrication technologies for aerospace applications (Preprint), GE Aviation, pp. 399- 412.

EOS GmbH, 2016. Additive manufacturing (online). Available at: http://www.eos.info/. Accessed: April 2019.

Fabriker, K., 2018. Ti6Al4V titanium alloys. Arcam EBM System, Sweden. Available at: http://www.arcam.com, Accessed: April 2018.

Facchini, L., Magalini, E., Robotti, P., Molinari, A., Höges, S., and Wissenback, K., 2010. Ductility of a Ti-6Al-4V alloy produced by selective laser melting of prealloyed powder. *Rapid Prototyping Journal*, 16, pp. 450-459.

Faulkner, M.G., Hatcher, D.C., and Hay, A., 1987. A three dimensional investigation of temporomandibular joint loading. *Journal of Biomechanics*, 20(10), pp. 997-1002.

Fischer, H., and Marx, R., 2002. Fracture toughness of dental ceramics: comparison of bending and indentation method. *Dental Materials*, 18(1), pp. 12-19.

Fischer, P., Romano, V., Weber, H.P., Karapatis, N.P., Boillat, E., and Glardon, R., 2003. Sintering of commercially pure titanium powder with a Nd:YAG laser source. *Acta Materialia*, 51, pp. 1651-1662,

Franz-Odendaal, T.A., Hall, B.K., and Witten, P.E., 2006. Buried alive: how osteoblast became osteosytes. *Developmental dynamics: An official publication of the American Association of Anatomists,* 235(1), pp. 176-190.

Frei, W., 2013. Meshing consideration for linear static problems. COMSOL. Available at: www.comsol.com/blogs/meshing-considerations-linear-static-problems/. Accessed: June 2018.

Fütterling, F., Klein, R., Straber, W., Weber, H., 1998. Automated Finite Element Modeling of a Human Mandible with Dental Implants. In: 6th International Conference in Central Europe on Computer Graphics and Visualization.

Gateno, J., Alfi, D., Xia, J. J., and Teichgraeber, J.F., 2015. A geometric classification of jaw deformation. *Journal of Maxillofacial Surgery*, 73(12), pp. 1-10.

Giang, K., 2018. 3D printing STL files: A step by step guide. 3D Hubs. Available at: http://www.3dhubs.com/knowledge-base/3d-printing-stl-files-step-step-guide. Accessed: Nov 2018.

Gibson I., Rosen D., Stucker B. (2010) Powder Bed Fusion Processes. In: *Additive Manufacturing Technologies*. Springer, Boston, MA. pp. 120-159.

Gong, H., Rafi, K., Gu, H., Starr, T., and Stucker, B., 2014. Analysis of defect generation in Ti-6Al-4V parts made using powder bed fusion additive manufacturing processes. *Additive Manufacturing*, pp. 87-98.

Gonzalez, S. M., 2008. Cortical bone thickness in the maxilla and mandible for mini-implant placement. Masters Thesis–Oral Biology and Oral Pathology Commons, p. 76.

Gray, H., 2018. Anatomy of the human body. Available at: www.bartleby.com/107/. Accessed: May 2018.

Griffin, B., 2018. How do muscles attach to bones. Whyzz. Available at: http://www.whyzz.com/how-do-muscles-attach-to-bones. Accessed: July 2018.

Griss, P., and Heimke, G., 1976, Record of discussion on stability of joint prostheses. In: Biocompatibility of Implant Materials, Williams, D., 52(68), Sector Publishing, London.

Groning, F., Fagan, M., and O'Higgins, P., 2012. Modeling the human mandible under masticatory loads: which input variables are important. *The Anatomical Record,* 295, pp. 853-863.

Hardie, D., and Ouyang, S., 1999. Effect of microstructure and heat treatment on fracture behaviour of smooth and precracked tensile specimens of Ti6Al4V. *Materials Science and Technology*, 15(9), pp. 1049-1057.

Hayden, R.E., Mullin, D.P., and Patel, A.K. 2012. Reconstruction of the segmental mandibular defect: current state of the art. *Current Opinion in Otolaryngol & Head and Neck Surgery*, 20(4), pp. 231-236.

Healthcare Market Report, 2020. *Global prosthetics and orthotics market by type by orthotics category by prosthetics category by region, industry analysis and forecast, 2019 – 2025.* Available at: https://www.reportlinker.com/p05876907/Global-Prosthetics-and-Orthotics-Market-By-Type-By-Orthotics-Category-By-Prosthetics-Category-By-Region-Industry-Analysis-and-Forecast.html?utm_source=GNW. Accessed: Sept 2020, pp. 203.

Henriques, V.A.R., 2009. Titanium production for aerospace applications. *Journal of Aerospace Technology and Management*, 1(1), pp 7-17.

Hou, P., Zhao, H., Ma, Z., Zhang, S., Li, J., Dong, X., Sun, Y., and Zhu, Z., 2016. Influence of punch radius on elastic modulus of three-point bending tests. *Advances in Mechanical Engineering.* 8(5), pp. 1-8.

Hsu, C.C., Yongyut, A., Chao, C.K., and Lin, J., 2010. Notch sensitivity of titanium causing contradictory effects on locked nails and screws. *Medical Engineering and Physics*, 32(5), pp. 454-460.

Huff, R., and Wohlers, T., 2018. Wohlers Report 2018. AM continues rapid ascent targets new markets. Fort Collins, CO., Wohlers Associates,

Hung, N.N., 2011. Basic knowledge of bone graft. Intech. Available at: www.intechopen.com/books/bone-grafting/basicknowledge-of-bone-grafting, pp. 12-38. Accessed: July 2018.

Ilavarasi, P. U. and Anburajan, M., 2011. Design and finite element analysis of mandibular prosthesis, *3rd International Conference on Electronics Computer Technology*, Kanyakumari, 2011, pp. 325-329.

Iranmanesh, P., Abedian, A., Nasri, N., Ghasemi, E., and Khazaei, S., 2014. Stress analysis of different prosthesis materials in implant-supported fixed dental prosthesis using 3D finite element method. *Dental Hypotheses*, 5(3), pp. 109-114.

Järvinen J.P., Matilainen,V., Xiaoyun, L., Piili, H., Salminen, A., Mäkelä, I., and Nyrhilä, O., 2014. Characterization of effect of support structures in laser additive manufacturing of stainless steel. *Physics Procedia*, 56, pp. 72-81.

Javaid, M., and Haleem, A., 2018. Additive manufacturing applications in medical cases: A literature based review. *Alexandria Journal of Medicine*, 54, pp. 411–422.

Jayakumar, P., and Di Silvio, L., 2010. Osteoblast in bone tissue Engineering. *Proceedings of the Institution of Mechanical Engineers. Part H, Journal of Engineering in Medicine*, 224(12), pp. 1415-1440.

Jedrusik-Paw1owska, M., Kromka-Szydek, M., Katra, M., and Niedzielska, I., 2013. Mandibular reconstruction—biomechanical strength analysis (FEM) based on a retrospective clinical analysis of selected patients. *Acta of Bioengineering and Biomechanics*, 15(2), pp. 23-31.

Jíša D., Liškutín P., Kruml T., and Polák J., 2010. Small fatigue crack growth in aluminium alloy EN-AW 6082/T6. *International Journal of Fatigue*, 32 (12), pp. 1913-1920.

Kamath, C., El-dasher, B., Gallegos, G.F., King, W.E., and Sisto, A., 2013. Density of additively-manufactured, 316L SS parts using laser powder-bed fusion at powers up to 400 W. *Technical report.* Lawrence Livermore National Laboratory, pp. 1-19.

Kardys, G., 2017. Factors to consider when 3D printing or additive manufacturing metal parts. Engineering360, https://insights.globalspec.com/article/7447/factors-to-consider-when-3d-printing-or-additive-manufacturing-metal-parts.

Karlsson, J., Snis, A., Engqvist, H., and Lausmaa, J., 2013. Characterization and comparison of materials produced by Electron Beam Melting (EBM) of two different Ti-6Al-4V powder fractions. *Journal of Material Process Technology*, 213(12), pp. 2109-2118.

Karlsson, S., and Carlsson, G.E., 1990. Characteristics of mandibular masticatory movement in young and elderly dentate subjects. *Journal of Dental Research*, 69(2), pp. 473-476.

Kazantseva, N, Krakhmalev, P, Thuvander, M , et al., 2018. Martensitic transformations in Ti-6Al-4V (ELI) alloy manufactured by 3D printing. *Materials Characterization*, 146, pp. 101–112.

Kazantseva, N., Krakhmalev, P., Yadroitsev, I., Fefelov, Merkushev, A. A., Ilyinikh, M,. Vinogradova, N., Ezhov I., Kurennykh, T. 2017. Oxygen and nitrogen concentrations in the Ti-6Al-4V Alloy manufactured by direct metal laser sintering (DMLS) process. *Materials Letters*, 209, pp. 311-314.

Kijak, E., Margielewicz, J., Gaska, D., and Kijak, D.L., 2015. Identification of mastication organ muscle forces in the biocybernetic perspective. *Journal of Biomedicine and Biotechnology*, pp. 1-11.

Kiliaridis, S., 1995. Masticatory muscle influence on craniofacial growth. *Acta Odontologica Scandinavica*, 53(3), pp. 196-202.

Kim, J.H., and Park, Y.C., 2011. Evaluation of mandibular cortical bone thickness for placement of temporary anchorage devices (TADs). *The Korean Journal of Orthodontics*, 42(3), pp. 110-117.

King, W.E., Anderson, A.T., Ferencz, R.M., Hodge, N.E., Kamath, C., Khairallah, S.A., and Rubenchik, A.M., 2015. Laser powder bed fusion additive manufacturing of metals; physics, computational, and materials challenges. *Applied Physics Reviews 2*, 2(4), pp. 1-53.

Klinge, A., Becktor, K., Lindh, C., and Becktor, J.P., 2017. Craniofacial height in relation to cross-sectional maxillary and mandibular morphology. *Progress in Orthodontics*, 18(1), pp. 1-10.

Klocke, F., and Wagner, C., 2003. Coalescence behaviour of two metallic particles as base mechanism of selective laser sintering. *CIRP Annals-Manufacturing Technology*. 52(1), pp. 177-180.

Knowles, C.R., Becker, T.H., and Tait, R.B., 2012. *The effect of heat treatment on the residual stress levels within direct metal laser sintered Ti-6Al-4V as measured using the hole-drilling strain gauge method. Proceedings of the 13th International RAPDASA Conference, Sun City.*

Kokubo, T., 2008. Bioceramics and their clinical application. Woodhead Publishing, 784 p.

Koolstra, J.H., 2002. Dynamics of the human masticatory system. *Critical Reviews in Oral Biology & Medicine*, 13(4), pp. 366-376.

Koshy, J.C., Feldman, E.M., Chike-Obi, C.J., and Bullocks, J.M., 2010. Pearls of mandibular trauma management. *Seminars in Plastic Surgery*, 24(4), pp. 357-374.

Kouprianoff, D-P.R., 2017. *Non-destructive testing of the parts manufactured by direct metal laser sintering.* MEng, Central University of Technology, Free State, pp. 1-143.

Kurzynowski, T., Chlebus, E., Kuznicka, B., and Reiner, J., 2012. Parameters in selective laser melting for processing metallic powders. Proc. of SPIE LASE, 8239, *High power laser materials processing: lasers, beam delivery, diagnostics, and applications*; 2012, San Francisco, California, United States, 6 February 2012, p. 823914,

Leuders, S., Thone, M., Riemer, A., Niendorf, T., Troster, T., Richard, H.A., and Maier, H.J. 2013. On the mechanical behaviour of titanium alloy Ti6Al4V manufactured by selective laser melting: fatigue resistance and crack growth performance. *International Journal of Fatigue*, 48, pp. 300-307.

Levrini, L., Paracchini, L., Mangano, C., Pisani, L., and Caprioglio, A., 2015. Evaluation of biomechanical effects of interocclusal surfaces on the mandible. *South European Journal of Orthodontics and Dentofacial Research*, 2(2), pp. 27-34.

Leyens, C., and Peter, M., 2003. Titanium and titanium alloys: Fundamentals and applications. Wiley-VCH Verlag GmbH & Co. KGaA, pp. 1-497.

Li, A., Zhang, Z., Wang, D., and Yang, J., 2010. Optimization method to fabrication orientation of parts in fused deposition modeling rapid prototyping, *International Conference on Mechanic Automation and Control Engineering*, Wuhan, 2010, pp. 416-419.

Li, L., 2006. Repair of directionally solidified superalloy GTD-111 by laser-engineered net shaping. *Journal of Materials Science*, 41(23), pp. 7886-7893.

Liu, Y., 2013. Effects of mesh density on finite element analysis. *SAE Technical Papers 2*, pp. 8.

Loier, C., Thauvin, G., Hazotte, A., and Simon, A., 1985. Influence of deformation on the β→α+β transformation kinetics of Ti-6 wt.%Al-4 wt.%V alloy. *Journal of the Less Common Metals*, 108(2), pp. 295-312.

Lopez, T.T., Crosato, E.M., Benedicto, E.N., de Paiva, L.A.S., Silva, D.C.B., and Biazevic, M.G.H., 2017. Accuracy of mandibular measurements of sexual dimorphism using stabilizer equipment. *Brazilian Oral Research*, 31, pp. 1-11.

Levrini, L et al., 2015. Evaluation of biomechanical effect of interocclusal surface on the mandible. *South European Journal of Orthodontics and Dentofacial Research,* 2(2), pp. 27-34.

Lütjering, G., 1998. Influence of processing on microstructure and mechanical properties of (α+β) titanium alloys. *Material Science and Engineering A*, 243 (1–2), pp..32-45.

Lutjering, G., and Williams, J.C., 2007. Titanium. Springer-Verlag Berlin Heidelberg, second edition, 24 pp.

Malefane, L. B., du Preez, W. B.. Maringa M. and A. du Plessis, 2018. Tensile and high cycle fatigue properties of annealed Ti6Al4V (ELI) specimens produced by direct metal laser sintering. *South African Journal of Industrial Engineering,* 29, pp. 299-311.

Mandibular fracture, 2018. Available at: http://www.en.wikipedia.org/wiki/Mandibular_fracture. Accessed: July 2018.

Mariano, L.O.H., Sartori, E.A., Broilo, J.R., Shinkai, R.S., Corso, L., and Marczak, R.J., 2012. Stresses in implant-supported overdentures with bone resorption: A 3-D finite element analysis. *Revista Odonto Ciência*, 27(1), pp. 41-46.

Markad, N., 2014. Mandible fractures. https://www.slideshare.net/nsavenature/mandible-fracture-symposium-march13. Accessed: Nov 2018.

Mason, T.O., 2018. Ceramic composition and properties. Encyclopaedia Britannica. Available at: http://www.britannica.com/technology/titanium-processing#ref623448. Accessed: Nov 2018.

Masticatory force 2018. Available at: http://www.dent-wiki.com/dental_technology/muscles-of-mandibular-movement/. Accessed: July 2018.

Masticatory muscles. Dental technology, 2017. Available at: http://www.dent-wiki.com/dental_technology/masticatory-muscles/. Accessed: July 2018.

Matthew, I.R., 2007. Surgical aids to prosthodontics, including osseointegrated implants. *Oral and Maxillofacial Surgery*, chapter 11, Elsevier, pp. 145-165.

Matthew, J., and Donachie, J., 2001. Heat treating titanium and its alloys. *Heat treating progress*, pp. 47-57.

MatWeb., 2018. Titanium Ti-6Al-4V ELI (Grade 23), Annealed. Available at: http://www.matweb.com/search/datasheet.aspx?matguid=c4297fb8f1094da189732c224e3be1ed. Accessed: Jan 2019.

McCollough, C.H., 2018. CT scans: Are they safe? Mayo Clinic, Available at: http://www.mayoclinic.org/tests-procedures/ct-scan/expert-answers/ct-scans/faq-20057860. Accessed: Nov 2018.

ME EN 7960 – Precision machine design., 2018. Contact stresses and deformations. Available at: https://my.mech.utah.edu/~me7960/lectures/Topic7-ContactStressesAndDeformations.pdf. Accessed: Nov 2018, pp. 1-20.

Mec-Engineering., 2015. Hertz contact. Available at: https://www.mec-engineering-spreadsheets.com/documentation-area/hertz-contact/. Accessed: Nov 2018.

Mezzetta, J., 2016. Process-Property relationships of Ti6Al4V fabricated through selective laser melting. *Department of Mining and Materials Engineering*, pp. 1-73.

Mierzejewska, Z.A., Hudak, R., and Sidun, J., 2019. Mechanical properties and microstructure of DMLS Ti6Al4V alloy dedicated to biomedical applications. *Materials (Basel)*, 12(1), 176 p.

Miles, B.A., Goldstein, D.P., Gilbert, R.W., and Gullane, P.J. 2010. Mandible reconstruction. *Current Opinion in Otolaryngol & Head and Neck Surgery*, 18(4), pp. 317-322.

Milewski, G., and Kromka-Szydek, M., 2010. Podstawy biomechaniki stomatologicznej. *Politechnika Krakowska Krakow*, pp. 7-89.

Miodowska, J., Kromka-Szydek, M., Bielski, J., and Hedrusik-Pawlowska, M., 2016. Numerical analysis of the mandibular reconstruction with the use of autogenous bone graft and dental implants. *Technical Transaction Mechanics*, pp. 76-85.

Miodowska, J., Kromka-Szydek, M., Bielski, J., and Jedrusik-Pawlowska, M., 2016. Numerical analysis of the mandibular reconstruction with the use of autogenous bone graft and dental implants. *Technical Transactions Mechanics*, pp. 76-85.

Moghaddam, N.S., Jahadakbar, A., Amerinatanzi, A., Skoracki, R., Miller, M., Dean, D., and Elahinia, M., 2017. Fixation release and the bone bandaid: A new bone fixation device paradigm. *Bioengineering (Basel).* Mar; 4(1) 5, PMID: 28952484.

Monaheng, L.F., 2017. *Finite element analysis of a Ti6Al4V (ELI) medical implant produced through additive manufacturing*. MEng dissertation, Central University of Technology, Free State.

Morgan, E.F., Unnikrisnan, G.U., and Hussein, A.I., 2018. Bone mechanical properties in healthy and diseased states. *Annual Review of Biomedical Engineering*. 20, pp. 119-143.

Moylan, S.P., Slotwinski, J.A., Cooke, A.C., Jurrens, K., and Donmez, M.A., 2013. Lessons learned in establishing the NIST Metal Additive Manufacturing Laboratory, NIST Technical Note 1801, 40 p.

MTS, 2018 MTS Exceed Series 40 Electromechanical Universal Test Systems. Available at: https://www.mts.com/cs/groups/public/documents/library/mts_2011071.pdf. Accessed: July 2019.

Munsch, M., 2017. 15- Laser additive manufacturing of customized prosthetics and implants for biomedical applications. *Laser Additive Manufacturing*, pp. 399-420.

Murray, J.M., 2013. Mandible fractures and dental trauma. *Emergency Medicine Clinics of North America*, 31(2), pp. 553-573.

Muscle Enthesis. Muscle attachment to bone as an unrecognised cause of pain, Available at: http://www.enthesis.info/anatomy/muscle_and_enthesis.html. Accessed: July 2018.

Nanci, A., 2017. Ten Cate's Oral Histology - E-Book: Development. Structure, and Function, *Elsevier Health Sciences*, 352 p.

Neupane, D., 2014. *Comparison of some FEM codes in static analysis*. Bachelor thesis in Mechanical Engineering Production Technology, University of Applied Science HAMK, pp. 71.

Newby, E.B., 2018. *Investigation of in-situ alloying grade 23 Titanium with Copper by Selective Laser Melting process for biomedical applications*. MEng. dissertation, Central University of Technology, Free State.

Niinomi, M., 2003. Recent research and development in titanium alloys for biomedical applications and healthcare goods. *Science and Technology of Advanced Material*, 4(5), pp. 445-454.

Niinomi, M., Hattori, T., and Niwa, S., 2004. Material characteristics and biocompatibility of low ridigity titanium alloys for biomedical applications. *Biomaterials in Orthopedics*, chapter 2, pp. 41-62.

Niinomi, M., Liu, Y., Nakai, M., Liu, H., and Li, H., 2016. Biomedical titanium alloys with Young's moduli close to that of cortical bone. *Regenerative Biomaterials*, pp. 173-185.

Norton, M.R., and Gamble, C., 2001. Bone classification: an objective scale of bone density using the computerized tomography scan. *Clinical Oral Implants Research*, 12(1), pp. 79-84.

Norton, R., 2006. Machine Design. Upper Saddle River, N.J.: Pearson Prentice Hall, 3, pp. 905-962.

Nouri, A., Hodgson, P.D., and Wen, C., 2010. Biomimetic porous titanium scaffolds for orthopedic and dental applications. Mukherjee A. (Ed.). Biomimetics, learning from nature. Intech Open Access Publisher, (21), pp. 415-450.

Nyeah, C., 2016. Mandibular fractures. Education, Available at: http://www.slideshare.net/chaitanyeah/mandibular-fractures-61418814. Accessed: Nov, 2018.

O'Brien, F.J., 2011. Biomaterials & scaffolds for tissue engineering. *Materials Today*, 14(3), pp. 88-95.

Okazaki, Y., Rao, S., Tateishi, T., and Ito, Y., 1998. Cytocompatibility of various metal and development of new titanium alloys for medical implants. *Materials Science and Engineering: A*, 243(1), pp. 250-256.

Ozturk, C.N., Ozturk, C., Bozkurt, M., Uygur, H.S., Papay, F.A., and Zins, J.E., 2013. Dentition, bone loss, and the aging of the mandible. *Aesthetic Surgery Journal*, 33(7), pp. 967-974.

Pandula, V., 2011. What are masticatory forces. *B. D. S, Human Anatomy*\. Available at: https://www.juniordentist.com/what-are-masticatory-forces.html. Accessed: July 2018.

Passi, D., Malkunje, L., Atri, M., Chahal, D., Singh, T.K., and Goyal, J., 2017. Newer proposed classification of mandibular fractures: A critical review with recent updates. *Oral and Maxillofacial Surgery*, 7, pp. 314-318.

Pepicelli, A., Woods, M., and Briggs, C., 2005. The mandibular muscles and their importance in orthodontics: a contemporary review. *American Journal of Orthodontics and Dentofacial Orthopedics*. 128(6), pp. 774-780.

Phatak, A.M., and Pande, S.S., 2012. Optimum part orientation in rapid prototyping using genetic algorithm. *Journal of Manufacturing Systems*, 31(4), pp. 395-402.

Polishetty, A., Manoharan, V., Littlefair, G., and Sonavane, C., 2013. Machinability assessment of Ti-6Al-4V for aerospace applications. *ASME Early Career Technical Journal*, 7 p.

Polmear, I.J., 2006. *Light Alloys: From traditional alloys to nanocrystals*, Butterworth-Heinemann, Oxford, UK.

Polo-Corrales, L., Latorre-Esteves, M., and Ramirez-Vick, J.E., 2014. Scaffold design for bone regeneration. *Journal of Nanoscience and Nanotechnology*, 14(1), pp. 15-56.

Proffit, W.R., Fields, H.W., and Sarver, D.M., 2014. Contemporary orthodontics-E-Book, 5th edition. *Elsevier Health Science*, 768 p.

Qiu, C., Adkins, N.J.E., and Moataz, M.A., 2013. Microstructure and tensile properties of selectively laser-melted and of HIPed laser-melted Ti–6Al–4V. *Materials Science and Engineering. A*, 578, pp. 230-239.

Quirynen, M., Mraiwa, N., van Steenberghe, D., and Jacobs, R., 2003. Morphology and dimensions of the mandibular jaw bone in the interforaminal region in patients requiring implants in the distal areas. *Clinical Oral Implants Research*, 14(3), pp. 280-285.

Rack, H., and Qazi, J., 2006. Titanium alloys for biomedical applications. *Materials Science and Engineering: C*, 26(8), pp. 1269-1277.

Ramos, A., Completo, A., Relvas, C., Mesnard, M., and Simões, J.A., 2011. Straight, semi-anatomic and anatomic TMJ implants: the influence of condylar geometry and bone fixation screws. *Journal of Oral and Maxillofacial Surgery*, 39(5), 343-350.

Reade International Corp., 2018. Titanium metal (Ti)/sponge/titanium powder. Your speciality chemical resource. Available at: http://www.reade.com/products/titanium-metal-ti-sponge-titanium-powder. Accessed: Nov 2018.

SAE AMS 2801:2003 (R2014). Heat treatment of titanium alloy parts. Warrendale, PA 15096,

Sames, W.J., List, F.A., Pannala, S., Dehoff, R.R., and Babu, S.S., 2016.The metallurgy and processing science of metal additive manufacturing. *International Materials Review*, 61(5) pp. 315-360.

Santomaso, A., Lazzaro, P., and Canu, P., 2003. Powder flowability and density ratios: the impact of granules packing. *Chemical Engineering Science*, 58(13) pp 2857-2874.

Sato, M., Takakuwa, O., Nakai, M., Niinomi, M., Takeo, F., and Soyama, H., 2016. Using cavitation peening to improve the fatigue life of titanium alloy Ti-6Al-4V manufactured by electron beam melting. *Materials Sciences and Applications*, 7, pp. 181-191.

Sauvage, J.B., Aufray, M., Jeandrau, J.P., Chalandon, P., Poquillon, D., and Nardin, M., 2017. Using the 3-point bending method to study failure initiation in epoxide-aluminum joints. *International Journal of Adhesion and Adhesives*, 75, pp. 181-189.

Schank, C., 2018. Titanium metal: Titanium medical metal of choice. Supra alloys, Available at: http://www.supraalloys.com/medical-titanium.php. Accessed March 2018.

Schmidt, M., Merklein, M., Bourell, D., Dimitrov, D., Hausotte, T., Wegener, K., Overmeyer, L., Vollertsen, F., and Levy, G.N., 2017. Laser based additive manufacturing in industry and academia. *CIRP Annals - Manufacturing Technology*, 66, pp. 561-583.

Schnabel, T., Oettel, M., and Mueller, B., 2017. Design for additive manufacturing. Guidelines and case studies for metal applications. http://canadamakes.ca/wp-content/uploads/2017/05/2017-05-15_Industry-Canada_Design4AM_141283.pdf Accessed: Nov 2018.

Seagle, S.R., 2018. Titanium processing. Encyclopaedia Britannica. Available at: http://www.britannica.com/technology/titanium-processing#ref623448. Accessed: Nov 2018.

Semiatin, S.L., Seetharaman, V., and Weiss, I., 1997. The thermo mechanical processing of alpha/beta titanium alloys. *The Journal of the Minerals, Metals & Materials Society*, pp. 33.

Shademan, S., Sinha, V., Soboyejo, A.B.O., and Soboyejo, W.O., 2004. An investigation of the effects of microstructure and stress ratio on fatigue crack growth in Ti–6Al–4V with colony α/β microstructures. *Mechanics of Materials*, 36(1-2), pp. 161-175.

Shahlaie, M., Gantes, B., Schulz, E., Riggs, M., and Crigger, M,. 2003. Bone density assessments of dental implant sites: 1. Quantitative computed tomography. *The International Journal of Oral & Maxillofacial Implants*, 18(2), pp. 224-231.

Sharratt, B.M., 2015. Non-Destructive techniques and technologies for qualification of additive manufactured parts and processes, https://cradpdf.drdc-rddc.gc.ca/PDFS/unc200/p801800_A1b.pdf. Accessed: Nov 2018.

Shuaib, M., Javaid, M., Kumar, L., and Haleem, A., 2016. Using additive manufacturing for improving building services. International conference and exhibition on building utilities organized by Department of Mechanical Engineering, Faculty of Engineering and Technology. *Jamia Millia Islamia, New Delhi*, pp. 53-64.

Shunmugavela, M., Polishetty, A., and Littlefaira, G., 2015. Microstructure and mechanical properties of wrought and additive manufactured Ti-6Al-4V cylindrical bars. *Procedia Technology*. 20, pp. 231-236.

Sieniawski, J., Ziaja, W., Kubiak, K., and Motyka, M., 2013. *Microstructure and mechanical properties of high strength two phase titanium alloys.* Titanium Alloys – Advances in Properties Control, Chapter 4, pp. 70-80.

Simonelli, M., Tse, Y.Y., and Tuck, C., 2014. Effect of the build orientation on the mechanical properties and fracture modes of SLM Ti-6Al-4V. *Material Science and Engineering: A*, 616, pp. 1-11.

Singh, C., 2015. Basic morphology & internal structures of mandible. Education, pp. 1-42.

Slotwinski, J.A., and Garboczi, E.J., 2015. Metrology needs for metal additive manufacturing powders. *Journal of the Minerals, Metals & Materials Society (TMS)*, 67(3), pp. 538-543.

Slotwinski, J.A., Garboczi, E.J., Stutzman, P.E., Ferraris, C.F., Watson, S.S., and Peltz, M.A., 2014. Characterization of metal powders used for additive manufacturing. *Journal of Research of the National Institute of Standards and Technology*, 119, pp. 460-493.

Soyama H. and Okura Y., 2018. The use of various peening methods to improve the fatigue strength of titanium alloy Ti6Al4V manufactured by electron beam melting. *AIMS Materials Science,* 5, pp. 1000-1015.

Spears, T.G., and Gold, S.A., 2016. In-process sensing in selective laser melting (SLM) additive manufacturing. *Integrating Materials and Manufacturing Innovation*, 5(2), pp. 2-25.

Srinivas, K., 2017. Tips and tricks Vol 1. Advanced Scientific and Engineering Sciences, Available at: https://www.advanses.com/abaqus-tips-and-tricks-vol-1. Accessed: Nov 2019.

Stierman, K., 2000. Mandible fractures. Department of Otolaryngology, University of Texas Medical Branch, pp. 1-59.

Struers., 2015. Available at: https://www.struers.com/en/Knowledge/Materials/Titanium#main-characteristics. Accessed: Jan. 2020.

Su, X., and Yang, Y., 2012. Research on track overlapping during selective laser melting of powders. *Journal of Materials Processing Technology*, 212(10), pp. 2074-2079.

Sul, Y.T., Johansson, C.B., Petronis, S., Krozer, A., Jeong, Y., Wennerberg, A., and Albrektsson, T., 2002. Characteristics of the surface oxides on turned and electrochemically oxidized pure titanium implants up to dielectric breakdown: the oxide thickness, micropore configurations, surface roughness, crystal structure and chemical composition. *Biomaterials*, 23(2), pp. 491-501.

Tarsitano, A., Mazzoni, S., Cipriani, R., Scotti, R., Marchetti, C., and Ciocca, L., 2014. The CAD-CAM technique for mandibular reconstruction: An 18 patients oncological case-series. *Journal of Cranio-Maxillofacial Surgery*, 42(7), pp. 1460-1464.

Taylor, B., 2016, Tutorial – Hertz Contact Stress. Available at: www.wp.optics.arizona.edu/optomech/wp-content/uploads/sites/53/2016/12/Tutorial_Taylor_Brian.pdf. Accessed: Nov. 2018.

Tec-Science, 2018. Available at: www.tec-science.com/material-science/material-testing/bending-flexural-test/. Accessed: Dec. 2019.

Thieme, C., 2016. How to create a good quality FE Model. *Whitepaper*, pp. 1-13.

Thijs, L., Verhaeghe, F., Craeghs, T., van Humbeeck, J., and Kruth, J.P., 2010. A study of the microstructural evolution during selective laser melting of Ti-6Al-4V. *Acta Materialia*, 58(9), pp. 3303-3312.

Todorov, E., Spencer, R., Gleeson, S., Jamshidinia, M., and Kelly, S.M., 2014. Nondestructive evaluation (NDE) of complex metallic additive manufacturing (AM) structures, Project 1, America Makes: *National Additive Manufacturing Innovation Institute (NAMII)*, pp. 1-62.

Tolochko, N.K., Mozzharov, S.E., Yadroitsev, I.A., Laoui, T., Froyen, L., Titov, V.I. and Ignatiev, M.B., 2004. Balling processes during selective laser treatment of powders. *Rapid Prototyping Journal*, 10, pp. 78-87.

Townsend, V., and Urbanic, J., 2012. Relating additive and subtractive processes in a teleological and modular approach. *Rapid Prototyping Journal*, 18(4), pp. 324-338.

Trevisan, F., Calignano, F., Lorusso, M., Pakkanen, J., Aversa, A., Ambrosio, E.P., Lombardi, M., Fino, P., and Manfredi, D., 2017. On the selective laser melting (SLM) of the AlSi10Mg alloy: process, microstructure, and mechanical properties. *Materials*, 10, pp. 76.

Tunis, T.S., Sarig, R., Cohen, H., Medlej, B., Peled, N., and May, H., 2017. Sex estimation using computed tomography of the mandible. *International Journal of Legal Medicine*, 131(6), pp. 1691-1700.

van Eijden, T.M., Koolstra, J.H., and Brugman, P., 1996. Three-dimensional structure of the human temporalis muscle. *The Anatomical Record*, 246(4), pp. 565-572.

van Eijden, T.M.G.J., 2000. Biomechanics of the mandible. *Critical Reviews in Oral and Biology and Medicine*, 11(1), pp. 123-136.

van Gastel, S., 2016. *Printing by the rules. Towards design guidelines for additive manufacturing*, MIKRONIEK 5 2016, pp. 13-16.

van Zyl, I., 2016. Residual stress of Ti6Al4V (ELI) parts manufactured by direct metal laser sintering. MEng dissertation. *Central University of Technology*, *Free State* pp. 1-144.

van Zyl, O., and Fagan, J., 2017. Vascularised free fibular flaps (fff) in head and neck reconstruction. Open Access Atlas Of Otolaryngology, Head & Neck Operative Surgery, South Africa. Available at: http://www.entdev.uct.ac.za. 22 p. Accessed: March, 2018.

Vandenbroucke, B., and Kruth, J.P., 2007. Selective laser melting of biocompatible metals for rapid manufacturing of medical parts. *Rapid Prototyping Journal*, 13(4), pp. 96-203.

Vayre, B., Vignat, F., and Villeneuve, F., 2012. Metallic additive manufacturing: State-of-the-art review and prospects. *Mechanics & Industry*, 13, pp. 89-96.

Vitković, N., Mitić, J., Manić, M., Trajanović, M., Husain, K., Petrović, S., and Arsić. S., 2015. The parametric model of the human mandible coronoid process created by method of anatomical features. *Computational and Mathematical Methods in Medicine*, pp. 1-10.

Walton, B., Resto, V., Quinn, F.B., and Quinn, M. S., 2010. Mandibular reconstruction: Special considerations in TMJ and condyle reconstruction. The University of Texas Medical Branch, Department of Otolaryngology, pp. 1-9.

Wang, X., Xu, S., Zhou, S., Xu, W., Leary, M., Choong, P., Qian, M., Brandt, M., and Xie, Y.M., 2016. Topological design and additive manufacturing of porous metals for bone scaffolds and orthopaedic implants: *A review. Biomaterials*, pp 127-141.

Wang, Z., and Li, P., 2018. Characterisation and constitutive model of tensile properties of selective laser melted Ti-6Al-4V struts for microlattice structures. *Material Science and Engineering: A*, 725, pp. 350-358.

Watzek, G., and Ulm, C., 2002. Compromised alveolar bone quality in edentulous jaws. In: Zarb, G., Lekholm, U., Albrektsson, T., Tenenbaum, H., editors. Aging, osteoporosis, and dental implants. Chicago: Quintessence Publishing Co., Inc. pp. 67-84.

Weickenmeier, J., Jabareen, M., Le Révérend, B.J.D., Ramaioli, M., and Mazza, E., 2017. Experimental and numerical characterization of the mechanical masseter muscle response during biting. *Journal of Biomechanical Engineering*, 139(12), 10 p.

Wohlers Associates, What is Additive Manufacturing, Available at: http://www.wohlersassociates.com. Accessed: June 2018.

Wohlers, T., and Caffrey, T., 2016. Wohlers report 2016. 3D printing and additive manufacturing state of the industry. Annual world-wide progress report. Fort Collins, CO., Wohlers Associates.

Wohlers, T., and Gornet, T., 2014. Wohlers report 2014. History of additive manufacturing. Fort Collins, CO.,Wohlers Associates.

Wong, R.C., Tideman, H., Kin, L., and Merkx, M.A. 2010. Biomechanics of mandibular reconstruction: a review. *International Journal of Oral and Maxillofacial Surgery*, 39(4), pp. 313-319.

Wong, R.C.W., Tideman, H., Merkx, M.A.W., Jansen, J., Goh, S.M., and Liao, K., 2011. Review of biomechanical models used in studying the biomechanics of reconstructed mandibles. *International Journal of Oral & Maxillofacial Surgery*, 40, pp. 393-400.

Wu, S., Kay, M., King, R., Vila-Parrish, A., and Warsing, D., 2014. Multi-objective optimization of 3d packing problem in additive manufacturing. *In: Guan Y., Liao H., editors. Industrial and Systems Engineering Research Conference; Montréal, Institute of Industrial and Systems Engineers (IISE), Canada (2014).*

Wycisk, E., Solbach, A., Siddique, S., Herzog, D., Walther, F., and Emmelmann, C., 2014. Effects of defects in laser additive manufactured Ti-6Al-4V on fatigue properties. *Physics Procedia*, 56, pp. 371-378.

Yadroitsava, I., Grewar, S., Hattingh, D., and Yadroitsev, I., 2015. Residual stress in SLM Ti6Al4V alloy specimens.*Materials Science Forum*, vol. 828-829, Trans Tech Publications, Ltd. pp. 305-310.

Yadroitsev, I., 2009. *Selective laser melting: Direct manufacturing of 3D-objects by melting of metal powders*. Saarbrucken: LAP Lambert Academic Publishing AG & Co. KG; 307 p.

Yadroitsev, I., and Smurov, I., 2010. Selective laser melting technology: from the single laser melted track stability to 3D parts of complex shape. *Physics Procedia 5*, pp. 551-560.

Yadroitsev, I., and Yadroitsava, I., 2015b. Evaluation of residual stress in stainless steel 316L and Ti6Al4V samples produced by selective laser melting, *Virtual and Physical Prototyping*, 10(2), pp. 67-76.

Yadroitsev, I., Krakhmalev, P., and Yadroitsava, I., 2015a. Hierarchical design principles of selective laser melting for high quality metallic objects. *Additive Manufacturing*, 7, pp. 45-56.

Yadroitsev, I., Krakhmalev, P., Yadroitsava I., and du Plessis, A., 2018. Qualification of Ti6Al4V ELI alloy produced by laser powder bed fusion for biomedical applications. *The Journal of the Minerals, Metals & Materials Society (TMS)*, 70 (3), pp. 372-377.

Yadroitsev, I., Krakhmalev, P., Yadroitsava, I., and du Plessis, A., 2017. Qualification of Ti6Al4V ELI alloy produced by laser powder bed fusion for biomedical applications. *SSF 2017-The 28th Annual International Solid Freeform Fabrication Symposium-An Additive Manufacturing Conference*, Austin, Texas, August 7-9, 2017.

Yang, Y., 2015. Investigation of the martensitic transformation and the deformation mechanisms occurring in the superelastic Ti-24Nb-4Zr-8Sn alloy. *Material Chemistry*, pp. 1-153.

Yasa, E., Deckers, J., and Kruth, J-P., 2011. The investigation of the influence of laser re-melting on density, surface quality and microstructure of selective laser melting parts. *Rapid Prototyping Journal*, 17, pp. 312-27.

Zebrowski, R., Walczak, M., Korga, A., Iwan, M., and Szala, M., 2019. Effect of shot peening on the mechanical properties and cytotoxicity behaviour of titanium implants produced by 3D printing technology. *Journal of Healthcare Engineering*, 8169538. https://doi.org/10.1155/2019/8169538.

Zhang, Y., and Bernard, A., 2014. An integrated decision-making model for multi-attributes decision-making (MADM) problems in additive manufacturing process planning. *Rapid Prototyping Journal*, 20(5), pp. 377-389.

Zhao, C., Fezzaa, K., Cunningham, R.W., Wen, H., De Carlo, F., Chen, L., Rollett, A.D., and Sun, T., 2017. Real-time monitoring of laser powder bed fusion process using high-speed X-ray imaging and diffraction. *Scientific Reports 7*, 3602.

Zhao, X.M., Chen, J., Lin, X., and Huang, W.D., 2008. Study on microstructure and mechanical properties of laser rapid forming Inconel 718. *Material Science and Engineering: A*, 478(1–2) pp. 119-124.

Ziółkowski, G., Chlebus, E., Szymczyk, P., and Kurzac, J., 2014. Application of X-ray CT method for discontinuity and porosity detection in 316L stainless steel parts produced with SLM technology. *Archives of Civil and Mechanical Engineering*, 14(4), pp. 608-614.

Zou, R., Xia, Y., Liu, S., Hu, P., Hou, W., Hu, Q., and Shan, C., 2016. Isotropic and anisotropic elasticity and yielding of 3D printed material. *Composites Part B: Engineering, 99*, pp. 506-513.

APPENDIX

APPENDIX 1: Mathematical calculations

A1.1. Second moment of area

Calculating the second moment of area for a beam perpendicular to the applied load viewing the cross-sectional area at the applied boundary load (Figure 94).

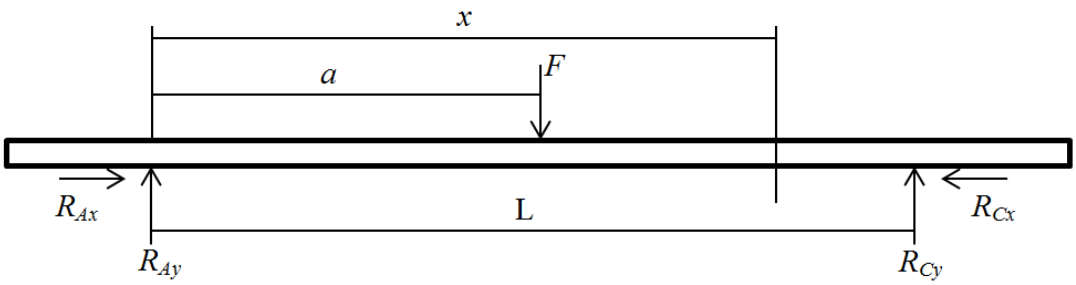

(a)

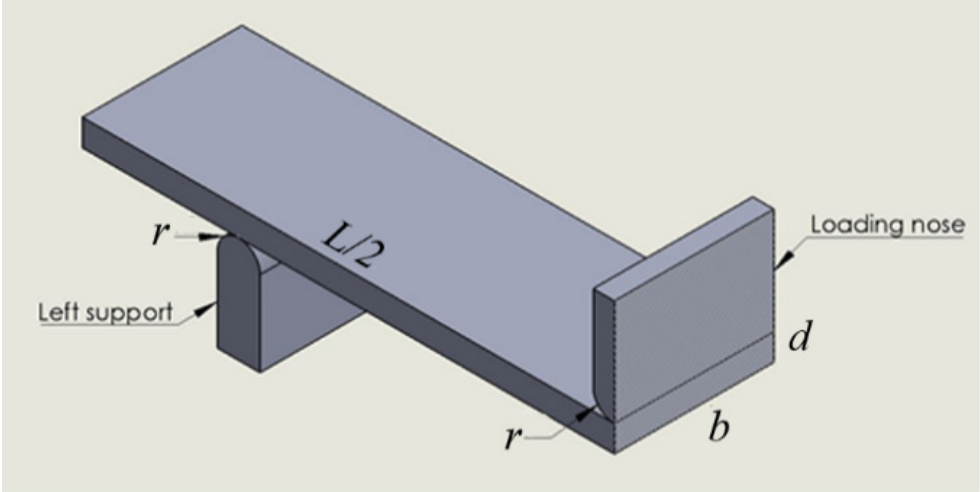

(b)

Figure 94: Free body diagram of a Ti6Al4V beam (a) and cross-sectional area view at applied boundary load (b).)

According to the loading direction the second moment of area I_x can be calculated (Figure 94a).

$$I_x = \frac{b \times d^3}{12} \qquad \textbf{Equation 1}$$

where b is width of the beam and d is the thickness.

A1.2. Maximum slope and deflection

The point of maximum deflection on the beam is obtained by setting the equation for slope (θ) to zero as this is also the point of zero slope. The point of maximum deflection (y_{max}) will occur between mid-span and the point of application of the point load (Figure 94). If we consider upwards and clockwise as positive, downwards and anti-clockwise as negative, then moments about point A can be as follows (Drotsky, 2011). Applying the principle of Static Equilibrium of moments about any point along a beam span:

$$\sum F_x = 0 = R_{ax} \qquad \textbf{Equation 2}$$

$$\sum F_y = 0 = F - \left(R_{Ay} + R_{Cy}\right) \qquad \textbf{Equation 3}$$

$$\sum F_{Az} = 0 = F\left(\frac{L}{2}\right) - R_{Cy} \times L \qquad \textbf{Equation 4}$$

$$R_{Cy} = \frac{F}{2}$$

from Equation 3

$$0 = F - \left(R_{Ay} + R_{Cy}\right), \qquad \textbf{Equation 5}$$

$$\text{so } R_{Ay} = F - R_{Cy}$$

The effect of the reaction force (R_{Ay}) at the point of support (A) is to create a sagging bending moment about the arbitrary cross-section located a distance (x) from the left end. Moreover, the effect of the applied load (F) is to create a hogging bending moment about the arbitrary cross-section located a distance (x) from the left end. The bending moment (M_x) at a distance (x) from the left end of the simply supported beam, that is located on the right half of the beam, is a combination of the effects of these two point loads and is equal to:

$$M_x = EI\frac{d^2y}{dx^2} = R_{Ay} \times x - F[x - a]$$

$$[x - a] = 0, for\ (x - a) < 0$$

$$[x - a]\ remains\ for\ (x - a) \geq 0$$

Integrating the foregoing equation twice with respect to the parameter (x) generates the following respective equations for slope and deflection of the loaded beam. The bending moments using Macaulay's Method, if L and x represents the total length of the beam,

$a = \frac{L}{2}$, and $R_{Ay} = \frac{F}{2}$

$$EI\frac{d^2y}{dx^2} = R_{Ay} \times x - F[x-a]$$

$$EI\frac{dy}{dx} = \frac{R_{Ay}}{2} \times x^2 - \frac{F}{2}[x-a]^2 + A \qquad \textbf{Equation 6}$$

$$EIy = \frac{R_{Ay}}{6} \times x^3 - \frac{F}{6}[x-a]^3 + Ax + B \qquad \textbf{Equation 7}$$

The values of the integration constants (A and B) were obtained by introducing boundary conditions into Equation 6 and Equation 7.

from Equation 6

$$EI\frac{dx}{dy}\Big|_{x=\frac{L}{2}} = 0 = \frac{R_{Ay}}{2} \times x^2 - \frac{F}{2}[x-a]^2 + A$$

$$EI\frac{dx}{dy}\Big|_{x=\frac{L}{2}} = 0 = \frac{F}{4} \times x^2 - \frac{F}{2}[x-a]^2 + A$$

$$0 = \frac{F}{4} \times \left(\frac{L}{2}\right)^2 - \frac{F}{2}\left[\frac{L}{2} - \frac{L}{2}\right]^2 + A$$

$$A = -\frac{FL^2}{16}$$

from Equation 7

$$EIy = \frac{R_{Ay}}{6} \times x^3 - \frac{F}{6}[x-a]^3 + Ax + B$$

$$EIy|_{x=0} = 0 = \frac{F}{12} \times x^3 - \frac{F}{6}[x-a]^3 + Ax + B \qquad \textbf{Equation 8}$$

$$0 = \frac{F}{12} \times (0)^3 - \frac{F}{2}[0]^3 + A(0) + B$$

$$B = 0$$

The point of maximum slope on the beam is determined by setting the differential $\left(\frac{d^2y}{dx^2}\right)$ to zero, noting that this is the equation for the Bending Moment, and then solving for the distance (x) along the length of the beam, thus:

$$EIy|_{x=\frac{L}{2}} = \frac{R_{Ay}}{6} \times x^3 - \frac{F}{6}[x-a]^3 + Ax + B$$

$$EIy|_{x=\frac{L}{2}} = \frac{F}{12} \times x^3 - \frac{F}{6}[x-a]^3 - \frac{FL^2}{16} \times x + 0$$

$$EIy = \frac{F}{12} \times \left(\frac{L}{2}\right)^3 - \frac{F}{6}\left[\frac{L}{2} - \frac{L}{2}\right]^3 - \frac{FL^2}{16} \times \frac{L}{2} + 0$$

$$y|_{MAX} = -\frac{FL^3}{48EI} \qquad \textbf{Equation 9}$$

$$EI\frac{dx}{dy}\Big|_{x=0} = \frac{R_{Ay}}{2} \times x^2 - \frac{F}{2}[x-a]^2 + A$$

$$EI\frac{dx}{dy}\Big|_{x=0} = \frac{F}{4} \times x^2 - \frac{F}{2}[x-a]^2 - \frac{FL^2}{16}$$

$$EI\frac{dy}{dx} = \frac{F}{4} \times (0)^2 - \frac{F}{2}[0]^2 - \frac{FL^2}{16}$$

$$\theta|_{MAX} = -\frac{FL^2}{16EI}\text{, then if } x = L \qquad \textbf{Equation 10}$$

A1.3. Contact modulus and contact area

The contact modulus represents two different materials that are coming in contact.

$$E^* = \left(\frac{1-{\nu_1}^2}{E_1} + \frac{1-{\nu_2}^2}{E_2}\right) \qquad \textbf{Equation 11}$$

For the contact area, references from various authors were taken into account: (Mec-Engineering 2015; Taylor, 2016; ME EN 7960–Precision machine design 2018), all have different methods of calculating the contact area of a cylinder on a flat plate.

For a cylinder pressed against a plane surface, the contact surface is a line (Figure 94).

$$\frac{1}{r} = \frac{1}{r_{Cylinder}} + \frac{1}{r_{Flat}}$$

A flat plate is defined as a cylinder with an infinitely large radius, thus

$r_{\_Flat}=\infty$ *and* $\frac{1}{r}=\frac{1}{r_{cylinder}}$

A contact area is defined as

$$b_{contact}=\sqrt{\frac{4\times F\times E^{*}}{\pi\times b\times R}} \qquad \textbf{Equation 12}$$

The contact stress is the ratio of the normal load to the true contact area:

$$P_{Max}=\frac{2\times F}{\pi\times b_{contact}\times b} \qquad \textbf{Equation 13}$$

A1.4. Calculations by experimental load-crosshead results

Modulus of elasticity in bending E_B can be calculated from the load – crosshead data:

$$E_B=\frac{L^3 m}{4bd^3} \text{ if } m=\frac{y_2-y_1}{x_2-x_1} \qquad \textbf{Equation 14}$$

where L is span length, m is slope of the tangent, b – beam width; d – beam thickness

A maximum bending (flexural) stress σ_f and (flexural) strain ε_f

$$\sigma_f=\frac{3FL}{2bd^2} \qquad \textbf{Equation 15}$$

$$\epsilon_f=\frac{6Dd}{L^2} \qquad \textbf{Equation 16}$$

where F is downwards force and D is deflection of the centreline of the specimen at the middle of the support span.

APPENDIX 2: Preliminary tests for aluminium results.

2.1 Three-point bending MTS load-crosshead results for Set A

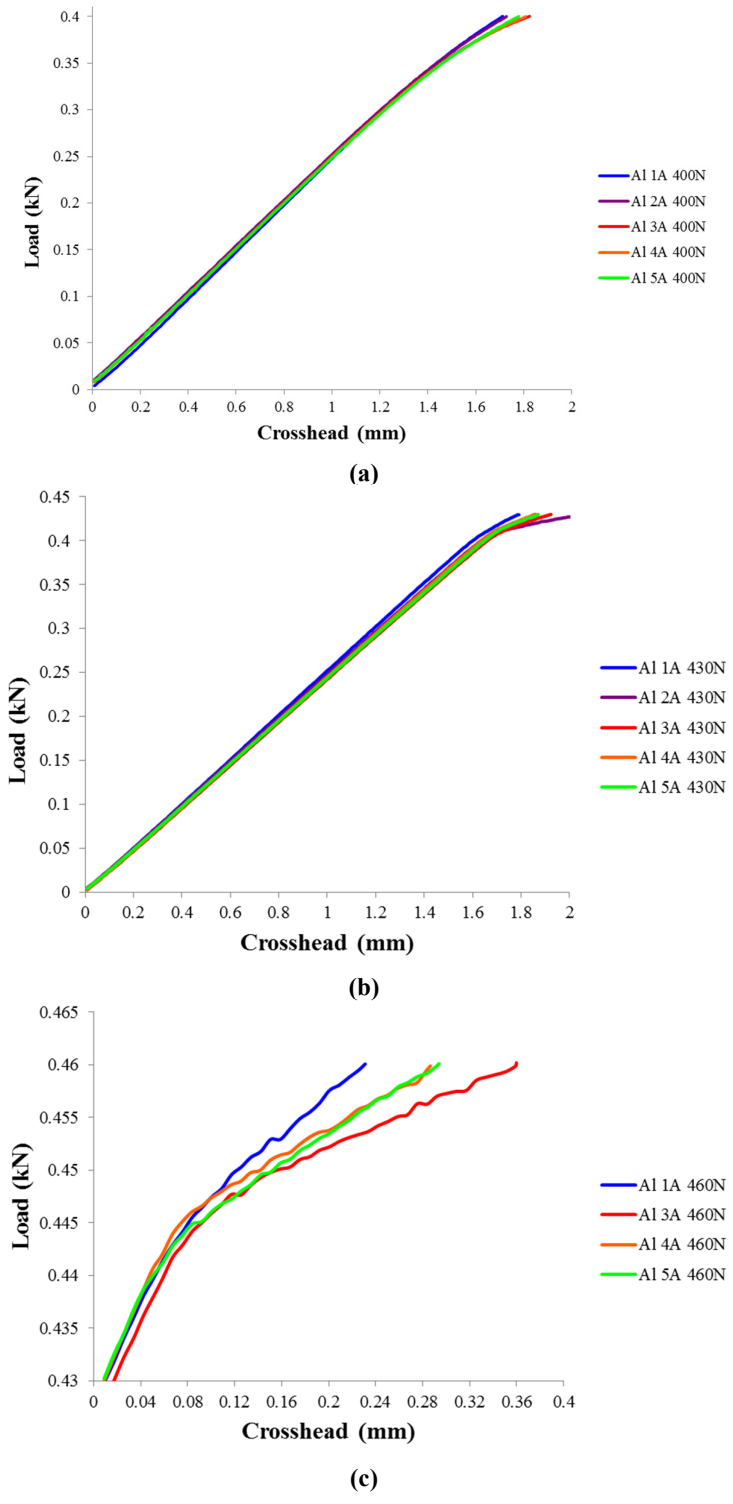

Figure 95: Load-displacement curve for Set 1 at 400 N (a), 430 (b) and 460 N load (c).
Sample Al 2A is not included as it had already reached catastrophic failure before the load increased to 460 N.

2.2 Load-displacement curve for solid Al sample 1B

Experimental:

Limiting sample 1B within the elastic range range before yielding the experimental elastic modulus through the use of the slope by substituting (x;y) values using Figure 96 and Equation 14:

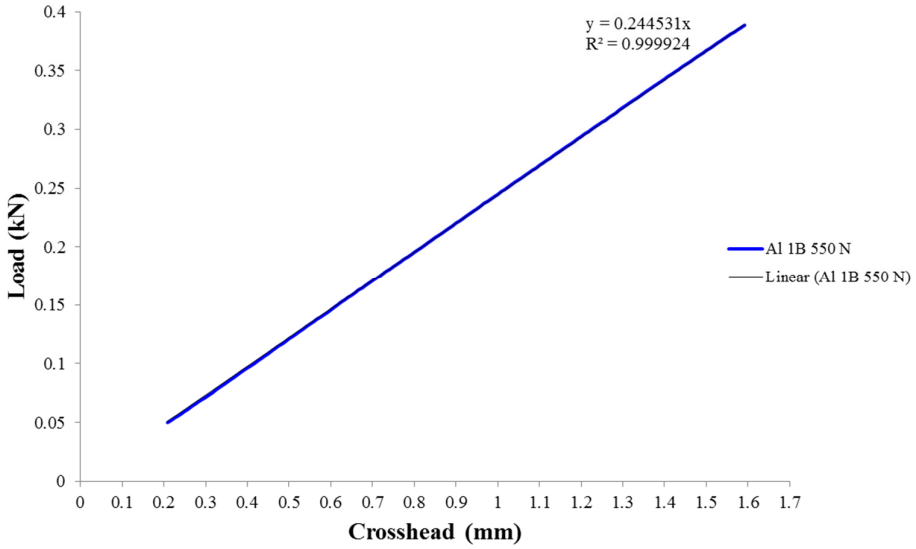

Figure 96: Experimental Al 1B 550 N MTS bending load-crosshead data.

$$m = \frac{y_2 - y_1}{x_2 - x_1} \text{ (for AL 1B)} \qquad E_B = \frac{L^3 m}{4bd^3}$$

$$= 0.244487 \text{ kN/mm} \qquad = 56.3 \text{ GPa}$$

Theoretical:

Coordinates (x;y) for two independent points on the load-crosshead line graph (Figure 97) within the elastic range, the experimental elastic modulus can be calculated using Equation 14:

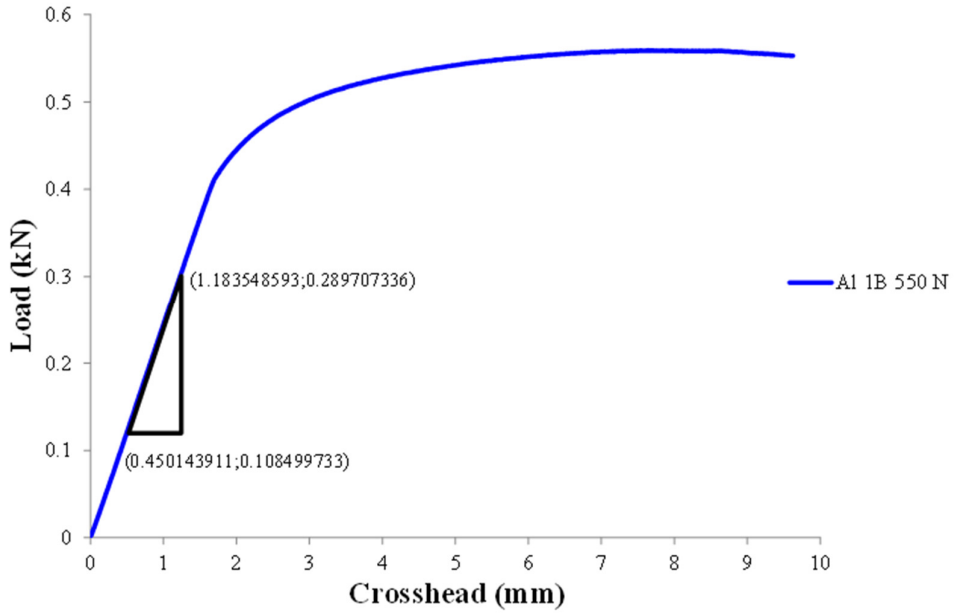

Figure 97: Theoretical Al 1B 550 N MTS data.

$m = \frac{y_2 - y_1}{x_2 - x_1}$ (for AL 1B)

$= 0.247077$ kN/mm

$E_B = \frac{L^3 m}{4bd^3}$

$= 56.9$ GPa

APPENDIX 3: Roughness of the top surface of LPBF Ti6Al4V ELI sample

As-built		Shot peened	
Ra, µm	Rz, µm	Ra, µm	Rz, µm
19.2	107.1	6.0	35.6
18.5	104.7	4.9	29.9
21.4	113.3	6.1	38.6
17.4	92.4	6.5	38.5
18.6	112.5	5.0	30.5
21.0	118.6	4.7	30.6
16.7	100.4	6.2	36.2
15.6	91.2	6.8	41.9
15.9	93.6	5.3	33.1
17.8	101.8	4.5	26.2
18.3	104.1	5.1	34.0
15.3	88.7	5.1	29.4
Average value ± Standard deviation			
18±2.0	102±9.6	5±0.8	34±4.8

APPENDIX 4: Load-displacement curve for Ti6Al4V ELI reference sample

Experimental:

By limiting the data for the RS 2 (Figure 98) sample to view a straight line within the elastic range. The experimental elastic modulus can then be calculated:

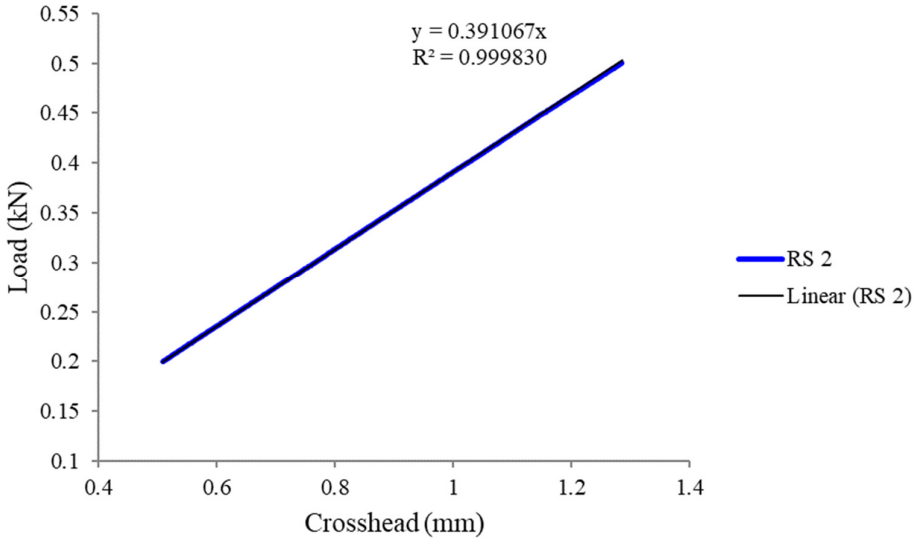

Figure 98: MTS bending slope calculation.

$m = \frac{y_2 - y_1}{x_2 - x_1}$ (for AL 1B)

$= 0.391067$ kN/mm

$E_B = \frac{L^3 m}{4bd^3}$

$= 90.1$ GPa

Theoretical:

Introducing (x;y) coordinates for two independent points on the load-crosshead line graph (Figure 99) within the elastic range, the experimental elastic modulus using Equation 14 can be calculated:

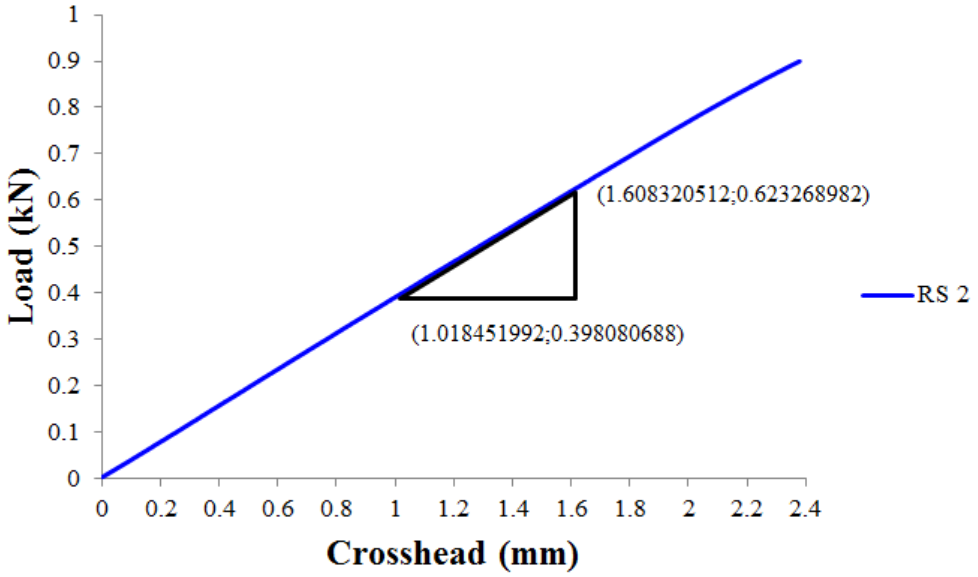

Figure 99: Calculations of flexural modulus by crosshead.

$m = \frac{y_2 - y_1}{x_2 - x_1}$ (for AL 1B)

$= 0.38176\ \text{kN/mm}$

$E_B = \frac{L^3 m}{4bd^3}$

$= 88.0\ \text{GPa}$

APPENDIX 5:

Laser powder bed fusion process defects and mechanical properties of Ti6Al4V ELI mandible implants

Wessels, J., du Plessis, A., Els, J., Yadroitsava, I., Yadroitsev, I.

In Proc. RAPDASA 19th International Conference "Additive Manufacturing as a key driver of the 4th Industrial Revolution", Resolution Circle Towers, Johannesburg, South Africa, November 6-9, 2018

ABSTRACT

Ensuring additive manufactured metal based components are free of major defects is crucial to fulfil medical requirements for clinical applications. Random porosity, high surface roughness and deformation during processing are the main current drawbacks in laser powder bed fusion parts. The prediction of defective samples' mechanical properties with numerical simulations is highly important to understand the effect of these defects. A step-by-step systematic approach of determining defects in laser powder bed fusion (LPBF) and their influence on mechanical properties will be used for the current research. This paper presents the first successful steps in this project.

1. INTRODUCTION

The need for new implant, treatments and prosthesis as well as prolonging the life span of current implants has increased, and has brought a robust change in people's quality of life [Khan, 2014]. Additive manufacturing of metals is growing steadily, and offers exciting possibilities for future development - producing parts with higher complexity with many applications including medical and aerospace [du Plessis, 2016a; Dunbar, 2016]. The endoprosthesis replacement of the lower jaw with an artificial implant is typically performed in the case of traumatic gunshot injuries, or when a large section of bone was destroyed by a chronic infection, when malignant neoplasms developed, and also in connection with osteomyelitis lesions. The clinical goal for mandibular implants is to serve as a replacement or anchor for muscle and mastication loading, which recreates the skeleton's original stress-strain trajectories. The mandible is the only movable stress bearing bone in the face and reconstruction of mandibular defects should restore the anatomical height and contour of the resected mandible. Ti6Al4V alloy is one of the most suitable materials of choice for such

implants, due to its incredible strength, low weight ratio, outstanding corrosion resistance and biocompatibility.

Quality control in metal based additive manufacturing is extremely important for effective control of dimensional inaccuracy, porosity and other defects that arise during the process [du Plessis, 2016b]. Grain morphology and texture of any part produced in laser powder bed fusion (LPBF) are strongly affected by the solidification rate, rapid cooling, and cyclic re-heating and cooling from adjacent tracks and subsequent layers. The inconsistency of the thermal processing throughout the part arises imprecisions from a variety of factors, including scan strategies, processing conditions, and geometric effects such as the reduced ability to conduct heat away from the melt pool when creating overhangs [Dunbar, 2016; Zhao, 2017;Yadroitsev, 2018]. Special microstructure and high residual stress are peculiarities of LPBF material that influence its mechanical properties. Also consecutive layer by layer delivering of powder particles sometimes tends to clump together causing inhomogenous powder layers, which result in unmelted areas and pores in the final product. Inappropriate selection of LPBF process parameters, scanning and manufacturing strategies of complex objects can lead to fractures, warps, and pores. CT scanning has previously been used for defect analysis of LPBF parts and it is clear that imperfections such as pores, etc., are prevalent in this process [du Plessis, 2018; du Plessis, 2016b].

1.1. Biomechanics of mandible

During mastication the following muscles serve in the movement of the mandible: masseter muscle, temporal muscle, medial pterygoid muscle, lateral pterygoid muscle, and buccinator muscle (Fig.1) [Emin, 2018; Kober, 2004; Ingawalé, 2012]. The mandible is the only movable stress bearing bone of the face, and disregarding the forces acting on the mandible can lead to reconstruction failure [Wong, 2011]. Loadings and bone properties are factors that have to be taken into account for modelling of mastication. For numerical simulations, during a mastication cycle the directions of the forces exerted by the jaw closing muscle can be assumed as uniform, due to the fibres running approximately parallel close to the insertion to the mandible; constant through the cycle, according to the small amplitude motion of their insertion points (Fig. 1) [Commisson, 2015].

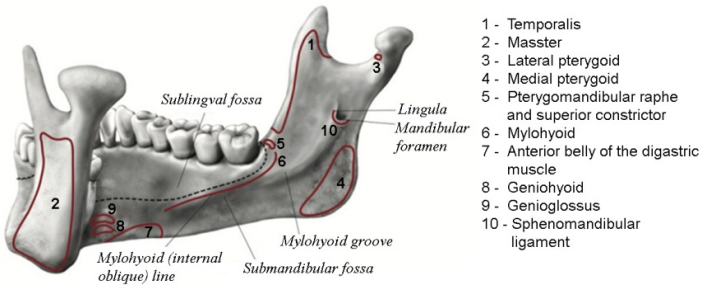

(a)

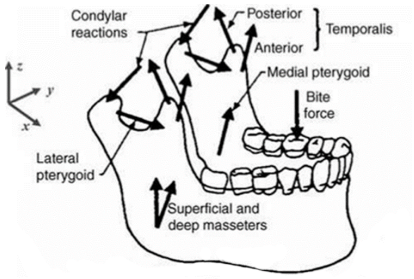

(b)

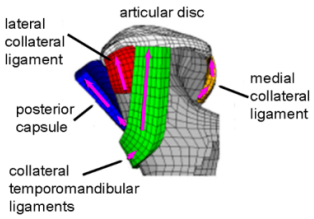

(c)

Fig. 1: Mandibular bone with respective muscle attachment (Posterolateral view) (a); typical loading forces, boundary conditions, and force vectors during mastication [Faulkne, 1987] (b) and forces working on the temporomandibular joint during mastication [Commisson, 2015] (c).

For numerical simulations, cortical bone material properties can be considered orthotropic in different anatomic regions of the mandibular bone, cancellous bone and reconstruction plates and screw can be defined as isentropic independent of directions. Loads can be applied to the five principal muscles (Table 1). Material properties of different bones found in the human mandible are shown in Table 2. Thus, typical mechanical properties of different areas of mandible and response of human mandible (strains and loadings) can be found in the literature.

Table 1: Muscular load action [Ramos, 2011]

Muscle action	Load (N)		
	X	Y	Z
Deep masseter	7.776	127.23	22.68
Superficial masseter	12.873	183.5	12.11
Medial pterygoid	140.38	237.8	-77.3
Temporalis	0.064	0.37	-0.13
Medial temporal	0.97	5.68	-7.44

Table 2: Material properties of different bone found in the human mandible [Vajgel, 2013]

Material property	Cortical bone			Cancellous bone
	Symphysis	Body	Angle	
Elastic Modulus, Ex (MPa)	20,492	21,728	24,607	1,500
Elastic Modulus, Ey (MPa)	12,092	12,700	12,971	1,500
Elastic Modulus Ez(MPa)	16,350	17,828	18,357	1,500
Poisson's ratio, Pxy	0.43	0.45	0.38	0.3
Poisson's ratio, Pyz	0.22	0.2	0.23	0.3
Poisson's ratio, Pxz	0.34	0.34	0.28	0.3

1.2. Mandible reconstruction by LPBF

Additive Manufacturing (AM) makes the manufacturing of any given design possible regardless the geometric complexity and allows the production of integrated components. This is extremely important towards the design of revolutionary shapes and lighter parts without the need to consider manufacturing constrains related to machining, moulding, etc. The production in AM does not need any special tooling, thus, making it easy and immediate to manufacture complex objects with various changes in geometry such as customised implants (Fig. 2).

AM mandible reconstructions begins from a CT scan of the patient of the diagnosed area; the CT scan is then converted to a 3D virtual and physical model (Fig. 2a, c and e). The result of this 3D model is used as an input to plan the resection planes and design of a cutting guide that allows surgeons to precisely cut around the tumor/ affected area without fault. A titanium alloy implant is designed to replace the affected area of the mandible (Fig. 2 b, d and f) to fit the required geometry in order to restore facial symmetry and to allow quick recovery.

In some author's expert opinion, a single screw in the anterior segment (Fig. 1a) may not prevent rotation, leading to implant failure (Mommaerts, 2016). Loading and contact boundary conditions are described by three main muscular forces during chewing operation; masseter, medial pterygoid, and temporalis. Each person's physique and bone structure differ from others which means the chewing load can vary in both magnitude and direction. Parameters to evaluate the design is the flexibility of the reconstructive implant, that is, the capability to absorb the chewing load, and the stress and strain distribution, ensuring the maximum stresses developed are lower when compared to the yield strength of Ti6AI4V ELI (Al-Ahmari, A, et al. 2015). Thus, at present implants are designed to withstand forces of 700N with a safety factor of two.

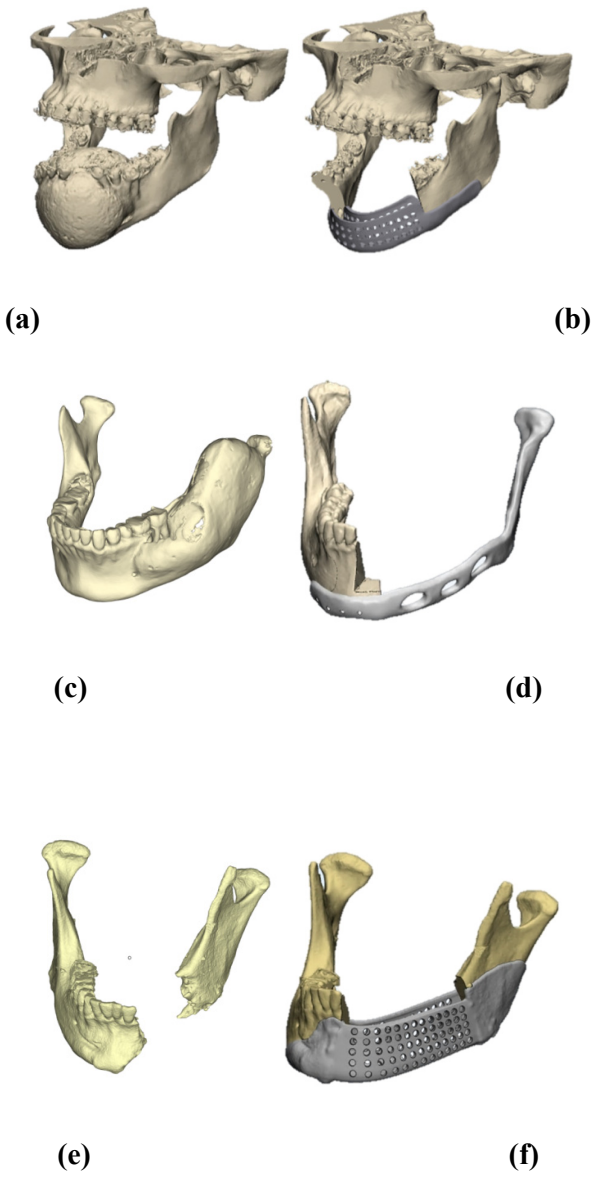

Fig.2: Design steps followed for reconstructing mandibular implants: 3D reconstructed CT scan of mandibular effected area (a,c and e); 3D rendering of designed titanium implant, (b, d and f).

A scaffolding is useful where there is bony contact, the friction provides primary stability as with any screw-fixed plate (Cordey, J, et al. 2000). Scaffolding (Fig. 2b, d, f) increases the overall elasticity to more closely approximate that of bone (Lin, C.Y, et al. 2004) and therefore reduce stress shielding and permanent loosening of an implant fixed to the weight-bearing mandible, and allows an easy method for weight reduction (Mommaerts, M.Y. 2016). In the present cases, implant thickness was 2 mm.

2. METHODOLOGY AND RESULTS

2.1. Methodology

Spatial distribution, size and shape of the defects of AM parts can be done by microCT to predict the effect of the pores on the mechanical properties of the part (du Plessis et al., 2017; Weiler et al., 2005). Vanderesse et al. (2011) and Nicoletto et al. (2010) used microCT in combination with FEA to highlight stress regions and correlate fatigue cracks with pores and their stress regions in aluminium castings. du Plessis et al. (2017) simulated static loads directly on CT scans voxel data. It was shown that combination of spatial data of pore's geometry and their locations is very suitable to predict the effect of the pores on the performance of the part. Failure location prediction by FEA for LPBF mandible implant could serve as a tool for optimizing the design of mandible implants as well as for quality control of produced implants having some porosity or other differences from the CAD model.

Main stages of the present study have to be mentioned:

- investigation of biomechanics and numerical simulations on human mandible functioning;
- analysis of stresses and critical points for different types of mandibular reconstruction;
- analysis of porosity in LPBF parts on the basis of CRPM's experience and literature sources;
- production and testing AM Ti6AL4V ELI samples with prescribed sizes, loadings, directions and porosity;
- numerical simulations and validation data compiled from numerical simulation with mechanical testing of LPBF samples after heat treatment.

Thus, test samples with defects and without defects will be manufactured by LPBF. The test samples will have geometrical characteristics similar to the mandible and mechanical testing will be done according mastication loadings.

2.2. Porosity in LPBF parts

In [Yadroitsev, 2018] LPBF Ti6Al4V ELI tensile samples were analysed by CT scans in as-built condition. It was found that maximum pore size was 132 µm for horizontal sample and 96 µm for vertical one (Fig. 3). The pores were randomly distributed throughout the volume. Although a statistically significant difference was found in the pore sizes for these samples, it can be stated that the porosity of the objects was insignificant: the estimated porosities were

0.0004% for vertical samples and 0.0018% for horizontal ones. The mechanical properties of the horizontal and vertical samples did not differ significantly. It should be mentioned how these samples were produced and analysed: 1) rectangular bars 10×10×60 mm were manufactured in horizontal and vertical directions; 2) round specimens with threaded ends were machined from bars accordingly to the geometry recommended by ASTM E8M standard (gauge length four times the diameter); 3) microCT scans were made for gages 4 mm in diameter and 20 mm in length.

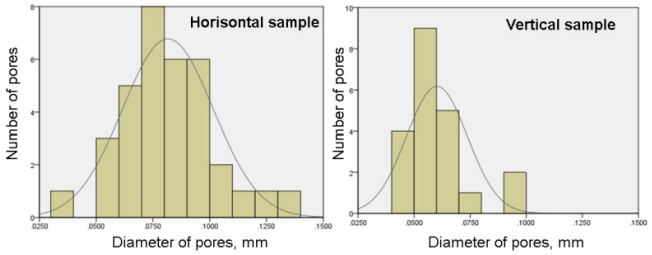

Fig. 3: Diameter of the pores measured by microCT scans in tensile samples.

In the presented study, for Ti6Al4V (ELI) samples density measured by microCT scans, was more than 99.99% (for pores >30 μm). It was found that the biggest pores were predominantly elongated in shape and can be considered as interlayer pores. Defects in LPBF are caused due to melt pool discontinuities and lack of melt pool overlapping. If the laser output is stable with prescribed scanning speed and power, with prescribed optimal scanning strategy, all voids are likely resulting from inhomogeneity in the powder layer. This inhomogeneity can be caused, in turn, by poor powder flowability, violation of loose powder layers during processing and deformation of the part during processing. Thus by LPBF, high density can be achieved at optimal process parameters and scanning strategy.

Fig. 4 shows the graphic steps followed to produce a complete approved Ti6AI4V metal facial implant of an adult human produced in CRPM, at Central University of Technology with an EOSINT M280. Biomaterials are used to engineer functional restoration of different tissues to improve human health and the quality of life. A key issue in the designing of a new implant of any given product through AM is the prediction of the mechanical properties of the material. Several experimental results show AM-based products are often affected by widespread porosity, low density regions within their volume and anisotropy. These factors are due to manufacturing process, despite efforts of improving the process parameters. AM offers a

product development for rapid iteration between designs, assembly and functional tests, (Fig. 4c) bringing about a remarkable decrease in both time and product development costs.

(a) (b) (c)

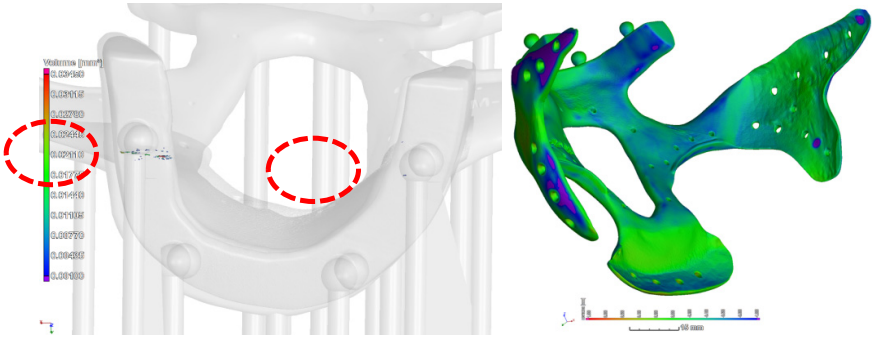

(d) (e)

Fig. 4: Facial titanium implant step preview (a) CT scan of human skull defected area (b) implant attachment after the use of a cutting guide, and (c) full 3D assembly, showing placement of implant with lower jaw to ensure no implant error; CT scans reconstruction of the facial Ti6Al4V ELI implant: pores (d) and the deviation of the LPBF part from prescribed CAD sizes (e).

Maxillofacial Ti6Al4V ELI implants produced by LPBF were analysed in terms of porosity by CT scans by General Electric VTomex L 240kV CT as described by du Plessis *et al.* in [du Plessis, 2016a-b]. First scans were done at 100 µm resolution and second time, when main porosity was identified, with 50 µm resolution to provide porosity details in the region of interest. In the first implant, two places were identified with serious defects, which run across the entire width of the sample (Fig. 4d). Under higher resolution, these type of porosity was recognised as layered defects. Analysis of the sample shows that layer pores were arisen due

to problems with the powder delivering. When the synthesis of the overhanging parts of the implant began, high residual stress led to the deformation of this part. That, in turn, caused the contact of the recoater with the deformed part and its vibration. The deformation confirmed by the high deviation of this part of the implant from prescribed sizes (Fig. 4e). After vibration, loose powder was compacted and settled, which led to a non-uniform delivering of the next powder layer and, subsequently, to the porosity of the part. For quality control of layered defects du Plessis et al. (2018) proposed to use witness specimens to ensure lack of layered or other unwanted types of defects, as this allows higher resolution to ensure these defects are not missed in a large-part scan [du Plessis, 2018].

In the other sample, the pores also were in a layer and form a porous plane through the samples tip which is up to 17.6 mm in length and the maximum pore's width in that region was 355 µm (Fig. 5). The recommendation was that the pores located in a load bearing section of the implants can influence on mechanical response of the implant and it was decided that this implant could not be suitable for the implant procedure. New implants with additional supports were produced and no internal defects more than 300 µm were identified by CT scans.

(a)

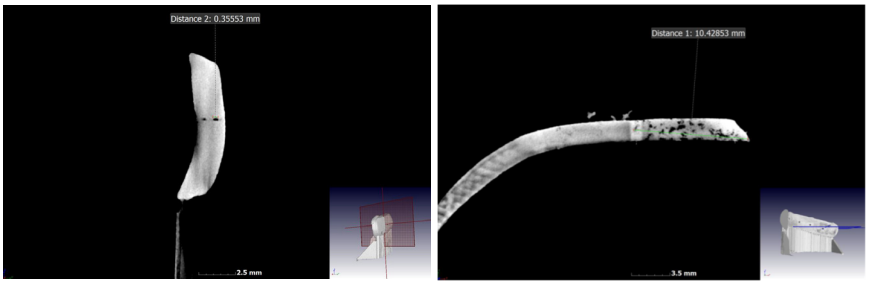

(b) (c)

Fig. 5: Total view of Ti6Al4V mandible implant; CT scans cross-section of mandibular implant: parallel (b) and perpendicular (c) to the build direction.

The new part with supports removed was then scanned and found defect free as mentioned above. This new part was subjected to microCT-based load simulation using the structural

mechanics simulation module of VGStudioMax 3.2. This is an immersed-boundary finite element method which allows calculation of displacements and stresses in voxel data using solid mesh elements, but not requiring a conformal mesh as in typical finite element software. This is computationally efficient and allows to evaluate the effect of real part geometries including defects, warping, internal porosity, etc. In this simulation, the inputs were linear isotropic material properties for Ti6Al4V: elastic modulus 115 GPa and Poisson's ratio 0.3, with loading direction selected as shown in Figure 6, with load 10 N. The stress distribution shows two major stress areas as shown where the stress reaches 100 MPa. This value is significantly lower than the yield stress of the material and hence, in this case, sufficiently safe for typical loads. However, much work remains in determining a suitable safety factor, validating this workflow, and assessing also the effect of such defects on fatigue life.

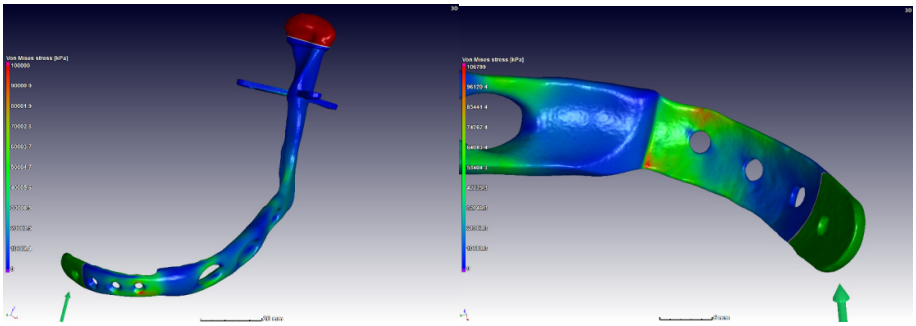

Figure 6: Mechanical simulation highlighting high stress areas in real part, using microCT data.

Quality control for complex shape objects such medical implants are of great interest; non-destructive quality control has to be performed on parts before implantation. ASTM had 21 standards for Ti alloys concerned medical device standards and implant standards to inspect and assess such instruments to ensure proper quality and workmanship [ASTM international]. But additionally, standard similar to "Standard practice for Computed Tomographic (CT) examination of castings", "Standard practice for radiographic examination of advanced aero and turbine materials and components", "New guide for non-destructive testing of Additive Manufactured metal parts used in aerospace applications" and "Standard guide for micro-computed tomography of tissue engineered scaffolds" should be developed for systematic CT scans non-destructive testing of AM Ti implants. It is very important that an implant does not contain critical pores. Understanding of critical porosity in general and maximum critical size of the pores permissible for different type of AM Ti implants are vital task for the new AM technology.

Detailed analysis of manufacturing strategy, build orientation and supports and its influence on porosity can be performed based on X-ray micro-computed tomography. Revealing of the typical shape of the pores and its size permit to produced samples with artificial defects and without it by LPBF. Analysis of porosity and mechanical properties of samples with defects will be compared against standard specimen samples and numerical simulations. Numerical simulation of various loading on test parts with defects and its evaluation by experimental data on loading permit to establish mechanical consequences of defects on manufactured customised mandible implants.

3. CONCLUSION AND FURTHER RESEARCH

A conclusion in the early stages of this work can be done on the basic expected outcomes of the research project:

- When conducting mechanical testing for the purpose of validation of the numerical simulations, all joint and forces during mastication must be tracked and included in both experiments and simulations, to assume ideal conditions for both cases, boundary conditions has to be taken into consideration.
- Defects are included in the design of mandibular Ti6Al4V test samples with different design geometries, thus to indicate to which size and direction of porosity will cause any significant defect in the geometry of a human mandible. An example of different test subjects will be subjected to porosity during LPBF with the aid of microCT-based simulations to validate experimental and simulated data.
- We believe that with the aid of mechanical testing in collaboration with numerical simulation and data analysis of different loaded porous implants open a new chapter in the development of reliable AM medical implants.

Acknowledgments

This work is based on the research supported by the South African Research Chairs Initiative of the Department of Science and Technology and National Research Foundation of South Africa (Grant №97994) and the Collaborative Program in Additive Manufacturing (Contract №CSIR-NLC-CPAM-15-MOA-CUT-01). The authors would like to acknowledge the

contributions made by the CRPM Team from the Central University of Technology, Free State as well as the Team from the CT Scanner Facility at the University of Stellenbosch.

REFERENCES

Al-Ahmari, A., Nasr, E.A., Moiduddin, K., Anwar, S., Al Kindi, M., Kamrani, A., 2015. A comparative study on the customized design of mandibular reconstruction plates using finite element method. *Advances in Mechanical Engineering*, 7(7), pp. 1-11

ASTM International, 2018. Medical Device Standards and Implant Standards. Available from: https://www.astm.org/Standards/medical-device-and-implant-standards.html.

Commisson, M. S., Martınez-Reina, J., Ojeda, J., Mayo, J., 2015. Finite element analysis of the human mastication cycle. *Journal of the mechanical behaviour of biomedical materials*, University of Seville, Spain, vol. 41, pp. 23-35.

Cordey, J., Borgeaud, M., Perren, S.M., 2000. Force transfer between the plate and the bone: relative importance of the bending stiffness of the screws friction between plate and bone. *Injury*, 31, pp. 21-28, 79, 84, 88, 92.

du Plessis, A., le Roux, A.G., Booysen, G., Els, J. 2016b. Quality Control of a Laser Additive Manufactured Medical Implant by X-Ray Tomography, *3D Printing and Additive Manufacturing*. 3(3), pp. 175-182.

du Plessis, A., le Roux, S.G., Els, J., Booysen, G. 2016a. Directionality of cavities and porosity formation in powder-bed laser additive manufacturing of metal components investigated using X-ray tomography, *3D Printing and Additive Manufacturing*. 3(1), pp. 48–55.

du Plessis, A., Sperling, P., Beerlink, A., le Roux, S.G., 2018. Standard method for microCT-based additive manufacturing quality control 5: witness specimen analysis. *MethodX*, in press.

du Plessis, A., Yadroitsava, I., le Roux, S.G., Yadroitsev, I., Fieres, J., Reinhart, Ch., Rossouw, P. 2017. Prediction of mechanical performance of Ti6Al4V cast alloy based on microCT-based load simulation. *Journal of Alloys and Compounds*, 724, pp. 267-274.

du Plessis A., Yadroitsava I., Yadroitsev I., le Roux S., X-ray micro computed tomography in additive manufacturing: a review of the current technology and applications. *3D printing and Additive Manufacturing*, 2018 *5*(3), pp.227-247.

Dunbar, A. J., 2016. *Analysis of the laser powder bed fusion additive manufacturing process through experimental measurement and finite element modelling*. PhD thesis, The Pennsylvania State University, USA, pp. 158.

Emin, A., 2017. The Mandible - Structure - Attachments – Fractures. TeachMeAnatomy, Available at: http://teachmeanatomy.info/head/osteology/mandible/, pp. 9 [Accessed March 20, 2018]

Faulkner et al., 1987. A three dimensional investigation of temporomandibular joint loading. *Journal of Biomechanics*, 20, pp. 997-1002

Ingawalé, S.M. and Goswami, T., 2012. Biomechanics of the Temporomandibular Joint, in: *Human Musculoskeletal Biomechanics*, Ed. T. Goswami, InTech, Available from: http://www.intechopen.com/books/human-musculoskeletal-biomechanics/biomechanics-of-thetemporomandibular-joint.

Khan, W., Muntimadugu, E., Jaffe, M., Domalb, A. J., 2014. Chapter 2 Implantable Medical Devices, *Focal controlled drug delivery*, pp. 33-59.

Kober, C., Erdmann, B., Lang, J., Sader, R., Zeilhofer, H. F., 2004. Adaptive finite element simulation of the human mandible using a new physiological model of the masticatory muscles. *In: Proc. Appl. Math. Mech*. 4, pp.332–333.

Lin, C.Y., Kikuchi, N., Hollister, S.J,. 2004. A novel method for biomaterial scaffold internal architecture design to match bone elastic properties with desired porosity. *Journal of Biomechanics,* 37, pp. 623−36.

Mommaerts, M.Y., 2016. Guidelines for patient−specific jawline definition with titanium implants in esthetic, deformity, and malformation surgery, *Annals of Maxillofacial Surgery*, 6(2), pp. 287-291

Nicoletto, G., Anzelotti, G., & Konečná, R., 2010. X-ray computed tomography vs. metallography for pore sizing and fatigue of cast Al-alloys. *Procedia Engineering*, 2(1), pp. 547-554.

Ramos, A., Ballu, A., Mesnard, M., Talaia, P., Simões, J. J., 2011. Numerical and Experimental Models of the Mandible, *Experimental Mechanics*, 10, pp. 1007.

Vagjel et al., 2013. Comparative Finite Element Analysis of the Biomechanical Stability of 2.0 Fixation Plates in Atrophic Mandibular Fractures. *Journal of Oral and Maxillofacial Surgery.* 71 (2), pp. 335-342.

Vanderesse, N., Maire, E., Chabod, A., & Buffière, J. Y., 2011. Microtomographic study and finite element analysis of the porosity harmfulness in a cast aluminium alloy. International *Journal of Fatigue*, 33(12), pp. 1514-1525.

Weiler, J. P., Wood, J. T., Klassen, R. J., Maire, E., Berkmortel, R., & Wang, G., 2005. Relationship between internal porosity and fracture strength of die-cast magnesium AM60B 333 alloy. *Materials Science and Engineering: A*, 395(1), pp. 315-322.

Whitaker, L.A., 1991. 1Aesthetic augmentation of the posterior mandible. *Plastic and Reconstructive Surgery*, 87, pp. 268−75.

Wong, R. C. W., Tideman, H., Merkx, M. A. W., Jansen, J., Goh, S. M., Liao, K., 2011. Review of biomechanical models used in studying the biomechanics of reconstructed mandibles. *Int. J. Oral Maxillofacial Surgeons*, vol. 40, pp. 393-400.

Yadroitsev, I., Krakhmalev, P., Yadroitsava I., du Plessis, A., 2018. Qualification of Ti6Al4V ELI alloy produced by laser powder bed fusion for biomedical applications. The Journal of The Minerals, Metals & Materials Society (TMS), 70 (3), pp. 372–377.

Zhao, C., Fezzaa, K., Cunningham, R.W., Wen, H., De Carlo, F., Chen, L., Rollett, A.D., Sun, T., 2017. Real-time monitoring of laser powder bed fusion process using high-speed X-ray imaging and diffraction, *Scientific Reports*, 7, pp. 61-230.

"Our deepest fear is not that we are inadequate. Our deepest fear is that we are powerful beyond measure, it is our light, not our darkness, that most frightens us. We ask ourselves 'Who am I to be brilliant, gorgeous, talented, and famous?' Actually, who are you not to be? You are a child of God. Your playing small does not serve the world. There is nothing enlightened about shrinking so that other people won't feel insecure around you. We were born to make manifest the glory of God that is within us. It's not just in some of us; it's in everyone. And as we let our own light shine, we unconsciously give other people permission to do the same. As we are liberated from our own fear, our presence automatically liberates others."

Maryanne Williamson